MODELING, ANALYSIS, AND DESIGN OF A PV-BASED GRID-TIED PLUG-IN HYBRID ELECTRIC VEHICLE BATTERY PACK CHARGER

Arash Shafiei

A Thesis

in

The Department

of

Electrical and Computer Engineering

Presented in Partial Fulfillment of the Requirements

for the Degree of Master of Applied Science at

Concordia University

Montréal, Québec, Canada

June 2013

CONCORDIA UNIVERSITY
School of Graduate Studies

This is to certify that the Thesis prepared

By: Arash Shafiei I.D. 9443371

Entitled: "Modeling, Analysis, and Design of a PV-based Grid-Tied Plug-In Hybrid Electric Vehicle Battery Pack Charger"

and submitted in partial fulfillment of the requirements for the degree of

Master of Applied Science

complies with the regulations of the University and meets the accepted standards with respect to originality and quality.

Signed by the final examining committee:

DR. ZAHANGIR KABIR Chair

DR. ANDREAS K. ATHIENITIS Examiner

DR. LUIZ A.C. LOPEZ Examiner

DR. SHELDON S. WILLIAMSON Supervisor

Approved by _____
Chair of Department or Graduate Program Director

_____
Dean of Faculty

Date _____

ABSTRACT

Modeling, Analysis, and Design of a PV-based Grid-Tied Plug-In Hybrid Electric Vehicle Battery Pack Charger

Arash Shafiei

Ever-increasing fossil fuels consumption in recent decades has emitted tremendous amounts of greenhouse gases, a big part of which cannot be absorbed by natural processes happening in nature. These gases have increased earth temperature by absorbing extra radiations from sunlight and turning them into heat. Global warming has had terrible effects for all creatures around the world and can threat life on Earth in future. Utilization of green or renewable energies during the recent years is getting more popular and can be a solution to this serious problem. A big source of these pollutants is transportation sector. Electrification of transportation can noticeably reduce greenhouse gasses if the electricity is obtained using renewable energy sources. Otherwise, it will just shift the problem from streets to fossil fuel power plants. Electric vehicles (EVs) were introduced around one century ago; however, they were replaced by internal combustion engine cars over time. Nevertheless, recently they are getting more interest because of their superior performance and clean operation.

Solar electricity which can be obtained using photovoltaic panels is one of the easiest ways as long as sun is available. They can be easily mounted on the roofs of buildings or roof tops of parking slots generating electric power to charge the battery pack of the EVs while providing shade for the cars. Since solar energy is intermittent and variable, power grid should be involved to ensure enough power is available. Conventional solar chargers inject power to the grid and use grid as the main source because of its reliability and being infinite. Hence, they use

grid as a kind of energy storage system. This approach can lead to problems for grid stability if solar panels are utilized in large scales and comparable to the grid.

In this work, a solar powered grid-tied EV/PHEV charger is introduced which uses all the available power from PV panels as the main energy source and drains only the remaining required power from the grid. The proposed configuration provides great flexibility and supports all the possible power flows. To design an efficient system the load should be known well enough first. A comprehensive study has been done about behavior, characteristics and different models of different chemistries of batteries. Specific phenomena happening in battery packs are outlined. A novel maximum power point tracking (MPPT) technique has been proposed specifically for battery charging applications. A specific configuration involving DC link coupling technique has been proposed to connect different parts of the system. Different possible topologies for different parts of the proposed configuration have been considered and the suitable ones have been selected. Dual active bridge topology is the heart of this configuration which acts as the bidirectional charger. A detailed state space modeling process has been followed for the power converters and various small signal transfer functions have been derived. Controllers have been designed for different power converters using SISO design tool of Matlab/Simulink. Different modes of operation for the charger including constant current mode (CCM) and constant voltage mode (CVM) have been analyzed and appropriate cascade controllers have been designed based on required time domain and frequency domain characteristics. Finally, simulation tests have been conducted and test results have been graphed and analyzed for different modes of operation, all possible power flows and various voltage and current set points.

ACKNOWLEDGMENTS

The author would like to express his sincere gratitude to his supervisor, Dr. Sheldon S. Williamson, for his patient and invaluable guidance, advice and friendship throughout the Master's program.

The author would like to thank his other distinguished professors and colleagues in the Power Electronics and Energy Research (PEER) group, within the P. D. Ziogas Power Electronics Laboratory.

Last, but not least, I would like to extend my most sincere gratitude to my family, specially my father, Dr. Mohammad Mehdi Shafiei and my mother. Without their steady support, encouragement and love the author would never be able to accomplish this work.

TABLE OF CONTENTS

ABSTRACT III

ACKNOWLEDGMENTS V

CHAPTER.1

Introduction 1

1.1 Research Background 1

1.2 Objectives 6

1.3 Contributions 6

1.4 Outline of the thesis 7

CHAPTER.2

Battery Features And Models in Vehicular Applications 8

2.1 Introduction 8

2.2 Battery Parameters 10

2.2.1 Battery Capacity 10

2.2.2 C Rate 10

2.2.3 State of Charge 11

2.2.4 Depth of Discharge 11

2.2.5 Energy Density 11

2.2.6 Charging Efficiency 12

2.3 Main Characteristics of Commonly Used Batteries in EV/PHEV Battery Packs .. 12
2.3.1 Lead-Acid (Pb-Acid) ... 13
2.3.2 Nickel Cadmium (Ni-Cd) ... 13
2.3.3 Nickel Metal Hydride (Ni-MH) ... 13
2.3.4 Lithium Ion (Li-Ion) ... 14
2.3.5 Lithium Polymer (Li-Po) ... 14

2.4 Charging Methods ... 15
2.4.1 Constant Voltage Charge ... 15
2.4.2 Constant Current Charge ... 16
2.4.3 Taper Current Charge ... 17
2.4.4 Pulse Charge ... 17
2.4.5 Reflex Charge ... 17
2.4.6 Float charge ... 18

2.5 Termination Methods ... 19
2.5.1 Time ... 19
2.5.2 Voltage ... 20
2.5.3 Voltage Drop (dV/dT) ... 20
2.5.4 Current ... 20
2.5.5 Temperature ... 21

2.6 Cell Balancing ... 21
2.6.1 Charging ... 23
2.6.2 Passive ... 24
2.6.3 Active ... 24

2.7 SoC Estimation ... 27
2.7.1 Complete Discharge ... 28
2.7.2 Ampere-Hour Counting ... 28
2.7.3 Measurement of Physical Characteristics ... 29
2.7.4 Open Circuit Voltage ... 29
2.7.5 Soft Computation Techniques ... 29

2.8 Charging Algorithm ... 30

2.9 Battery Models 33
2.9.1 Electrochemical Models 34
2.9.2 Stochastic Models 35
2.9.3 Analytical Models 35
2.9.4 Electrical Circuit Models 36
2.9.5 Thermal Models 41
2.9.6 Other Models 42
2.9.7 Utilized Battery Model 44

2.10 Summary 53

CHAPTER.3

A Novel Maximum Power Point Tracker For Battery Charging Applications 55

3.1 Introduction 55

3.2 PV Array Model 57

3.3 Control System Design 60

3.4 Simulation Results 68

3.5 Summary 70

CHAPTER.4

Power Electronics Interface 71

4.1 Introduction 71

4.2 Conventional structures of PV systems 73
4.2.1 Central Inverters: 74
4.2.2 String Inverters: 74

4.2.3 Module integrated inverters: 75

4.3 Topologies for PV inverters: 76
4.3.1 PV inverters with DC-DC converter and isolation: 76
4.3.2 PV inverters with DC-DC converter and without isolation: 77
4.3.3 PV inverters without DC-DC converter and with isolation: 78
4.3.4 PV inverters without DC-DC converters and without isolation: 78
4.3.5 Possible PV interconnection schemes: 79
4.3.6 Proposed Structure: 81

4.4 Power Converters Topology 84
4.4.1 MPPT Stage 84
4.4.2 Rectifier / Inverter Stage 85
4.4.3 Charger Stage: 85

4.5 Summary 87

CHAPTER.5

System Modeling and Controller Design 88

5.1 Introduction 88

5.2 PV Stage 90

5.3 Rectifier / Inverter Stage 94

5.4 DAB Stage 107
5.4.1 DAB Steady State Operation 110
5.4.2 DAB State-Space Average Model 115
5.4.3 DAB Small-Signal Linear Model 123
5.4.4 DAB Small-Signal Transfer Functions 125
5.4.5 DAB Design: 130
5.4.6 DAB Controllers Design: 152

5.5 Summary 163

CHAPTER.6

Simulation Results 165

6.1 Mode 1 166

6.2 Mode 2 168

6.3 Mode 3 170

6.4 Mode 4 172

6.5 Mode 5 174

6.6 Mode 6 176

CHAPTER.7

Conclusions and Potential Future Work 178

7.1 Conclusions 178

7.2 Potential Future Work 181

REFERENCES 183

LIST OF FIGURES

Fig. 1.1 U.S. Greenhouse Gas Emissions by Gas Type 2

Fig. 1.2 U.S. Energy-Related Carbon Dioxide Emissions by Major Fuel, 2011 2

Fig. 1.3 U.S. Energy-Related Carbon Dioxide Emissions by Sector Fuel, 2011 3

Fig. 2.1 Charging algorithm of a typical Lead-acid battery 31

Fig. 2.2 Kinetic Battery Model (KiBaM) 36

Fig. 2.3 (a) Thevenin-based (b) Impedance-based (c) runtime-based battery models 37

Fig. 2.4 Electrochemical Equivalent Circuit Model 39

Fig. 2.5 Typical Voltage response of Li-ion battery discharged by a pulse discharge current 40

Fig. 2.6 Matlab/Simulink Battery Model 45

Fig. 2.7 Voltage characteristic of 45 Ah Li-ion battery 46

Fig. 2.8 Voltage characteristic of 45 Ah Li-ion battery from 30% to 90% SoC 47

Fig. 2.9 Parallel RC Battery Model 48

Fig. 2.10 Voltage characteristic and derivative of 45 Ah Li-ion battery from 30% to 95% SoC. 49

Fig. 2.11 Simulation results for Matlab battery model and paralle RC model for 100% SoC window 51

Fig. 2.12 Simulation results for Matlab battery model and paralle RC model for 60% SoC window 52

Fig. 3.1 Typical photovoltaic cell characteristics: a) I-V curve b) P-V or P-I curve 55

Fig. 3.2 Typical circuit based photovoltaic cell model 58

Fig. 3.3 Proposed hybrid PV model for simulation in MATLAB/Simulink 59

Fig. 3.4 Proposed Maximum Power Point Tracker 60

Fig. 3.5 Buck converter as MPPT stage 61

Fig. 3.6 The proposed block diagram configuration for capturing MPP 64

Fig. 3.7 Bode plot of Eq. (3.10) 67

Fig. 3.8 Simulations results: a) Instantaneous value of short circuit current of the PV panel b) Saturation detection by the relay c) Current reference d) Actual output current e) Average PV power 69

Fig. 4.1 Conventional PV structures: a) Central Inverter b) String Inverter c) Module Inverter . 73

Fig. 4.2 Multi-string Inverter structure 75

Fig. 4.3 Power Configurations for PV inverters 76

Fig. 4.4 PV inverter configurations with DC-DC converter and isolation: a) Transformer on LF side, b) Transformer on HF side 77

Fig. 4.5 PV inverter configuration with DC-DC converter and without isolation..... 77

Fig. 4.6 PV inverter configuration without DC-DC converter and with isolation..... 78

Fig. 4.7 PV Inverter configuration without DC-DC converter and without isolation 79

Fig. 4.8 A typical P-V curve of a partially shaded PV array 80

Fig. 4.9 Different cell interconnections: Series-Parallel (SP), Total-Cross Tied (TCT) and Bridge-Link (BL) 81

Fig. 4.10 System Structure..... 82

Fig. 4.11 Modes of operation..... 83

Fig. 4.12 Rectifier / Inverter stage 85

Fig. 4.13 DAB with Half-Bridge converter at one side 86

Fig. 5.1 Basic PV stage model in Matlab/Simulink..... 91

Fig. 5.2 Modified PV stage model in Matlab/Simulink..... 92

Fig. 5.3 Simulation results for PV stage 93

Fig. 5.4 Rectifier / Inverter stage 94

Fig. 5.5 Input current and voltage phasor diagram of Rectifier / Inverter 96

Fig. 5.6 Principles of hysteresis current control 99

Fig. 5.7 Controller block diagram for HCC 101

Fig. 5.8 Bode diagram of control to output for Rectifier / Inverter stage 102

Fig. 5.9 Step response of control to output for Rectifier / Inverter stage 102

Fig. 5.10 Bode plot and root locus of the new open loop transfer function..... 103

Fig. 5.11 Closed loop step response of Rectifier / Inverter stage with controller..... 104

Fig. 5.12 Simulation results for Rectifier / Inverter stage in Rectification mode 105

Fig. 5.13 Simulation results for Rectifier / Inverter stage in Inversion mode 106

Fig. 5.14 DAB with Half-Bridge converter at one side 107

Fig. 5.15 DAB circuit for operation analysis 108

Fig. 5.16 Simplified circuit of DAB 109

Fig. 5.17 Fundamental frequency model of DAB..... 109

Fig. 5.18 Equivalent circuits for different time intervals..... 111

Fig. 5.19 Voltage and current waveforms of DAB 112

Fig. 5.20 Power flow of DAB in p.u. versus phase shift in rad 115

Fig. 5.21 T_A^+, T_{B2}, T_{B3} conducting 119

Fig. 5.22 T_A^+, D_{B1}, D_{B4} conducting..... 119

Fig. 5.23 D_A-, D_{B1}, D_{B4} conducting 120

Fig. 5.24 Small-signal representation of the regulated DAB 129

Fig. 5.25 Transformer RMS current vs. L, f_{sw}, V_{DC} and R for 180 degrees phase shift range for resistive load 140

Fig. 5.26 I0, I1 & I2 vs. angle for constant voltage load 142

Fig. 5.27 Voltage and current waveforms of inductor and load of DAB 147

Fig. 5.28 Bode plot for control-to-state transfer function 153

Fig. 5.29 Poles and zeros of control-to-output transfer function 154

Fig. 5.30 Step response of control-to-output transfer function 154

Fig. 5.31 Bode diagram of open loop control-to-state transfer function and Ci 155

Fig. 5.32 Step response of inner closed loop for 45º and 70º phase margin 156

Fig. 5.33 Root Locus diagram for current loop with the controller 157

Fig. 5.34 Simulation results for current controller of DAB 158

Fig. 5.35 Bode diagram of voltage open loop transfer function 159

Fig. 5.36 Bode plot of voltage open loop including $G_{OL,v}$ and $G_{\varphi x2}$ 160

Fig. 5.37 Step response of outer closed loop for 60º and 70º phase margin 161

Fig. 5.38 Simulation results for voltage controller of DAB 162

Fig. 6.1 Mode 1 of operation 166

Fig. 6.2 Simulation results for Mode 1 167

Fig. 6.3 Mode 2 of operation 168

Fig. 6.4 Simulation results for Mode 2 169

Fig. 6.5 Mode 3 of operation 170

Fig. 6.6 Simulation results for Mode 3 171

Fig. 6.7 Mode 4 of operation 172

Fig. 6.8 Simulation results for Mode 4 173

Fig. 6.9 Mode 5 of operation 174

Fig. 6.10 Simulation results for Mode 5 175

Fig. 6.11 Mode 1 of operation 176

CHAPTER.1

INTRODUCTION

1.1 Research Background

Earth temperature has risen by 1.1° to 1.6°F over the past century as assessments by Intergovernmental Panel on Climate Change (IPCC) show. This has caused noticeable climate change evidences such as ice mass loss and decreasing snow cover in both the northern and southern hemispheres, rising sea levels, more frequent extreme weather events, floods, more sever tropical storms and hurricanes, volcanoes, acidification of oceans and much more. These are all due to increased greenhouse gasses made by human activities. Since large-scale industrialization began around 150 years ago, levels of several important greenhouse gasses have increased by about 40%. Fossil fuels constitute around three-fourths of human-made emissions during the past 20 years. Some of the emitted greenhouse gasses can be absorbed by natural processes happening in the nature but the remaining will be added to the atmosphere. On an annual average basis, 7.2 billion metric tons of greenhouse gasses are produced each year, 4.1 billion metric tons of which are added to the atmosphere annually. The process which increases the Earth temperature can be simply described by extra absorption of radiations coming from the Sun by additional greenhouse gasses made by human activities and converting them to heat.

Greenhouse gas emissions include different types of gases, each of which include a portion of the total emissions. Considering United States, a highly industrial country emitting large amounts of pollutants each year as an example, the latest available data provided by U.S. Energy Information Administration (EIA) shows that carbon dioxide (CO_2) emissions constitute

81.5% of total gas emissions in U.S. as shown in Fig. 1.1. Other gases include Methane, Nitrous Oxide, Fluorinated Gases and other carbon dioxide gases constituting 11.1%, 3.3%, 2.7% and

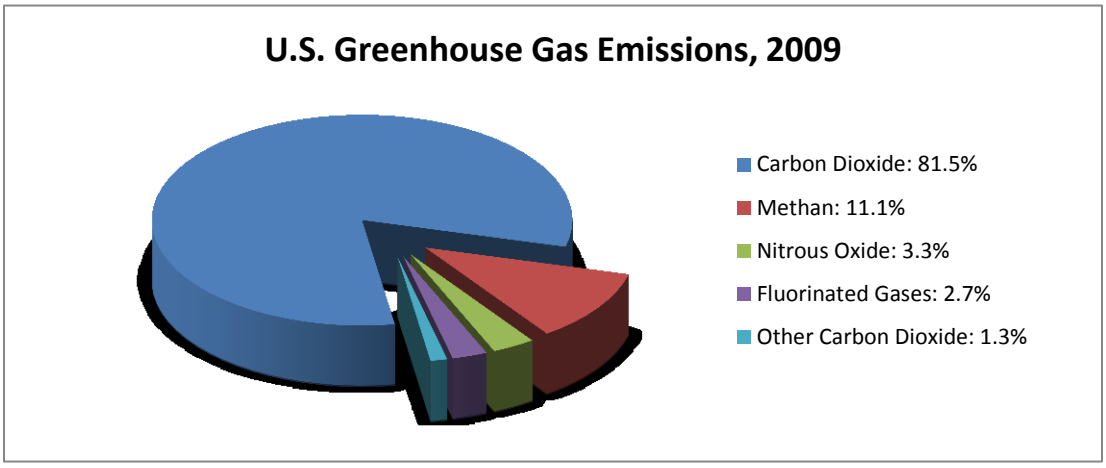

Fig. 1.1 U.S. Greenhouse Gas Emissions by Gas Type

1.3% accordingly. According to the big portion of CO_2 emissions the sources of this gas should be considered. The biggest carbon dioxide emitting sector in U.S is the energy sector. About 87% of the total amount of U.S. greenhouse gases emitted in 2010 has been energy-related and 91% of those energy-related gases have been carbon dioxide from the combustion of fossil fuels. Main energy-related fossil fuels used in U.S. are petroleum, coal and natural gas as depicted in Fig. 1.2.

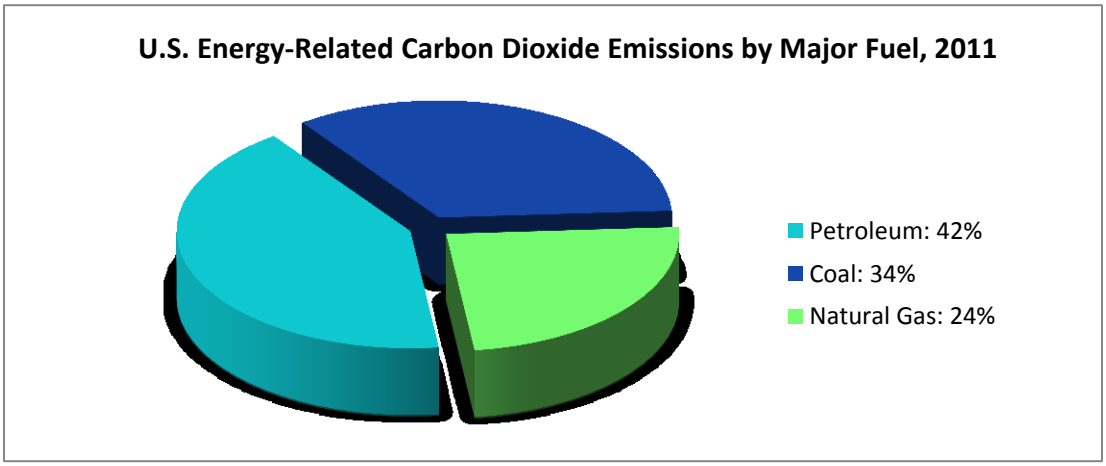

Fig. 1.2 U.S. Energy-Related Carbon Dioxide Emissions by Major Fuel, 2011

The major fuels are used in different sectors of the U.S. economy each one contributing to the greenhouse gas emissions. Electric power generation is the biggest part emitting 40% of the total carbon dioxide and transportation stays on the second level with 34% as illustrated in Fig. 1.3. The remaining is due to the direct use of fossil fuels in residential and commercial buildings and by industry. Emissions by electric power generation and transportation section together have increased at an average rate of 0.8% per year in the period of 1990 to 2011.

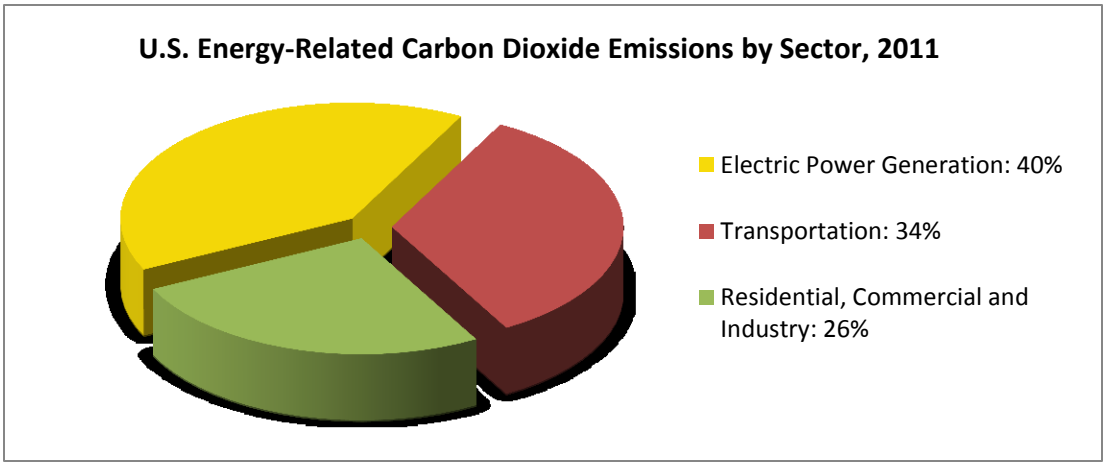

Fig. 1.3 U.S. Energy-Related Carbon Dioxide Emissions by Sector Fuel, 2011

The abovementioned data in addition to the lack of sources of fossil fuels and their rising price clearly illustrates the ever-increasing necessity of independency from fossil fuels in sectors such as transportation. This has caused the attraction towards Electric Vehicles (EVs). The introduction of EVs is not recent and goes back to around 100 years ago. Actually, the first cars have been electric cars; however, because of problems such as short mileage and lack of power electronics technology at that time, they disappeared over time. This was due to the small energy density of batteries. Although battery technology has improved a lot over the previous century, batteries are still the main challenge of commercialization of EVs because of their weight and limited amount of stored energy compared to gasoline. Fortunately, this problem is getting

solved over time with the introduction of new chemistries like Lithium-based batteries and new technologies like Nano-Technology. Despite this problem, some short range pure EVs have been introduced to the market such as Nissan Leaf, Chevy Volt, ZENN and others. EVs with comparable range to conventional Internal Combustion Engines have also been introduced like ROADSTER. However, because of their very big battery pack they are very expensive and non-affordable for most of the customers (a $125,000 electric vehicle with a $53,000 battery pack!). To overcome the battery problem in short term, Hybrid Electric Vehicles (HEVs) and Plug-in Hybrid Electric Vehicles (PHEVs) have been introduced as a temporary solution.

According to Fig. 1.3 electrification of transportation is very beneficial environmentally. However, this is one side of the coin. According to published data by U.S. EIA for 2010 around 70% of the total electricity in U.S. has been generated using coal, petroleum, natural gas and other gases. Only the remaining 30% electricity generation has been achieved using conventional hydroelectric power, geothermal, waste, solar/photovoltaic, wind or renewable energy in general. This shows that merely electrification of transportation will not solve the problem, but just shifts the problem from streets to the power plants. Even neglecting the destructive effects of greenhouse gases emitted in fossil fuel power plants, charging millions of EVs and PHEVs battery packs with considerable charging power levels coming to the market in near future using the existing power grids seems impossible and expansions of power grids and establishing new costly power plants is inevitable. Therefore, the long term solution will be definitely moving towards renewable energy, preferably, generating power near the load instead of thousands of kilometers far from the load involving lots of power losses in transmission and distribution lines. Charging EVs and PHEVs using renewable energies near the load has lots of benefits such as making these loads independent of the power grid and consequently reducing greenhouse gases,

saving money since the source of electricity which is Sun is free, the ability of selling this electricity to the grid and earning money or at least reducing electricity bills, working as an emergency power source in the events of blackout and more. Among different renewable energy sources, solar energy is freely available everywhere and easily achievable. Photovoltaic (PV) Panels can be integrated to the commercial and residential buildings roofs without the need of specifying and investing for separate areas.

In addition, environmental regulations are getting more stringent every year forcing automakers to improve the fuel economy of their productions which is encouraging them towards manufacturing of EV/PHEVs. Besides, the ever-increasing price of gasoline is encouraging customers towards using EV/PHEVs. Governments are supporting this goal by defining different programs like California Solar Initiative (CIS) which has the goal of installing 3,000 megawatts of solar electricity by 2016. The solar carport installed at the Indian Pueblo Cultural Center (IPCC) located in Albuquerque, New Mexico is one of the projects currently generating electricity. This solar system generates over 11 kW of DC power at peak hours in summer, 25 MWh of clean free electric energy annually, while providing car shading at the same time. This installation results in around $3,500 per year savings on the electric bill of the IPCC. In addition to the financial benefits, environmental benefits are of great importance. The utility grid powering the IPPC obtains 70% of its power from a coal-fired plant and the remaining 30% from a nuclear power plant. Huge amounts of water are required for producing steam and cooling down purposes in power plants. Annually, the solar carport in IPCC saves 660,045 gallons of water in coal-fired plant and 413,100 gallons in nuclear plant. Besides, it avoids over 27 tons of carbon dioxide each year.

1.2 Objectives

Objectives of this thesis are to do a comprehensive study to address issues related to EV/PEHV chargers using solar energy such as characteristics of EV/PHEV battery packs, Maximum Power Point Tracking (MPPT) techniques, required power electronics circuits and designing a proper charger accordingly to consider both battery pack lifetime and overall system efficiency.

1.3 Contributions

The contributions of this work are:

- A comprehensive study of characteristics of battery packs, different chemistries, issues affecting their life cycle, different charging schemes and suitability of them for each battery chemistry.
- An overview of battery models with specific focus on EV/HEV/PHEV battery packs and their suitability for different applications and finally introduction of a new method for parameter identification of a proper model for charger application.
- Introduction of a novel Maximum Power Point Tracking (MPPT) technique for battery charging applications.
- Introduction of a PV model suitable for solar system design for use in Matlab/Simulink
- An overview of available converter topologies and selection of a proper circuit topology for EV/PHEV battery pack charger application based on required criteria.

- Derivation of a detailed small-signal control-oriented model of the DAB converter representing the dynamic behavior of the EMI filters connected to the converter ports.
- Design and analysis of controllers based on time domain requirements of the application.

1.4 Outline of the thesis

This thesis is organized as follows:

CHAPTER.1 outlines the background of the research by an introduction of effects of utilization of fossil fuels for transportation and electric power generation.

CHAPTER.2 comprehensively studies battery features and mentions battery models with specific focus on vehicular applications. Besides, it selects a suitable battery model for this work.

CHAPTER.3 classifies Maximum Power Point Tracking (MPPT) techniques and finally introduces a novel MPPT technique appropriate for battery charging applications.

CHAPTER.4 studies conventional PV system configurations and proposes a suitable configuration for a grid-tied PV based battery charger and chooses suitable converter topologies.

CHAPTER.5 addresses the modeling and control issues of Dual Active Bridge (DAB) converter using a detailed small-signal control-oriented model.

CHAPTER.6 includes the simulation results.

CHAPTER.7 includes conclusions and potential future work.

CHAPTER.2

BATTERY FEATURES AND MODELS IN VEHICULAR APPLICATIONS

2.1 Introduction

One of the biggest challenges in electric transportation is storing electrical energy for use in desired times and desired amounts. Batteries are mostly considered because of their high energy density compared to their counterparts and also their ability to get charged providing regenerative braking capability. The electrochemical nature of batteries has a highly nonlinear behavior and dependent on many factors such as state-of-charge, state-of-health, runtime, temperature, ageing, load profile and charging algorithm. A very important concern is related to storage, because in order to have a given amount of energy for a reasonable All Electric Range (AER), tens or hundreds of cells should be connected in series and parallel for the desirable voltage and current ratings of the battery pack. This causes the nonlinear behavior of cells to be more prominent. Furthermore, there are some phenomena that are observed only in battery packs and not in single cells, such as thermal unbalance among the cells in pack.

EV and PHEV battery packs are relatively expensive compared to the price of the whole car, because of high number of cells, chemistry types such as Lithium-based, and protection circuits. Accordingly, the life cycle of these battery packs are very important for a cost-effective user's point of view. Therefore, lower cost for final customer can be achieved with increasing the battery pack life cycle, resulting in less frequent replacements of the whole pack. As a real

example related to Honda Civic, recently, there has been news [1] about Honda Company regarding the battery packs of Honda Civics produced during 2006 to 2008. Apparently, some of the battery packs in the second-generation Honda Civic hybrids are failing prematurely after 5 years. According to regulations in California, there is a 10-year, 150,000-mile warranty requirement on the components of the hybrid system. Although Honda Company took recall actions, some customers were not satisfied and preferred to change themselves the battery packs. It has been reported that those battery packs cost about $2,000 excluding tax, shipping and installation.

This case shows the importance of the battery packs price in the commercialization of EVs and PHEVs in a large scale. A factor that highly impacts the life cycle of battery packs is the charging algorithm. There are other factors also involved such as the charging time that plays an important role in high attraction to EVs and PHEVs. These topics and all other ones related to this area should be mainly handled with a multi-level control and power system called Battery Management System (BMS) which takes care of all or some of the aspects affecting batteries in any way. While charging the battery pack, BMS works in collaboration with the charger. Depending on the architecture of the system, BMS can be integrated to the charger. The more accurate and comprehensive the BMS is the more reliable, safer and faster the charging procedure can be done. Designing a highly efficient BMS needs very good understanding of the behavior of single cells according to the variations of different parameters and also parameter variation and behavior change in a packed large number of cells.

2.2 Battery Parameters

To design an efficient, precise, reliable and safe charger, parameters of the battery pack should be determined. A brief definition of battery parameters are mentioned here which will be used later.

2.2.1 Battery Capacity

Measured in Ampere-Hour (Ah), battery capacity indicates the amount of charge that can be drawn from a fully charged battery until it gets fully discharged. An important effect in batteries is that the higher amount of current drawn from a battery, the lower capacity the battery will have. Hence, theoretically, battery capacity is defined as the current value that if the battery is discharged with that value, the battery completely discharges it in one hour. However, in practice battery manufacturers specify a table showing the amount of time the battery runs with different constant current loads and different constant power loads. In practice, this table provides more practical information rather than standard definitions, because, after production different loads with different characteristics may be connected to the battery.

2.2.2 C Rate

This parameter is used to show the amount of current used for charging the battery. For example, for a 10 Ah battery, when it is mentioned to terminate the charging process when the charging current falls below C/10 rate (10 hour rate), it means the charging should be stopped when current becomes less than the amount of current with which the battery is discharged after 10 hours, or specifically 10Ah/10h = 1 Amp.

2.2.3 State of Charge

State of Charge (SoC) is the percentage of charge available from a battery to the whole capacity of the battery. SoC is difficult to measure directly and usually some methods are used to estimate it indirectly. Besides, according to ageing the rated capacity of the battery reduces over time, hence, for determining accurate SoC, the rated capacity should be measured or calculated regularly.

2.2.4 Depth of Discharge

Depth of Discharge (DoD) is defined as (100 – SoC) in percentage, i.e. the percentage of total charge of the battery which has been utilized. This parameter is usually used in discharge patterns recommendations. For example, the battery manufacturer may recommend the user not to go over 70% DoD according to lifetime issues.

2.2.5 Energy Density

Energy density can be defined based on volume or weight, i.e. Wh/L or Wh/Kg. The "Volumetric Energy Density", which is defined as the amount of available energy from a fully charged battery per unit volume (Wh/Liter). As we know Liter is used for measuring the volume of liquids, however, even for solid electrolytes such as Lithium Polymer batteries, the same unit is usually used. The other way of defining the Energy Density is "Gravimetric Energy Density" which is also referred as "Specific Energy" and defined as the available energy from a fully charged battery per unit weight (Wh/Kg). Based on application and based on the importance of the volume or weight, either definition can be used. In the case of EVs/PHEVs usually weight is a more important factor than volume, so, mostly Specific Energy used.

2.2.6 Charging Efficiency

The chemical reactions inside the battery during charge and discharge are not ideal and there are always losses involved. Therefore, not all the energy used to charge the battery, is available during discharge. Some of this energy is wasted as heat dissipation. The charging efficiency can be defined as the ratio of available energy from the battery in a complete discharge to the amount of energy needed to completely charge the battery. This parameter may be mentioned by other names such as “Coulombic Efficiency” or “Charge Acceptance”. In general, the coulombic efficiency for a new battery is high, but reducing as the battery ages.

Next section discusses some aspects of different battery types used in EVs and PHEVs regarding charging. This will help in designing more efficient and flexible chargers based on battery behaviors which will finally lead to improvement of battery packs lifetime.

2.3 Main Characteristics of Commonly Used Batteries in EV/PHEV Battery Packs

Knowledge of characteristics of different battery chemistries is necessary for designing a reliable and efficient charger. There are hundreds of types of batteries described in reference books [2] and technical literature. Most of them are demonstration prototypes, working under laboratory conditions and still under investigation, not commercialized maybe because of costs, non-mature technology, low energy density, safety, toxic components and so on. The most widely available batteries are Pb-Acid, Ni-Cd, Ni-MH, Li-Ion, and Li-Polymer which are described below:

2.3.1 Lead-Acid (Pb-Acid)

For over one century, lead acid batteries have been utilized for various applications including traction. Their well improved structure has led to Valve Regulated Lead Acid (VRLA) batteries which can be considered as maintenance free batteries, which is a desirable characteristic for PHEVs. In terms of charge efficiency they have a high efficiency in the range of 95% to 99%. The main disadvantage of Lead-acid batteries is their weight, in other words, they have a low specific energy (30 - 40 Wh/Kg) compared to their counterparts.

2.3.2 Nickel Cadmium (Ni-Cd)

Considering low power applications Nickel Cadmium (Ni-Cd) batteries also benefit from a mature technology but considering traction applications their specific energy is low as well. The typical specific energy for this type is 45 - 60 Wh/Kg. The main applications are in portable devices, but they are also recommended when high instantaneous currents must be provided. They are typically used when long life and reasonable costs are desired. However, they have environmental concerns for recycling because they contain toxic metals [3].

2.3.3 Nickel Metal Hydride (Ni-MH)

Comparing to previous types they have higher specific energy at the expense of lower cycle life. In general, for the same size batteries, NiMH batteries can have up to two or three times more energy than a Ni-Cd type. The typical value for the specific energy of the present technology NiMH batteries is in the range of 75 - 100 Wh/Kg. This type is widely used in EV and PHEV applications.

2.3.4 Lithium Ion (Li-Ion)

This type has noticeably high specific energy, specific power and great potential for technological improvements providing EVs and PHEVs with perfect performance characteristics such as acceleration performance. Their specific energy is in the range of 100 - 250 Wh/Kg. Because of their nature, Li-ion batteries can be charged and discharged faster than Pb-Acid and Ni-MH batteries, making them a good candidate for EV and PHEV applications. Besides all, Li-ion batteries have an outstanding potential for long life if managed in proper conditions, otherwise, their life can be a disadvantage. One of the main reasons is almost the absence of memory effect in Li-based batteries. A weak point of Li-based batteries is safety since they are highly potential for explosion due to overheating caused by overcharging. They can almost easily absorb extra charge and get exploded. The use of advanced battery management systems (BMS) can ensure reliable range of operation of Li-ion batteries even in cases of accidents. Another advantage is that Li-ion batteries have environmentally friendly materials when compared with Nickel based batteries.

2.3.5 Lithium Polymer (Li-Po)

Li-Po batteries have the same energy density as the Li-ion batteries but with lower cost. This specific chemistry is one of the most potential choices for applications in EVs and PHEVs. There have been significant improvements in this technology. Formerly, the maximum discharge current of Li-Po batteries was limited to about 1C rate; however, recent enhancements have led to maximum discharge rates of almost 30 times the 1C rate, which greatly improves and simplifies the storage part of the EVs and PHEVs in terms of power density, since this can even eliminate the need of ultra-capacitors. Besides, there have been outstanding improvements in charging times. Recent advances in this technology have led to some types which can reach over

90% SoC in a couple of minutes which can significantly increase the attraction towards EVs and PHEVs because of noticeable reduction of charging time. Because this type is a solid state battery, having solid electrolyte, the materials would not leak out even in the case of accidents. One of the other advantages of this type is that it can be produced in any size or shape which offers flexibility to vehicle manufacturers.

2.4 Charging Methods

Charging in general is the action of putting energy back to the battery i.e. restoring energy. It is important to know that different chemistries may require completely different charging methods. Other factors affecting the choice of charging method are capacity, required time or other factors. The most common techniques are mentioned here:

2.4.1 Constant Voltage Charge

As it is clear from the name "Constant Voltage" or CV is when a constant voltage is applied to the battery pack. This voltage is a pre-set value given by the manufacturer. This method is accompanied with a current limiting circuit most of the time, especially for the beginning periods of charging where the battery easily takes high rates of current comparing to its capacity. The current limitation value mainly depends on the capacity of the battery. Depending on the battery type to be charged, this pre-set voltage value is chosen. For example, for Li-ion cells the value of 4.200 V +/- 50 mV is desirable, so the pre-set value for the whole battery pack can be obtained by multiplying this value with number of cells in series. An accurate set point is necessary, since overvoltage can damage the cells and under-voltage causes partial charge which will reduce life cycle over time. Therefore, the circuit used for charging,

which can be a simple buck, boost or buck/boost topology depending on the voltage ratio of input and output, should be accompanied with a controller to compensate for source and load changes over time. When the cell reaches the pre-set voltage value, this causes the battery to be in a standby mode, ready for later use. The amount of this idle time should not be very long and should be limited based on the manufacturer recommendations. This method is usually used for lead acid batteries, also for Li-ion batteries while using current limiter to avoid overheating the battery especially in the first stages of the charging process [4].

2.4.2 Constant Current Charge

Constant current charging method is applying a constant current to the battery with low percentage of current ripples independent of the battery state of charge or temperature. The abbreviation for this method is CC in the literature. This is achieved by varying the voltage applied to the battery using control techniques such as current mode control to keep the current constant. CC technique can be implemented using a “Single Rate Current” or “Split Rate Current”. In single rate only one pre-set current value is applied to the battery which is useful in balancing the cells. However, backup circuits must be used to avoid overcharging. In the split rate CC different rates of current are applied based on SoC, time of charge, voltage, or combination of them in different stages of charging. This gives more accurate and balanced charging and circuits should be used to avoid overvoltage of the cells. In some cases, for prolonging dead batteries, CC method with high rates and low duration can be utilized to extend the lifetime of the battery. But, this is a very cautious procedure and must be done carefully. Ni-Cd and Ni-MH batteries are charged using CC. Ni-MH batteries can be easily damaged due to overcharging, so, they should be accurately monitored during charging [5].

2.4.3 Taper Current Charge

This method can be used when the source is a non-regulated. It is usually implemented with a transformer with a high output voltage comparing to the battery voltage. A resistance should be used to limit the current flowing to the battery. A diode can also be used to ensure unidirectional power flow to the battery. In this method the current starts at full rating and gradually decreases as the cell gets charged. This technique is only applicable to Sealed Lead Acid (SLA) batteries.

2.4.4 Pulse Charge

This technique involves using short time current or voltage pulses for charging. By changing the width of pulses the average of the current or voltage can be controlled. Pulse charging provides two significant advantages, (I) it reduces charging time and, (II) the conditioning effect of this technique highly improves the life cycle. The intervals between pulses called rest times play an important role, they provide some time for chemical reactions inside the battery to take place and stabilize. Since in this method high rates of current or voltage can be used, it reduces undesirable chemical reactions that happen at the electrodes, such as gas formation and crystal growth, which are the most important reasons of life cycle reduction in batteries.

2.4.5 Reflex Charge

During charging procedure some gas bubbles appear on the electrodes, especially amplified during fast charging. This phenomenon is called “burping”. Applying very short discharge pulses or negative pulses which can be achieved for example by short circuiting the battery for very small time intervals compared to charging time intervals in a current limited

fashion, typically 2 to 3 times bigger than the charging pulses during the charging rest period resulting in depolarizing the cell will speed up the stabilization process and hence the overall charging process. This technique is called with other names such as “Burp Charging” or “Negative Pulse Charging”. Different control modes of charging along with waveforms and diagrams are described in [6]. There are other charging methods such as Current Interrupt or CI which will be thoroughly explained in the charging algorithm section.

2.4.6 Float charge

For some applications when the charging process is complete and the battery is fully charged, the batteries should be maintained at 100% SoC for a long time to be ready for time of use. Uninterruptable Power Supplies (UPS) are one of such applications where the batteries should always remain fully charged. However, because of self-discharge of batteries, they get discharged over time; for example, they may lose 20% or 30% of their charge per month. To compensate for self-discharge, a constant voltage which is determined based on the battery chemistry and ambient temperature is applied permanently. This voltage is called “Float Voltage”. In general, float voltage should be decreased with the increase of temperature. This causes a very low rate of current, for example C/300 to C/100 rate to the battery which continuously compensates for the self-discharge rate and also prevents sulfate formation on the plates. This technique is not recommended for Li-ion and Li-Po batteries and it is not necessary for EV/PHEVs which are frequently used every day. In addition, float charging should involve a protection circuit to avoid overcharging. This circuit adjusts the float voltage automatically and interrupts charging at some intervals based on battery voltage and temperature.

2.5 Termination Methods

When the charging is in process, it is very important to decide when to terminate the charging. This is because of two main reasons. One is to avoid undercharge, i.e. making sure the battery is fully charged, not partially, in order to use the full capacity of the batteries. The other one is to avoid overcharging which is very dangerous especially in the case of high energy density Lithium-based battery packs. If not terminated on time, the overcharging of batteries can lead to over gassing of the cells, especially in liquid electrolyte cells which results in increase in the volume of individual cells, a situation that cannot be tolerated in a rigidly packed battery pack. Another issue is overheating of the cells especially in Lithium-based batteries which can easily lead to the explosion and firing of the whole pack, since; Lithium is a very active material and easily combines with oxygen in the air. The only thing needed to begin the combination is enough heat.

Choosing different termination criteria leads to different termination methods. Selecting the type of termination of charging process depends on different factors such as the application and the environment where the battery is used. The conventional termination methods that can be used are mentioned here:

2.5.1 Time

Using time is one of the simplest methods which is mainly used as a backup for fast charging or normally used for regular charging for specific types of batteries. This method is very simple and inexpensive, but because of diminishing battery capacity over time due to aging,

the time should be reset for a reduced capacity aged battery to avoid overcharging of old batteries.

2.5.2 Voltage

As mentioned before, voltage can be used as a termination factor, i.e. terminating the charging process when the battery voltage reaches a specific value. This method has some inaccuracies, because real open circuit voltage is obtained when the battery is left disconnected for some time after charging. This is because chemical reactions happening inside the battery need some time to stabilize. Nevertheless, this method is widely used. In addition, this technique is usually used with constant current technique to avoid overheating damage to the battery.

2.5.3 Voltage Drop (dV/dT)

In some chemistries like Ni-Cd when charged using constant current method, the voltage increases up to the fully charged state point and then the voltage begins to decrease. This is due to oxygen build-up inside the battery. This decrease is significant, so the derivative of the voltage versus time can be measured to indicate overcharge. When this parameter becomes negative it shows that the fully charged state has been passed and the temperature begins to rise. After this point the charging method can be switched to trickle, or float charge, or terminated completely.

2.5.4 Current

In the last stages of charging, if constant voltage method is used, the current begins to decrease as the battery reaches fully charge state. A preset current value such as C/10 rate can be defined and when the current goes below this value the charging would be terminated.

2.5.5 Temperature

In general, during charging the battery temperature increases to some extent, however, extra increase in temperature is a sign of overcharge. Using temperature sensors highly increases the cost of system. Nevertheless, for some chemistries such as Ni-MH, methods such as Voltage Drop is not recommended, since the voltage drop after full charge state is not significant to be relied on. In this case, temperature increase is a good indication of overcharge and can be used.

2.6 Cell Balancing

For high power/energy demanding applications such as EVs/PHEVs a large number of cells should be connected in series to provide a high voltage stack and connected in parallel in order to provide a high output current. There are some concerns related to a battery stack. Single cells produced by different manufactures can be recharged hundreds of times, but when connected in series the life cycle dramatically decreases. This is because of cell imbalances. Just to get an idea about the significance of this effect, the results of a real experiment from [7] is mentioned here. In an experiment, 12 cells were connected in series. Despite claiming life cycle of 400 cycles by the manufacturer, it reduced to only 25 to 30 cycles in a string. This shows how devastating cell imbalance can be. To deal with this, the reasons of cell imbalance should be known and managed. Batteries are electro-chemical devices. Even in the case of a simple resistor while manufactured there is a percentage of inaccuracy. In the case of batteries which are electrochemical components, this is magnified. Two different cells produced in the same factory at the same time will have slight differences in their parameters. One of these parameters is capacity. In the case of a battery pack there are different reasons leading to cell imbalance. As mentioned in [8] there are four fundamental factors leading to cell imbalance. They are

manufacturing variations, differences in self-discharge rate, differences in cell age and also charge acceptance variance. Similarly, in [9] cell imbalance is classified as Internal Sources which include "Variations in Charge Storage Volume" and "Variations in Internal Battery Impedance" and External Sources resulting from "Protection Circuits" and "Thermal Differential Across the Battery Pack".

A simple analogy can be made with water tanks in order to understand how different battery cells, with different capacities, operate when connected in series. By assuming that water tanks have different volumes connected to each other using pipes at the bottom of tanks, if the first tank is supplied with water the level of water in all the tanks will evenly rise. After some time the tanks with lower capacity get full of water while others with higher capacity are partially filled. To completely fill up higher capacity tanks, there is no way other than over filling the lower capacity tanks.

Coming back to the real situation, now it is easy to guess what happens in the case of battery strings. Fully charging the high capacity cells involves overcharging low capacity cells. This will lead to excessive gassing and premature dry out of lower capacity cells and at the same time sulphate formation in partially charged cells leading to lifetime reduction. The only way to manage such situation is using cell equalization circuits and custom control algorithms. An important distinction between batteries for EVs versus HEVs/PHEVs is that for the first case the batteries are usually charged up to 100% SoC (cell balancing becomes an important issue), while for PHEVs the batteries are usually kept in the range of 40% to 80% enabling them to provide enough energy, while being able to absorb regenerative power at the same time.

It is important to note that in cell balancing SoC is the main factor and not voltage. Measuring actual SoC involves discharging the battery completely and calculating the percentage of charge which is not practical. Hence, usually SoC is estimated. Voltage is correlated with SoC and can be used an indicator of SoC. Accuracy of estimated SoC using voltage depends on battery chemistry and other factors. If other techniques can be used that can determine SoC more accurately, they may be used depending on the allowable cost of the system. Different SoC estimation techniques will be presented in section 2.7. Cell balancing in a series string really means equalizing the SOC of the cells which is approximately (not exactly) equivalent to voltage balancing [10].

There are three main cell equalization techniques: 1) Charging 2) Passive, and 3) Active

2.6.1 Charging

Charging method is simply continuing charging the cells until they are all balanced to some degree. This implies overcharging the cells in a controlled manner which leads to the full charge of high capacity cells. This method is applicable to lead-acid and Nickel-based batteries since they can tolerate some overcharge without significant damage. However, this technique should be carefully implemented since extra overcharge leads to overheating of the cells and finally premature drying of the electrolyte. Despite simplicity and low cost of this method, there are disadvantages such as low efficiency and long times required to obtain cell balance. Experimental results [11] show that for complete cell equalization of 48 volt batteries of a specific chemistry, a time on the range of weeks is required. Furthermore, results from [7] show that the extra time required for cell balancing of more cells using this method increases with the square ratio of the number of cells added to the string.

2.6.2 Passive

In this method extra energy in lower capacity cells is dissipated in resistive elements connecting two terminals of the cells. This will provide enough time for higher capacity cells to get fully charged. This method has low efficiency because of energy dissipation but has a higher speed than the charging method. Passive technique is inexpensive, easy to implement and the control algorithm can be easily designed.

2.6.3 Active

Active cell balancing uses active devices such as transistors, op-amps and diodes to control the power flow between different cells. This flow can be between groups of cells or single cells. Extra charge is removed from lower capacity cells and transferred to higher capacity cells. This technique highly speeds up the charging procedure and no energy is dissipated. Of course a small amount of power is dissipated in the circuitry which can be minimized using zero-voltage or zero-current switching techniques.

Lithium-ion batteries are one of the most attractive candidates for EV/PHEVs. Their voltage should be carefully monitored and rigorously controlled in the range of 4.1 to 4.3 Volts/cell since the threshold voltage leading to break down of the cell is very close to the fully charged cell voltage rating. Because Lithium batteries do not tolerate overcharging, the charging technique is not applicable to them. According to safety considerations, for Lithium-based batteries the only reliable cell equalization technique is active balancing.

Various types of cell balancing techniques can be found in the literature. Hence, there is a need to categorize them based on a criterion. Based on energy flow they can be classified into four different groups: 1) Dissipative 2) Single cell to pack 3) Pack to single cell 4) Single cell to

single cell. It is possible to imagine the operation of each category based on the name with some pros and cons for each group. For instance, dissipative shunting resistor technique is an inexpensive technique and easy to control because of simple structure leading to simple implementation [12].

In addition to energy flow criterion for classification, cell balancing techniques can be split into three main groups based on the circuit topology: 1) Shunting 2) Shuttling 3) Energy converter.

Non dissipative techniques like PWM controlled shunting technique have high efficiency but it needs accurate voltage sensing and is somewhat complex to control [13]. Besides, the high number of elements leads to an expensive system. Using resonant converters highly increases the efficiency because of very low switching losses but on the other hand increases further the complexity of the control system [14].

Shuttling techniques work based on transferring extra charge of low capacity cell or cells to an energy storage element such as a capacitor or a group of capacitors, and then transferring it to the high capacity cell or cells [15]. The system would be cheaper using only one high capacity capacitor, but the equalization is faster when multiple capacitors are used each one assigned to a group of cells. Utilizing a group of low capacity capacitors instead of one high capacity capacitor is a good idea, although it increases the complexity of the control system.

Most of the energy converter cell equalization techniques utilize transformers where isolation becomes an advantage at the expense of weight and costs. A model and transfer

function of the energy converter cell equalization system is derived in [16] which can be used for control designing purposes.

The abovementioned cell balancing techniques are all summarized and explained along with circuit topologies in [17]. The question that arises here is that how much the cells should be balanced. The balance should be in the range of volt, mill volt or some other range? As experiments from [10] show for lead-acid batteries, cell to cell voltage matching should be in the range of 10 mV which corresponds to a SoC range that provides reasonable improvement in life cycle. This is an important factor, since, for example if the voltage matching should be in the range of 1 mV it means that the sensors should be 10 times more accurate and also the algorithm may need to be improved for this case. This means more cost and complexity. Therefore, there is a trade-off between cost of the system and life cycle. This parameter should be experimentally verified for different chemistries, environments and applications.

Since EV/PEHV battery packs do not possess a mature technology yet and also not many experimental data is available, sometimes contradictory claims may be seen in the literature, one of which is mentioned here. As mentioned before, battery packs used in HEVs are usually controlled to remain in the mid-range of SoC. The principle is that the battery should be in a state with the ability of absorbing regenerative energy while being able to support enough power during acceleration. If the battery is in 100% SoC, absorbing regenerative current will lead to the overcharge of the battery. Cell overcharge is usually sensed through measuring the cell voltage. Some literature support that switched capacitor cell equalization technique (Shuttling Method) is a suitable candidate for applications with no end of charge state like HEVs because there is no need for intelligent control and it can work in both charge and discharge mode [17]. On the other

hand, some researchers support that according to the nearly flat shape of open circuit terminal voltage of Lithium-Ion cells in the range of 40% to 80% the suitability of charge shuttling methods for HEV applications is denied because of the negligible voltage deviation of cells [12], and more complex SoC estimation techniques should be utilized, as discussed in the next section.

2.7 SoC Estimation

One of the most important information needed for safe charging is SoC. Charging algorithms are mainly based on SoC directly or indirectly. Hence, the knowledge of SoC value is a key parameter in accurate charging. Unfortunately, direct measuring of SoC is somehow impossible or at least very hard and expensive to implement and in some applications doesn't make sense, so, mostly SoC is estimated based on other variables or states of the battery. This involves battery models based on which different estimation methods can be utilized or observers can be designed. Precise estimation of SoC is not an easy task, hence, in typical applications battery voltage which is a sign of SoC can be used. In the case of high power/high energy EV/PHEV battery packs more accurate methods are advisable although being more expensive and complex in implementation. The more accurate SoC estimation is, the better the charging algorithms can be implemented resulting in life cycle improvement.

As mentioned before, SoC is mainly the ratio of available charge to the rated capacity of the cell. One of the important points in SoC estimation to take care of is rated capacity change over time due to aging resulting from degradation of electrolyte, corrosion of plated and other factors. Research in this field is defined as "State of Health (SoH) Estimation". Here, some SoC estimation techniques are mentioned and described.

2.7.1 Complete Discharge

The most precise method is to completely discharge the battery and measure the SoC. Although simple, it is very time consuming and not practical to completely discharge a battery just to measure SoC. Knowledge of SoC is useful for the current situation of the battery, so, if the battery is discharged the state of the battery has changed and there is no more use of previous state SoC knowledge. Especially in the case EV/PHEV this method is not applicable. Although this method is not used on-line, it may be used periodically after long intervals just to calibrate other SoC methods.

2.7.2 Ampere-Hour Counting

Another method is Ampere Hour Counting which measures and calculates the amount of charge entering the battery or leaving it by integrating the current over time. This is one of the most common methods used; however there are some deficiencies and drawbacks, initially, because there is always inaccuracy in sensors. Although very small, because it is being integrated over time it can sum up to a considerable value leading to significant errors. Besides, even supposing a very accurate current sensor, because this integration is being implemented usually by digital processors and numerical methods, there are always calculations errors involved and again can show up in high errors over time. Even if assuming both deficiencies to be solved in some way there is another reason leading to inaccuracy. Even if the amount of charge entering the battery is exactly calculated, because of coulombic efficiency which states that a certain amount of charge entering the battery during charge will not be the same when leaving the battery, this method has some inaccuracy. One way to reduce these inaccuracies is to recalibrate the integration process every time a specific known set point (such as fully discharged state or fully charged state) is reached.

2.7.3 Measurement of Physical Characteristics

Another method for SoC estimation is called Measurement of Physical Characteristics of Electrolyte. Obviously, this method is applicable only to liquid electrolyte batteries, not solid ones like Li-Po. In this method a chemical fact is used and that is the relation between changes of some parameters in electrolyte and change of SoC. One of these parameters is the density of acid. There is an almost linear relation between changes in acid density versus SoC. This method is very well known specially in Lead-Acid batteries. Acid density can be measured directly or indirectly using parameters such as viscosity, conductivity, ion-concentration, refractive index, ultrasonic response and so on.

2.7.4 Open Circuit Voltage

As discussed before, the Open Circuit Voltage of the batteries can also be used as an indicator of SoC. The uncertainty in this method is due to the fact that batteries under operation need some rest time for their open circuit voltage to stabilize. This time for some cases can be up to hours; however, this method is widely use. The key point in this method is the linear relationship of open circuit voltage versus SoC in a specific range of SoC. This range and its slope are different for various chemistries which should be taken into account.

2.7.5 Soft Computation Techniques

There are other techniques categorized under soft computation techniques such as fuzzy neural network [18] or adaptive neuro-fuzzy modeling [19] which can also be utilized for SoC estimation. Other approaches categorized as heuristic interpretation of measurement curves mentioned in [20] such as Coup de Fouet, Linear Model, Artificial Neural Network, Impedance

Spectroscopy, Internal resistance and Kalman filters can also be utilized which are more precise methods but more complicated to implement.

2.8 Charging Algorithm

Charging algorithm can be defined as the combination of what was mentioned up to here and controlling all or part of the parameters affecting battery performance and life cycle in such a way to achieve battery pack charging safely, efficiently and terminated on time. Managing the charging procedure of a high power battery pack with hundreds of cells involves many issues as already discussed in this chapter. To control all of these parameters, efficient and accurate algorithms with reliable safety and backup circuits are required. The trend towards fast charging with huge amounts of current flowing to the battery pack producing lots of heat requires accurate and reliable supervisory control algorithms to ensure safe charge. Managing such complex task can be handled with advanced control techniques like fuzzy logic, supervisory control, and decentralized control and so on. In general, each battery-chemistry requires a unique charging algorithm. Depending on the algorithm it may be applied to some other types as well, however, this should be carefully done according to life cycle and safety issues.

For precise battery charging the charge/discharge profile of the battery provided by the manufacturer must be used. However, the profile is valid for brand new batteries, hence, some techniques like data acquisition methods must be used to acquire the charge/discharge profile of the battery with deterioration due to aging. Novel techniques regarding this issue is being introduced in the literature every often [21].

As mentioned before Lead-acid batteries have mature technology and infrastructure already exists, but they still have poor life cycles in the order of 300-400 cycles. A lot of efforts have been put into research for increasing the life cycle of lead-acid batteries because of their advantages such as low cost and availability. This chemistry has a common charging algorithm which includes four different stages or three based on the application, as indicated in Fig. 2.1.

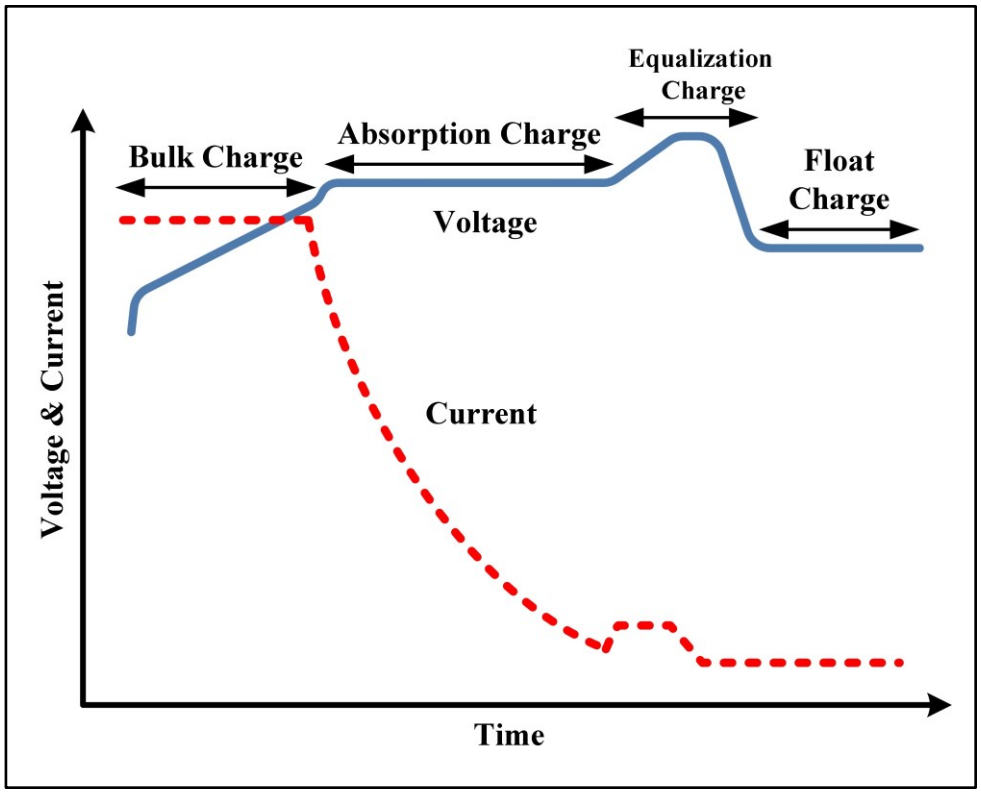

Fig. 2.1 Charging algorithm of a typical Lead-acid battery

In the first stage a predefined constant current is applied to the battery pack which charges the cells rapidly. In this stage the cell voltages increase gradually because of SoC increase. This stage is called “Bulk Charge” stage. The process is continued until a predefined maximum voltage is reached. These values are all recommended by the manufacturer in the datasheet. In the next stage called “Absorption Charge” stage, a constant voltage is applied to the battery pack. At this stage the current decreases gradually until it reaches a predefined C rate

value and the cells are approximately charged but not equalized because of cell imbalance. At this stage a relatively higher voltage than constant voltage in absorption stage can be applied to the pack for some time to balance all the cells inside the pack. This stage is called “Equalization Charge” stage. The equalization can also be achieved with other techniques as mentioned before. After some prescribed time, the charger applies a lower constant voltage in order to keep the battery in a ready to use state. This is called “Float Charge” stage and depending on the application it can be considered or omitted.

As the battery ages, its internal characteristics also change, hence, an adaptive charging algorithm could be used to take into account these parameters variations. Experimental results show that the value of voltage of the third stage should be increased over time to get the same amount of energy as the battery ages [22],[23],[24]. The equalization stage is the key part of this algorithm and has great influence on the life cycle of the battery. As mentioned before, the voltage of this stage should be increased but this increases the current and also the heat generated which has negative impact on the life cycle. One way to get the same amount of current with lower heat dissipation is by using pulses of current. Although this technique seems the same as pulse charging, it is actually different because the time intervals are significantly bigger than pulse charge time periods which are in the range of kilo hertz. This method is called “Current Interrupt” or “CI”. This technique has shown significant life cycle improvements [25]. Using this algorithm, Pb-Acid batteries can reach 50% of the initial capacity after 500 cycles which is a significant improvement in life cycle. Although this algorithm is useful, it puts the battery under stress while it reaches the end of life because of permanently increasing the overvoltage value. This algorithm can be implemented in an alternative way. Instead of using this method for each cycle, which puts high stress on the battery, it can be utilized every 10 cycles. This algorithm is

called “Partial-State-of-Recharge cycling (PSOR)” [25] and has approximately the same effect with the advantage of less stress on the battery. This algorithm has been claimed to enable the battery deliver up to 80% of initial capacity even after 780 cycles [25] which is a really noticeable improvement in life cycle.

As can be seen these complicated algorithms cannot be done using simple PI, PID controllers. They require DSP based controllers to be programmable with numerical data dependent on the battery chemistry, state of health, and other factors.

Continuously, different algorithms are being proposed and tested for improving life cycle of the batteries. This is a vast research area and is currently under development, getting a lot of attention as EVs/PHEVs become popular and available in the market.

2.9 Battery Models

Electrochemical nature of batteries has led to their highly nonlinear behavior dependent on many factors and has made it difficult to predict their characteristics such as V-I characteristic, state-of-charge, state-of-health, runtime, etc. Estimating their characteristics needs appropriate and accurate models. There are numerous battery modeling approaches and techniques in literature, each of which is more appropriate for some specific design aspects and highlighting specific effects. In general, there are many factors such as temperature, discharge current rate, age, etc. affecting the behavior of batteries. The question that arises is that for designing a transportation system or charger system “Should all these features be taken into consideration?” and if not “Which ones should be considered?” and “How much precision is required?” Numerous researches have been done about modeling of batteries for low power and

very low power applications such as laptops, cell phones, battery powered digital processors, sensors, etc. In general, these studies mainly deal with behaviors of single cells or small number of cells. However, in the case of EVs/PHEVs including high power battery packs containing hundreds of cells some phenomena are exaggerated or even some can be observed only in battery packs and not in single cells, like electrical characteristics unbalance in series strings or thermal unbalance through battery pack. This shows that modeling battery packs of EVs/PHEVs needs special considerations. Unfortunately, because of their non-mature and expensive technology, not many data and experimental results are available. Hence, there seems a gap between experimentally confirmed battery models available for single cells which can be cheaply verified in any lab on one side and models of expensive battery packs of hundreds of cells with cell equalization circuits, complex controllers, protection circuits and data acquisition systems which need to be under test for months or years on the other side. Here we first summarize and categorize different models available in the literature with specific focus on vehicular applications and finally will introduce a model which has sufficient precision and is suitable for charger application.

2.9.1 Electrochemical Models

Electrochemical models are based on chemical reactions occurring inside the battery cells. As a result, they are the most accurate models, since they simulate the cells at the microscopic scale. They are mostly consisted of six coupled, non-linear differential equations. Hence, the simulations may need hours or even days of time which makes them not a good candidate for vehicular applications, since, the control systems usually need real time data.

2.9.2 Stochastic Models

Stochastic models are less descriptive but more intuitive compared to the electrochemical models. They are mainly based on discrete-time Markov chains. In its simplest form, the net charge inside the battery is divided to equal charge units, each of which represents the required amount of energy for a unit to be transferred into or out of the cell.

2.9.3 Analytical Models

The analytical models generally use some heuristic techniques or empirical formulas to model specific characteristics of batteries. One of the simplest and oldest analytical methods is the Peukert's equation ($C = K / (I^a)$) which shows the dependence of battery capacity on the discharge rate of the battery. Some modifications can be implemented to Peukert's equation to improve it such as integrating the current. However, because of other nonlinear effects like recovery effect this equation can still have high errors in practice. An experimental setup showing the discharge effect of a Lithium-Ion battery for constant power load can be found in [26]. Another example is the Kinetic Battery Model (KiBaM). Batteries can be physically modeled as a combination of two connected reservoirs of water [27] resembling the charge of the battery as shown in Fig. 2.2. This model evidently illustrates the relaxation effect in the batteries. Another analytical model known as Rakhmatov and Vrudhula's diffusion model [28] uses the concentration of active materials in the electrolyte as a key point in modeling process. This model shows the unavailable charge inside the battery and predicts the runtime of the battery. It can be proved that the diffusion model is in fact a continuous version of the KiBaM [29].

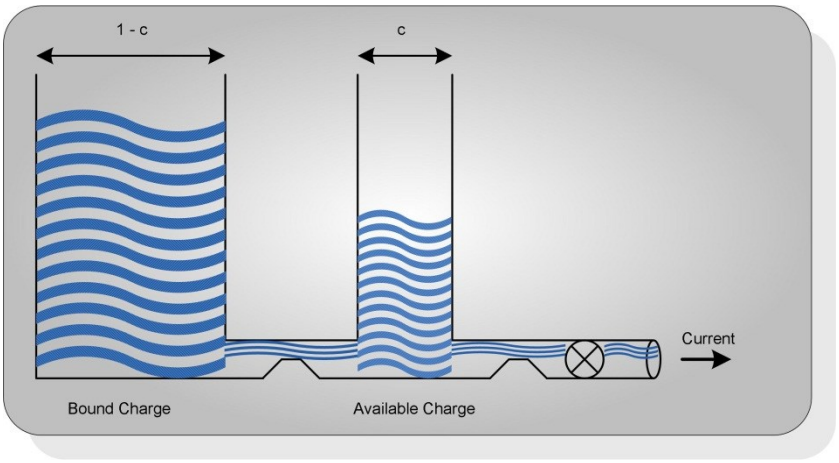

Fig. 2.2 Kinetic Battery Model (KiBaM)

2.9.4 Electrical Circuit Models

The electrical circuit models generally use electrical components to model the behavior of a battery. These are the most suitable models for electrical engineering simulation purposes because of their electrical nature which makes them possible to get connected directly to the electrical network. Batteries may be modeled with a constant voltage source or a constant voltage source in series with a resistance in its simplest form, a controlled voltage source or a very large capacity capacitor. Other effects can be modeled by adding more components to the capacitor. For example, the discharge rate capacity can be modeled by adding a controlled voltage source in series with the capacitor with reverse voltage polarity and the coefficients related to different current rates can be stored in a look-up table. The above mentioned types of battery models are oversimplified and are mainly for investigating the performance of the circuit connected to them rather than evaluating themselves. For instance, the validity of voltage source in series with a resistor is valid for limited purposes such as steady state DC conditions and short amounts of time, since this model cannot consider the discharge of the battery. Other models,

although considering more effects, still are unable to describe dynamic or transient behavior of short time constant load profiles such as pulse discharge. In general, the electrical circuit models can be mainly classified to three main categories [30]: (a) Thevenin-based models (b) Impedance-based models and (c) runtime-based models. The above mentioned electrical circuit models are shown in their simple form in Fig. 2.3. More complicated ones can be found in literature.

The impedance based models constitute a very important category and are still under investigation and need more research. They can describe the dynamic behavior of the batteries accurately and this is a very important point for battery management systems, hence, they are described more deeply here. This model category utilizes the fact that impedance characteristics

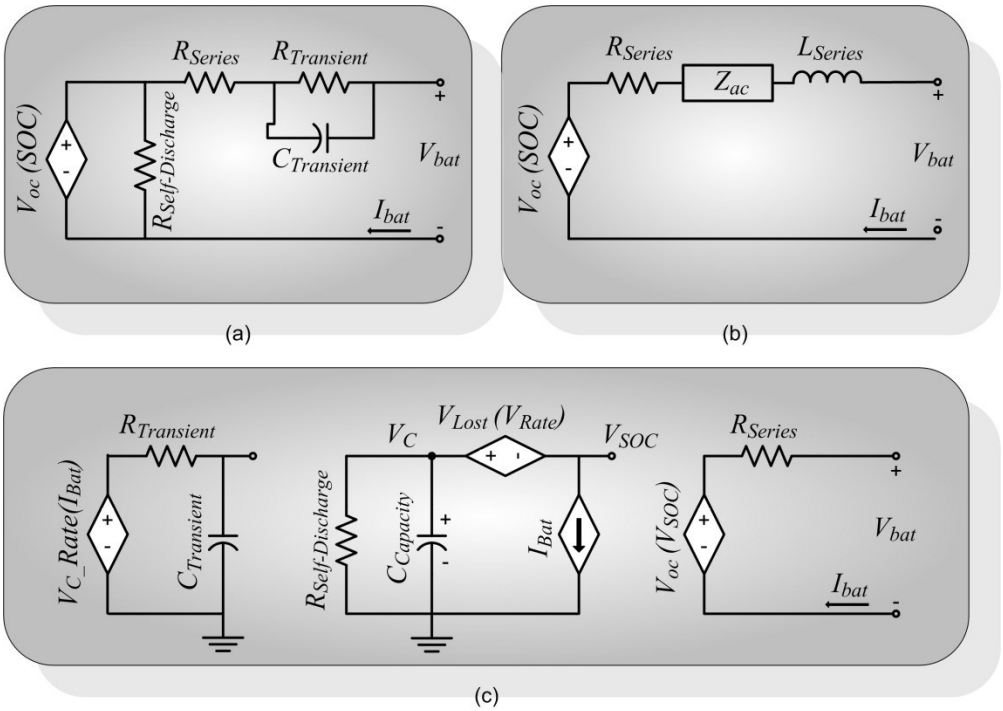

Fig. 2.3 (a) Thevenin-based (b) Impedance-based (c) runtime-based battery models

of batteries provide some information about the state of the batteries in general. This information is dependent on different factors such as SOC, temperature, life cycle and charge/discharge current, etc. The method which is used for measuring the impedance spectra is called "Electrochemical Impedance Spectroscopy (EIS)" which can be used for any electrochemical system such as fuel cells, electrochemical capacitors, ultra capacitors, batteries, etc. This is mainly implemented by applying a small amplitude sinusoidal current or voltage signal to the system and monitoring the response for different frequencies. The reason of choosing small amplitude is to keep the system in the linear region; hence, the response will have the same wave shape with probably different amplitude and phase angle. Using the input signal and response signal, the impedance can be calculated and plotted for different frequencies. In general, there are different chemical reactions happening and different elements inside a battery such as solution resistance, diffusion layer, electrode double layer capacitance, electrode kinetics, etc. By applying different frequencies, some reactions keep happening and others will have lower effect and attenuate for some frequency ranges. This provides the opportunity of modeling different reactions and parameters inside the battery with different electrical components in the electrical circuit model. Despite this, still the response will be a combination of different effects and this makes the EIS analysis somewhat difficult [31]. There are different approaches for analyzing the EIS, however, the most conventional and suitable one is interpreting the results in circuit language. The complete electrochemical equivalent circuit model for Lithium-ion batteries is shown in Fig. 2.4. Other chemistries such as lead-acid may also be presented with the same configuration. Each of the elements is modeling a phenomena or element inside the battery. For example, the electrodes of the battery are porous. At high frequencies, this causes the electrodes to show an inductive behavior. The inductors L_a and L_c are modeling this behavior. The letter "a"

stands for anode and “c” stands for cathode. The interpretation of other elements can be found in [32]. Other configurations are also possible, such as ladder circuit representation [33].

Choosing the circuit model configuration is the first step. The second step is to determine the values of parameters depending on the battery chemistry, Ampere-hour capacitance, SoC, type of electrodes and electrolyte, load profile, etc., in other word, system identification. There are different approaches available in the literature, one of which proposed in [33] is a universal

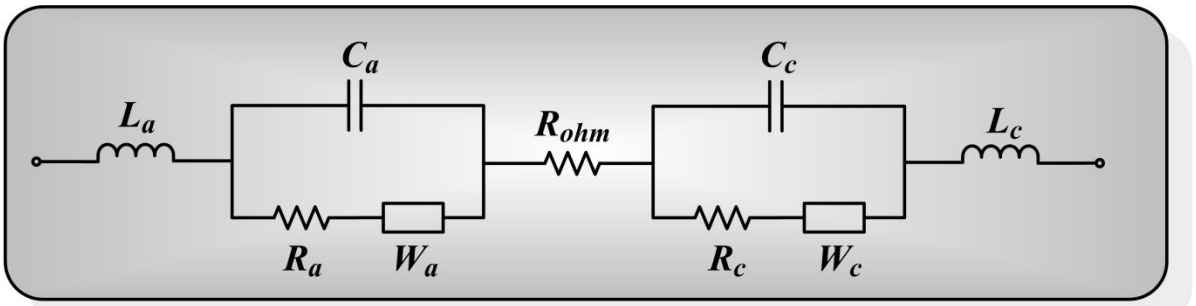

Fig. 2.4 Electrochemical Equivalent Circuit Model

parameterization technique which can be applied to different chemistries with different capacitance and charge/discharge ratings. Despite the effectiveness of these configurations and approaches for design purposes, sometimes they are too complex and time consuming for real time control applications. This problem is discussed in [34] and a simplified model and identification technique suitable for real time applications is proposed, which is the case for battery management systems in EVs/PHEVs.

Another modeling approach is based on modeling the ohmic resistance of batteries. In general the internal resistance of batteries can be divided into two main parts: ohmic resistance and polarization resistance. The ohmic resistance mainly consists of electrode resistance, electrolyte resistance, separator resistance and contact resistance. On the other side, polarization resistance is dependent on chemical polarization and electrolyte concentration. These two types of resistances are illustrated in Fig. 2.5, which is the result of applying a pulse discharge current to the battery and monitoring the voltage profile.

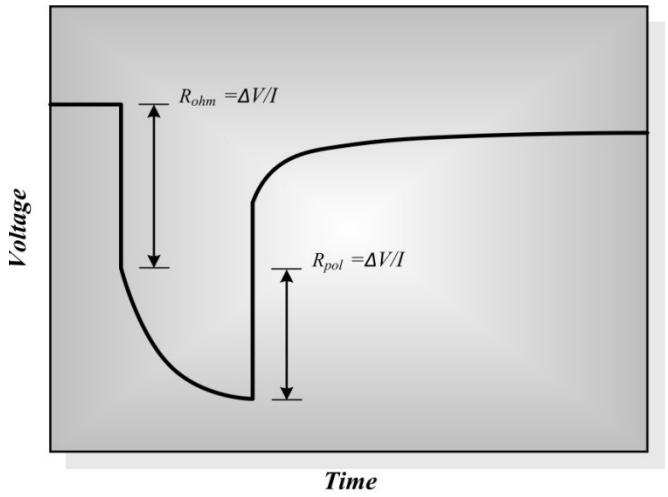

Fig. 2.5 Typical Voltage response of Li-ion battery discharged by a pulse discharge current

The immediate vertical voltage drop is due to the ohmic resistance "R_{ohm}", while the exponential voltage drop is due to the polarization resistance "R_{pol}" which happens slowly. Ohmic resistance has some information about state of the battery. For instance, higher battery ohmic resistance will cause lower battery voltage, more ohmic loss, shorter discharge time and lower power available from the battery. Hence, modeling the ohmic resistance of a battery provides some valuable input to the battery management system for better utilization of cells inside the pack which will eventually lead to better life cycle. Paper [35] investigates the relation

of ohmic resistance with life cycle, discharge rate, depth of discharge (DoD), temperature, SoC and finally comes up with a model which can be used in lifetime evaluation of batteries. Similarly, [36] proposes a nonlinear resistance dependent on SoC which can add to the accuracy of the battery model while used.

2.9.5 Thermal Models

Another significant factor affecting battery packs performance and life cycle is temperature. Experimental results show that each 10°C increase in the operating temperature compared to the nominal temperature of the designed battery pack will reduce the life cycle of the batteries approximately to half of the nominal life cycle. This simply shows the importance of the temperature factor. As mentioned before, there are some affects that are only observed in the battery packs and not in single cells. One of these effects is the temperature difference through a battery pack. For example, cells which are in the middle of the battery pack have higher temperature compared to those at the edges of the pack because of less ventilation. Since battery parameters change with temperature variation, different cells inside a pack will have different characteristics. This cell mismatch will significantly reduce the life cycle of the whole pack. This effect and other effects contributing to the life cycle of battery packs are investigated in [37]. This shows the need of thermal models of the battery packs which helps designing a more effective battery management system. These thermal effects are being investigated in laboratories like National Renewable Energy Laboratory (NREL) and results can be found in their reports [38],[39],[40].

The importance of temperature effects is not only for improving performance. Safety issues for Lithium-based batteries are highly dependent on temperature. Thermal runaway of

Lithium-ion batteries is a very important safety point and must be considered in the battery management systems. This involves the availability of accurate thermal models of battery packs. It is worth mentioning some of the models available in the simulation softwares used for vehicular applications. One of the well-known simulators is ADVISOR by the National Renewable Energy Laboratory written in Matlab/Simulink environment. The models which have been used by this software are: (i) internal resistance model (ii) resistance-capacitance (RC) model (iii) PNGV capacitance model (iv) neural network lead acid model. Detailed description of these models and their accuracy can be found in [41].

2.9.6 Other Models

Battery models can be categorized based on different approaches they are driven. However, there are other important factors that battery models can be classified based on. Some of them can be mentioned as [42]: (i) the types of load profiles supported (e.g. constant current vs. variable current or constant power vs. variable power), (ii) supported battery chemistries (Lithium-ion, Pb-Acid, etc.), (iii) battery effects that are modeled (e.g. relaxation effect, current rate capacity effect, thermal effect, etc.), (iv) computational efficiency (being fast enough for real-time control purposes) and (v) degree of precision in predicting real-life behavior of the batteries. In addition to the abovementioned models, there are more advanced modeling techniques such as Extended Kalman Filter (EKF) for estimating the parameters of a battery model which increases accuracy especially in the case of variable current load profile which is the case for vehicular applications [43]. It is noted that Kalman filtering is a least-squares optimal estimation algorithm for linear dynamic systems where modeling and measurement errors are assumed as Gaussian white noises [44]. The algorithm recursively improves the state estimate such that the variance of the estimation error at any iteration is minimized. First, the

previous state estimate and its error covariance are updated using the state-space model. Then, the updated estimate is corrected based on the latest output measurement in an optimal fashion. On the other hand, EKF is the extended form of this estimation algorithm to nonlinear dynamic systems. While the nonlinear state-space model is directly employed for the state estimate update, the other operations are done using the linearized model. Modeling the transient behavior or relaxation effect of batteries can be modeled by parallel-connected RC circuits putting in series with the battery model. By increasing the number of these brunches the accuracy of the model increases, however it causes the increased complexity and simulation time as mentioned before. In [45] it is shown that the selection of an appropriate battery model for a certain PHEV application can be formulated as a multi-objective optimization problem balancing between the model accuracy and the computational complexity. This multi-objective optimization problem is mapped into a weighted optimization problem to solve. Genetic Algorithm has also been used for battery modeling purposes. Sometimes it is very useful to derive a model based on data sheets available from manufacturers. In [46] the charge and discharge characteristics of the battery supplied by the original equipment manufacturers (OEMs) are used to find the parameters of an equivalent circuit model (ECM) for a battery. A multi-objective optimization genetic algorithm (MOOGA) is proposed to find the model parameters. This reduces the time of parameter extraction and also eliminates the need of extensive experimentation in the early phases of design. A genetic algorithm (GA), a sub-class of the larger class of evolutionary computation techniques, is a randomized search method for finding the global solution to an optimization problem, based on the principles of natural evolution, such as inheritance, mutation, selection, and so on [47]. In this method, an initial population of solution candidates evolves toward an improved generation. In each generation, the fitness of any candidate solution is evaluated to

form a new population of solutions. This iteration is continued till a specific number of generations is produced and/or a satisfactory fitness level is generated [48].

2.9.7 Utilized Battery Model

First of all, it is important to note that every battery model is suitable for a specific application and design purpose. Having a very detailed and accurate model is not necessarily an advantage for any kind of application. The accuracy and complexity of a model should be justified for any specific application to avoid unnecessary calculations and complexity. Since our application is a battery pack charger and charging process happens during hours of time, the battery pack is a very slow dynamic system with a very big time constant compared to power electronics circuits connected to it which have time constants of time scales of milliseconds or even microseconds. This fact will be reminded during the battery modeling process. In addition, considering all the details and effects in EV/PHEV battery packs such as cell equalization circuits, sensors, controllers, thermal effects, relaxation effect and so on is not practical since they add extra complexity to the system without any valuable advantage for designing a battery charger. This is a realistic consideration in simulation packages as well. For example, the battery model [49] used in Matlab/Simulink which we will also use for verification of our model has some limitations and assumptions such as constant internal resistance, neglecting Peukert's effect, temperature, self-discharge and memory effect. Despite all of these limitations, this model gives very accurate results compared to practical data and manufacturer datasheets. This model is shown in Fig. 2.6. Using this detailed model and connecting it directly to the power electronics circuit doesn't seem practical and beneficial in terms of mathematical complexity. Neglecting small differences in single cells characteristics, we can assume the battery pack with all of its components and effects as a very big single battery cell. For our simulation purposes we have

chosen the battery pack of commercialized Chevy Volt as an example which has been introduced to the market recently as a successful PHEV with a noticeable sale in North America, Europe and Asia with lots of awards from different organizations. The specifications of this battery pack can be summarized as a 16 kWh, 45 Ah Lithium-Ion battery pack, 10.4 kWh of which is allowed to be used according to the battery management system for life cycle assurance. It consists of 288 individual cells arranged into 9 modules (32 series cells per module) with nominal voltage of 355 volts.

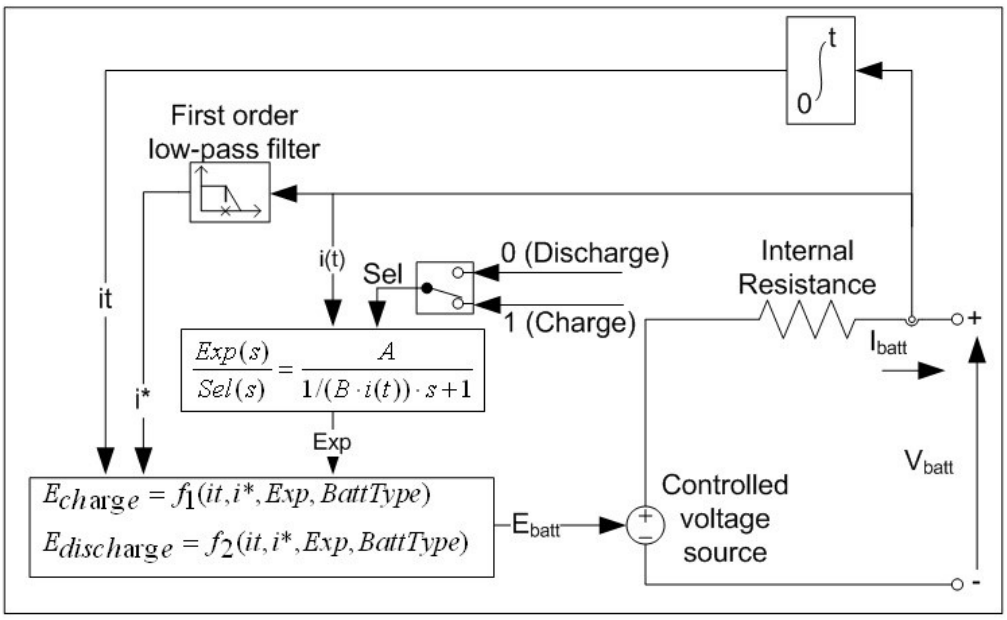

Fig. 2.6 Matlab/Simulink Battery Model

A typical voltage characteristic and SoC versus time is depicted in Fig. 2.7 which is obtained using Matlab/Simulink battery model with the specifications of Chevy Volt battery pack by connecting a 15 amps DC current source charging the battery.

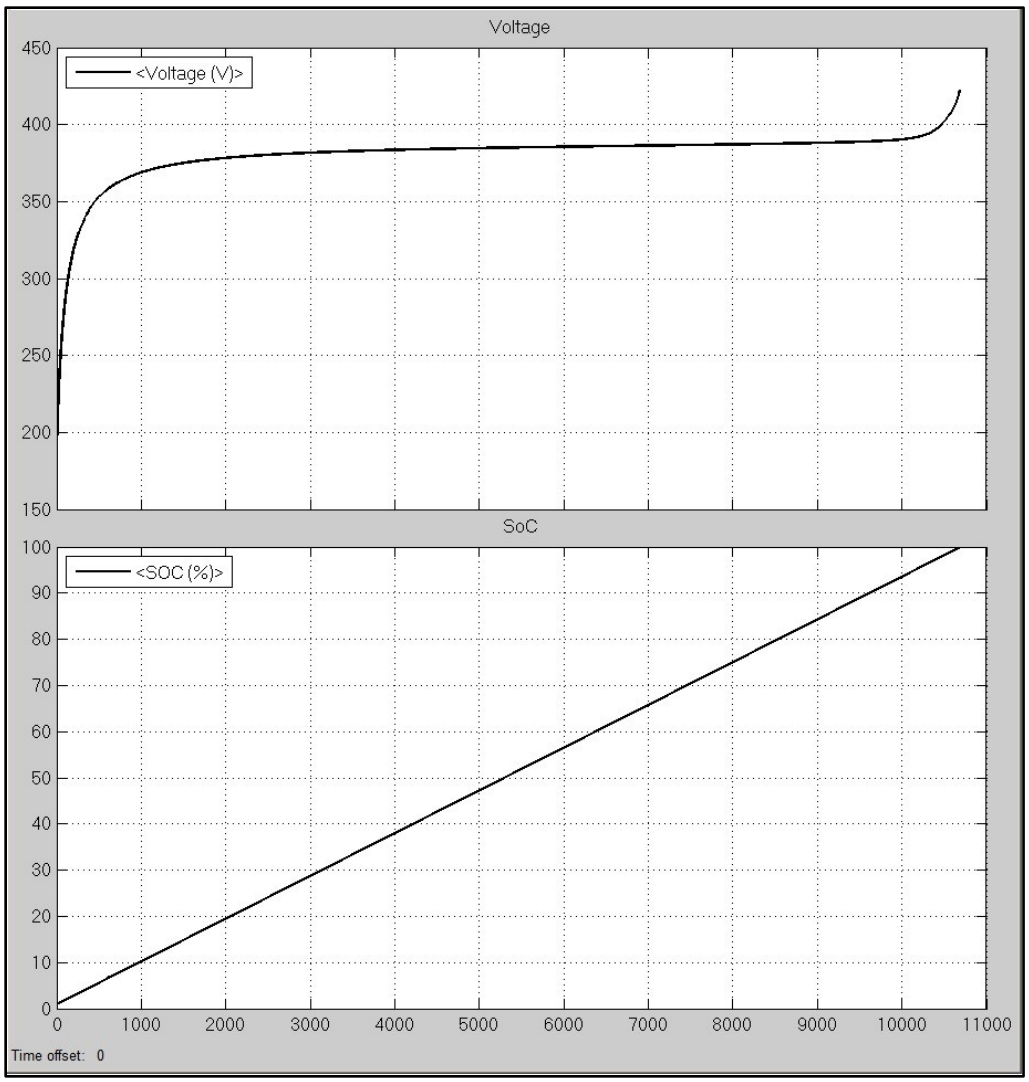

Fig. 2.7 Voltage characteristic of 45 Ah Li-ion battery

For prolonging life cycle of battery packs battery management systems are usually set to operate the battery packs over 30% and less than 90% of SoC. This is valid also for Chevy Volt which allows the battery pack to operate only in a 60% SoC window. If Fig. 2.7 is shown just for SoC range of 30% to 90% Fig. 2.8 will be obtained.

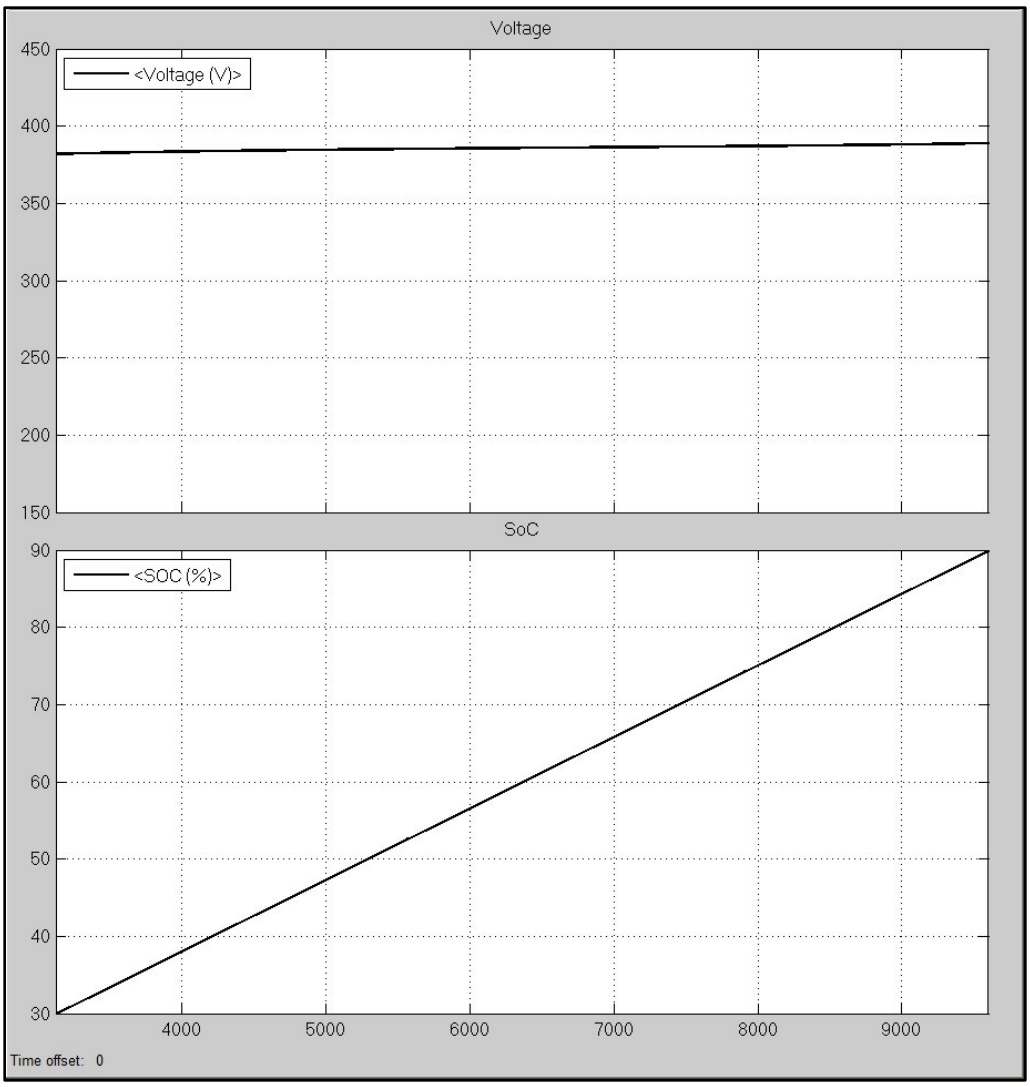

Fig. 2.8 Voltage characteristic of 45 Ah Li-ion battery from 30% to 90% SoC

As it can be seen from Fig. 2.8 the voltage characteristic of Li-ion battery is fairly linear with an almost constant slope for the range of 30% to 90% SoC which is our SoC range of interest. This reminds of a big capacitor in parallel with a resistor getting charged by a constant current source. So we use the model shown in Fig. 2.9 as our battery model.

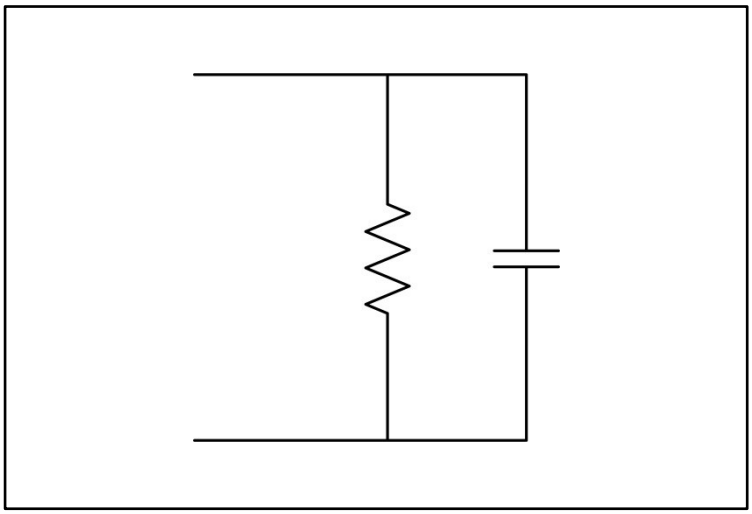

Fig. 2.9 Parallel RC Battery Model

To find the proper value of capacitor, according to the equation $i_c = C\ dV/dt$ and constant current value, if the derivative of voltage is known the C value can be calculated. Fig. 2.10 shows voltage derivative along with voltage and SoC. As visible in Fig. 2.9 the voltage derivative of the battery pack is around 10^{-3} (V/s) which results in a capacitor value of 15,000 F. The resistor in parallel with the capacitor may seem unnecessary; however, considering it has some advantages. First of all it can model the self-discharge of the battery pack. In addition, since most of the available power converter models assume a resistor in parallel with a filter capacitor as a load this approach is compatible with existing power converter models and minimizes the probable required modifications while connecting the battery model to the power converter which highly simplifies the modeling procedure of the overall system. The value of this resistor can be calculated based on the self-discharge rate of the battery which is dependent on the temperature and is variable for different chemistries. For Lithium-ion batteries the self-discharge rate per month is 8% at 21 °C, 15% at 40 °C and 31% at 60 °C [50]. Since battery packs warm up during charging process because of generated heat and they are enclosed in a

package, we assume 40 °C for our calculations as a reasonable average temperature. During self-discharge according to the battery model, the capacitor is discharging through the parallel resistor, so a simple KCL equation results in dV/dt = V/(R*C). Since the charge in a capacitor is linearly dependent to the voltage of the capacitor (q = C*V), self-discharge can be measured using the voltage. According to Fig. 2.10 voltage of the battery pack at 90% SoC is around 390 V. According to 15% per month rate of self-discharge, the battery pack voltage will decrease around 0.15 * 390 V = 58.5 V per month. Using the KCL equation mentioned above (58.5/(30*24*60*60) = 390/(R*15000)) the resistor value will be calculated as around 1150 Ω.

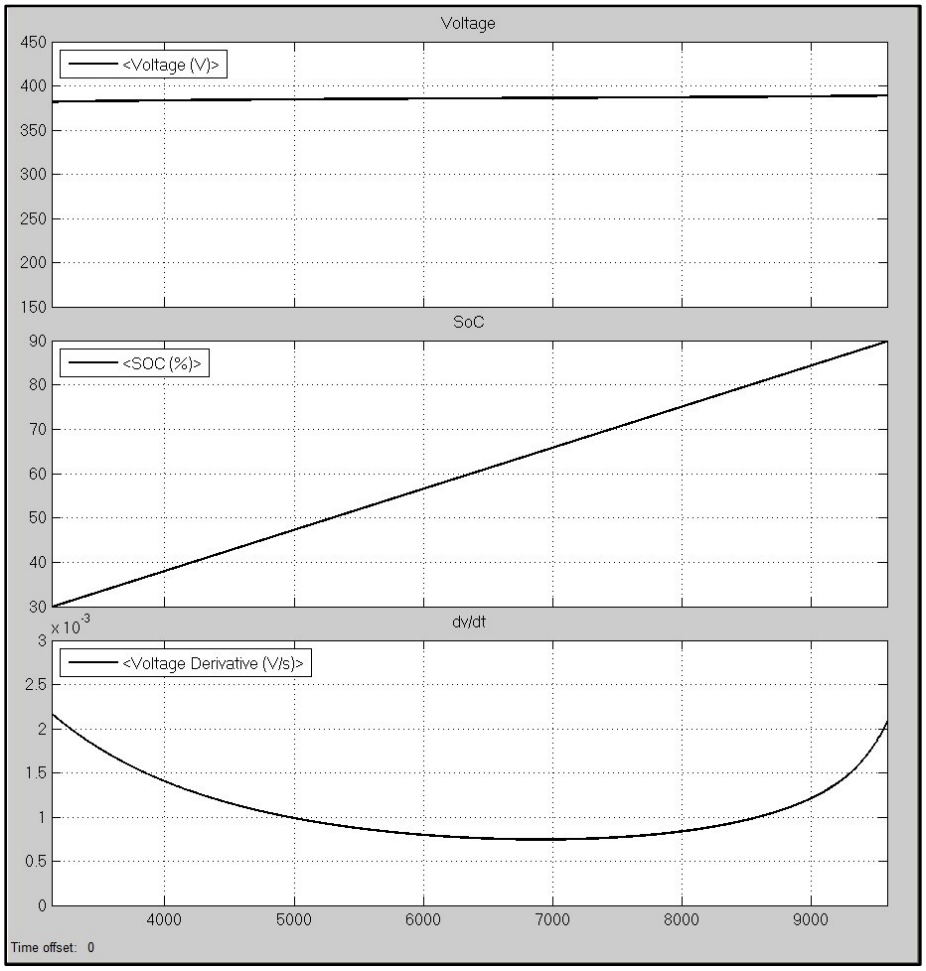

Fig. 2.10 Voltage characteristic and derivative of 45 Ah Li-ion battery from 30% to 95% SoC

To verify the validity of the derived model with the parameter values calculated above, the results from the battery model in Matlab along with the results from the parallel RC model are shown on the same plot as in Fig. 2.11. The continuous black line shows the results from Matlab battery model and the dashed magenta line shows the data from parallel RC model with calculated parameter values. First row of Fig. 2.11 shows the voltage of the battery, second row shows the SoC change, third row represents the voltage derivative versus time and forth row explains the voltage error between two models. There may seem a big difference between voltages and voltage derivatives and huge voltage error, however, if we consider only from 30% SoC to 90% SoC Fig. 2.12 will be obtained which shows very good match between two models. As visible from Fig. 2.12 the voltage error between two models is less than 1 volt which means less than 0.3% error which is a great match.

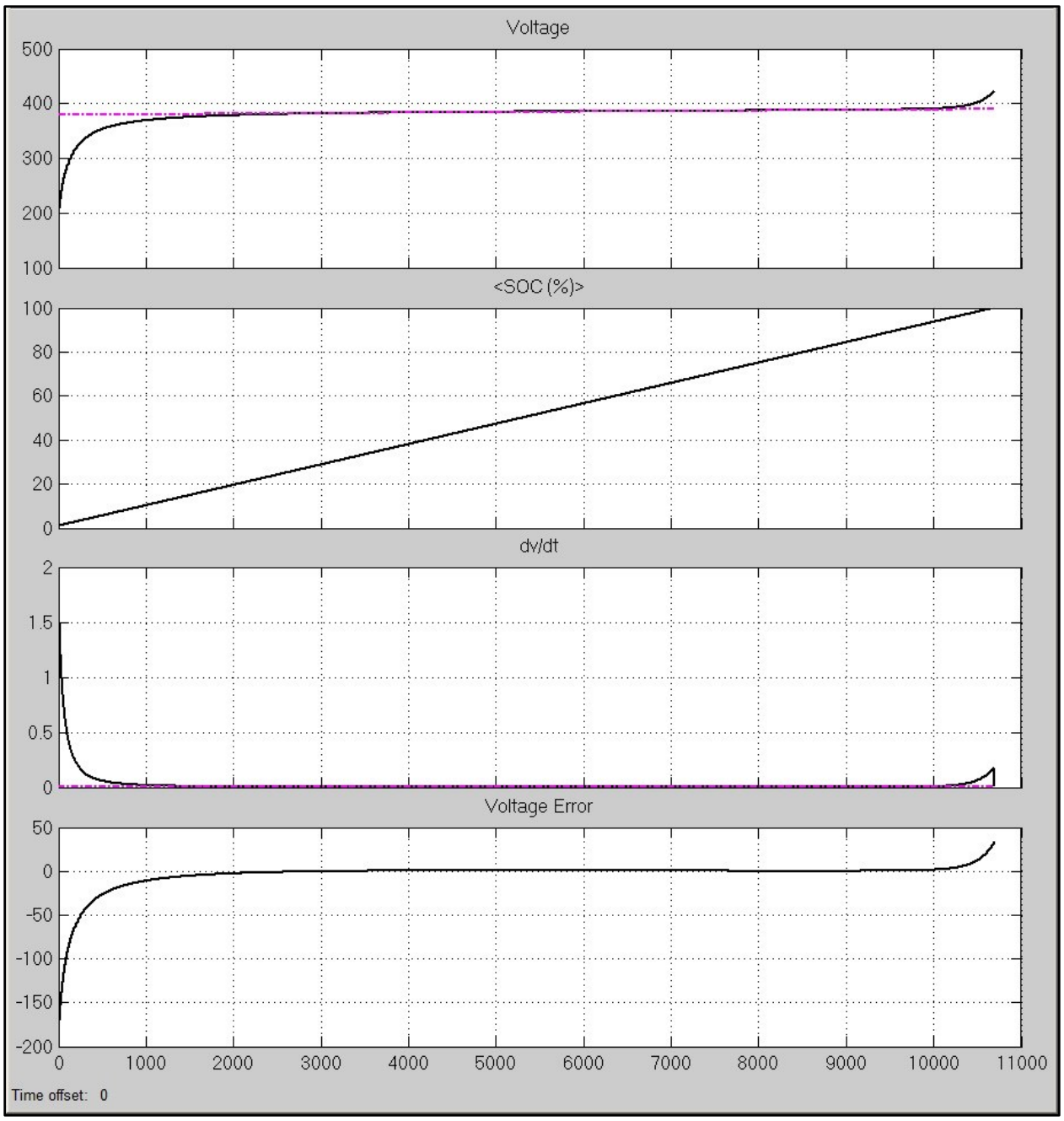

Fig. 2.11 Simulation results for Matlab battery model and paralle RC model for 100% SoC window

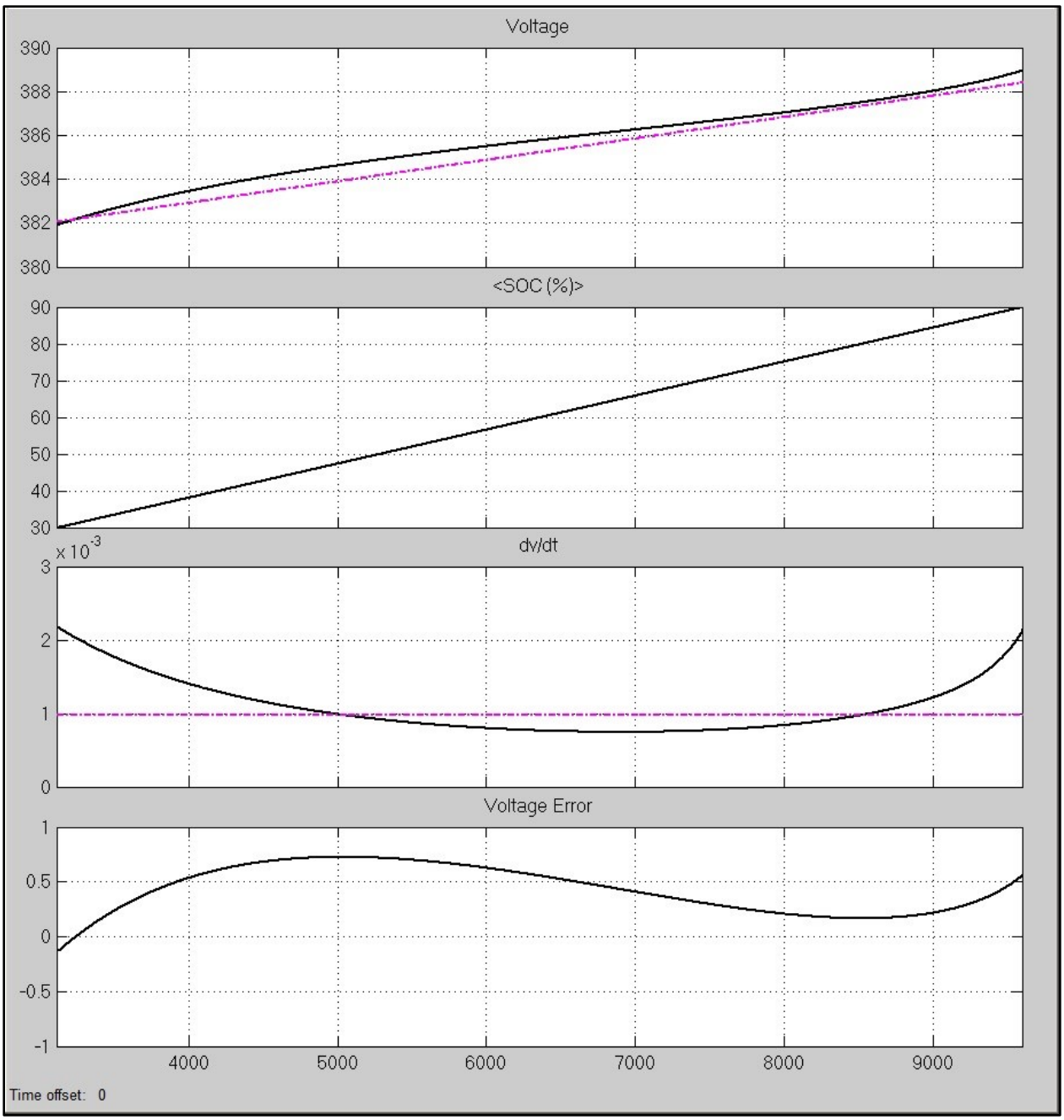

Fig. 2.12 Simulation results for Matlab battery model and paralle RC model for 60% SoC window

2.10 Summary

In this chapter, battery parameters such as capacity, C rate, SoC, DoD and etc. which are used to characterize batteries were introduced. Characteristics of commonly used batteries in vehicular applications such as Lead-Acid, Nickel Cadmium, Nickel Metal Hydride, Lithium Ion and Lithium Polymer were studied. Different chemistries may need different charging methods. Various charging schemes such as constant voltage charging, constant current charging, taper current charging, pulse charging, reflex charging and float charging were mentioned. It is very important to terminate the charging process on time in order to avoid damaging expensive battery packs. Several termination methods were reviewed including time, voltage, voltage drop, current and temperature.

Cell balancing which is a very important issue in extending the life time of battery packs was described and its effects were investigated. Different cell balancing techniques such as charging, passive and active were studied. Importance of SoC estimation in the performance of battery charger was mentioned and different SoC estimation techniques such as complete discharge, ampere-hour counting, measurement of physical characteristics, open circuit voltage and soft computation techniques were investigated. Charging algorithm was defined and a typical charging algorithm for Lead-Acid batteries was mentioned.

Not only the performance and accuracy of the battery charger highly depends on the battery model, for designing any type of system the model of the load should be appropriately selected to ensure reliable and efficient performance of the system. Various types of battery models such as electrochemical models, stochastic models, analytical models, electrical circuit models, thermal models and etc. were comprehensively studied in this chapter. According to our

application and the required accuracy a simplified battery model has been utilized which shows acceptable accuracy.

CHAPTER.3

A NOVEL MAXIMUM POWER POINT TRACKER FOR BATTERY CHARGING APPLICATIONS

3.1 Introduction

Solar energy is one of the most interesting types of renewable energy because of relatively well established technology and efficiency enhancement every day with great efforts toward higher performance Photovoltaic (PV) panels. However, nonlinearity of PV panels characteristics and their dependence on atmospheric conditions such as sunlight irradiance level and temperature variations needs a Maximum Power Point Tracking (MPPT) unit, which is usually a converter to track the maximum power to ensure maximum efficiency of the system. Direct connection of PV panels to the load involves over sizing the panels to ensure load supply and in other words increased loss of the whole system. A typical PV panel characteristic is plotted in Fig. 3.1.

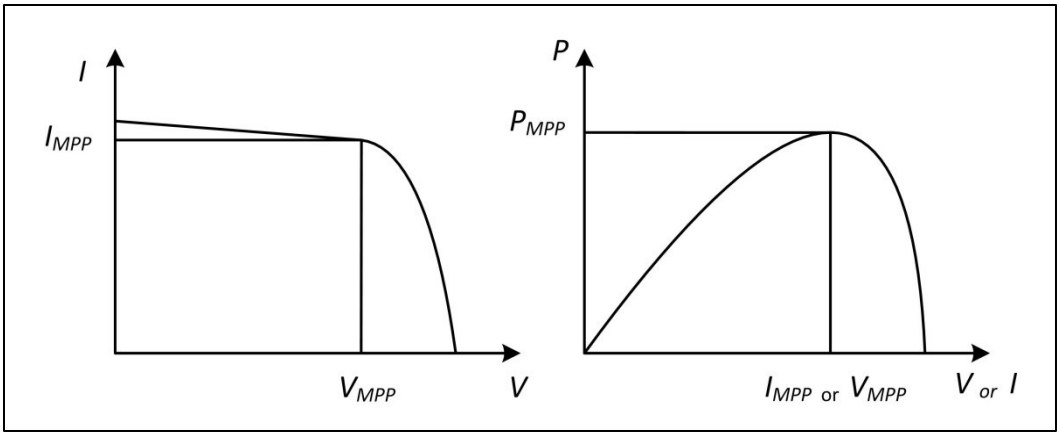

Fig. 3.1 Typical photovoltaic cell characteristics: a) I-V curve b) P-V or P-I curve

In general, the task of MPPT technique is to automatically shift the operating point to the maximum power point. There are numerous techniques in the literature. They may be categorized in different ways. In [51] MPPT methods are classified into two major groups based on the size of the system: 1) Large scale PV systems which utilize digital signal processors (DSP) 2) Small scale PV systems which don't use DSP based methods. However, based on operation principles MPPT methods can be divided into various categories [52]: 1) Hill Climbing/P&O 2)Incremental Conductance 3) Fractional Open-Circuit Voltage 4) Fractional Short-Circuit Current 5) Fuzzy Logic Control 6) Neural Network 7) Ripple correlation control (RCC) 8)Current Sweep 9) DC-Link Capacitor Droop Control 10) Load Current or Load Voltage Maximization 11) dP/dV or dP/dI Feedback Control 12) Array Reconfiguration 13)Mathematical Calculation of MPP 14) State based MPPT 15) best fixed voltage (BFV) algorithm 16) linear reoriented coordinates method (LRCM) and etc. All these methods are summarized and briefly described in [52] along with their major characteristics such as PV array dependence, true or approximate MPPT, analog or digital implementation, periodic tuning, convergence speed, implementation complexity and sensed parameters. Based on MPPT technique characteristics, one or more types are more suitable for a specific application.

One of the most common applications is battery charging which may be the main purpose of the whole PV system such as PHEV battery pack charger (stand-alone system), or a subsidiary part of the PV system as an energy storage element for storing extra energy produced, such as power injection to the grid in distributed generation systems (grid connected system). A novel MPPT algorithm is introduced in this chapter and the first scenario is of interest of this thesis. However, this technique can be easily applied to more complex PV systems [53]. According to [54] among single pole double switch converters, the buck-boost converter has the highest

energy conversion efficiency, however, since our goal here is not to investigate the energy conversion efficiency of the proposed algorithm among different topologies, we have chosen a simple buck converter as the MPPT stage just to prove the validity of the proposed algorithm. However, this algorithm is independent of the converter topology as will be described later. As concluded in [55] the MPPT can be achieved only with sensing one of the output variables, output voltage or output current. This method mainly falls into load current maximization category, however, with some advantages such as independence from circuit topology and high degree of simplicity of low-level controller. Besides, it can be easily implemented using low cost analog circuits with low implementation complexity. This chapter is organized as follows: in section 3.2 the PV array used will be introduced. The control system design procedure will be described in section 3.3. Simulation results will be illustrated in section 3.4 and finally the conclusions will be made in section 3.5.

3.2 PV Array Model

For designing and simulation purposes the PV model is required. Very accurate mathematical models such as double exponential model [56] exist which are not our concern here, since; our goal is not introducing an improved PV model. However, models with moderate complexity and acceptable accuracy exist [57] such as the one shown in Fig. 3.2 which are very suitable for circuit simulation purposes. The two main parts of the model are sunlight insolation dependent current source and diode. The other two elements, namely, shunt resistance R_{SH} and series resistance R_S add to the accuracy of the model, however, for system level design purposes they can be assumed infinity and zero respectively. We will consider these two elements because of higher degree of accuracy.

The main modeling approaches can be classified as mathematical models, circuit models, lookup tables (Data Sheets) and etc. Since we are using MATLAB/Simulink software and

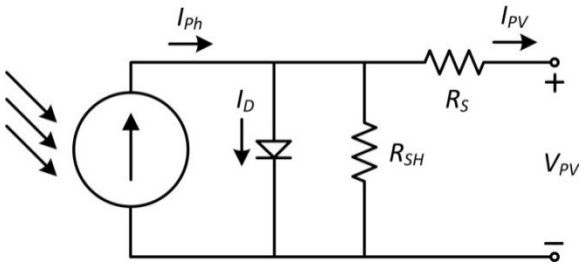

Fig. 3.2 Typical circuit based photovoltaic cell model

SimPowerSystems library, the use of power diode in the model will result in inaccurate results mainly because of getting a sharp angle at maximum power point instead of a curve. This is because of the piecewise linear model of the diode used in SimPowerSystems library which models the diode in on state as a negative voltage source in series with a resistance. This neglects the exponential curve of diode characteristics which is described with Shockley diode equation:

$$I_D = I_S * (e^{V_D}/(n * V_t) - 1) \tag{3.1}$$

where I_D, I_S, V_D, n and Vt are diode current, reverse bias saturation current, diode voltage, ideality factor and thermal voltage respectively. To solve this problem, we use a hybrid type model which incorporates both circuit based model and mathematical based model. To consider the curvature of the maximum power point we use the Shockley equation for diode instead of using the diode block itself which gives acceptable degree of accuracy. This is illustrated in Fig. 3.3 which is the circuit implemented in Matlab/Simulink.

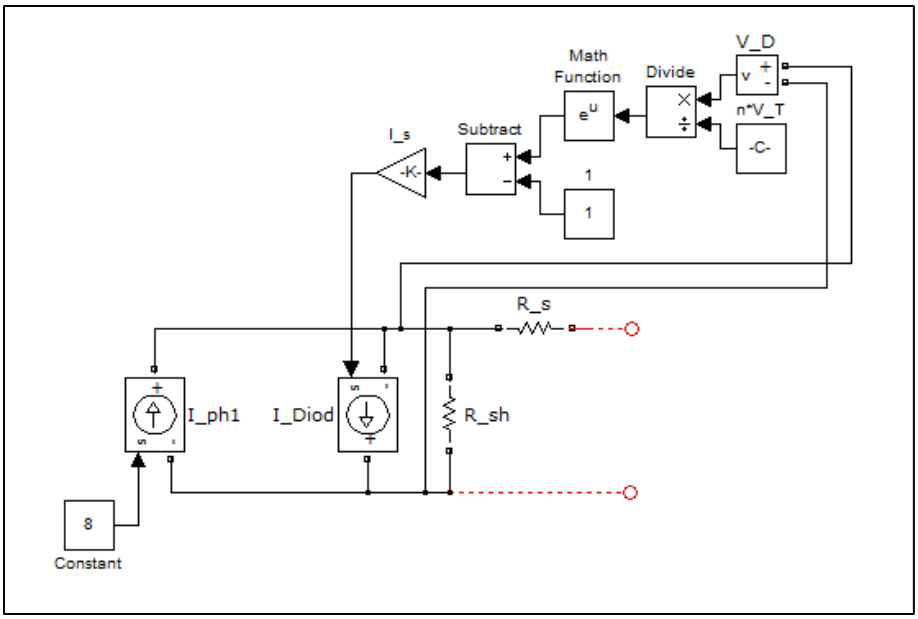

Fig. 3.3 Proposed hybrid PV model for simulation in MATLAB/Simulink

As it can be seen, the controlled current source is used for modeling the dependence of PV on the insolation level and also for modeling the diode. For the insolation dependency a constant or variable signal can be fed to the model. The value of this signal is the short circuit current of the PV. For the diode, however, this approach introduces a problem called Algebraic Loop. An algebraic loop generally occurs when an input port with direct feed through is driven by the output of the same block, either directly, or by a feedback path through other blocks with direct feed through. As it is evident from Shockley equation and illustrated in Fig. 3.3, the voltage of the diode is used to decide the value of the diode current. This algebraic loop will generate error during simulations since for each step the data from previous step may be not available, because no state exists in the model. To deal with this problem we can add a capacitor to the output of the model, which is the practical case in real world to reduce the voltage ripple of the PV panel. This capacitor is an energy storage element and adds a state (capacitor voltage) to the model and solves the problem of algebraic loop since the value of the state for each step is available from the previous step.

3.3 Control System Design

The proposed method is based on maximizing the load power which leads to PV output power maximization assuming a lossless converter stage. In the case of constant voltage type battery load this is translated to maximizing the output current. To achieve this goal the maximum power point tracker shown in Fig. 3.4 is proposed. This system mainly consists of maximum power point (MPP) capturing system, exponential reference maker and current controller. The current controller is designed to control the output filter inductor current to the desired value. Exponential reference maker is utilized to produce an exponentially increasing current reference. Current controller is mainly a simple constant gain and its output is compared with a fixed frequency carrier waveform through a comparator or op-amp to produce pulse-width-modulated (PWM) signal.

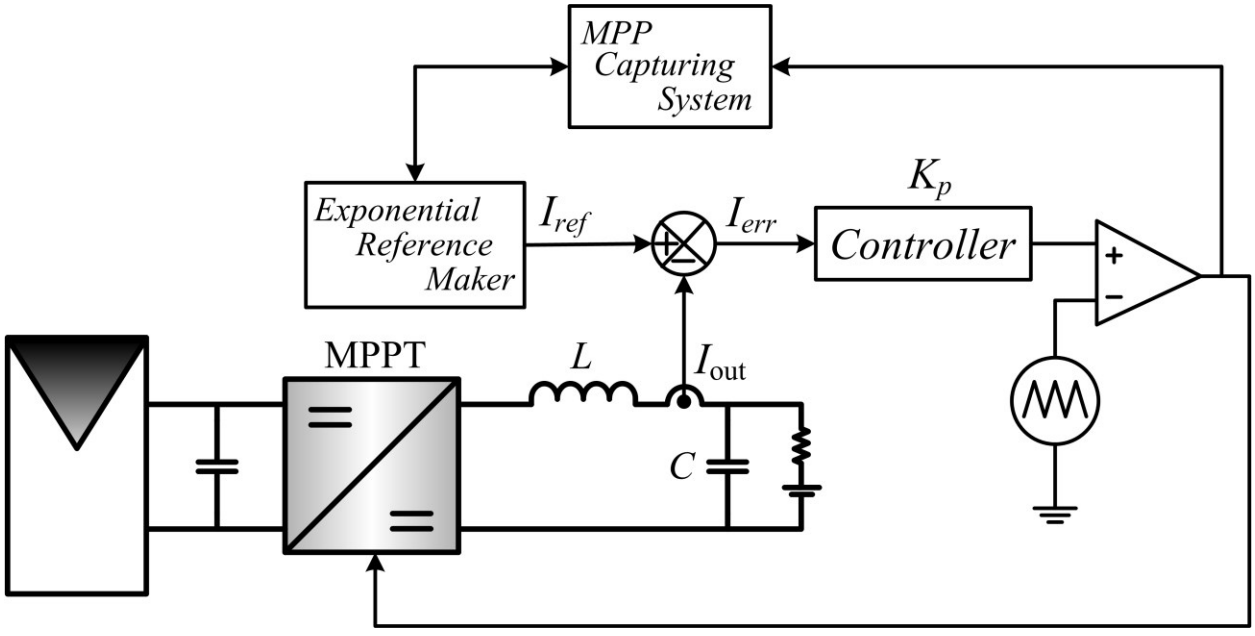

Fig. 3.4 Proposed Maximum Power Point Tracker

The exponential reference maker circuit increases the current reference exponentially to a high predefined value with an adjustable speed. Hence, the current controller increases the output current exponentially as well. This cannot continue infinitely, since, the PV output power has a limited maximum value based on atmospheric conditions, especially, sunlight intensity. Therefore, after some time the actual current cannot follow current reference and this will cause the PWM modulator to saturate and current error begins to increase dramatically. Monitoring this saturation at the output of comparator with MPP capturing system is the key point and when happens indicates that the maximum available output current or equivalently, maximum available PV power has been passed. At this time the MPP capturing system sets the reference maker set point to the value at which saturation has happened. To implement this idea a buck converter is used as the MPPT stage and the battery is simply modeled as a DC source in series with internal resistance as illustrated in Fig. 3.5.

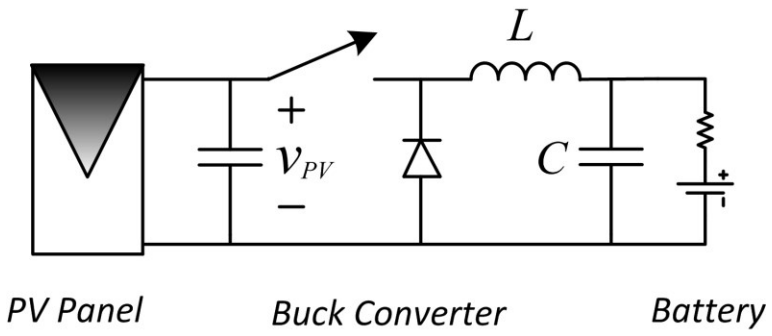

Fig. 3.5 Buck converter as MPPT stage

There are some reasons for choosing this battery model. The MPPT stage is a fast dynamic system compared to the load which is considered a battery here. So battery is a slow dynamic system compared to the MPPT stage and can be considered as a constant voltage source since the voltage variations of the battery is negligible according to very small time scales of the

converter. Besides, our goal in this chapter is just to validate the operation of the proposed MPPT method and not charging process of the battery. In addition, in our final battery pack charger system, this MPPT stage is not directly connected to the battery pack, rather, it is connected to another power stage through DC link with constant voltage which will be described in CHAPTER.4. So considering the battery as a constant voltage source in series with internal resistance is a valid model for verification of the proposed MPPT technique.

For designing the current controller a simple constant gain K_P is used. The first concern that may arise is about not using an integrator in the controller which will cause the output to have steady state error, however, this will not be the case for our algorithm, since, the MPP capturing system will search for the highest output current possible even with the existence of the steady state error in the current control loop. For example, if the maximum PV output power is equivalent to 10 amps at the output inductor current and the current controller has a steady state error of 1 amp, what the MPP capturing will sense is that maximum PV power happens at I_{out} = 11 amps, while in reality maximum PV power has happened at I_{out} = 10 amps. Nevertheless, this will not affect the performance of the system for capturing the maximum power point, since, the 11 amps for MPP capturing system is equivalent to 10 amps for I_{out}. In other words, the exact value that MPP capturing system will detect is not important directly, but, the output current value to which the captured value is equivalent is important since the captured value considers both real output value and steady state error of the loop. So even if the MPP capturing system sets the reference maker set point to the wrong value of 11 amps, the current value that will flow through the output inductor will be 10 amps. This is an advantage of the proposed method which simplifies current loop to a very simple current controller involving only a simple constant gain.

Implementing the idea described before with circuit components is a little tricky. According to what mentioned before, we want the current reference to have an exponential behavior beginning from a constant value and exponentially converging to another higher constant value. Suppose we want the output current, namely, "y(t)" to begin from an initial condition y(t = 0) = y(0) and exponentially converge to the final value y(t → ∞) = y(∞) with the time constant of 1/α . The infinite value for time is theoretical. In practice, after four time constants we reach 97% of the final value which can be considered as steady state. This behavior is the same as that of a first order system, such as voltage response of a RC circuit getting charged with constant current. This fact reminds the following equation for first order systems:

$$y_{(t)} = y_0 e^{-\alpha t} + y_\infty (1 - e^{-\alpha t}) \tag{3.2}$$

Expanding the equation and multiplying both sides by $e^{\alpha t}$ we get:

$$e^{\alpha t} y_{(t)} - y_0 = e^{\alpha t} y_\infty - y_\infty \tag{3.3}$$

Derivation of both sides gives us:

$$\alpha e^{\alpha t} y_{(t)} + e^{\alpha t} y'_{(t)} = \alpha e^{\alpha t} y_{(\infty)} \tag{3.4}$$

If we divide both sides by $e^{\alpha t}$ we will get:

$$\alpha y_{(t)} + y'_{(t)} = \alpha y_{(\infty)} \tag{3.5}$$

$$y'_{(t)} = \alpha\left(y_{(\infty)} - y_{(t)}\right) \tag{3.6}$$

$$y_{(t)} = \alpha\left(\int y_{(\infty)} - \int y_{(t)}\right) \tag{3.7}$$

(3.7) is the key equation for the controller design. The parameter "α" determines the speed of convergence. The bigger the parameter "α" is, the faster the reference will be generated. However, implementation complexity increases. A trade-off should be considered between speed and complexity. We have chosen α = 20 as an example. Implementation of (3.7) is clear using integrator; however, how to capture the reference value at which saturation happens is not that much obvious. There may be different ways to implement this; however, one way is using resettable integrator with adjustable initial condition in a configuration shown in Fig. 3.6.

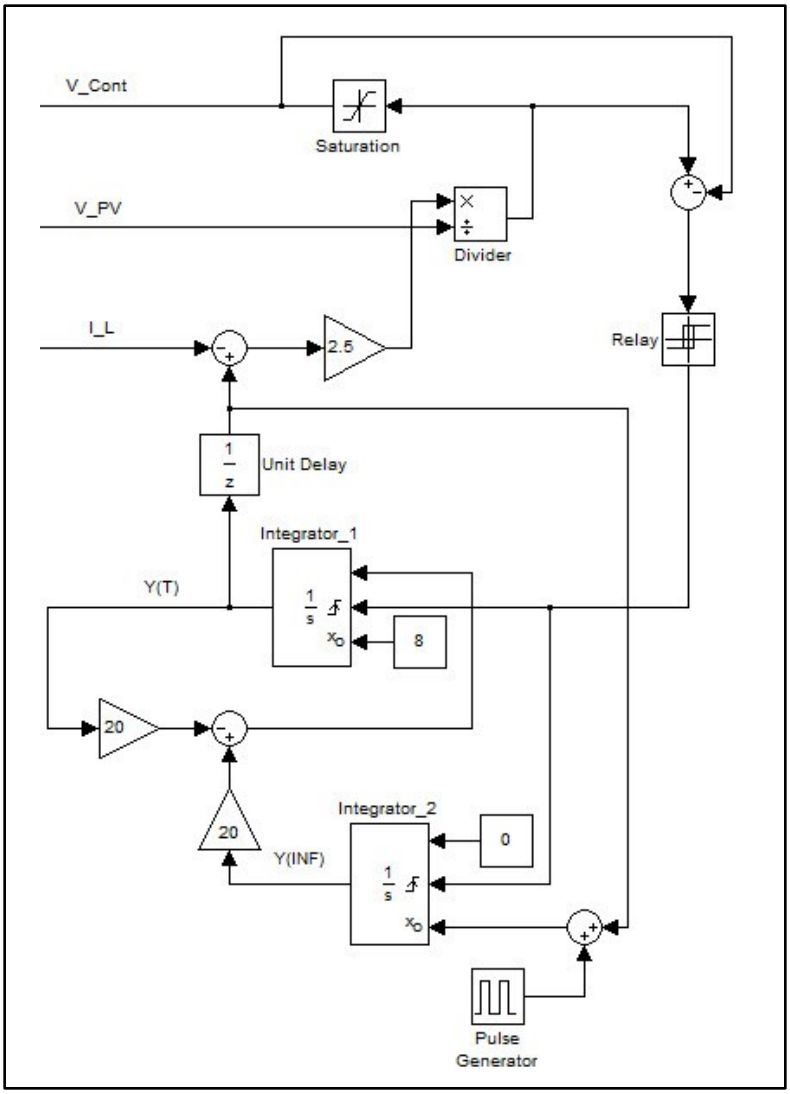

Fig. 3.6 The proposed block diagram configuration for capturing MPP

As shown in Fig. 3.6 the output of the Integrator_1 is y(t) and that of Integrator_2 is y(∞). In the startup time of the circuit, the pulse generator produces a very small duration pulse of a relatively high predefined value. This value should be set to the maximum possible short circuit current of the PV panel which can show up in the output. This happens in highest sun intensity (usually 1000 W/m2) and vertical position of the sun (Solar noon) which is available from PV datasheet and can be calculated for output stage of any converter like buck converter used here. In our case we assume this value equal to 20. This pulse at the circuit start up sets the initial value of integrator_2 to 20 and since it is integrating zero the output of this integrator will be equal to the initial condition. This output is then multiplied by 20 which produces a big value. As described before mathematically, this is the final value that output current should reach. Besides, the output of integrator_2 is y(t), in other words, the present value of current reference. In this way the current reference is increasing exponentially with a high speed and actual value of inductor current which is shown in Fig. 3.6 as I_L is tracking the reference by the current loop controller that is a simple gain of 2.5 which will be described in the following. The output of this gain is the variable (V(cont)*V_{PV}), hence, by dividing this signal by V_{PV} we get V(cont). This signal is fed into a limiter with an upper limit of 1 and lower limit of 0. To detect saturation the signal after the limiter is subtracted from the signal before limiter and fed into a relay to produce a signal indicating saturation. The procedure described here will continue until the saturation happens. At this time the value of y(t) is exactly the current reference signal at which saturation has happened. This value has been added to the output of pulse generator which now is zero because it has produced a pulse just at start up. This means the output value of the summation going toward initial condition of integrator_2 is the current reference value at which saturation has happened. Because of reset signal produced by the relay and sensed by integrator_2, it will

reset to its new initial condition which is the current value at which maximum power has been produced. This is the main idea of this algorithm.

Now the design procedure of current controller loop will be described. The current loop design procedure is as follows. First of all we need the model of the system. Here, we follow state space averaging approach. According to high switching frequency and the capacitor parallel to the PV the averaged state space equations can be written as follows:

$$L\frac{di_L}{dt} = d_{(t)}v_{PV} - v_c \tag{3.8}$$

$$C\frac{dv_C}{dt} = i_L - \frac{v_C - v_b}{r_b} \tag{3.9}$$

As it can be seen from state space equations, there is a multiplicative nonlinearity in the term (d(t) V_{PV}), hence, the system is nonlinear. To overcome this, the conventional approach is using small signal perturbation; however, this is not the approach we consider here. We utilize a heuristic technique. Let's consider the whole term (d(t) V_{PV}) as a variable. Looking at the system in this way changes the nonlinear system to a linear system. In other words, instead of d(t) we assume (d(t) V_{PV}) as the control parameter. Since our goal is to control the current, we need the control to output transfer function. Applying Laplace Transform and after some mathematical operations we get the transfer function as follows. For simplicity and clarity of the concept, we don't use the subscript "s" to show s-domain.

$$\frac{i_L}{d_{(t)}v_{PV}} = \frac{Cs + {}^1/_{r_b}}{LCs^2 + {}^L/_{r_b}s + 1} \tag{3.10}$$

Setting the switching frequency to 20 kHz as a trade-off between filter components size and switching losses, we choose 20% of the switching frequency, 4 kHz as the cross over frequency of the compensated system. Choosing the typical values of C=100μF, L=100μH gives the corner frequency of 1.6 kHz for the filter which is small enough compared to switching frequency for good attenuation of switching ripples. Internal resistance of the battery approximately equal to r_b=0.1Ω is chosen for a 4.2 volt single cell Li-ion battery. The bode diagram of the plant transfer function is shown in Fig. 3.7. According to the -7.93 dB gain at 4 kHz a simple P controller with Kp = 2.5 will shift the cross over frequency to 4 kHz with a phase margin of almost 90 degrees which is high enough for stability. As it is visible from Fig. 3.7 the slope of the magnitude diagram at low frequencies is zero, not -20dB/dec or less which means steady state error, however, this is not important in our algorithm, since, it will automatically consider this error. This is one of the advantages of the proposed algorithm as mentioned before.

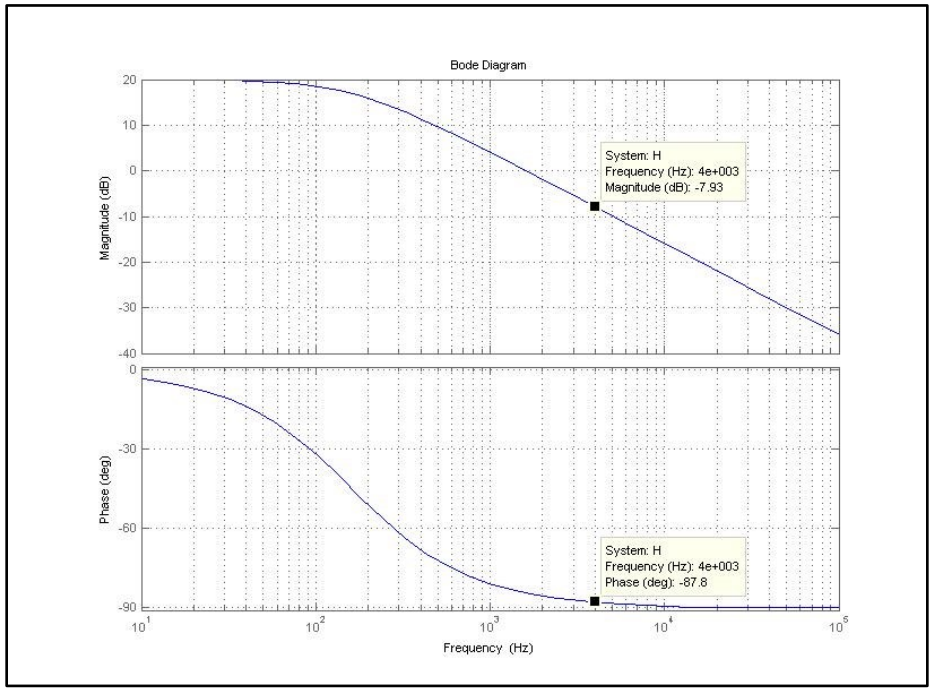

Fig. 3.7 Bode plot of Eq. (3.10)

3.4 Simulation Results

The system described in previous parts is simulated in MATLAB/Simulink to verify the performance of the control algorithm proposed. As will be shown in the results, the MPPT algorithm can easily handle large signal disturbances. For testing this case we change the value of short circuit current of the PV panel by changing the constant value signal feeding the controlled current source shown before in Fig. 3.3. First the simulation begins with the value of 18 amps. Results show good performance of the control in finding the maximum current value. Relatively high speed steady state is achieved. Then at the time of 0.4 second the short circuit current is reduced from 18 amps to 12 amps which is a large signal disturbance. Again after some time the operating point automatically shifts to the maximum power point. At the time of 0.7 second the short circuit current again reduces from 12 to 8 amps and the MPPT algorithm again finds the maximum power point. The instantaneous value of short circuit current of the PV panel, saturation detection by the relay, current reference, actual output current, instantaneous PV power, average PV power are all illustrated in Fig. 3.8 (a) through (f) respectively.

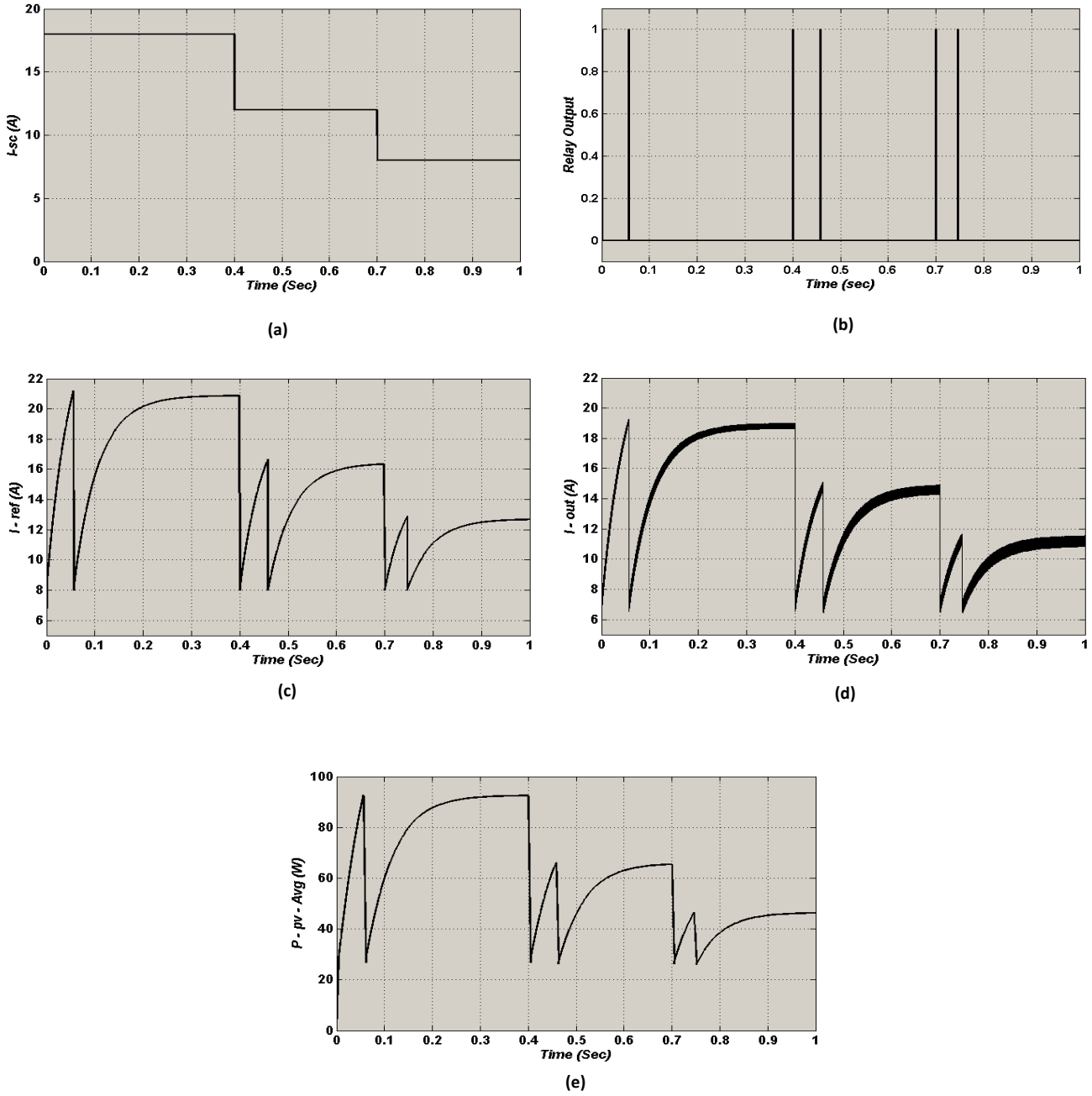

Fig. 3.8 Simulations results: a) Instantaneous value of short circuit current of the PV panel b) Saturation detection by the relay c) Current reference d) Actual output current e) Average PV power

3.5 Summary

In this chapter various MPPT techniques and their applications were studied. Pros and cons of each method were mentioned. A new PV model suitable for Simulink was proposed to avoid algebraic loop problem. A novel MPPT technique was proposed for battery charging applications. This method mainly finds the maximum power point of the PV panel by increasing the current reference of the power converter until the operating point which is unable to be tracked by the converter. This point will lead to saturation in the controller which will be used as a set point indicating the maximum power point. The main advantage of this method is its independency from the power converter topology. Simulation results verify the validity of the proposed technique.

CHAPTER.4

POWER ELECTRONICS INTERFACE

4.1 Introduction

As different electrical sources, loads and storage devices have different characteristics, power electronics plays a key role in reliable and efficient operation of electrical systems. Power electronics have dramatically developed over the previous decades in different aspects such as speed, reliability, performance, control and etc. Besides, enormous effort has been put into development in different areas of power electronics such as novel converter topologies, converter control and modeling and power flow management to improve the performance and increase the efficiency and reduce the cost of power converters. Without reliable and low-cost power converters, deployment of renewable energy sources for residential and industrial applications is impossible. Power electronic converter systems can be categorized based on different criteria. For single input single output converters power flow is a general criterion for classification which leads to two important classes, namely, unidirectional converters and bidirectional converters. Multi-input single-output, single-input multi-output and multi-input multi-output converters are generally classified under multiport converters category.

For the EV/PHEV battery pack charger application using solar energy, PV panels are not used to charge the battery pack directly because of the intermittent nature of renewable sources. This is because of the necessity of the presence of enough power during the charging process. If the PV panels are directly connected to battery pack using an MPPT stage, when the required power by the battery pack is more than the available power from the PV panels, the battery pack

cannot be charged based on the specified charging algorithm by the manufacturer. This will lead to battery degradation and reduced life cycle over time and also prolonged charging times which is not acceptable for users. Due to this fact, what is being applied in solar charging stations currently is injecting the available power from PV panels to the grid using inverters and charging the battery packs from the grid separately which can be considered an infinite source providing any amount of required power to the load. Using this method is like using the grid as a storage device which stores power from PV panels when available and delivers power to the load when required, specifically, if the charging process doesn't coincide with the required solar irradiation. This configuration has some problems or may cause some other problems for the grid in future. First, all of the injected power from the PV panels to the grid will not necessarily enter the battery pack and may flow through other paths and other loads far from the source which involves electric losses. In some cases, the generation plant and charger can be very far from each other which will lead to lots of electrical losses in the transmission lines. Second, if the number of these charging stations increases a lot over time, assuming each house installs a solar charger and they all utilize the grid as storage, this can cause problems for the stability of the grid. What author has in mind is to propose a structure which forces the available power from PV panels to enter the battery pack directly when PV power is less than required battery pack power and obtain only the remaining required power from the grid simultaneously.

4.2 Conventional structures of PV systems

In this section, we will have an overview on the existing PV structures to be able to compare existing structures with the proposed one. A general PV system consists of PV panels, power converters, filters, controllers and electrical load or power system. Different configurations can be utilized to convert solar power to processed electrical power. They are mainly [58]: a) Central inverters. b) String inverters. c) Module integrated inverters as shown in Fig. 4.1.

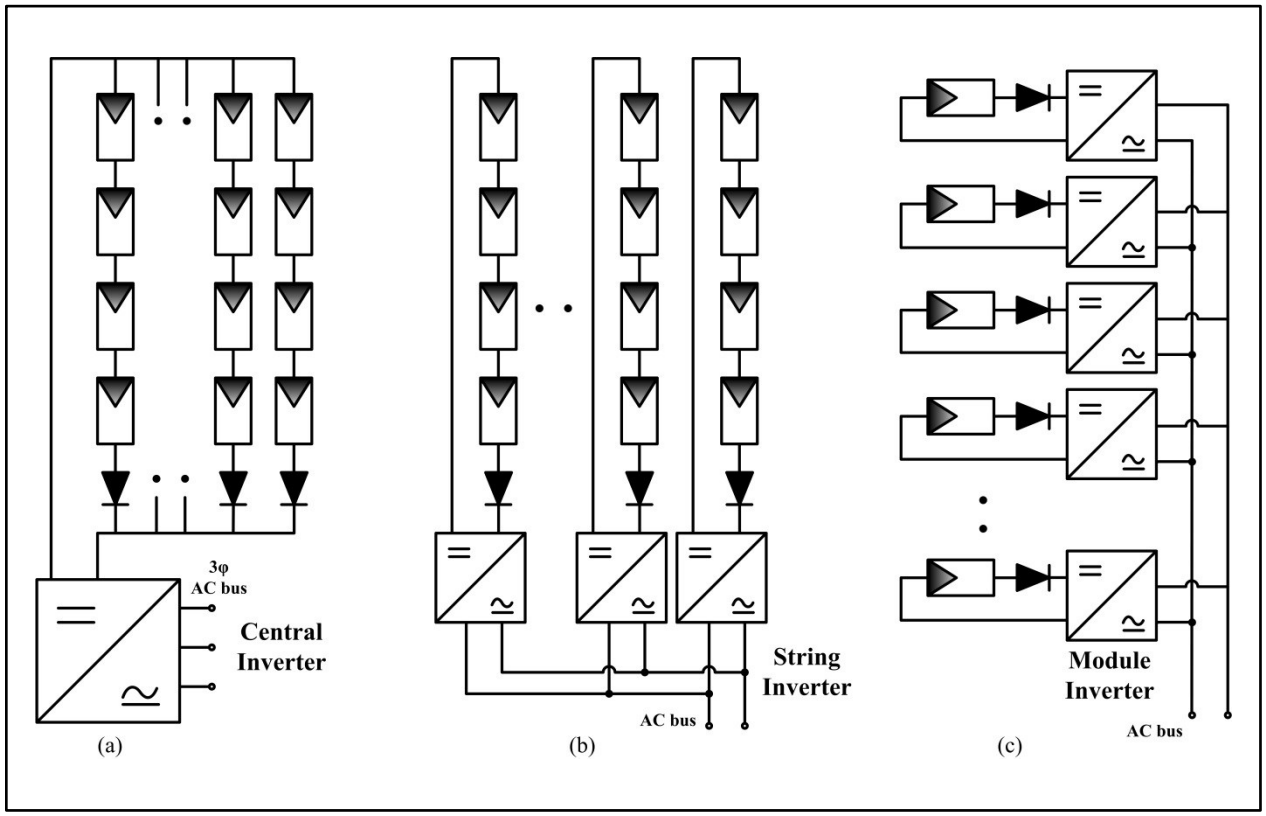

Fig. 4.1 Conventional PV structures: a) Central Inverter b) String Inverter c) Module Inverter

In Fig. 4.1 the converters are shown as DC-AC inverters. However, they don't have to be necessarily an inverter. They can also be DC-DC converters implementing MPPT based on the nature of the load, coupling of sources or power system connected to the other side.

4.2.1 Central Inverters

In this configuration (usually for more than 10 kW), some PV strings are paralleled and connected to a single converter. This has some advantages and some disadvantages. According to initial and maintenance cost, it is beneficial because of single converter. On the other side, this topology has lower efficiency compared to others because of inherent characteristic mismatch among different PV panels. In addition, partial shading in this case cannot be handled in an efficient manner [59]. After all, according to reliability point of view, this configuration is not reliable, since failure of the converter will result to failure of the whole system.

4.2.2 String Inverters

As depicted in Fig. 4.1_b in the case of string inverters, the whole PV arrays are divided into parallel strings of series connected PV panels and each string is connected to a singular converter. This increases the whole energy harvested from solar energy due to better and more accurate MPPT capability, since each string is controlled separately and partial shading and PV panels mismatch can be considered in a more efficient manner. Because of utilization of multiple converters the whole system has higher reliability compared to centralized configuration.

A subclass of string converters exists and is called Multi-String Inverters. In this category a DC-DC converter is utilized for each string and finally only one DC-AC inverter is used for conversion to AC as shown in Fig. 4.2. This configuration combines the benefits of both string and centralized configurations. This multi-string topology allows the integration of different technologies of PV panel strings and also different orientations. The typical operating power range of multi-string topology is 3-10 kW.

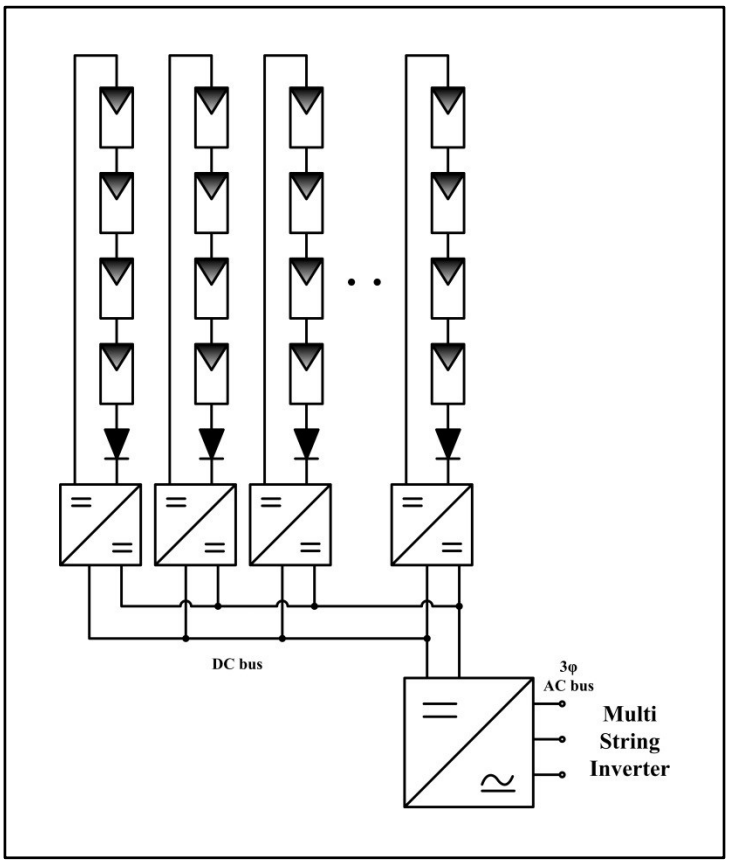

Fig. 4.2 Multi-string Inverter structure

4.2.3 Module integrated inverters

This configuration uses one converter for each PV panel and according to energy point of view the maximum possible electrical energy is harvested out of each panel because of implementing MPPT at panel level. This eliminates the losses due to panels mismatch. This system has a very high reliability; however, maintenance procedure is very complicated. Although this configuration is very costly at the moment, some researchers believe that according to progressing technology of packaging and every day decreasing price of semiconductors, this topology will be the most suitable one for the future of PV plants according to modularity and plug and play capability.

4.3 Topologies for PV inverters

During recent years PV inverter technologies have evolved increasingly [60]. There are various power configurations possible. These can be summarized as shown in Fig. 4.3.[58]

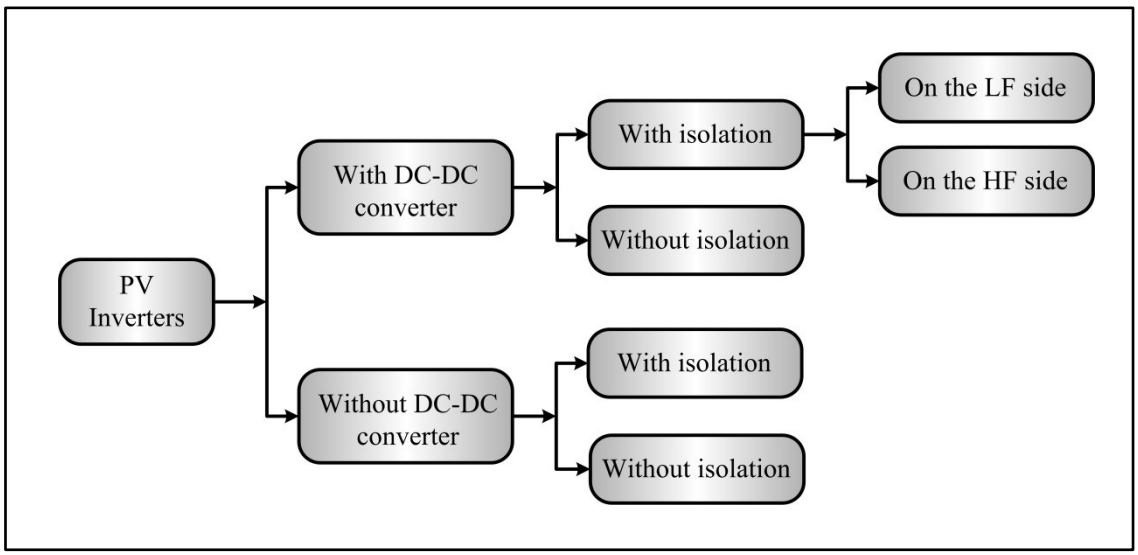

Fig. 4.3 Power Configurations for PV inverters

Using or not using a DC-DC converter depends of the configuration of PV panels and number of PV panels in series. If the number of PV panels in series is high enough to produce higher voltage than load side voltage for most of the times the use of a boost DC-DC converter can be avoided. The isolation depends on the safety standards and requirements.

4.3.1 PV inverters with DC-DC converter and isolation

Isolation is usually achieved using a transformer. This transformer can be on the Low Frequency (LF) side (Fig. 4.4a) or interleaved in the High Frequency (HF) side (Fig. 4.4b) which is an intermediate AC stage. The second configuration is smaller and lighter due to smaller transformer; however, transformer should be of higher quality because of higher losses.

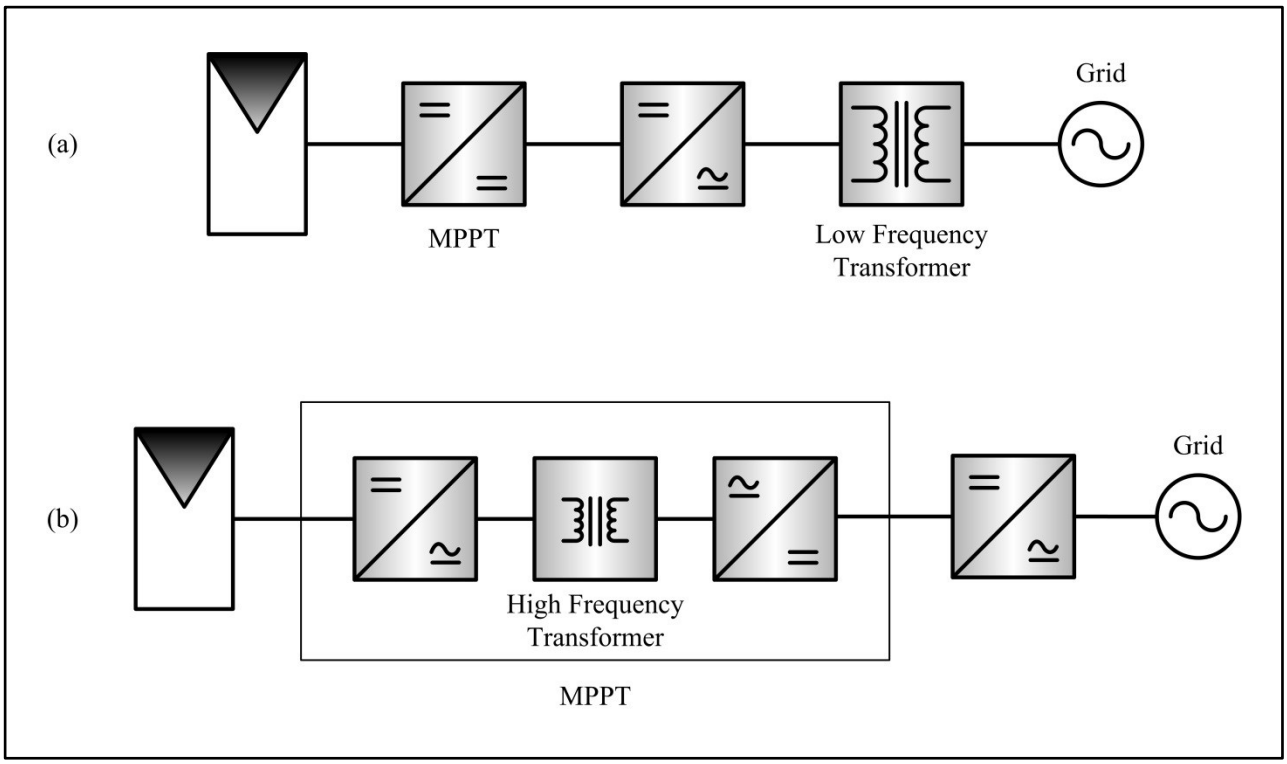

Fig. 4.4 PV inverter configurations with DC-DC converter and isolation: a) Transformer on LF side, b) Transformer on HF side

4.3.2 PV inverters with DC-DC converter and without isolation

Depending on the safety regulations, if isolation is not mandatory the transformer can be eliminated and a more simple system will be achieved as shown in Fig. 4.5.

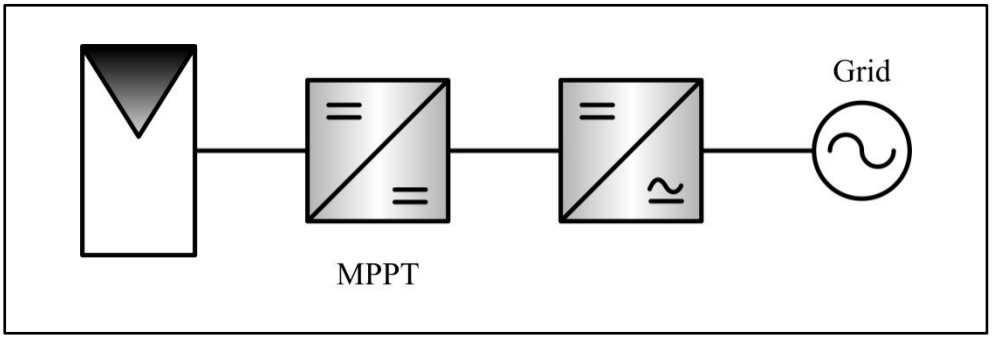

Fig. 4.5 PV inverter configuration with DC-DC converter and without isolation

4.3.3 PV inverters without DC-DC converter and with isolation

Eliminating the DC-DC converter stage and using only the DC-AC inverter involves MPPT and inversion stages to be integrated resulting in a more complex control algorithm. Besides, since the transformer is on the low frequency side it is bigger and heavier. A typical block diagram of this configuration is illustrated in Fig. 4.6.

4.3.4 PV inverters without DC-DC converters and without isolation

This configuration is the simplest configuration possible and at the same time has the least reliability comparing to its counterparts. Any fault in the source side or load side can easily expand to the other side and endanger the operation of the system. So an efficient protection

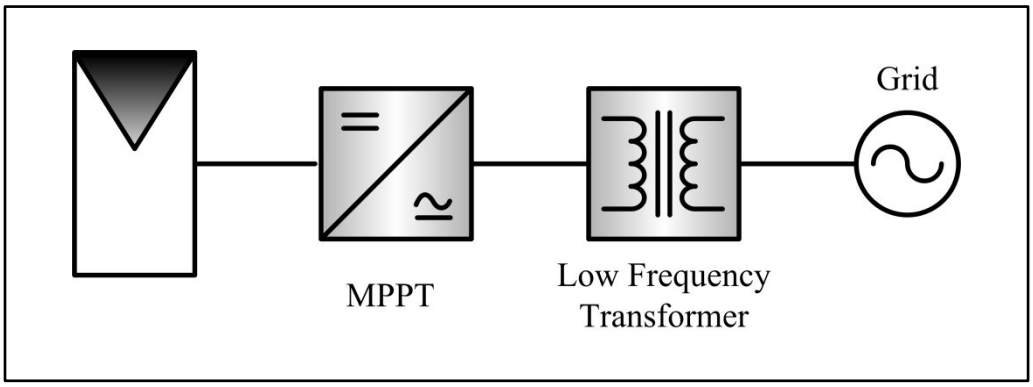

Fig. 4.6 PV inverter configuration without DC-DC converter and with isolation

system is required. Besides, any DC current can be injected to the load or power system side. This configuration can be utilized if the number of PV panels in series is high enough to produce a voltage higher than AC side voltage level. This configuration is shown in Fig. 4.7.

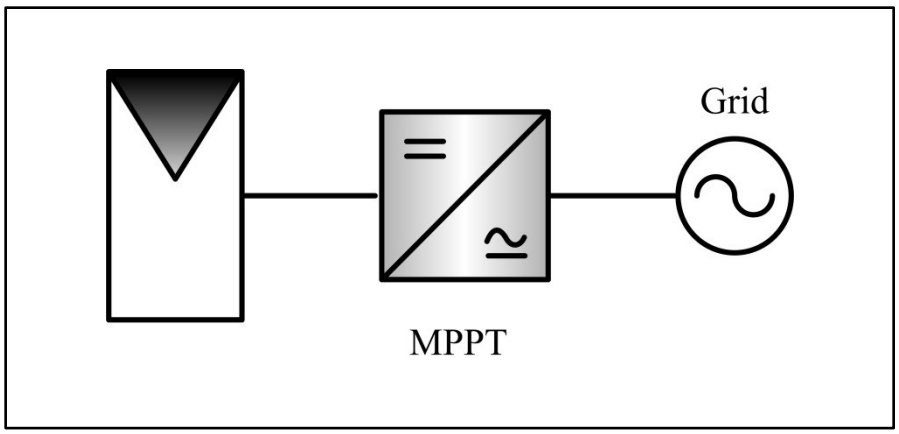

Fig. 4.7 PV Inverter configuration without DC-DC converter and without isolation

4.3.5 Possible PV interconnection schemes

Comparing output power and energy results from PV systems obtained using simulations during design stages with the real experimental results over the previous decades has exposed a significant difference [61]. This is due to numerous reasons one of which is mismatch losses. Mismatch losses are mainly constituted of two main reasons [62]-[67]. The first reason is dispersion of electrical properties and non-uniformity PV cell illumination among the array. This is mainly due to manufacturer's tolerances or degradation processes. The other important reason is partial shading of the PV array and variation of the tilt angles of different PV panels. Test results from various commercially available inverters show that the power loss due to partial shading can be as high as 70% [67]. If partial shading happens in a PV array or different PV panels with different angles are connected to one converter this will cause the power versus voltage/current characteristics of the PV array to have multiple local maximum point as shown in Fig. 4.8, however; only one of them is the global peak (GP) [68].

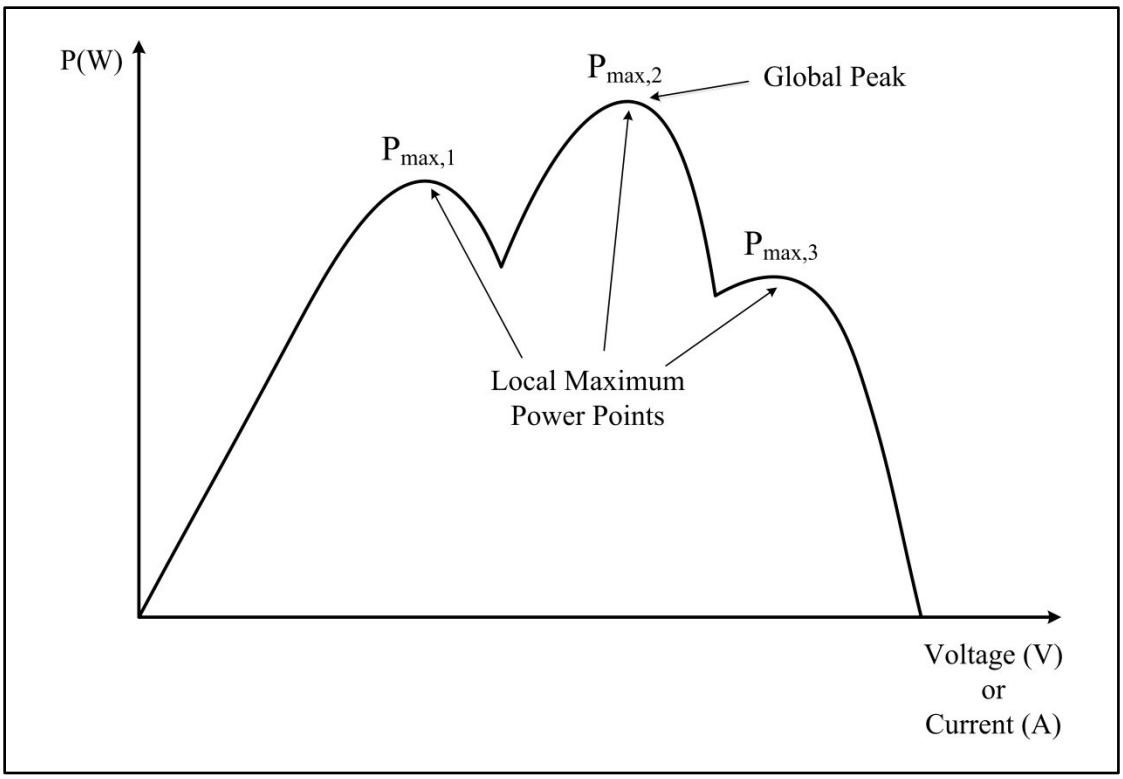

Fig. 4.8 A typical P-V curve of a partially shaded PV array

The existence of such local maximums can cause some Maximum Power Point Tracking Techniques (MPPT) especially Perturb and Observe (P&O) or Incremental Conductance methods to fail tracking the global maximum point ($P_{max,2}$ in Fig. 4.8). Eliminating or reducing this power loss resulting from mismatch of panels or different tilt angles can be performed by utilizing more efficient MPPT techniques, adding more converters or static/dynamic reorganizing cell/module connections. The usual interconnection of panels is connecting them in series and making strings of cells and paralleling the strings as was previously shown in Fig. 4.1 and Fig. 4.2. This interconnection is called Series-Parallel (SP). Other cell interconnections have been proposed which can reduce the mismatch power loss [62]-[64],[69]-[70][71]. They are called Total-Crossed Tied (TCT) and Bridge-Link (BL). They are shown in Fig. 4.9.

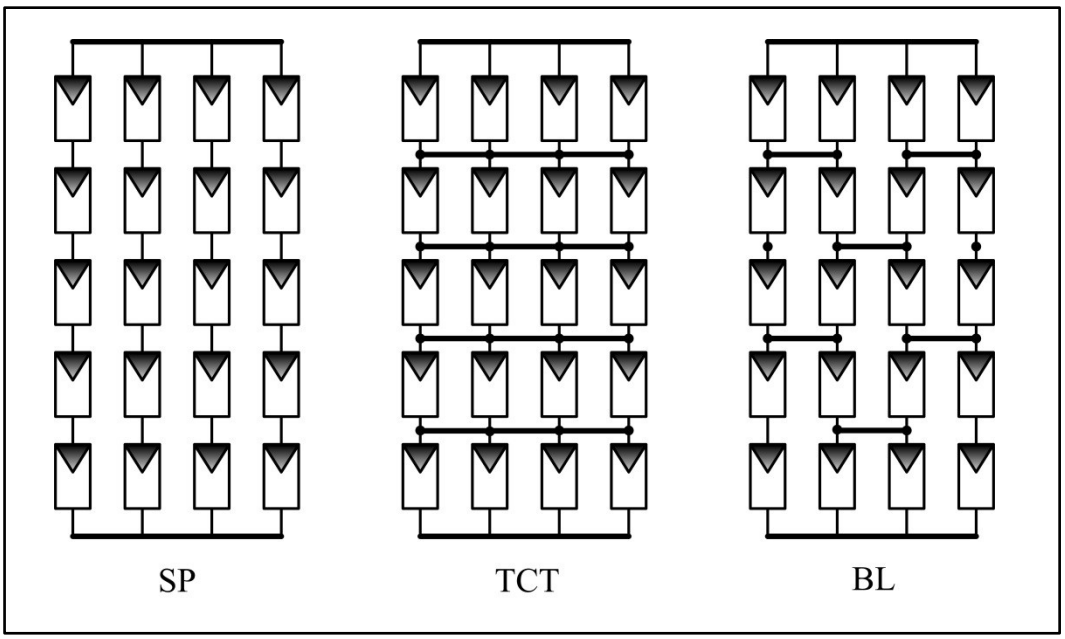

Fig. 4.9 Different cell interconnections: Series-Parallel (SP), Total-Cross Tied (TCT) and Bridge-Link (BL)

4.3.6 Proposed Structure

As mentioned in the introduction, our goal is to propose a structure which is able to inject the PV power directly to the battery pack and obtain the remaining power from the grid. The system diagram of the proposed structure is depicted in Fig. 4.10. This configuration has some advantages. First, the PV power can be directly injected to the battery pack and not to the grid then from the grid to the battery which reduces the overall losses. Second, this configuration provides great flexibility for different power flows. Depending on the amount of available power from PV panels and required power by the battery pack, different modes of operation may happen. If available power from PV is more than the required power for charging the battery pack the remaining can be injected to the grid (mode 1). If PV power is not enough, grid will be involved to supply the remaining power (mode 2). If there is no power available from the PV panels battery pack can be charged solely by the grid (mode 3). If the battery pack is not

connected to the system, PV power can be injected to the grid to reduce the electricity bill of the house (mode 4). If needed, the battery pack can be discharged to the grid during specified times performing as a configuration supporting Vehicle to Grid (V2G) (mode 5). Even in the case of

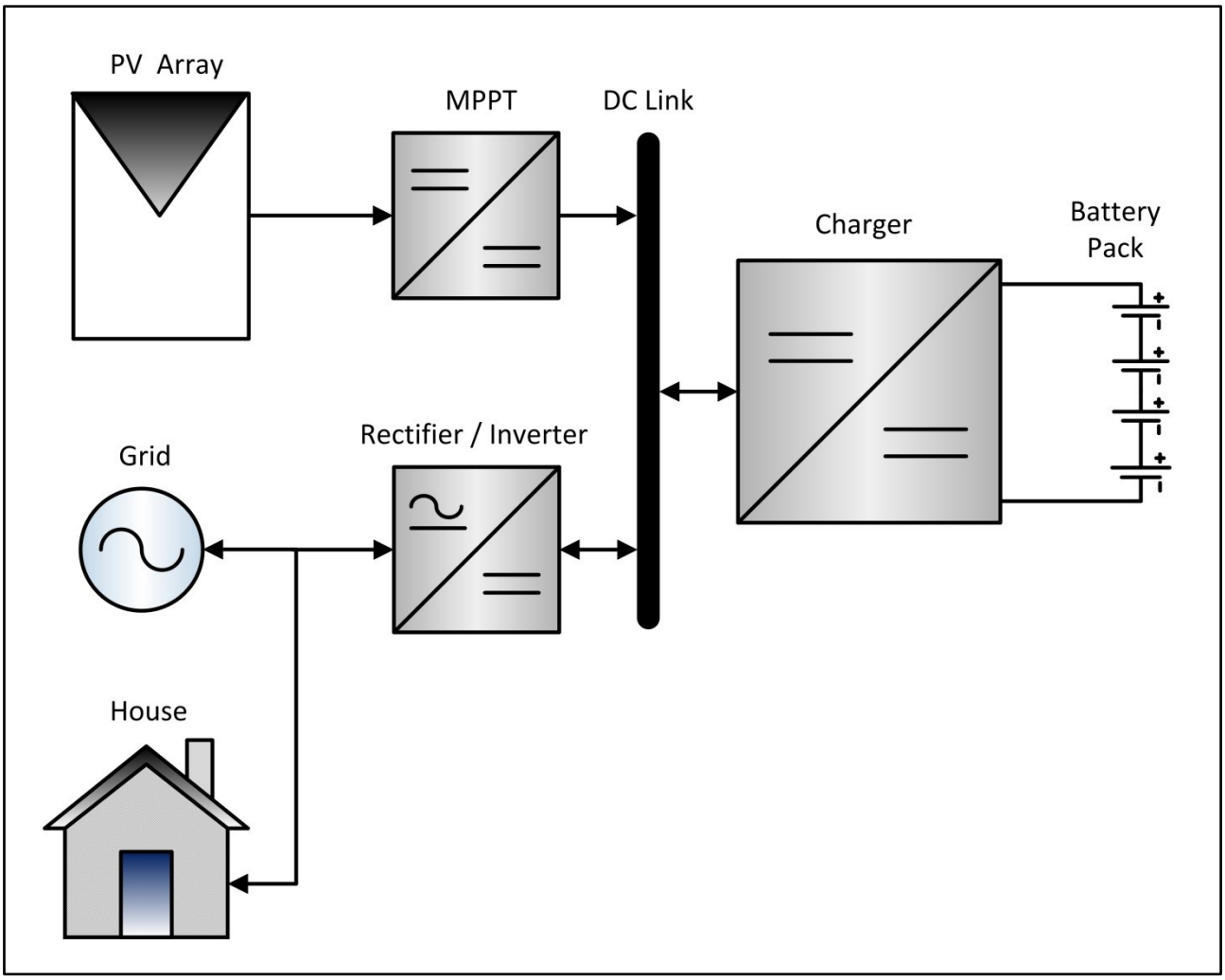

Fig. 4.10 System Structure

blackouts the battery pack can perform as an energy source and supply the power to the house for some time depending on the battery pack capacity (mode 6). This flexibility in power flows and modes of operation facilitates implementing concepts like smart grid. Different modes of operation are illustrated in Fig. 4.11.

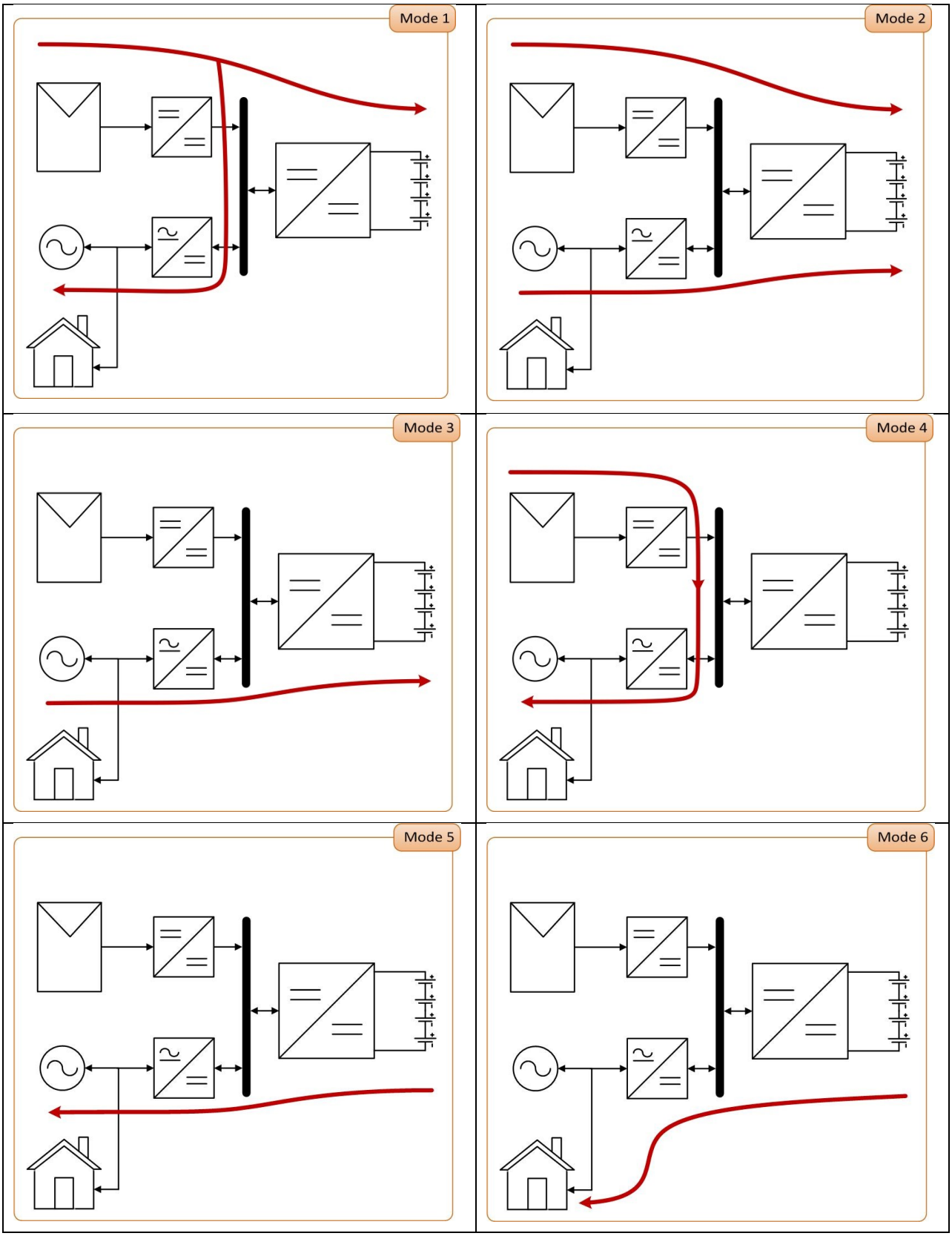

Fig. 4.11 Modes of operation

4.4 Power Converters Topology

There is variety of choices of converter topologies for the proposed configuration. There is not a unique best selection of topologies for this system like any other system; however, based on the operation principle of the configuration and nature of sources and loads the number of choices can be limited. According to the power flow directions depicted in Fig. 4.11 the category of the three converters in the system can be recognized.

4.4.1 MPPT Stage

Since PV panels are unidirectional source of energy, the Maximum Power Point Tracker (MPPT) stage can be unidirectional and doesn't need to be bidirectional. This part of the system was described in detail in CHAPTER.3. Depending on the desired power rating of the system, maximum power and voltage rating of the PV panels, maximum number of possible PV panels to be installed in a limited area (roof of a house); different topologies can be chosen. In chapter 3 a simple buck converter was used to show the validity of the proposed MPPT algorithm, however, as mentioned there the algorithm is independent of the converter topology as long as the topology can be current mode controlled. For example, non-isolated converters such as buck, boost and buck-boost or their isolated topology such as fly-back, forward and push-pull converters can be used. Each one has its own advantages and disadvantages. Depending on the design criteria which can be cost, efficiency, filter requirements, control simplicity, durability or other factors the topology can be chosen. PV panels can be connected in series/parallel and finally connected to the MPPT stage, or separate MPPT stages can be mounted on each PV panel and finally all of them connected in series or parallel or other combinations as was shown

previously for inverters in Fig. 4.1 and Fig. 4.2. Any other conventional MPPT method such as perturb and observe can also be used.

4.4.2 Rectifier / Inverter Stage

As shown in Fig. 4.11 the rectifier / inverter stage should be bidirectional to be able to operate in both directions depending on the desired mode of operation. Full bridge converter is a suitable candidate for this application, since it can operate both as a rectifier or an inverter with the same topology and just by changing the switching scheme. Different switching schemes are available for this topology and it has been widely analyzed in the literature. Because of the antiparallel diodes in full-bridge converter, all four quadrants of operation are accessible which provides reversible power flow direction. The rectifier / inverter stage is shown in Fig. 4.12.

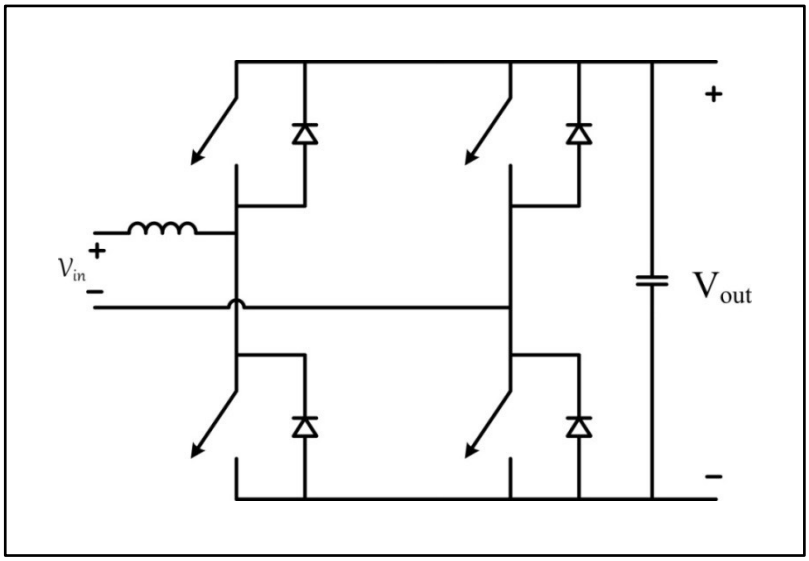

Fig. 4.12 Rectifier / Inverter stage

4.4.3 Charger Stage:

As depicted in Fig. 4.11 the charger converter has to be bidirectional and DC at both sides. Our assumption for next generations of EVs/PHEVs is that we have direct access to the

battery pack via DC terminal, eliminating AC/DC charger which is currently being used. This increases the efficiency of the overall system since one stage has been eliminated. Besides, because of the safety of the user, this converter should provide isolation, so in case of short circuit at the battery pack side the user remains safe. These features are all available in Dual Active Bridge (DAB). DAB was first introduced in [72]-[74] and modifications to this topology were later investigated. DAB is a bidirectional converter with high power density suitable for high efficiency applications. This converter has some desirable features such as bidirectional power flow, electrical or galvanic isolation, buck-boost operation, low device stress and low switching losses, small filter components because of high possible switching frequency, small and light isolation transformer because of high switching frequency and utilization of transformer leakage inductance as inductive energy transfer component. Based on the reverse voltage stress requirements of the switches other configurations can be recognized. For example, if the switches can tolerate the reverse voltages equal to input or output voltage, then the full-bridge converters can be substituted by half-bridge converters leading to Dual Half Bridge (DHB) converter. Another possible configuration is to have one full-bridge converter on one side and one half-bridge converter on the other side as shown in Fig. 4.13.

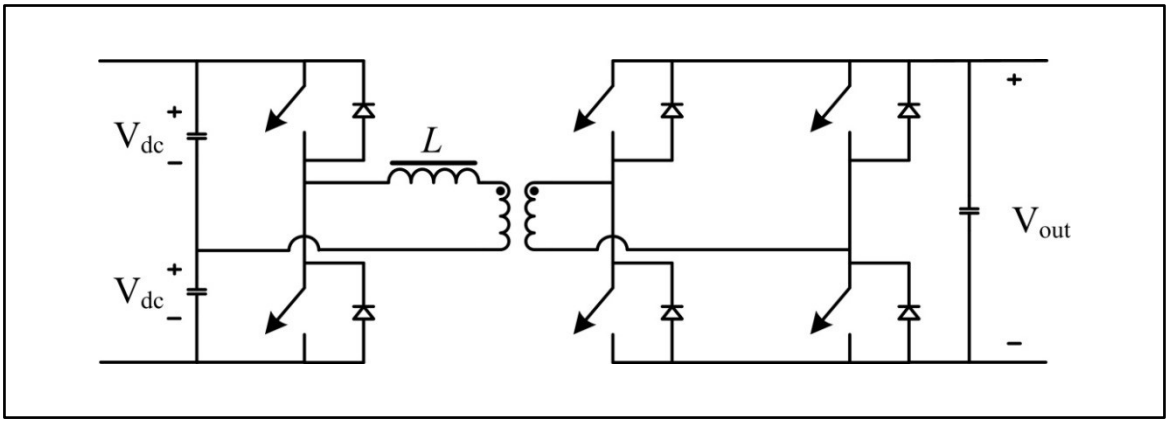

Fig. 4.13 DAB with Half-Bridge converter at one side

4.5 Summary

In this chapter conventional structures of PV systems and their applications were reviewed. Each category has its own pros and cons. They mainly include central inverters, string inverters and module integrated inverters. Inverters were classified based on different factors such as utilization of DC-DC converter or implementing isolation. They can be mainly categorized as: 1) PV inverters with DC-DC converter and isolation. 2) PV inverters with DC-DC converter and without isolation 3) PV inverters without DC-DC converter and with isolation 4) PV inverters without DC-DC converters and without isolation.

The phenomenon of local maximum power points and their reasons were introduced. Tracking a non-global maximum power point can lead to huge losses in the system and will decrease the efficiency of the system noticeably. Some MPPT techniques can avoid falling in a local maximum power point. Another way to reduce the losses caused by cell mismatch or partial shading is using more advanced PV interconnection schemes. Some conventional schemes include Series-Parallel (SP), Total-Cross Tied (TCT) and Bridge-Link (BL).

A configuration was proposed which makes it possible to inject all the available power from PV panels to the battery pack and drain just the remaining required power from the grid. Advantages of this configuration were outlined, one of which is providing the power flow in all possible directions and configurations and supporting modes such Vehicle to Grid (V2G) which can be used in smart grid applications. The most useful six modes of operations were shown graphically. Suitable power converter topologies were chosen for each part of the system such as Full bridge and Dual-Active-Bridge (DAB) converter.

CHAPTER.5

SYSTEM MODELING AND CONTROLLER DESIGN

5.1 Introduction

Power electronics mainly involves control of energy flow. Depending on the load and application the output of any system as well as switching power converters should be controlled to some extent to obtain the desired behavior and performance. Without control action the behavior of switching power converters is dependent on environment and system conditions such as temperature, supply voltage, load change, system parameter deviations over time and external disturbances in general which is not desirable for precise electrical loads and applications. For high power high energy battery pack charging application which can be very dangerous if not controlled and charged properly, regulation is considered critical. One of the most significant advantages of switching power converters is their ability of automatic control action. For regulation of the power converter systems at least one control parameter should be available and adjusted continuously. Control parameter is mainly a parameter of the system that can change the behavior of a system during operation. Duty ratio, phase angle and phase shift are examples of control parameter. Different concepts, aspects and techniques in control theory can be applied to switching power systems. One of the most common techniques is feedback control which is mainly measuring the output of the system, comparing to the desired value and finally taking action based on the value of error. Since power converters use energy storing elements like capacitors and inductors constituting states of the system, any disturbance or deviation in the input of the switching converter takes some time to show up at the output which may result in a

slow reaction of the feedback control system. This can be improved by using another concept called feedforward control. Besides, the response speed of a system can be improved by modifying the controller of the feedback loop; however, it may involve increasing the complexity or cost of the system. Hence, sometimes a combination of feedback control and feedforward control is desirable. In general, designing a suitable controller for the power converter system may not be unique and depends on different factors such as nature of the system, expertise of the designer, desired response and allowed cost of the whole system. Desired behavior of a power converter can be summarized as static response and dynamic response. The usual purpose of a good static response is to keep the output constant. Keeping the output constant doesn't necessarily mean a constant voltage or constant current. It can be an AC output voltage with constant RMS voltage and constant frequency. On the other side, a good dynamic response is related to the ability of the controller to bring the output of the system back to the desired value with the specified speed after a very fast change of a parameter like a step change in input voltage. Besides, the controller should be able to keep the system stable within a specific range of changes in parameters as specified in the design procedure, for example a specific percentage of deviation of input voltage.

5.2 PV Stage

Photovoltaic stage was thoroughly discussed in CHAPTER.3 along with a novel maximum power point tracking technique. The power converter used was buck converter. To make system level simulations much easier and faster and not to worry about type of converter or utilized MPPT technique a model of PV stage is proposed. Whatever the meteorological conditions are and whatever type of converter topology and MPPT technique is used the total PV stage along with MPPT stage can be considered as a Unidirectional Variable Power Source (UVPS). The output power of UVPS is dependent on meteorological conditions such as sunlight intensity and temperature; however, at any given time it has a specific value. The output power of PV stage changes very slowly over time period ranges of minutes and hours while the sun angle is changing during the day. Hence, for designing purposes and running simulations of seconds or milliseconds and considering switching frequencies of kHz of power converters, the output of PV stage can be considered constant. In other words, other parts of the system such as batteries, power converters and controllers sense the PV stage as an almost constant power source at any given time or small periods of time. Such characteristics may be modeled using different configurations or techniques. One simple but very efficient configuration used by author is shown in Fig. 5.1. The operation of the circuit can be described as follows. The output of the circuit will be connected to the DC link which will have a constant DC voltage. Since the output is DC the output power is equal to voltage multiplied by current. Hence, if the desired reference output power is divided by the measured output voltage, the reference current to be applied to the resistor is obtained and applied with the Controlled Current Source (CCS). Part of the power injected by CCS is dissipated in the resistor and the remaining will be injected to the DC link. So if the value of resistor is very big then the dissipated power will be very small.

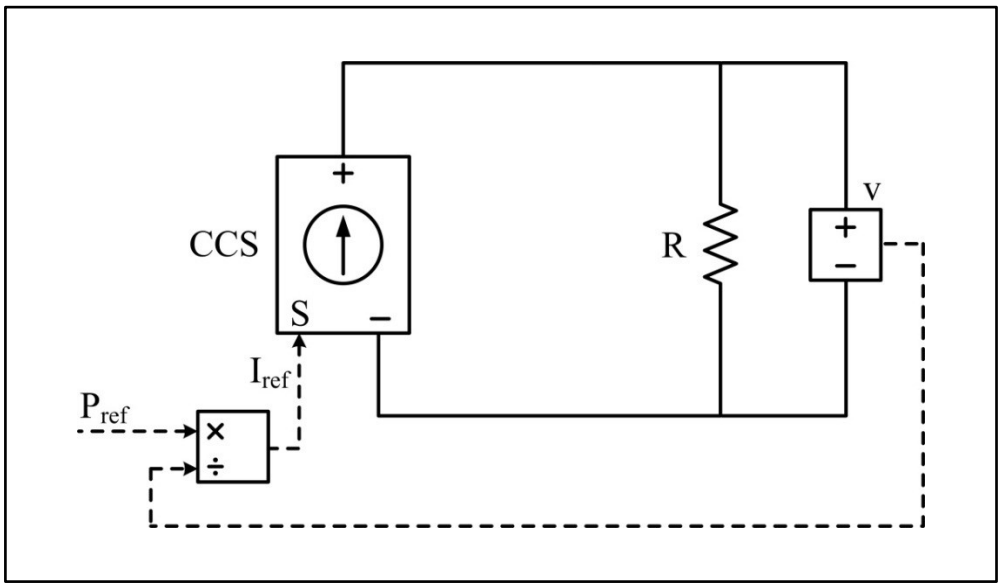

Fig. 5.1 Basic PV stage model in Matlab/Simulink

For example, if the voltage of the designed DC link is kept at 400 V and the value of resistor is chosen to be equal to 160 kΩ the dissipated power in resistor will be $400^2/160000=1$W which is negligible compared to the power rating of the system which is 6 kW.

If the circuit shown in Fig. 5.1 is implemented in Matlab/Simulink exactly as is shown an error will be generated which is called algebraic loop. This error happens when the information needed to calculate the parameters of the current step is in the next step or after the calculations of current step. For example, in Fig. 5.1 for calculating the vaule of I_{ref} for current time step, the vaule of ouput voltage in current step is required. Besides, the value of output voltage of current time step depends on the value of resistor current. So we have two unknowns depending on each other. This problem can be solved by adding a state to the circuit which will store information about the previous step and can be used for current time step. For example, a parallel capacitor can be added to the output resistor to solve the problem of algebraic loop.

Other than algebraic loop another error may happen because of the division block. If the output voltage is equal to zero for example at the beginning of simulation then a value is divided by zero which will generate NaN or Inf error. This problem can also be solved by adding a bias block to the voltage feedback loop which adds a value to the signal value making it non-zero. This value can be chosen to be very small, for example, equal to 0.001 or even smaller. This value is so small that will have no effect on the operation of the circuit especially, when the output voltage reaches around its actual value which is 400 V. The modified PV stage model is shown in Fig. 5.2.

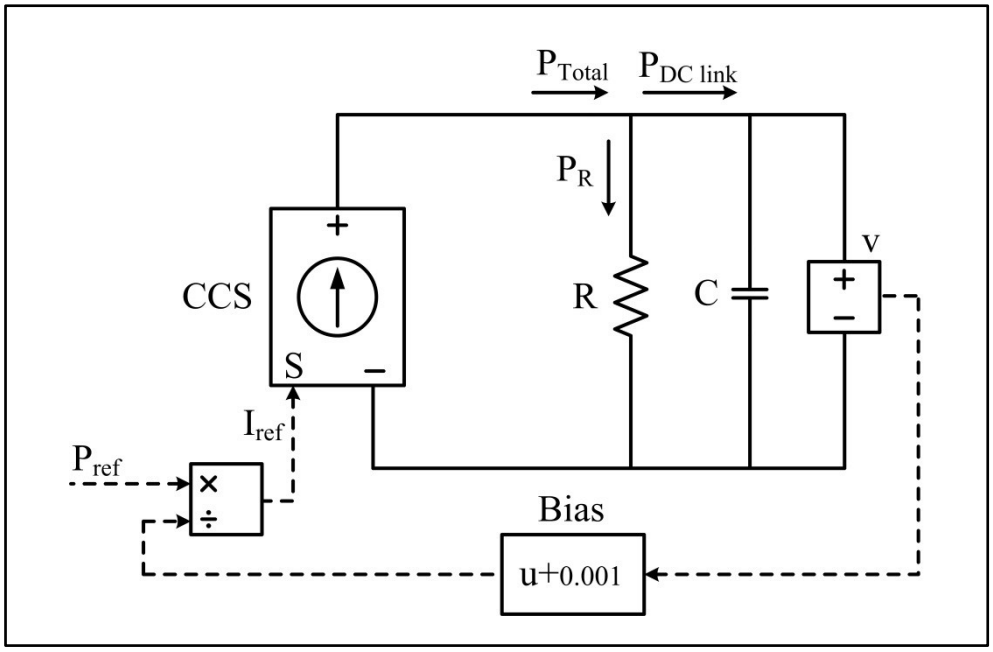

Fig. 5.2 Modified PV stage model in Matlab/Simulink

Some tests have been performed to show the performance of the proposed model during different situations. The results are shown in Fig. 5.3. Although the output voltage is deviating largely, $P_{DC\ link}$ follows P_{ref} perfectly. P_{ref} is changed each 3 seconds and output voltage is changing each second to study performance of the model under large perturbations.

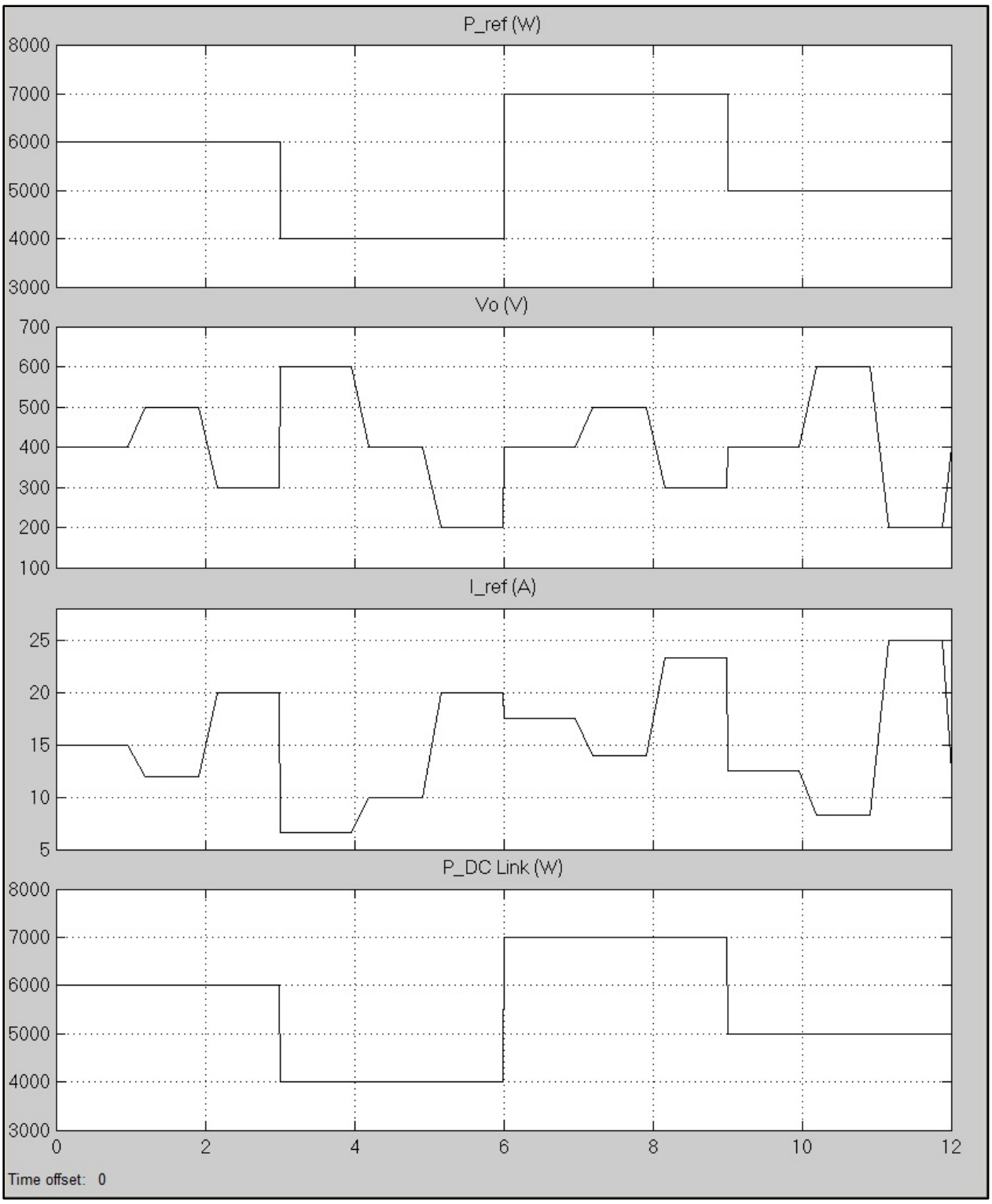

Fig. 5.3 Simulation results for PV stage

5.3 Rectifier / Inverter Stage

As described in 4.4.2 the rectifier / inverter stage topology has been chosen to be a full-bridge converter. The circuit along with grid and resistive load is depicted in Fig. 5.4.

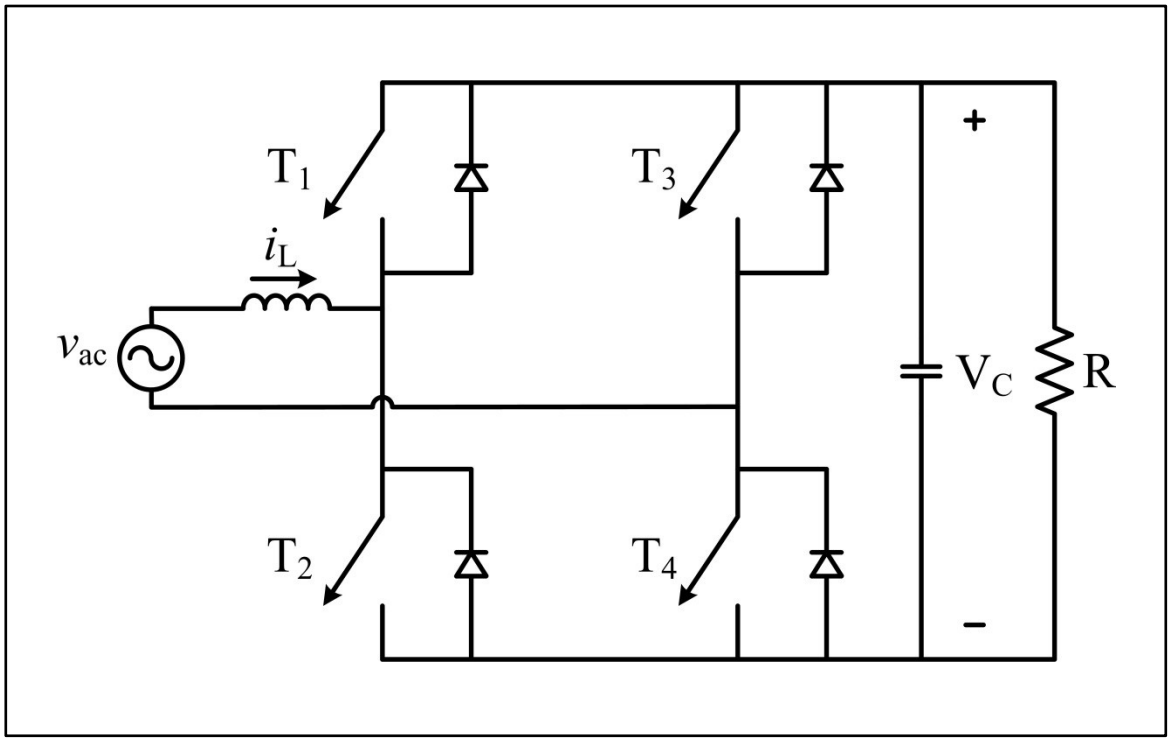

Fig. 5.4 Rectifier / Inverter stage

The main role of this stage is to keep the voltage of the DC link constant so the other parts of the system like the charger stage and the PV stage can operate properly. But how can this be achieved? While the battery is being charged according to the charge profile provided by the manufacturer, at any time the battery is absorbing a specific amount of power through DAB. At the same time a specific amount of power is being generated by the PV panel through the MPPT stage which can range from zero to P_{max} depending on the meteorological conditions. The power produced by the PV panels is not necessarily equal to the power absorbed by the battery

pack. If PV power is more, then the stored energy in the DC link capacitor increases leading to the increase in DC link voltage. Similarly if the PV power is less than battery absorbed power, DC link voltage will reduce. In both cases the system cannot work properly or even may become unstable. To compensate for these power differences the rectifier/inverter stage should be present to inject the required power to the DC link working in rectification mode or absorb extra power from DC link working in inversion mode.

If a voltage controller is properly designed for the rectifier/inverter to keep the DC link voltage constant, all mentioned above will be achieved automatically. To understand the design procedure we begin from current phasor concept. Assuming the ac side current is a sinusoidal waveform with a phase shift relative to input ac voltage which is grid voltage and considering the ac current waveform as a rotating vector we can write:

$$v_{ac}(t) = V_m \sin(\omega t) \tag{5.1}$$

$$i_L(t) = I_m \sin(\omega t - \varphi) \tag{5.2}$$

$$\Longrightarrow i_L(t) = I[\sin(\omega t)\cos(\varphi) - \cos(\omega t)\sin(\varphi)] \tag{5.3}$$

$$= \underbrace{[I\cos(\varphi)]}_{I_p}\sin(\omega t) - \underbrace{[I\sin(\varphi)]}_{I_q}\cos(\omega t) \tag{5.4}$$

$$i_L(t) = I_p \sin(\omega t) - I_q \cos(\omega t) \tag{5.5}$$

This can be illustrated in phasor diagram as shown in Fig. 5.5.

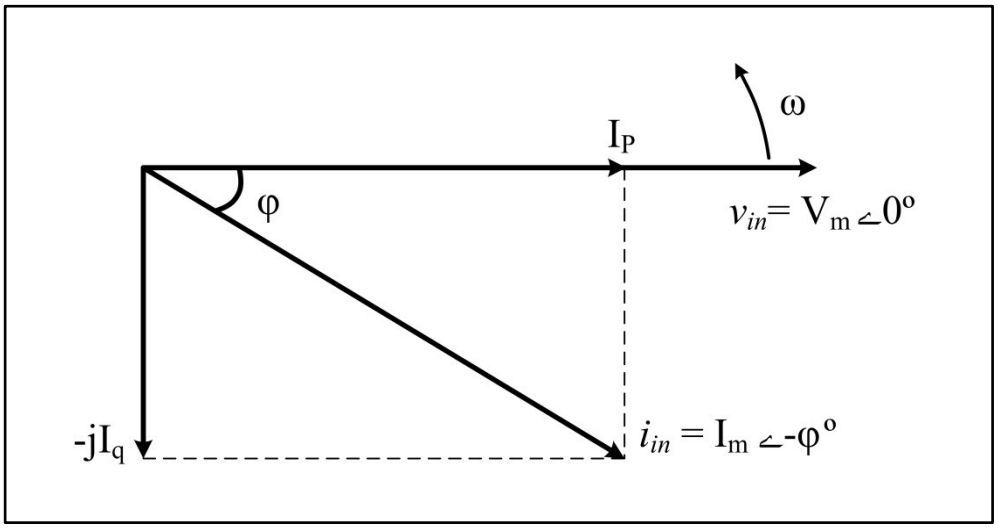

Fig. 5.5 Input current and voltage phasor diagram of Rectifier / Inverter

According to Fig. 5.5 the average active and reactive power injected to the circuit from grid can be written as:

$$P = \frac{1}{2} V_m I_m \cos(\varphi) = \frac{1}{2} V_m I_p \tag{5.6}$$

$$Q = \frac{1}{2} V_m I_m \sin(\varphi) = \frac{1}{2} V_m I_q \tag{5.7}$$

Considering efficiency of the circuit, if reactive power equals zero or in other words the power factor is equal to one, then the circuit will have maximum efficiency which will be theoretically 100% if the circuit is ideal with no switching losses. To achieve this, the current should be controlled in such a way that $I_q = 0$ and $I_p = I_m$. In other words, the current should be in phase with voltage. On the other side, current is aimed to be equal to I_p. Therefore, I_p is the control parameter and V_{out} is the parameter to be controlled. The value of I_p is determined by the required average power P and using (5.6). The current at the input is in the form of AC but the

conventional controller design techniques are mainly for DC quantities. To solve this problem a rotating frame with the angular speed of ω is assumed to rotate with current phasor as was shown previously in Fig. 5.5. Using this transformation for single phase ac waveforms results in I_p and I_q which are DC quantities. Therefore, for designing a voltage controller for this circuit we need the relationship between ΔV_{out} and ΔI_p. In other words, the effect of small signal perturbations in $i_p(t)$ on $v_{out}(t)$ should be analyzed. Making some assumptions such as considering the system to be lossless (no switching losses), switching frequency is high enough and L is small enough we can conclude:

$$P_{AC} = P_{DC} = P_C + P_R \tag{5.8}$$

$$P_C = \frac{dE_C}{dt} = \frac{1}{2} C \frac{dV_C{}^2}{dt} \tag{5.9}$$

$$P_R = \frac{V_C{}^2}{R} \tag{5.10}$$

$$Laplace \Longrightarrow \frac{1}{2} V_m I_p = \frac{1}{2} sCV_C{}^2 + \frac{V_C{}^2}{R} \tag{5.11}$$

$$Small\ Perturbations \Longrightarrow \begin{cases} I_p = I_{p0} + \tilde{\imath}_p \\ V_C = V_{C0} + \tilde{v}_C \end{cases} \tag{5.12}$$

$$\Longrightarrow \frac{1}{2} V_m \left(I_{p0} + \tilde{\imath}_p\right) = \frac{1}{2} sC (V_{C0} + \tilde{v}_C)^2 + \frac{(V_{C0} + \tilde{v}_C)^2}{R} \tag{5.13}$$

$$\Longrightarrow \frac{1}{2} V_m \tilde{\imath}_p = sCV_{C0}\tilde{v}_C + \frac{2V_{C0}\tilde{v}_C}{R} \tag{5.14}$$

$$Linearized\ small\ signal\ model: \boxed{\frac{\tilde{v}_C}{\tilde{\imath}_p} = \frac{\frac{V_m R}{4V_{c0}}}{\left(1 + s\frac{CR}{2}\right)}} \tag{5.15}$$

For the controller part, different control techniques may be utilized, however, since the required current or power injected/absorbed to/from the DC link varies over a wide range during the operation of the whole system, the utilized control technique to be used should be very robust, hence, Hysteresis Current Control (HCC) has been chosen for this stage. HCC mainly involves a hysteresis band (H) which can be defined based on the desired current ripple. This hysteresis band can be constant or variable using adaptive control techniques. Here, for simplicity we choose constant hysteresis band. If the value of I_p which is determined by the voltage controller is multiplied by a sinusoidal waveform in phase and with the same frequency as input ac voltage, then the reference current is determined. Reference current, upper band and lower band are defined as:

$$i_{ref} = I_{p,ref} \sin(\omega t) \tag{5.16}$$

$$i_{up} = i_{ref} + \frac{H}{2} \tag{5.17}$$

$$i_{low} = i_{ref} - \frac{H}{2} \tag{5.18}$$

According to Fig. 5.4 when switches T2 and T3 are turned on, the inductor current i_L will increase. If i_L is about to exceed i_{up} then T2 and T3 are turned off and T1 and T4 are turned on. In this configuration i_L will reduce. T1 and T4 are kept on until i_L is about to fall behind i_{low}. At this moment T1 and T4 are turned off and again T2 and T3 are turned on. Using this switching scheme, i_L will remain in the hysteresis band. Switching function S_a can be defined as follows:

$$T1\,,T4\;ON\;\;\&\;\;T2\,,T3\;OFF \Longrightarrow S_a = 1 \tag{5.19}$$

$$T2\,,T3\;ON\;\;\&\;\;T1\,,T4\;OFF \Longrightarrow S_a = -1 \tag{5.20}$$

Applying KVL to the circuit and using the switching function we have:

$$L\frac{di_{L(t)}}{dt} = v_{ac(t)} - S_{a(t)}V_C \tag{5.21}$$

The unique solution to (5.21) depends on the initial condition [75]. The current flowing to the load of Fig. 5.4 in terms of switching function can be written as:

$$i_{Load(t)} = S_{a(t)}i_{L(t)} \tag{5.22}$$

Principles of HCC are depicted in Fig. 5.6.

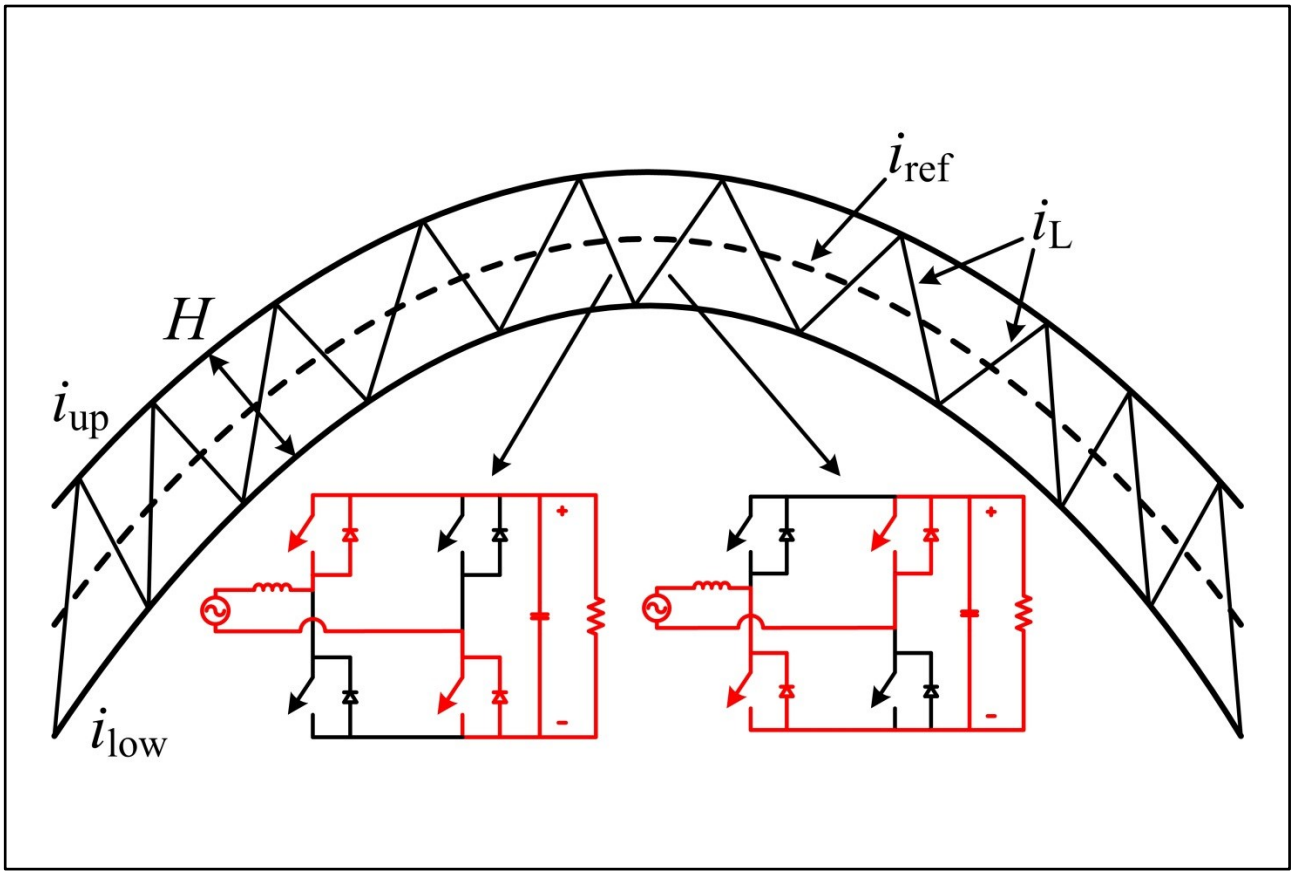

Fig. 5.6 Principles of hysteresis current control

An important point about HCC is that the switching frequency is not constant. Since variations of i_{ref} which is sinusoidal is minimum at peak points, minimum switching frequency will happen at these points. Similarly, since variations of i_{ref} is maximum at zero crossing points, maximum switching frequency will happen at these points. This makes the design procedure hard. For example, for designing the filter elements like capacitor, the impedance usually should be known for the switching frequency which is constant for PWM switching schemes. But switching frequency is variable in the case of HCC.

If H is reduced the accuracy of controlled current will increase, however, the switching frequency and losses will increase as well, hence, the efficiency will reduce since i_L reaches upper and lower bands faster and vice versa. The inductor value also plays an important role in determining the speed of response and should be chosen properly. If L is very small the inductor current will change and reach the bands very fast, hence, the switching frequency will increase and efficiency will reduce. Similarly, if L is very big then the inductor current changes slowly and even the circuit may not be able to track the reference current. As previously was shown in Fig. 4.10 the system includes three main parts, i.e. MPPT stage, charger stage and rectifier/inverter stage. According to the role of rectifier/inverter stage which is to compensate for power variations in DC link, this stage should have a very fast speed of response compared to other stages in order to be able to achieve this goal otherwise, variations in DC link voltage will last for long periods and may affect the operation of other stages. So the controller should be designed accordingly. The controller block diagram is shown in Fig. 5.7.

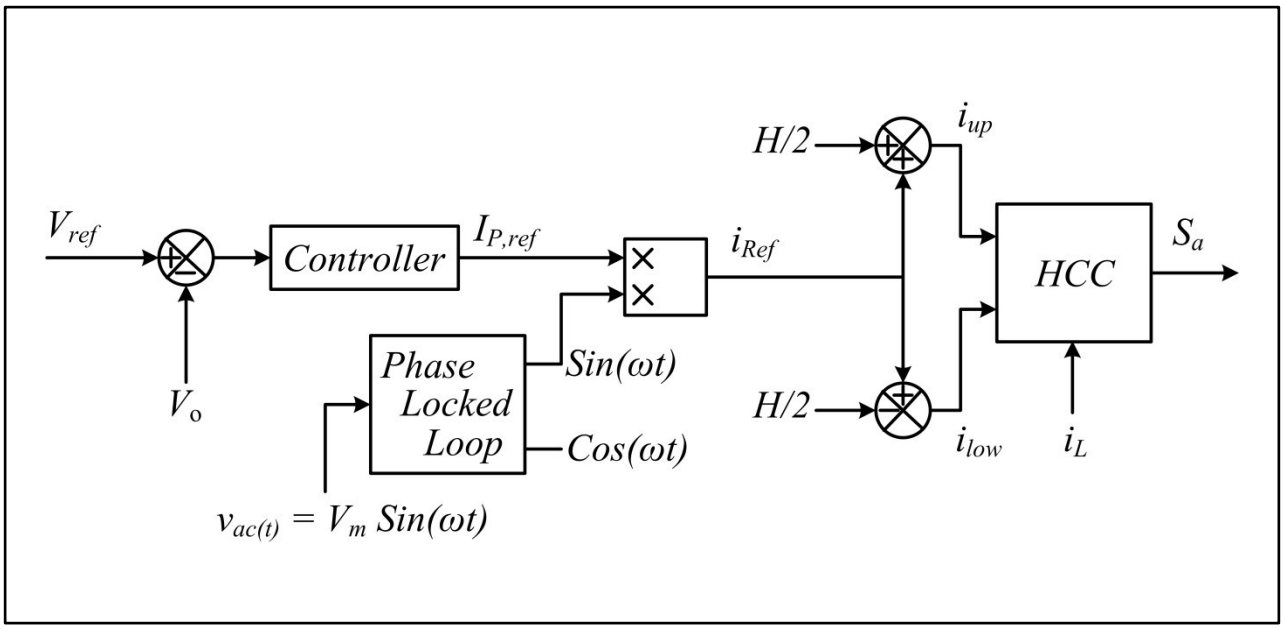

Fig. 5.7 Controller block diagram for HCC

To design circuit parameters a specific case can be considered and then the controller can be designed based on the initial design. According to Fig. 5.4 a 160Ω resistor will sink a power equal to $(400)^2/160 = 1000$ W. According to descriptions mentioned above, parameter values of L = 2.5 mH and C = 5 mF provides a reasonable average switching frequency of about 80 kHz and a good open loop response. According to (5.15) the small signal control to output transfer function will be equal to:

$$\frac{\tilde{v}_C}{\tilde{\imath}_p} = \frac{12}{0.4\,s + 1} \tag{5.23}$$

The bode plot and step response of control to output transfer functions is depicted in Fig. 5.8 and Fig. 5.9 respectively.

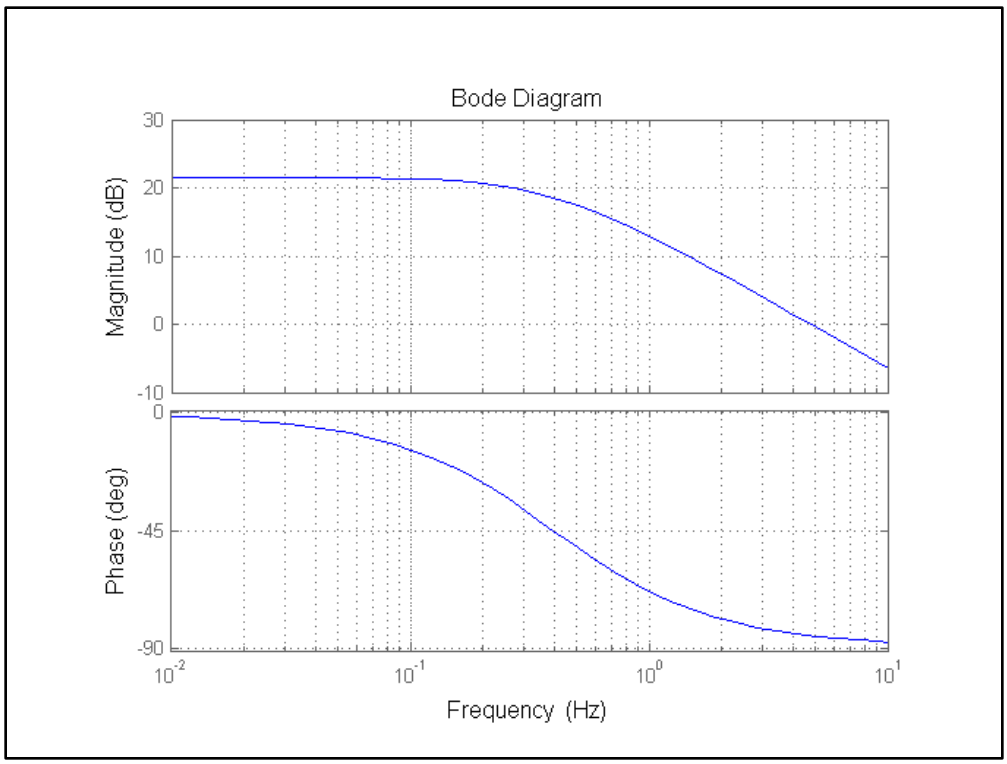

Fig. 5.8 Bode diagram of control to output for Rectifier / Inverter stage

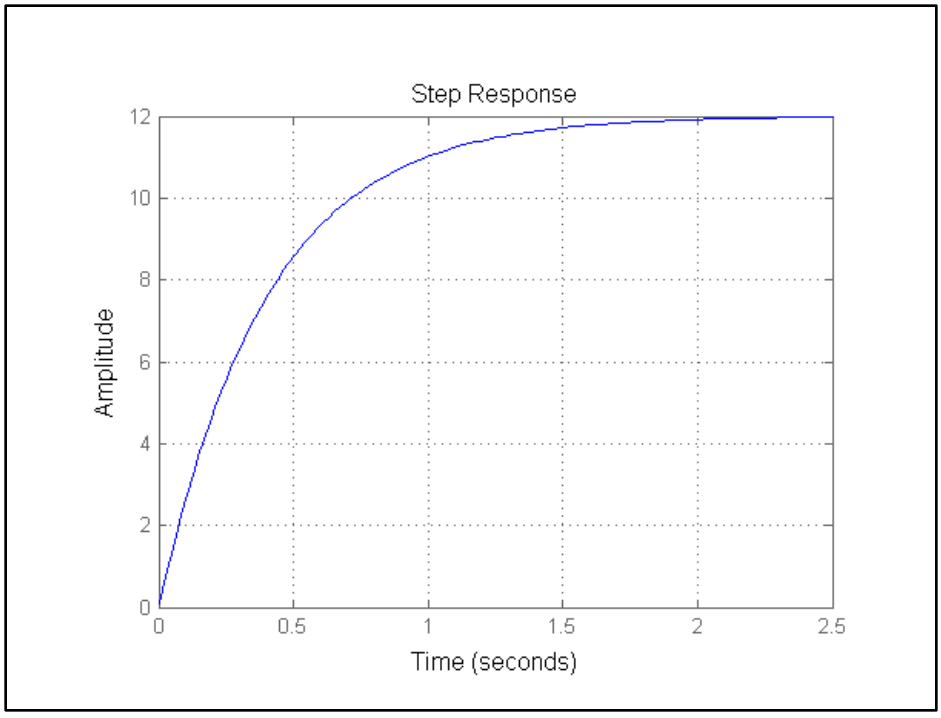

Fig. 5.9 Step response of control to output for Rectifier / Inverter stage

Fig. 5.8 suggests the use of an integrator to have zero steady state error; however, merely using an integrator with a gain will lead to a relatively slow system. Since this stage should have a fast speed of response adding a real zero at a suitable frequency will noticeably increase the speed of response without a significant overshoot. The designed controller is obtained as:

$$G_c = 1.9816\,\frac{s + 3.55}{s} \tag{5.24}$$

The bode plot and root locus of the new open loop transfer function is shown in Fig. 5.10.

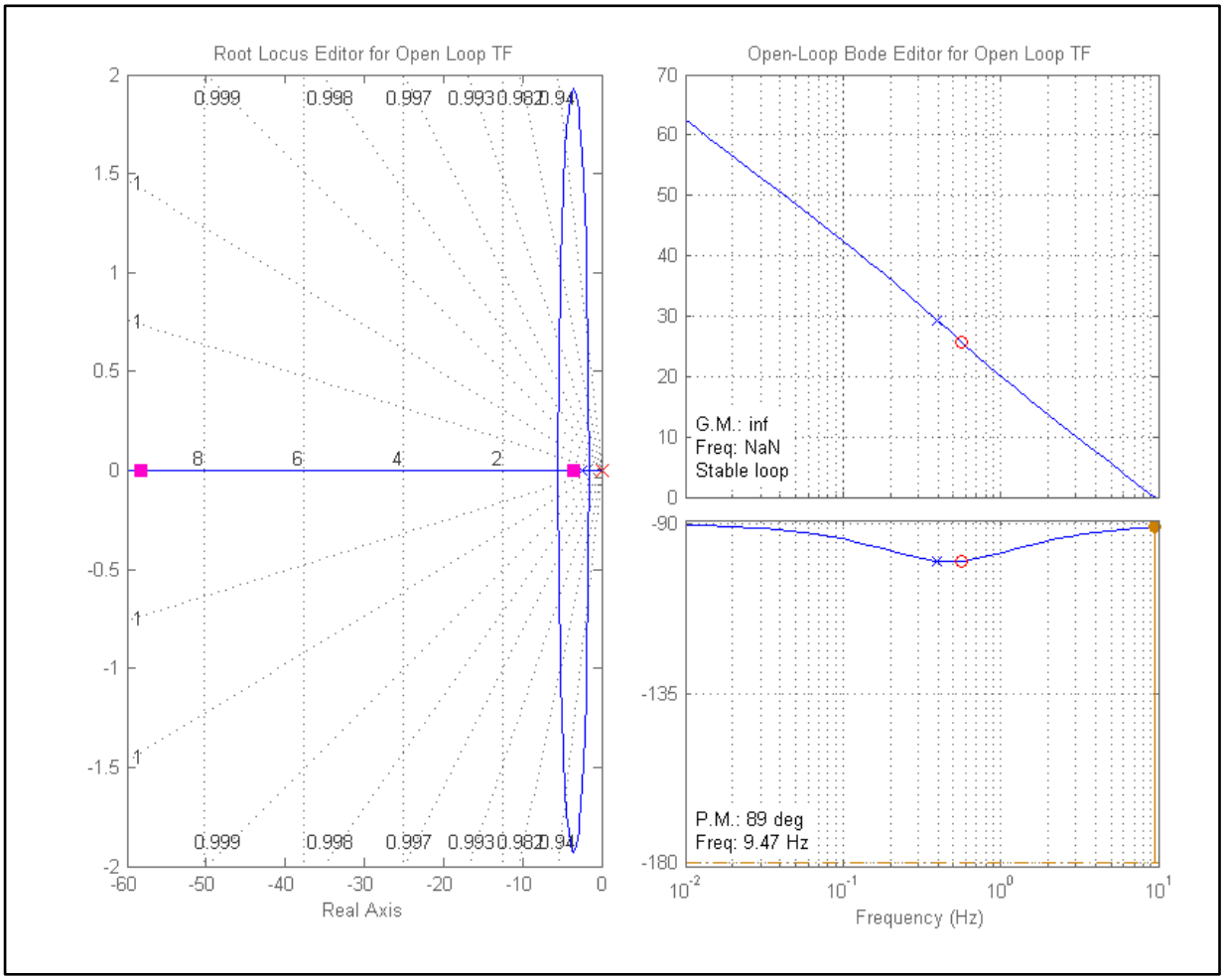

Fig. 5.10 Bode plot and root locus of the new open loop transfer function

The closed loop step response of the new system with the controller is shown in Fig. 5.11 with 57 ms settling time which is fast enough as will be shown in simulation results.

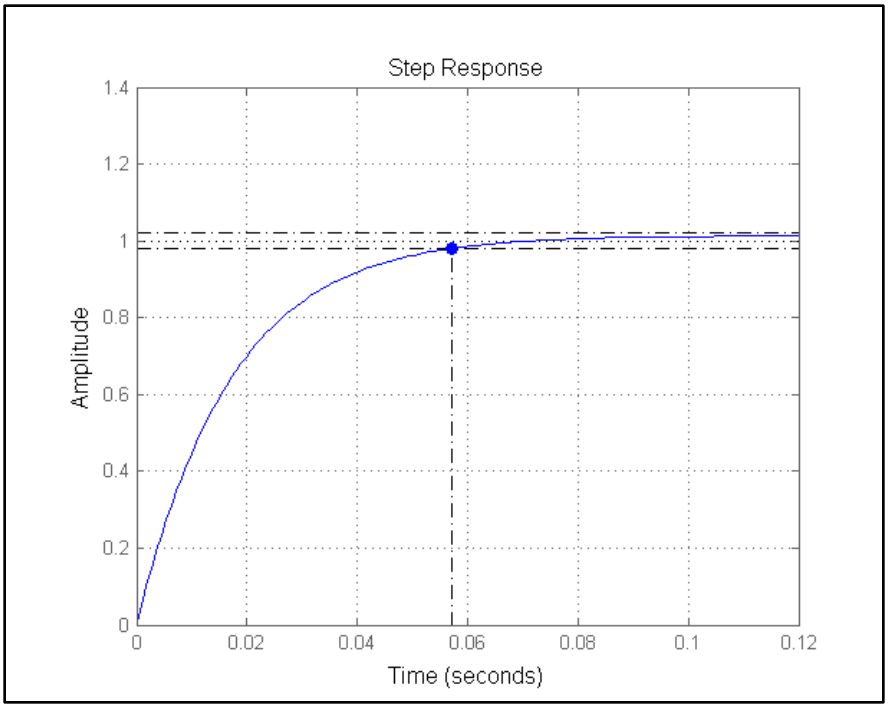

Fig. 5.11 Closed loop step response of Rectifier / Inverter stage with controller

To verify the functionality and robustness of the designed system a set of tests have been done. First, the circuit is tested in rectification mode. Different loads are connected to the circuit at the intervals of 1.5 sec to see the response of the system as shown in Fig. 5.12. Output voltage, I_P, input active and reactive power injected to the circuit, inductor current and total harmonic distortion of input current are shown in rows 1 to 5 respectively. Although the output load power variations are very huge, for example 3 kW change at t=6 sec which is 50% variation still the controller reacts very fast and keeps the output voltage ripple in the range of 10% which is ±20V. As THD graph shows, other than spikes happening at very small transient times, THD stays between 5-7% leading to power factor (PF) of 0.9975 to 0.9987 assuming displacement PF of 1.

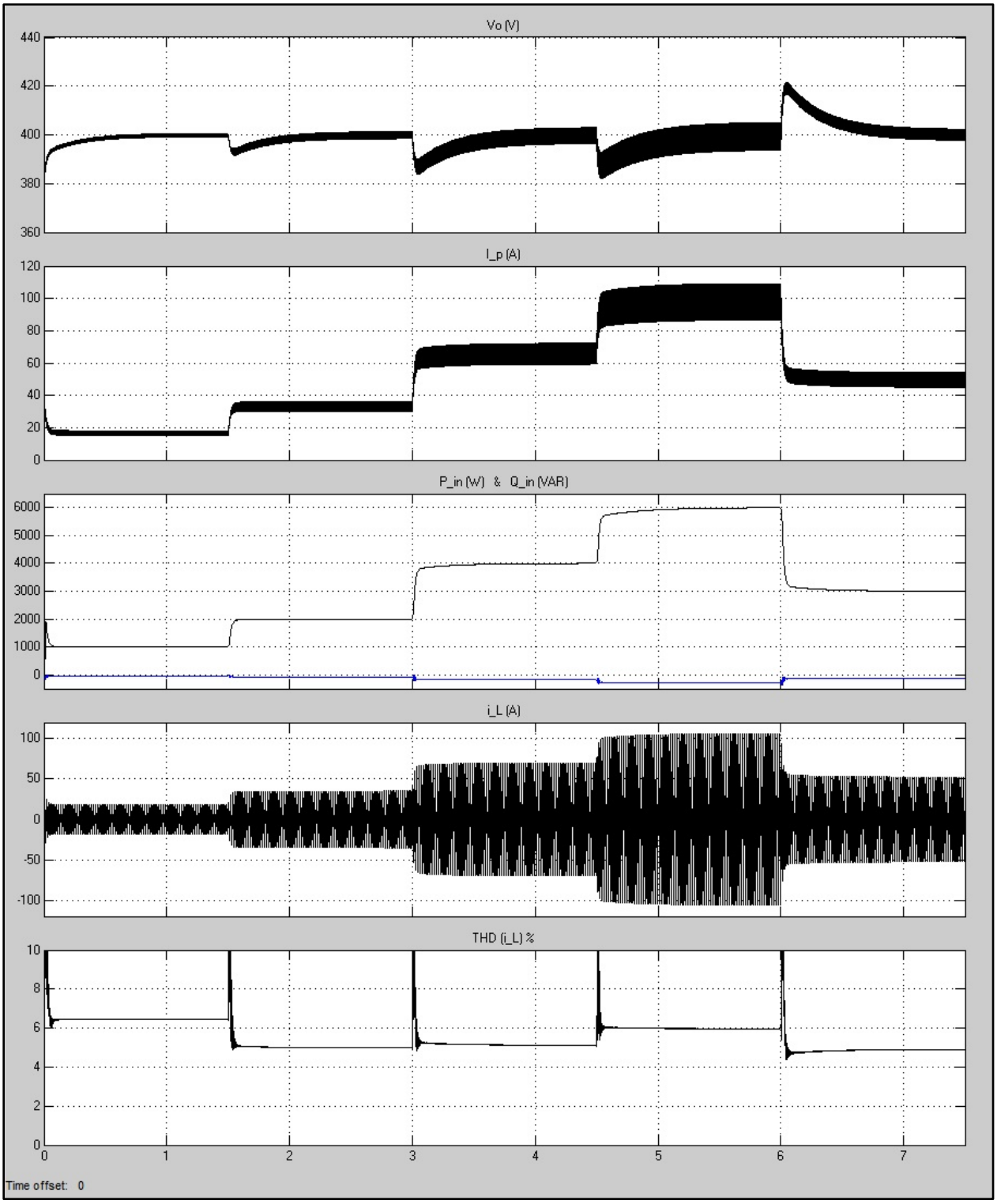

Fig. 5.12 Simulation results for Rectifier / Inverter stage in Rectification mode

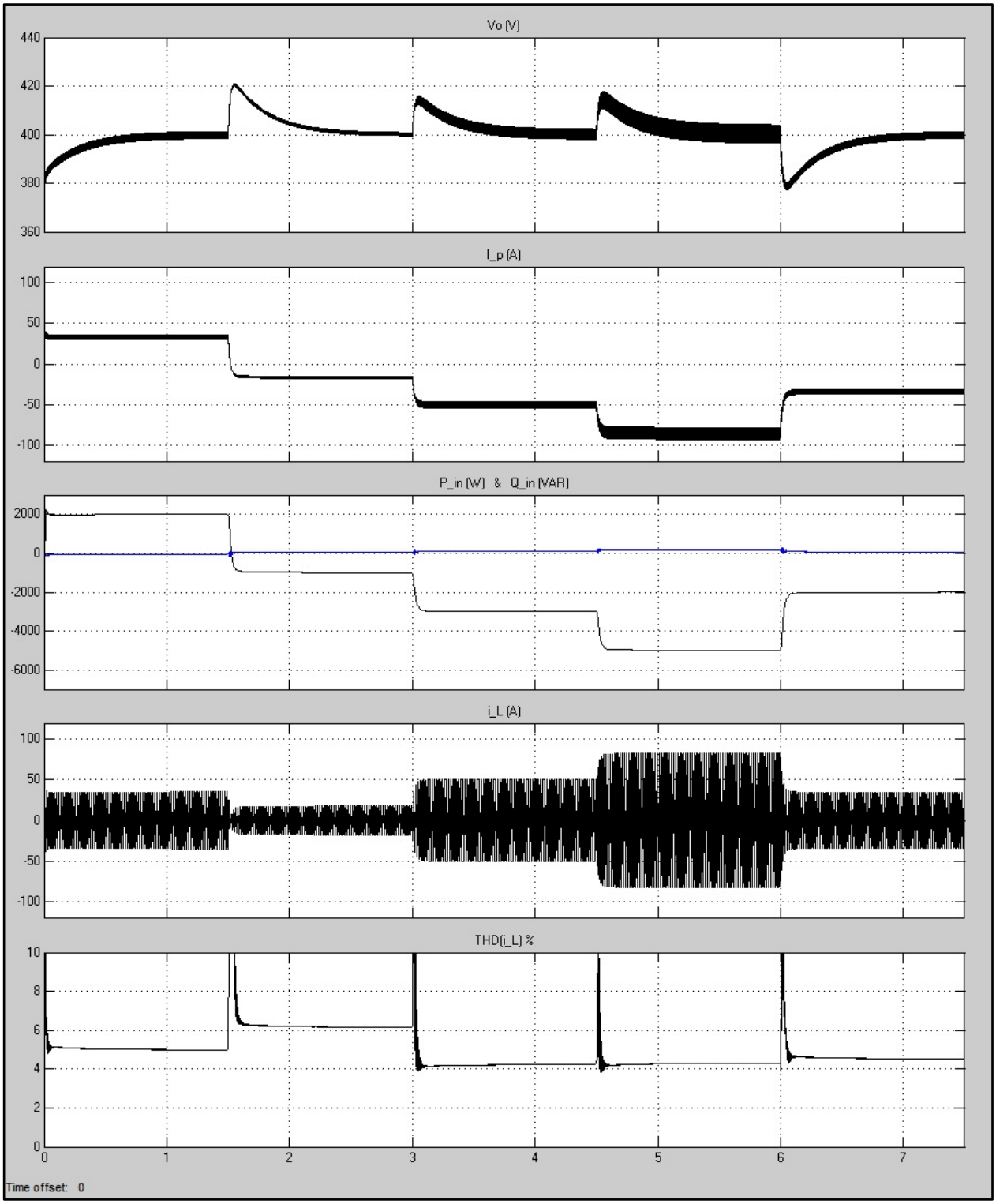

Fig. 5.13 Simulation results for Rectifier / Inverter stage in Inversion mode

Fig. 5.13 shows the result of the circuit in inversion mode. In this scenario the load acts a power source and the power is injected to the grid. At t = 1.5 sec the operation of the circuit switches from rectification mode to inversion. The controller reacts very well during this important transition and no instability happens which ensures the switching of the circuit between different modes of operation safely.

5.4 DAB Stage

Dual Active Bridge (DAB) was briefly described in section 4.4.3. DAB mainly consists of two switch-mode active bridges which can be half-bridge or full-bridge, one of which operates in inversion mode and the other operating in rectification mode. DAB includes a high-frequency transformer which provides electrical isolation and bidirectional power flow as shown in Fig. 5.14.

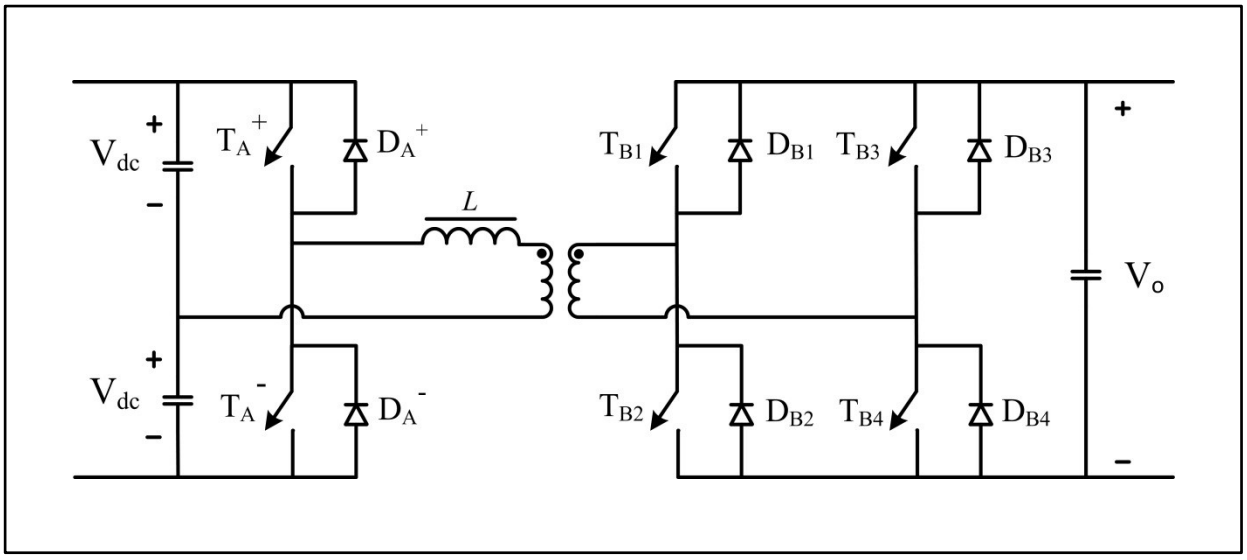

Fig. 5.14 DAB with Half-Bridge converter at one side

Assuming the capacitors are big enough, the input and output voltages can be considered almost constant during small switching time intervals; so for analysis the capacitors can be simply replace by ideal DC sources. To achieve Zero Voltage Switching (ZVS), snubber circuits can be utilized to achieve higher switching frequencies and higher power densities. Snubber for this circuit can be simply capacitors in parallel with the switches. Besides, a simple resistor load can be considered at the output for the purpose of analysis. This parallel RC configuration as load is compatible with the battery model used in CHAPTER.2. The resulting circuit is shown in Fig. 5.15.

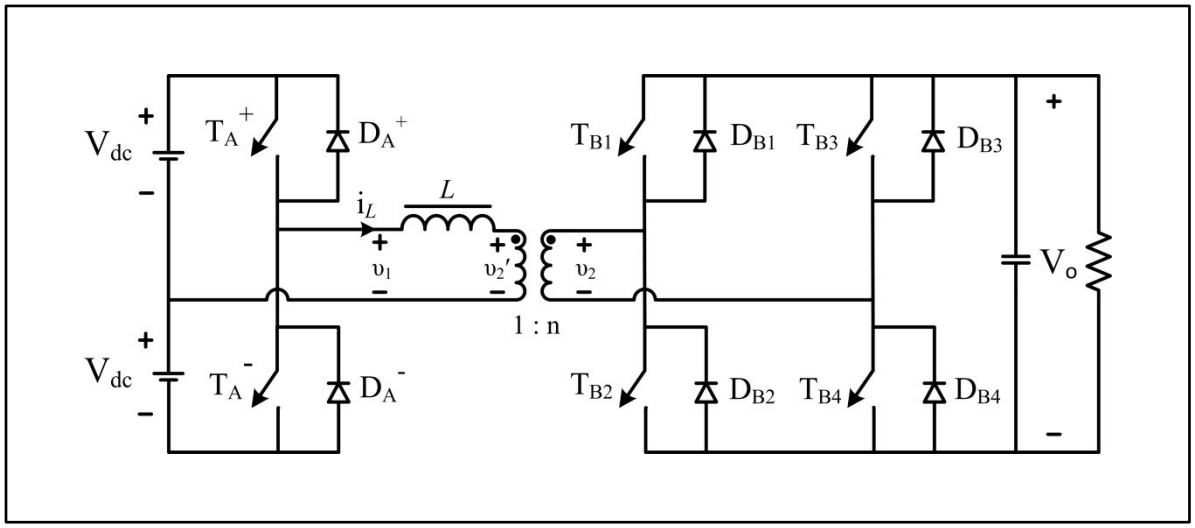

Fig. 5.15 DAB circuit for operation analysis

By controlling the switches of each bridge and depending on the direction of the current, square wave voltage of $\pm V_{dc}$ will be applied to the input of the transformer and $\pm V_o$ to the output. By controlling the phase shift φ between transformer input and output voltages, the power flow can be controlled through the inductor L which represents the sum of the primary-referred transformer leakage inductance and possible external bulk inductors. As will be shown later the

direction of power flow can be reversed by applying a negative phase shift. To get an idea of basic operation of DAB, if we substitute bridges with square wave voltages we get Fig. 5.16.

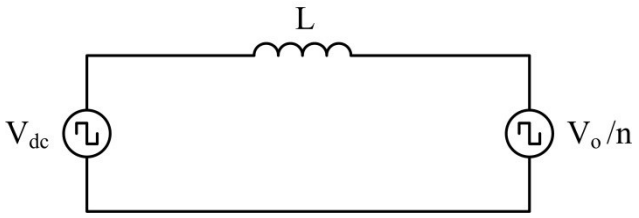

Fig. 5.16 Simplified circuit of DAB

If square wave voltage sources are replaced with their fundamental frequency components Fig. 5.17 will be obtained which reminds the operation of synchronous machine.

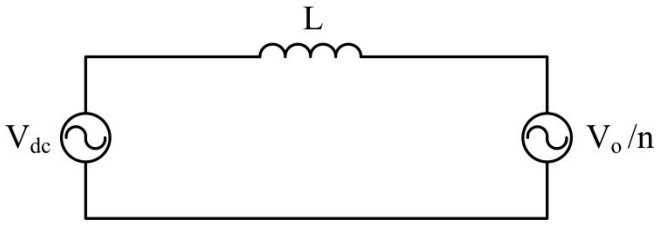

Fig. 5.17 Fundamental frequency model of DAB

5.4.1 DAB Steady State Operation

Steady state operation analysis can be started from any time instant. We assume that at the beginning the inductor current is negative and flowing through D_A^+ at the input half-bridge and through D_{B2} and D_{B3} at the output full-bridge bridge as shown in Fig. 5.18(a). The absolute value of current will be decreasing (reaching zero in the negative region) during this period since it is entering the positive terminal at the input and at the output, so after some time (t_1) the current should reach zero. Any time before this instant, T_A^+, T_{B2} and T_{B3} are turned on and since their antiparallel diodes are conducting they are turned on under Zero Voltage Switching (ZVS) condition as shown in Fig. 5.18(b). After inductor current reaches zero at t_1 it begins to become positive and increase, so at this time the current commutates from D_A^+, D_{B2} and D_{B3} to T_A^+, T_{B2} and T_{B3} respectively as shown in Fig. 5.18(c). The current will increase and after some time (t_2) T_{B2} and T_{B3} will be turned off, so because of the stored energy in the inductor, the current will commutate from T_{B2} and T_{B3} to D_{B1} and D_{B4} as shown in Fig. 5.18(d). The antiparallel capacitors provide ZVS. In this interval the rate of current increase will reduce since the current in the output is entering the positive terminal. After some time (t_3) T_A^+ is turned off and because of inductor stored energy, current will commutate from T_A^+ to D_A^- as depicted in Fig. 5.18(e). Snubber capacitor provides ZVS. When T_A^+ is conducting, the snubber capacitor is at zero voltage and discharged. When T_A^+ is turned off the capacitor will take over the inductor current and get charged over time providing enough time for T_A^+ to get turned off. Besides, the snubber capacitor parallel with T_A^- which has been charged before T_A^+ turns off, will take over the inductor current after T_A^+ turn off and will discharge and finally forward biases D_A^-. According to the symmetrical operation of the circuit, the operation of T_A^-, T_{B1} and T_{B4} can be analyzed using the same procedure.

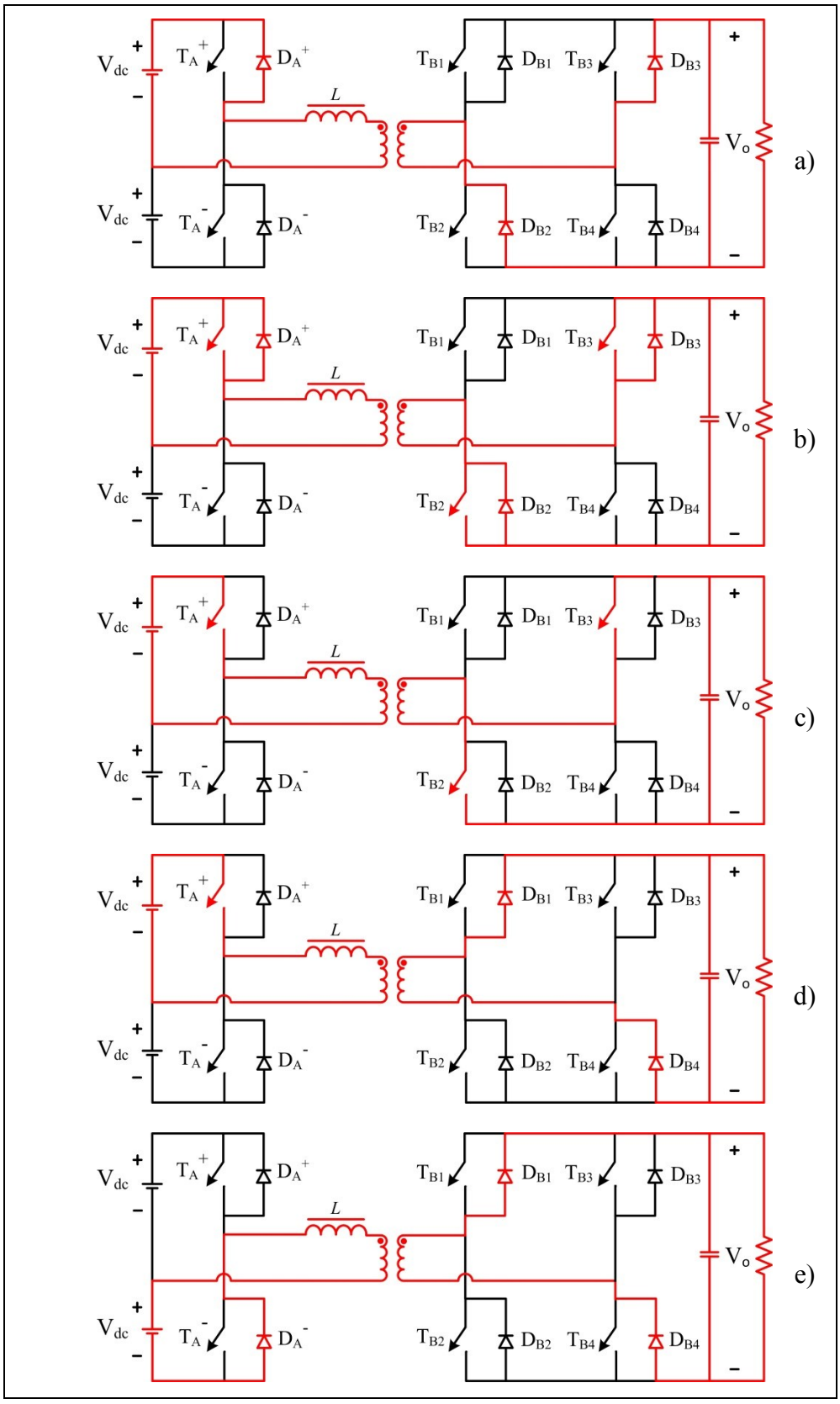

Fig. 5.18 Equivalent circuits for different time intervals

For further analysis, the voltage applied to the input and output of the transformer and inductor current diagram is depicted in Fig. 5.19.

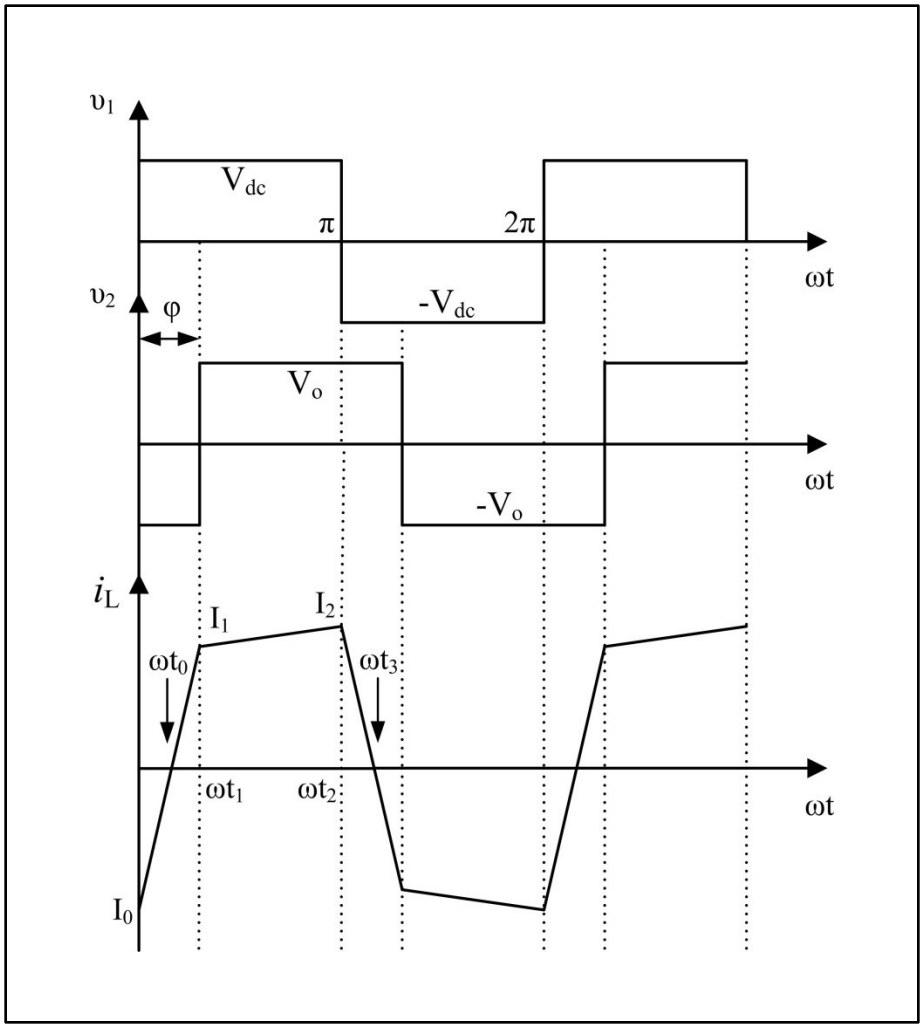

Fig. 5.19 Voltage and current waveforms of DAB

The power flow equation can be obtained as follows beginning from inductor equation:

$$v_L = L\frac{di}{dt} = \omega L\frac{di}{d(\omega t)} = \omega L\frac{di}{d\theta} \tag{5.25}$$

If the switching frequency is high enough compared to the natural frequency of the circuit, the current waveforms will be piecewise linear as shown in Fig. 5.19. Hence, (5.25) can be written as:

$$v_L = \omega L \frac{\Delta i}{\Delta \theta} \implies \Delta i = \frac{v_L}{\omega L} \Delta \theta \tag{5.26}$$

Defining the DC conversion ratio (M) as:

$$M = \frac{V_o}{n V_{dc}} \tag{5.27}$$

$$I_1 = \frac{V_{dc} + V_o/n}{\omega L} \varphi + I_0 \Longrightarrow I_1 = \frac{V_{dc}(1+M)}{\omega L} \varphi + I_0 \tag{5.28}$$

$$I_2 = \frac{V_{dc} - V_o/n}{\omega L} (\pi - \varphi) + I_1 \Longrightarrow I_2 = \frac{V_{dc}(1-M)}{\omega L} (\pi - \varphi) + I_1 \tag{5.29}$$

According to the energy transfer balance due to zero energy loss in the inductor and symmetrical voltage and current waveforms we have:

$$I_2 = -I_0 \tag{5.30}$$

Now we have three unknowns I_0, I_1, I_2 and three equations (5.28), (5.29) and (5.30). After some calculations we will get:

$$I_0 = \frac{V_{dc}}{\omega L} \left[\frac{\pi}{2} (M-1) - \varphi M \right] \tag{5.31}$$

$$I_1 = \frac{V_{dc}}{\omega L} \left[\frac{\pi}{2} (M-1) + \varphi \right] \tag{5.32}$$

$$I_2 = -I_0 \tag{5.33}$$

To calculate the average delivered power by source or absorbed by load we begin from basic definition of average power which is the average of instantaneous voltage multiplied by instantaneous current over one period cycle:

$$P = \frac{1}{T}\int_0^T v_{(t)} i_{(t)} dt = \frac{1}{2\pi}\int_0^{2\pi} v_{(\omega t)} i_{(\omega t)} d(\omega t) \tag{5.34}$$

According to the symmetry of the waveforms, average power can be calculated just over half period (0→π) and multiplied by 2. As depicted in Fig. 5.19 since the input voltage is constant over half period, according to (5.10) average power equals V_{dc} multiplied by average inductor current. Using the equation for calculating the area of a trapezoidal we can write:

$$P_{in} = 2 \times V_{dc} \times \frac{1}{2\pi}\left(\frac{1}{2}(I_0 + I_1)\varphi + \frac{1}{2}(I_1 + I_2)(\pi - \varphi)\right) \tag{5.35}$$

Or based on absorbed load power, we can write:

$$P_{out} = 2 \times V_o \times \frac{1}{2\pi}\left(\frac{-1}{2}(I_0 + I_1)\varphi + \frac{1}{2}(I_1 + I_2)(\pi - \varphi)\right) \tag{5.36}$$

Using (5.4), (5.5), (5.6) and (5.11) and after some manipulations we get:

$$P = \frac{{V_{dc}}^2}{\omega L} M\varphi\left(1 - \frac{|\varphi|}{\pi}\right) = \frac{V_{dc} V_o/n}{\omega L}\varphi\left(1 - \frac{|\varphi|}{\pi}\right) \tag{5.37}$$

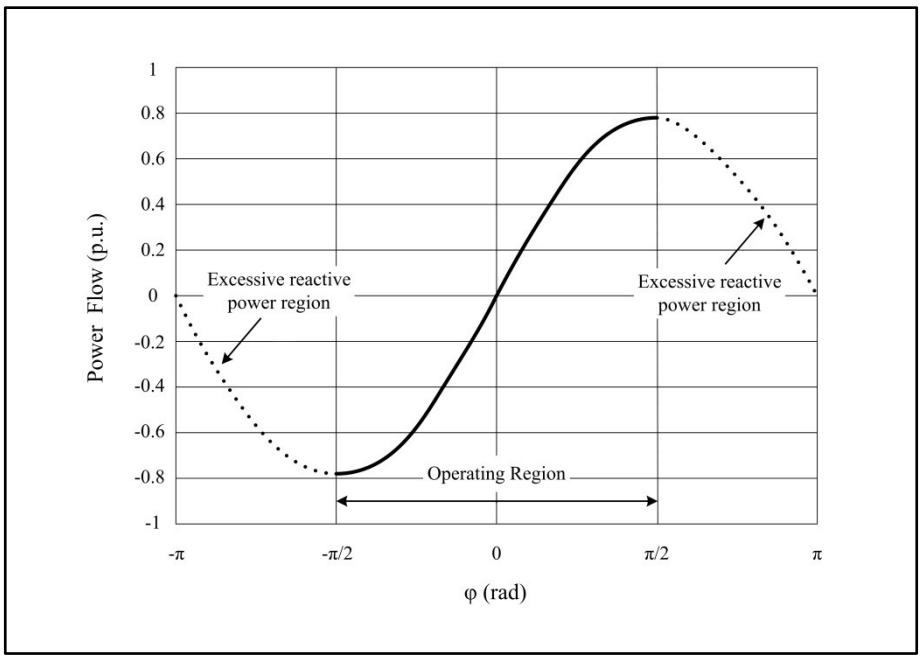

(5.38)

Fig. 5.20 Power flow of DAB in p.u. versus phase shift in rad

Maximum power occurs at $\varphi = \pi / 2$. Although the phase shift can range from $-\pi$ to π, only operating region of $-\pi / 2$ to $\pi / 2$ is utilized to avoid excessive reactive power [76]. The power flow in per unit versus phase shift is plotted in Fig. 5.20 and base power is selected as:

5.4.2 DAB State-Space Average Model

The first step for designing controller for a system or analyzing its behavior is deriving the model of the system. Having the model of the system, many different design techniques can be utilized. For power converters there are mainly two different methods for deriving models. One of them is circuit averaging [77] and the other is state space averaging. Basically, because of the utilization of switches in switching power converters, they are non-continuous non-linear systems since the topology of the circuit is changing during each cycle. Circuit averaging technique tries to represent the elements of the circuit with their average values such as average current or average voltage. State-space averaging mainly allows a switched system to be

approximated as a continuous non-linear system. Averaged models are not necessarily linear, so they can be linearized over an operating point. The result will be small-signal linearized model. The main advantage of linear models is mainly their compatibility with control design methods based on linear systems theory and Laplace transform. For DAB modeling we use state-space averaging. In practice some criteria should be met so the state-space averaged model holds valid. First, the natural frequencies of the circuit and all modulation or signal frequencies of interest must be sufficiently low compared to the switching frequency. This will provide validity of continuity approximation. Second, the criterion for linearity approximation is that the time variations or ac perturbations around the DC operating point should be sufficiently small.

Here we don't want to mention the theory behind state-space averaging, but just as a reminder, assuming a power converter with just two switches, i.e. a simple buck converter including a controllable switch and a diode, if we call the configuration when the switch is on #1 and the configuration when the diode is on #2 and write the state space equations, we will have:

$$\dot{\mathrm{X}} = A_1\mathrm{X} + B_1\mathrm{U} \qquad \#1 \tag{5.39}$$

$$\dot{\mathrm{X}} = A_2\mathrm{X} + B_2\mathrm{U} \qquad \#2 \tag{5.40}$$

where X is the state variable vector consisting of inductor current and capacitor voltage. It can be proved that this non-continuous system can be represented by a new state variable vector Y driven by new input vector V such that:

$$\dot{\mathrm{Y}} = \bar{A}Y + \bar{B}V \tag{5.41}$$

$$\bar{A} = A_1D_1 + A_2D_2 \tag{5.42}$$

$$\bar{B} = B_1 D_1 + B_2 D_2 \tag{5.43}$$

D_1 is the duty ratio of the controllable switch and D_2 is the duty ratio of the diode. As it can be seen, instead of two sets of equations (5.39) and (5.40) for two different configurations, the system can be defined with just one state-space equation (5.41). In fact (5.41), (5.42) and (5.43) represent the average behavior of the same system. Average behavior means no switching is reflected in the model, so states do not exhibit any ripple. In other words, the new states y(t) in the new state-space equation (5.41) track the average behavior of x(t) in (5.39) and (5.40), provided that v(t) is defined to track the average behavior of u(t) and the switching frequency is high enough. In (5.41) without loss of generality, the name of state vector Y can be changed to X and input vector of V can be changed to U as was used in the original system, since X and U are more common. So averaged state-space model of the system can be rewritten as:

$$\dot{\mathrm{X}} = \bar{A}\mathrm{X} + \bar{B}\mathrm{U} \tag{5.44}$$

where $\bar{A}$ and $\bar{B}$ are defined in (5.42) and (5.43) respectively. When the buck converter is operating in Continuous Conduction Mode (CCM) only two possible configurations are possible, so if the duty ratio of the controllable switch is shown with the parameter "d" we will have:

$$D_1 = d \tag{5.45}$$

$$D_1 + D_2 = 1 \Longrightarrow d + D_2 = 1 \Longrightarrow D_2 = 1 - d \tag{5.46}$$

$$\bar{A} = A_1 d + A_2(1 - d) \tag{5.47}$$

$$\bar{B} = B_1 d + B_2(1 - d) \tag{5.48}$$

The example above involved only two different possible configurations, however, more configurations are possible. For example, in the case of a buck converter if the converter operates in Discontinuous Conduction Mode (DCM) there will be three different configurations and consequently three sets of matrices A_1, B_1 and A_2, B_2 and A_3, B_3 instead of two.

There are lots of state-space averaged models available in the literature for conventional DC-DC converters such as buck, boost, buck-boost and Cuk converter [78],[79],[80],[81]. Analysis of these converters is simple since they employ only two switches, one controllable switch and one diode. Maximum number of possible configurations in these converters is three while operating under DCM conditions. For converters with more switches, the possible number of configurations increases dramatically. For example for the case of DAB as shown in Fig. 5.18 the possible number of configurations increases to 6 in CCM while it is only 2 for a buck converter operating in CCM. Cuk in [81] derives a state-space averaged model which is extended to converters with multi-structural topological modes; however, multi-structural state-space averaged model presented in [81] is applicable only when the inductor current is DC with an AC component [82]. In the case of DAB as was shown in Fig. 5.19 the inductor current has a zero average due to the symmetry of the waveforms. If the state-space equations for all the configurations are written and time-averaged over one complete cycle period, lots of the components of the coefficient matrices will cancel out each other because of the symmetry relative to the time axis and the averaged state-space model will provide no useful information. So in the case of DC-DC converters with zero inductor current average like DAB, state-space averaging cannot be used directly. Instead, an extension of state-space averaging which is called extended state-space averaging technique should be used. This technique is mainly based on the fact that the average power delivered during the positive cycle is equal to the averaged power

delivered during the negative cycle. So the state-space model can be time-averaged over only half of a cycle (positive or negative).

According to Fig. 5.18 and Fig. 5.19 the equivalent circuit and state-space equations of each time interval can be obtained:

1) $\omega t_0 \leq \omega t < \omega t_1$: T_A^+, T_{B2}, T_{B3} conducting:

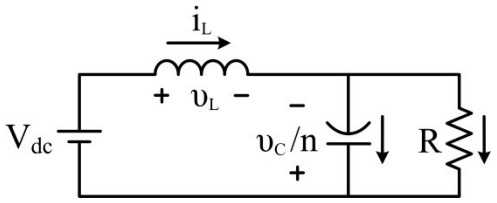

Fig. 5.21 T_A^+, T_{B2}, T_{B3} conducting

$$v_L = V_{dc} + \frac{v_c}{n} \Longrightarrow \frac{di_L}{dt} = \frac{v_c}{nL} + \frac{V_{dc}}{L} \tag{5.49}$$

$$-i_c - \frac{v_c}{nR} = i_L \Longrightarrow \frac{dv_c}{dt} = \frac{-v_c}{nRC} - \frac{i_L}{C} \tag{5.50}$$

$$\Longrightarrow \begin{bmatrix} di_L/dt \\ dv_c/dt \end{bmatrix} = \begin{bmatrix} 0 & \frac{1}{nL} \\ \frac{-1}{C} & \frac{-1}{nRC} \end{bmatrix} \begin{bmatrix} i_L \\ v_c \end{bmatrix} + \begin{bmatrix} \frac{1}{L} \\ 0 \end{bmatrix} V_{dc} \tag{5.51}$$

2) $\omega t_1 \leq \omega t < \omega t_2$: T_A^+, D_{B1}, D_{B4} conducting:

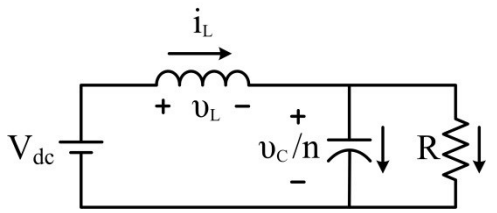

Fig. 5.22 T_A^+, D_{B1}, D_{B4} conducting

$$v_L = V_{dc} - \frac{v_c}{n} \Longrightarrow \frac{di_L}{dt} = \frac{-v_c}{nL} + \frac{V_{dc}}{L} \tag{5.52}$$

$$i_c + \frac{v_c}{nR} = i_L \Longrightarrow \frac{dv_c}{dt} = \frac{-v_c}{nRC} + \frac{i_L}{C} \tag{5.53}$$

$$\Longrightarrow \begin{bmatrix} {di_L}/{dt} \\ {dv_c}/{dt} \end{bmatrix} = \begin{bmatrix} 0 & \frac{-1}{nL} \\ \frac{1}{C} & \frac{-1}{nRC} \end{bmatrix} \begin{bmatrix} i_L \\ v_c \end{bmatrix} + \begin{bmatrix} \frac{1}{L} \\ 0 \end{bmatrix} V_{dc} \tag{5.54}$$

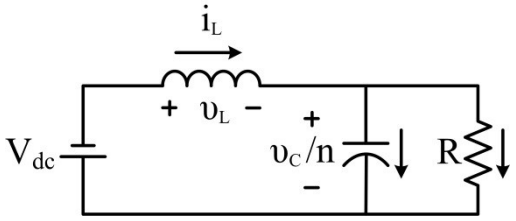

Fig. 5.23 D_A-, D_{B1}, D_{B4} conducting

3) $\omega t_2 \leq \omega t < \omega t_3$: D_A^-, D_{B1}, D_{B4} conducting:

$$v_L = -V_{dc} - \frac{v_c}{n} \Longrightarrow \frac{di_L}{dt} = \frac{-v_c}{nL} - \frac{V_{dc}}{L} \tag{5.55}$$

$$i_c + \frac{v_c}{nR} = i_L \Longrightarrow \frac{dv_c}{dt} = \frac{-v_c}{nRC} + \frac{i_L}{C} \tag{5.56}$$

$$\Longrightarrow \begin{bmatrix} {di_L}/{dt} \\ {dv_c}/{dt} \end{bmatrix} = \begin{bmatrix} 0 & \frac{-1}{nL} \\ \frac{1}{C} & \frac{-1}{nRC} \end{bmatrix} \begin{bmatrix} i_L \\ v_c \end{bmatrix} + \begin{bmatrix} \frac{-1}{L} \\ 0 \end{bmatrix} V_{dc} \tag{5.57}$$

To average the state-space model, (5.51), (5.54) and (5.57) should be multiplied by their corresponding duty ratios which are d_1, d_2 and d_3 respectively and then added together. The duty ratios of each interval can be calculated as follows:

1) $\omega t_0 \leq \omega t < \omega t_1$: T_A^+, T_{B2}, T_{B3} conducting:

$$i_L(\omega t) = I_0 + \frac{V_{dc} + V_o/n}{\omega L}\omega t \Longrightarrow i_L(\omega t_0) = I_0 + \frac{V_{dc}(1+M)}{\omega L}\omega t_0 = 0 \tag{5.58}$$

$$\Longrightarrow \omega t_0 = \frac{\varphi M - (M-1)\,\pi/2}{1+M} \tag{5.59}$$

$$\omega t_1 = \varphi \tag{5.60}$$

$$d_1 = \frac{\omega t_1 - \omega t_0}{2\pi} \Longrightarrow \cdots \Longrightarrow d_1 = \frac{2\varphi + \pi(M-1)}{4\pi(M+1)} \tag{5.61}$$

2) $\omega t_1 \leq \omega t < \omega t_2$: T_A^+, D_{B1}, D_{B4} conducting:

$$d_2 = \frac{\omega t_2 - \omega t_1}{2\pi} = \frac{\pi - \varphi}{2\pi} \Longrightarrow d_2 = \frac{1}{2}\left(1 - \frac{\varphi}{\pi}\right) \tag{5.62}$$

3) $\omega t_2 \leq \omega t < \omega t_3$: D_A^-, D_{B1}, D_{B4} conducting:

The same as two previous time intervals, d_3 can also be calculated, however, there is no need to that, since d_3 is dependent on d_1 and d_2 and can be obtained as:

$$d_1 + d_2 + d_3 = 1 \Longrightarrow d_3 = 1 - d_1 - d_2 \tag{5.63}$$

According to Fig. 5.18 and Fig. 5.19 during the time interval of $\omega t_0 \leq \omega t < \omega t_2$ the switch T_A^+ conducts, so d_{T_A+} which we call it d for simplicity can be calculated as:

$$d = d_{T_A+} = d_1 + d_2 \tag{5.64}$$

There is an important point here to note. As shown in Fig. 5.18(b) and Fig. 5.19 during the time interval $0 \leq \omega t < \omega t_0$ the gating signal is applied to switch T_A^+ however, this switch

doesn't conduct until the current through D_A^+ reaches zero. This situation is different from conventional DC-DC converters like buck, boost, buck-boost or Cuk. In these converters the current commutates from the diode to the controllable switch almost instantly after applying the gating signal. In these converters the gating signal can be used to calculate the duty ratios, however in DAB the gating signal does not necessarily determine the duty ratio, instead, conduction time of the switch is important.

Finally, the averaged state-space model of DAB can be obtained. Using (5.51), (5.54), (5.57), (5.63) and (5.64) we will get:

$$\begin{bmatrix} {di_L}/{dt} \\ {dv_c}/{dt} \end{bmatrix} = \begin{bmatrix} 0 & \frac{2d_1 - 1}{nL} \\ \frac{1}{C} & \frac{-1}{nRC} \end{bmatrix} \begin{bmatrix} i_L \\ v_c \end{bmatrix} + \begin{bmatrix} \frac{2d-1}{L} \\ 0 \end{bmatrix} V_{dc} \tag{5.65}$$

The equation above is the averaged state-space model of DAB. This model is a continuous but non-linear model. It is non-linear because d and d_1 can be a function of any combination of x_1, x_2 and u. This nonlinearity can be shown mathematically. Since V_{dc} is the input of the system (u) and V_o is the capacitor voltage (v_c) or x_2 we will get:

$$v_L = L\frac{di_L}{dt} \Longrightarrow u + {x_2}/{n} = L\frac{I_1}{(t_1 - t_0)} \Longrightarrow (t_1 - t_0) = \frac{LI_1}{u + {x_2}/{n}} \tag{5.66}$$

$$\Longrightarrow d_1 = \frac{1}{T_s}\left(\frac{LI_1}{u + x_2/n}\right) \tag{5.67}$$

$$v_L = L\frac{di_L}{dt} \Longrightarrow u - {x_2}/{n} = L\frac{(I_2 - I_1)}{(t_2 - t_1)} \Longrightarrow (t_2 - t_1) = \frac{L(I_2 - I_1)}{u - {x_2}/{n}} \tag{5.68}$$

$$\Rightarrow d_2 = \frac{1}{T_s}\left(\frac{L(I_2 - I_1)}{u - x_2/n}\right) \tag{5.69}$$

As it is calculated in (5.67) and (5.69), d_1 and d_2 and hence $d=d_1+d_2$ are non-linear functions of input (u) and state of the system (x_2). Non-linear model (5.65) can be used directly using non-linear techniques or can be approximated as a linear system around its DC operating point.

5.4.3 DAB Small-Signal Linear Model

Considering a system in state-space representation form we have:

$$\dot{X} = AX + BU \tag{5.70}$$

Assuming the state vector X, input vector U and duty ratio d have a DC average value plus a small ac perturbation in the vicinity of DC operating point, they can be rewritten as:

$$X = X_0 + \tilde{X} \tag{5.71}$$

$$U = U_0 + \tilde{U} \tag{5.72}$$

$$d = D + \tilde{d} \tag{5.73}$$

Where X_0, U_0 and D are the DC components and $\tilde{X}$, $\tilde{U}$ and $\tilde{d}$ are the AC components. Substituting (5.71), (5.72) and (5.73) into (5.70) will result in:

$$\begin{aligned}\left(\dot{X_0} + \dot{\tilde{X}}\right) = &\left[(D + \tilde{d})A_1 + \left[1 - (D + \tilde{d})\right]A_2\right](X_0 + \tilde{X}) \\ &+ \left[(D + \tilde{d})B_1 + \left[1 - (D + \tilde{d})\right]B_2\right](U_0 + \tilde{U})\end{aligned} \tag{5.74}$$

Since the product of small-signal perturbations is very small compared to other terms, they can be assumed almost zero:

$$\tilde{X}\tilde{U} \approx \tilde{X}\tilde{d} \approx \tilde{d}\tilde{U} \approx 0 \tag{5.75}$$

Applying (5.75) to (5.74) and dividing (5.74) into DC and AC equations, we will get:

DC:	$0 = [A_1 D + A_2(1-D)]X_0 + [B_1 D + B_2(1-D)]U_0$	(5.76)
AC:	$\dot{\tilde{X}} = [A_1 D + A_2(1-D)]\tilde{X} + [B_1 D + B_2(1-D)]\tilde{U} + [(A_1 - A_2)X_0 + (B_1 - B_2)U_0]\tilde{d}$	(5.77)

To simplify the equations, the following coefficients can be defined:

$$A_0 = A_1 D + A_2(1-D) \tag{5.78}$$

$$B_0 = B_1 D + B_2(1-D) \tag{5.79}$$

$$E = (A_1 - A_2)X_0 + (B_1 - B_2)U_0 \tag{5.80}$$

Using (5.78), (5.79) and (5.80) we can rewrite (5.76) and (5.77) as:

DC: $$0 = A_0 X_0 + B_0 U_0 \tag{5.81}$$

AC: $$\dot{\tilde{X}} = A_0\tilde{X} + B_0\tilde{U} + E\tilde{d} \tag{5.82}$$

When non-linear averaged state-space model (5.65) is linearized after lots of calculations the final result will be [82]:

$$\begin{bmatrix}\dot{\tilde{x}}_1\\ \dot{\tilde{x}}_2\end{bmatrix}=\begin{bmatrix}A_{11} & A_{12}\\ \frac{1}{C} & -\frac{1}{nRC}\end{bmatrix}\begin{bmatrix}\tilde{x}_1\\ \tilde{x}_2\end{bmatrix}+\begin{bmatrix}B_{11}\\ 0\end{bmatrix}\tilde{V}_{dc}+\begin{bmatrix}E_{11}\\ 0\end{bmatrix}\tilde{\varphi} \tag{5.83}$$

Where:

$$A_{11}=-\frac{2V_{dc0}}{T_s(V_{dc0}+x_{20})} \tag{5.84}$$

$$A_{12}=\frac{1}{2}\left(\frac{V_{dc0}T_s\big((\varphi_0-3\pi)V_{dc0}-2x_{20}\pi\big)+4\pi Lx_{10}V_{dc0}-\pi T_s{x_{20}}^2}{\pi T_sL(V_{dc0}+x_{20})^2}\right) \tag{5.85}$$

$$B_{11}=\frac{x_{20}(T_s\varphi_0x_{20}-2\pi Lx_{10})+\pi T_sV_{dc0}(V_{dc0}+2x_{20})}{\pi T_sL(V_{dc0}+x_{20})^2} \tag{5.86}$$

$$E_{11}=\frac{x_{20}}{\pi L(M+1)} \tag{5.87}$$

Subscript zero denotes DC operating point.

5.4.4 DAB Small-Signal Transfer Functions

Linear averaged state-space model of DAB was finally obtained in (5.83), (5.84), (5.85), (5.86) and (5.87). To study the dynamic behavior of a system in terms of poles and zeros we should derive the transfer functions of the system. Considering (5.82) as a general system, since the equation is linear the Laplace transformation can be applied and will result in:

$$\tilde{X}_{(s)}=(s\,I-A_0)^{-1}B_0\,\tilde{U}_{(s)}+(s\,I-A_0)^{-1}E\,\tilde{d}_{(s)} \tag{5.88}$$

Different transfer functions can be obtained such as control-to-state and source-to-state.

Control-to-state transfer function:

$$G_{dx_{(s)}} = \left(\frac{\tilde{X}_{(s)}}{\tilde{d}_{(s)}}\right)_{\tilde{U}_{(s)}=0} = (s\,I - A_0)^{-1}E \tag{5.89}$$

Source-to-state transfer function:

$$G_{ux_{(s)}} = \left(\frac{\tilde{X}_{(s)}}{\tilde{U}_{(s)}}\right)_{\tilde{d}_{(s)}=0} = (s\,I - A_0)^{-1}B_0 \tag{5.90}$$

In (5.89) the duty ratio is assumed to be independent of the other parameters of the converter. This is true in a simple DC-DC converter like a buck converter. In a buck converter, duty ratio can be independently controlled by the switching signal. However, in more complicated cases like DAB as was previously shown in (5.67) and (5.69) duty ration is dependent on states and input. In other cases such as resonant converters, duty ratio will be dependent on switching frequency as well. So a linearized general control law for duty ratio can be defined as [82]:

$$\tilde{d}_{(s)} = F^T\,\tilde{X}_{(s)} + Q^T\,\tilde{U}_{(s)} + S^T\,\tilde{F}_{(s)} \tag{5.91}$$

Matrices F^T, Q^T and S^T expresses the dependency of the control law on the states, input and frequency vector of the system respectively.

Applying Laplace transform on (5.82) as a general system will yield:

$$s\,\tilde{X}_{(s)} = A_0\,\tilde{X}_{(s)} + B_0\,\tilde{U}_{(s)} + E\,\tilde{d}_{(s)} \tag{5.92}$$

Inserting the linearized general control law (5.91) into (5.92) will result in:

$$s\,\tilde{X}_{(s)} = A_0\,\tilde{X}_{(s)} + B_0\,\tilde{U}_{(s)} + E\left[F^T\,\tilde{X}_{(s)} + Q^T\,\tilde{U}_{(s)} + S^T\,\tilde{F}_{(s)}\right] \tag{5.93}$$

$$\Rightarrow\ s\,\tilde{X}_{(s)} - A_0\,\tilde{X}_{(s)} - E\,F^T\,\tilde{X}_{(s)} = B_0\,\tilde{U}_{(s)} + E\,Q^T\,\tilde{U}_{(s)} + E\,S^T\,\tilde{F}_{(s)} \tag{5.94}$$

$$\Rightarrow [s\,I - A_0 - E\,F^T]\,\tilde{X}_{(s)} = (B_0 + E\,Q^T)\,\tilde{U}_{(s)} + \ E\,S^T\,\tilde{F}_{(s)} \tag{5.95}$$

$$\Rightarrow\ \tilde{X}_{(s)} = [s\,I - A_0 - E\,F^T]^{-1}\left[(B_0 + E\,Q^T)\,\tilde{U}_{(s)} + \ E\,S^T\,\tilde{F}_{(s)}\right] \tag{5.96}$$

According to (5.96) when the switching frequency is the control parameter, the control-to-state transfer function will be:

$$G_{dx(s)} = \left(\frac{\tilde{X}_{(s)}}{\tilde{F}_{(s)}}\right)_{\tilde{U}_{(s)}=0} = [s\,I - A_0 - E\,F^T]^{-1}[\,E\,S^T] \tag{5.97}$$

The source-to-state transfer function can also be obtained as:

$$G_{ux(s)} = \left(\frac{\tilde{X}_{(s)}}{\tilde{U}_{(s)}}\right)_{\tilde{F}_{(s)}=0} = [s\,I - A_0 - E\,F^T]^{-1}[B_0 + E\,Q^T] \tag{5.98}$$

Using above-mentioned equations different small-signal transfer functions can be derived.

- *Small-signal control-to-output transfer function:*

$$G_{\varphi x_2(s)} = \left(\frac{\tilde{X}_{(s)}}{\tilde{d}_{(s)}}\right)_{\tilde{U}_{(s)}=0} = \left(\frac{\tilde{x}_{2(s)}}{\tilde{\varphi}_{(s)}}\right)_{\tilde{U}_{(s)}=0} = [s\,I - A_0]^{-1}[E] = \frac{N_{\varphi x_2(s)}}{\Delta_{(s)}} \tag{5.99}$$

$$N_{\varphi x_1(s)} = \frac{E_{11}}{C} \tag{5.100}$$

$$\Delta_{(s)} = s^2 + s\left(\frac{1}{RC} - A_{11}\right) - \frac{A_{11}}{RC} - \frac{A_{12}}{C} \tag{5.101}$$

- *Small-signal control-to-state transfer function:*

$$G_{\varphi x_1(s)} = \left(\frac{\tilde{X}_{(s)}}{\tilde{d}_{(s)}}\right)_{\tilde{U}_{(s)}=0} = \left(\frac{\tilde{x}_{1(s)}}{\tilde{\varphi}_{(s)}}\right)_{\tilde{U}_{(s)}=0} = [s\,I - A_0]^{-1}[E] = \frac{N_{\varphi x_1(s)}}{\Delta_{(s)}} \tag{5.102}$$

$$N_{\varphi x_1(s)} = \frac{x_{20}}{\pi L(M+1)}\left(s + \frac{1}{RC}\right) \tag{5.103}$$

- *Small-signal source-to-output transfer function:*

$$G_{ux_2(s)} = \left(\frac{\tilde{X}_{(s)}}{\tilde{U}_{(s)}}\right)_{\tilde{d}_{(s)}=0} = \left(\frac{\tilde{x}_{2(s)}}{\tilde{U}_{(s)}}\right)_{\tilde{\varphi}_{(s)}=0} = [s\,I - A_0]^{-1}[B_0\,] = \frac{N_{ux_2(s)}}{\Delta_{(s)}} \tag{5.104}$$

$$N_{ux_2(s)} = \frac{B_{11}}{C} \tag{5.105}$$

- *Small-signal source-to-state transfer function:*

$$G_{ux_1(s)} = \left(\frac{\tilde{X}_{(s)}}{\tilde{U}_{(s)}}\right)_{\tilde{d}_{(s)}=0} = \left(\frac{\tilde{x}_{1(s)}}{\tilde{U}_{(s)}}\right)_{\tilde{\varphi}_{(s)}=0} = [s\,I - A_0]^{-1}[B_0\,] = \frac{N_{ux_1(s)}}{\Delta_{(s)}} \tag{5.106}$$

$$N_{ux_2(s)} = B_{11}\left(s + \frac{1}{RC}\right) \tag{5.107}$$

Using the small-signal transfer functions obtained above, the small-signal representation of the DAB including controllers can be depicted as Fig. 5.24. C_i and C_v are inner current loop controller and outer voltage loop controller respectively. Controller design is mainly based on the small-signal analysis of the converter. As shown in Fig. 5.24 four different transfer functions, i.e. control-to-output, source-to-output, control-to-state and source-to-state are utilized to completely describe the behavior of DAB. These four transfer functions define the power stage. Each of these transfer functions has a physical interpretation, e.g. control-to-output transfer function expresses the output capacitor voltage sensitivity to small variations of the duty ratio around its steady-state, or input-to-state transfer function describes the inductor current sensitivity to small variations of the input voltage around its steady-state operating point and so on.

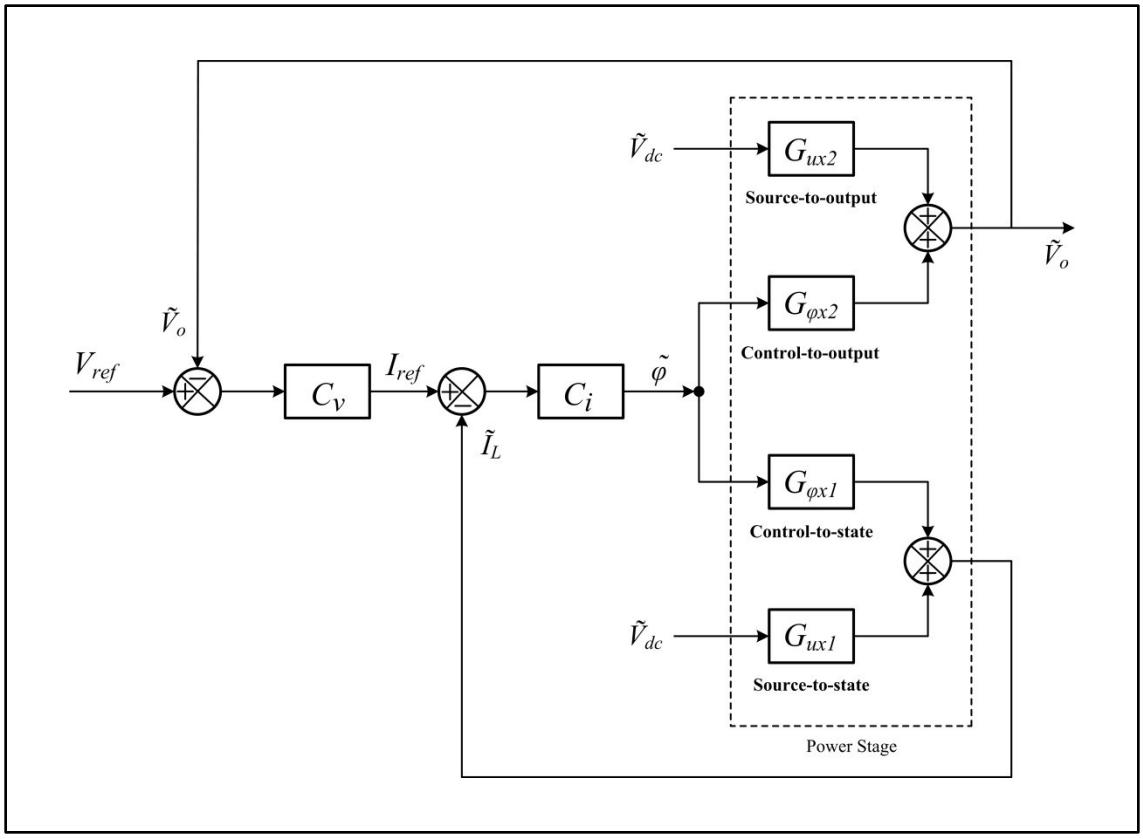

Fig. 5.24 Small-signal representation of the regulated DAB

5.4.5 DAB Design

For design of parameters of DAB more descriptive equations should be derived to describe different characteristics based on the parameters of the circuit. Inductance of the transformer is a very important parameter to be designed. Analysis of the effect of this element on the operation of circuit will provide valuable insight to the DAB circuit. We begin from the average current value of the inductor. According to Fig. 5.19 and equations derived in section 5.4.1 we have assumed zero average current, however, this is the case only in steady state operation. During transients, this assumption is not necessarily valid so average inductor current should be calculated without zero average current assumption, so I_0 can begin from any point on current axis and (5.30) which is $I_2 = -I_0$ is not necessarily valid. Average current can be written as:

$$i_{L(avg)} = I_L = \frac{1}{2\pi}\left[\frac{1}{2}\left(I_0 + \left(I_0 + \frac{V_{dc}(1+M)}{\omega L}\varphi\right)\right)\varphi + \frac{1}{2}\left(\left(I_0 + \frac{V_{dc}(1+M)}{\omega L}\varphi\right) + \left(I_0 + \frac{V_{dc}(1+M)}{\omega L}\varphi + \frac{V_{dc}(1-M)}{\omega L}(\pi-\varphi)\right)\right)(\pi-\varphi) + \frac{1}{2}\left(\left(I_0 + \frac{V_{dc}(1+M)}{\omega L}\varphi + \frac{V_{dc}(1-M)}{\omega L}(\pi-\varphi)\right) + \left(I_0 + \frac{V_{dc}(1+M)}{\omega L}\varphi + \frac{V_{dc}(1-M)}{\omega L}(\pi-\varphi) - \frac{V_{dc}(1+M)}{\omega L}\varphi\right)\right)\varphi + \frac{1}{2}\left(\left(I_0 + \frac{V_{dc}(1+M)}{\omega L}\varphi + \frac{V_{dc}(1-M)}{\omega L}(\pi-\varphi) - \frac{V_{dc}(1+M)}{\omega L}\varphi\right) + \left(I_0 + \frac{V_{dc}(1+M)}{\omega L}\varphi + \frac{V_{dc}(1-M)}{\omega L}(\pi-\varphi) - \frac{V_{dc}(1+M)}{\omega L}\varphi - \frac{V_{dc}(1-M)}{\omega L}(\pi-\varphi)\right)\right)(\pi-\varphi)\right] = \cdots = \quad I_0 + \frac{V_{dc}}{2\omega L}[(1+M)\varphi + (1-M)(\pi-\varphi)] \Longrightarrow$$

$$I_L = I_0 + \frac{V_{dc}}{\omega L}\left[M\varphi + \frac{\pi}{2}(1-M)\right] \tag{5.108}$$

I_L can be written based on other points of the waveform such as I_1 or I_2 also. If I_L is zero which is true while operating under steady state conditions (5.108) will be equal to (5.31) which was calculated in section 5.4.1. In fact (5.108) is a more general case which describes both transient and steady state conditions. Another important parameter that can be calculated to describe the behavior of DAB with more detail is the average of load current which is the current that flows to the parallel resistor capacitor load which is calculated as follows:

$$\begin{aligned} I_{Load} = \frac{1}{4\pi}\Bigg[& \left(-2I_0 - \frac{V_{dc}(1+M)}{\omega L}\varphi\right)\varphi \\ & + \left(2I_0 + 2\frac{V_{dc}(1+M)}{\omega L}\varphi + \frac{V_{dc}(1-M)}{\omega L}(\pi-\varphi)\right)(\pi-\varphi) \\ & + \left(2I_0 + \frac{V_{dc}(1+M)}{\omega L}\varphi + 2\frac{V_{dc}(1-M)}{\omega L}(\pi-\varphi)\right)\varphi \\ & - \left(2I_0 + \frac{V_{dc}(1-M)}{\omega L}(\pi-\varphi)\right)(\pi-\varphi)\Bigg] = \cdots \Longrightarrow \end{aligned} \tag{5.109}$$

$$I_{Load} = \frac{V_{dc}}{\omega L}\varphi\left(1 - \frac{\varphi}{\pi}\right) \tag{5.110}$$

RMS current which flows through the inductor is a key factor for choosing the inductor value. Calculating the RMS value of the current waveform shown in Fig. 5.19 directly is not easy, so we try to simplify the calculations using a specific case mentioned here. The current waveform shown in Fig. 5.19 can be considered as piecewise linear waveforms. Considering a general straight line equation as y = ax + b we can write:

$$y = ax + b \Longrightarrow y^2 = a^2x^2 + 2abx + b^2 \Longrightarrow \tag{5.111}$$

$$\int_{x_0}^{x_1} y^2 dx = \int_{x_0}^{x_1} (a^2x^2 + 2abx + b^2)dx = \left[\frac{a^2}{3}x^3 + abx^2 + b^2x\right]_{x_0}^{x_1} \tag{5.112}$$

$$\int_{x_0}^{x_1} y^2 dx = \frac{a^2}{3}({x_1}^3 - {x_0}^3) + ab({x_1}^2 - {x_0}^2) + b^2(x_1 - x_0) \tag{5.113}$$

For different parts of current waveform, integral of square of waveform equation can be calculated using (5.89), so we can write:

1) $0 \leq \omega t < \varphi$

$$i_L(\omega t) = \underbrace{I_0}_{b} + \underbrace{\frac{V_{dc}(1+M)}{\omega L}}_{a}\omega t \tag{5.114}$$

$$\Longrightarrow A1 = \int_0^{\omega t_1} {i_L}^2(\omega t)d(\omega t) = \frac{1}{3}\left(\frac{V_{dc}(1+M)}{\omega L}\right)^2 \varphi^3 + \frac{V_{dc}(1+M)}{\omega L} I_0 \varphi^2 + {I_0}^2 \varphi \tag{5.115}$$

2) $\varphi \leq \omega t < \pi \rightarrow 0 \leq \omega t - \varphi < \pi - \varphi \rightarrow 0 \leq \omega t' < \pi - \varphi$

$$i_L(\omega t') = \underbrace{\left(I_0 + \frac{V_{dc}(1+M)}{\omega L}\varphi\right)}_{b} + \underbrace{\frac{V_{dc}(1-M)}{\omega L}}_{a}\omega t' \tag{5.116}$$

$$\Longrightarrow A2 = \int_0^{\pi-\varphi} {i_L}^2(\omega t')d(\omega t')$$

$$= \frac{1}{3}\left(\frac{V_{dc}(1-M)}{\omega L}\right)^2(\pi-\varphi)^3$$

$$+\left(I_0 + \frac{V_{dc}(1+M)}{\omega L}\varphi\right)\left(\frac{V_{dc}(1-M)}{\omega L}\right)(\pi-\varphi)^2 \quad (5.117)$$

$$+\left(I_0 + \frac{V_{dc}(1+M)}{\omega L}\varphi\right)^2(\pi-\varphi)$$

3) $\pi \le \omega t < \pi + \varphi \rightarrow 0 \le \omega t - \pi < \varphi \rightarrow 0 \le \omega t'' < \varphi$

$$i_L(\omega t'') = \underbrace{\left(I_0 + \frac{V_{dc}(1+M)}{\omega L}\varphi + \frac{V_{dc}(1-M)}{\omega L}(\pi-\varphi)\right)}_{b} \underbrace{-\frac{V_{dc}(1+M)}{\omega L}}_{a}\omega t'' \quad (5.118)$$

$$\Longrightarrow A3 = \int_0^{\varphi} {i_L}^2(\omega t'')d(\omega t'')$$

$$= \frac{1}{3}\left(-\frac{V_{dc}(1+M)}{\omega L}\right)^2\varphi^3$$

$$-\left[\frac{V_{dc}(1+M)}{\omega L}\left(I_0 + \frac{V_{dc}(1+M)}{\omega L}\varphi + \frac{V_{dc}(1-M)}{\omega L}(\pi-\varphi)\right)\varphi^2\right] \quad (5.119)$$

$$+\left[\left(I_0 + \frac{V_{dc}(1+M)}{\omega L}\varphi + \frac{V_{dc}(1-M)}{\omega L}(\pi-\varphi)\right)^2\varphi\right]$$

4) $\pi + \varphi \le \omega t < 2\pi \rightarrow 0 \le \omega t - (\pi + \varphi) < \pi - \varphi \rightarrow 0 \le \omega t''' < \pi - \varphi$

$$i_L(\omega t''')$$

$$= \underbrace{\left(I_0 + \frac{V_{dc}(1+M)}{\omega L}\varphi + \frac{V_{dc}(1-M)}{\omega L}(\pi-\varphi) - \frac{V_{dc}(1+M)}{\omega L}\varphi\right)}_{b} \underbrace{- \frac{V_{dc}(1-M)}{\omega L}}_{a}\omega t''' \quad (5.120)$$

$$\Longrightarrow A4 = \int_0^{\pi-\varphi} {i_L}^2(\omega t''')d(\omega t''')$$

$$= \frac{1}{3}\left(-\frac{V_{dc}(1-M)}{\omega L}\right)^2(\pi-\varphi)^3$$

$$-\left[\frac{V_{dc}(1-M)}{\omega L}\left(I_0 + \frac{V_{dc}(1-M)}{\omega L}(\pi-\varphi)\right)(\pi-\varphi)^2\right] \quad (5.121)$$

$$+\left[\left(I_0 + \frac{V_{dc}(1+M)}{\omega L}(\pi-\varphi)\right)^2(\pi-\varphi)\right]$$

Now we can calculate the RMS current as:

$$I_{L,rms} = \sqrt{\frac{1}{2\pi}\int_0^{2\pi} {i_L}^2(\omega t)d(\omega t)} = \sqrt{\frac{1}{2\pi}(A1+A2+A3+A4)} \quad (5.122)$$

$$\Longrightarrow I_{L,rms} = \frac{1}{\sqrt{\pi}}sqrt\left[\frac{\varphi^3}{3}\left(\frac{V_{dc}(1+M)}{\omega L}\right)^2 + \frac{V_{dc}(1+M)}{\omega L}I_0\varphi^2 + {I_0}^2\varphi\right.$$

$$+\frac{(\pi-\varphi)^3}{3}\left(\frac{V_{dc}(1-M)}{\omega L}\right)^2$$

$$+\left(I_0 + \frac{V_{dc}(1+M)}{\omega L}\varphi\right)\left(\frac{V_{dc}(1-M)}{\omega L}\right)(\pi-\varphi)^2 \quad (5.123)$$

$$\left.+\left(I_0 + \frac{V_{dc}(1+M)}{\omega L}\varphi\right)^2(\pi-\varphi)\right]$$

Results obtained till here are general and independent of the load type. However, more results can be obtained for specific types of load. If load is resistive then the filter capacitor is very small compared to resistor value and most of the power is consumed by the resistor. By equating transferred average power (5.37) and absorbed average power in the output resistor:

$$P = \frac{V_{dc}\, V_o/n}{\omega L}\varphi\left(1 - \frac{|\varphi|}{\pi}\right) = \frac{{V_o}^2}{R} \tag{5.124}$$

Substituting (5.27) in (5.124) we get:

$$P = \frac{{V_o}^2/Mn^2}{\omega L}\varphi\left(1 - \frac{|\varphi|}{\pi}\right) = \frac{{V_o}^2}{R} \tag{5.125}$$

For deriving more useful and practical equations it is better to get rid of the absolute value sign, so we can consider positive φ and negative φ separately. When φ is positive, the average power is transferred from primary (left) to secondary (right) and while φ is negative and with the same absolute value, the value of average power remains constant but flows from secondary to primary. For briefness, we just calculate for positive φ while negative φ can be calculated exactly with the same procedure. Using (5.125) M can be calculated based on the parameters of the circuit and control parameter φ:

$$M = \frac{R}{n^2\omega L}\left(\varphi - \frac{\varphi^2}{\pi}\right) \tag{5.126}$$

Since all the parameters other than control parameter φ of the designed converter will remain constant, (5.126) is a useful equation for calculating the steady state average output voltage of DAB. When M is calculated for any arbitrary positive φ then V_o can be calculated using (5.27):

$$V_o = \frac{Mn}{V_{dc}} = \frac{R}{n\omega L V_{dc}}\left(\varphi - \frac{\varphi^2}{\pi}\right) \tag{5.127}$$

We can use (5.126) in another way. If (5.126) is written as a quadratic equation based on φ we get:

$$\varphi^2 - \pi\varphi + \frac{Mn^2\omega L\pi}{R} = 0 \tag{5.128}$$

The roots of this quadratic equation are the values of φ which will lead to the desired M and the corresponding V_o. In other words, to get the desired V_o required values of φ can be calculated using (5.128). The roots of this equation like any other quadratic equation may or may not be distinct and may be real or complex. Since φ is the phase shift between primary and secondary, it should be a real value. In order to have real roots, delta of (5.128) should be equal or greater than zero, hence:

$$\Delta = \pi^2 - 4\frac{Mn^2\omega L\pi}{R} \geq 0 \tag{5.129}$$

This will lead to an important inequality:

$$M \leq \frac{R\pi}{4n^2\omega L} \tag{5.130}$$

In other words, the desired M should satisfy (5.130) in order to have real solutions for angles. This can help in the design procedure. We call the right side of (5.130) M_{max}.

$$M_{max} = \frac{R\pi}{4n^2\omega L} \tag{5.131}$$

Some more results can be obtained regarding specific points of the inductor current waveform such as I_0, I_1 and I_2 which are important points. Recalling I_2 from (5.33) and (5.31) we get:

$$I_2 = \frac{V_{dc}}{\omega L}\left[\varphi M - \frac{\pi}{2}(M-1)\right] = \frac{V_{dc}}{\omega L}\left[M\left(\varphi - \frac{\pi}{2}\right) + \frac{\pi}{2}\right] \tag{5.132}$$

Substituting (5.126) into (5.132) gives:

$$I_2 = \frac{V_{dc}}{\omega L}\left[\frac{R}{n^2\omega L}\left(\varphi - \frac{\varphi^2}{\pi}\right)\left(\varphi - \frac{\pi}{2}\right) + \frac{\pi}{2}\right] = \frac{V_{dc}}{\omega L}\left[\frac{R}{n^2\omega L}\left(-\frac{\varphi^3}{\pi} + \frac{3}{2}\varphi^2 - \frac{\pi}{2}\varphi\right) + \frac{\pi}{2}\right] \tag{5.133}$$

The derivative of I_2 relative to φ will be:

$$\frac{dI_2}{d\varphi} = \frac{V_{dc}}{\omega L}\left[\frac{R}{n^2\omega L}\left(-\frac{3}{\pi}\varphi^2 + 3\varphi - \frac{\pi}{2}\right)\right] \tag{5.134}$$

To find maximum or minimum points of I_2 the roots of (5.134) should be found:

$$\frac{dI_2}{d\varphi} = 0 \Longrightarrow -\frac{3}{\pi}\varphi^2 + 3\varphi - \frac{\pi}{2} = 0 \Longrightarrow \varphi^2 - \pi\varphi + \frac{\pi^2}{6} = 0 \tag{5.135}$$

$$\Longrightarrow \begin{cases} \varphi_{2,1} = \dfrac{\pi}{2}\left(1 - \dfrac{1}{\sqrt{3}}\right) \approx 38° \\ \varphi_{2,2} = \dfrac{\pi}{2}\left(1 + \dfrac{1}{\sqrt{3}}\right) \approx 142° \end{cases} \tag{5.136}$$

To find out if they are a maximum or minimum point the second derivative of I_2 relative to φ should be calculated:

$$\frac{d^2I_2}{d\varphi^2} = \frac{V_{dc}R}{(n\omega L)^2}\left[-\frac{6}{\pi}\varphi + 3\right] \tag{5.137}$$

$$\Longrightarrow \left[\frac{d^2I_2}{d\varphi^2}\right]_{\varphi_1} = \sqrt{3} > 0 \quad , \quad \left[\frac{d^2I_2}{d\varphi^2}\right]_{\varphi_2} = -\sqrt{3} < 0 \tag{5.138}$$

So minimum of I_2 occurs at φ_1 and maximum of I_2 occurs at φ_2.

I_1 can also be analyzed the same way. Substituting (5.126) into (5.32) we will have:

$$I_1 = \frac{V_{dc}}{\omega L}\left[\frac{\pi}{2}(M-1)+\varphi\right] = \frac{V_{dc}}{\omega L}\left[\frac{\pi}{2}\left(\frac{R}{n^2\omega L}\left(\varphi-\frac{\varphi^2}{\pi}\right)-1\right)+\varphi\right] \tag{5.139}$$

$$\Longrightarrow \frac{dI_1}{d\varphi} = \frac{V_{dc}}{\omega L}\left[\frac{\pi}{2}\left(\frac{R}{n^2\omega L}\left(1-\frac{2}{\pi}\varphi\right)\right)+1\right] \tag{5.140}$$

$$\frac{dI_1}{d\varphi} = 0 \Longrightarrow \frac{\pi R}{2n^2\omega L}\left(1-\frac{2}{\pi}\varphi\right)+1 = 0 \tag{5.141}$$

$$\Longrightarrow \varphi_1 = \frac{\pi}{2}+\frac{\omega L}{R} \tag{5.142}$$

To find out if this is a maximum or minimum point we calculate second derivative:

$$\frac{d^2I_2}{d\varphi^2} = \frac{V_{dc}}{\omega L}\left[\frac{\pi}{2}\left(\frac{R}{n^2\omega L}\left(-\frac{2}{\pi}\right)\right)\right] = -\frac{V_{dc}R}{(n\omega L)^2} < 0 \tag{5.143}$$

Therefore, φ_1 is a maximum point for I_1. Minimum points happen at the roots of (5.140) which will give zero value. It should be noted that angles at which maximum and minimum of I_2 occurs are independent of circuit parameters but the angle at which maximum of I_1 happens is dependent on f_{sw}, L and R.

As was previously investigated in (5.123), RMS value of inductor current is a function of various parameters such as transformer inductance, switching frequency, input DC voltage and output resistor. This dependency on different parameters is difficult to be investigated analytically. So it can be shown graphically to get a more visual sense of the rate of change of inductor RMS current relative to different parameters versus phase shift angle in a 3-D fashion. This is depicted in Fig. 5.25. The z-axis of right hand side 3-D graphs of Fig. 5.25 show RMS

value of transformer inductor current in amps relative to transformer inductance in Henry, switching frequency in Hertz, input DC voltage in volt and load resistance in Ohm from top to bottom versus phase shift angle in degree. The left hand side graphs show a 2-D illustration of their right hand 3-D graphs, while clarifying the maximum points connected together through a vertical line. The reason that the vertical line seems discrete rather than continuous is the limited number of points analyzed. Here we have considered 30 different points as a reasonable number of points since considering more points will cause displaying difficulty without providing extra valuable information. Inductance values range from 50 μH to 200 μH, switching frequency ranges from 20 kHz to 100 kHz, input DC voltage ranges from 100 V to 400 V and resistor value ranges from 100 Ω to 500 Ω. In each case when one parameter is changing, all other parameters are kept constant to analyze the effect of change of only that specific parameter. These graphs can help in choosing a suitable inductor, switching frequency or input DC voltage as long as RMS inductor current is considered.

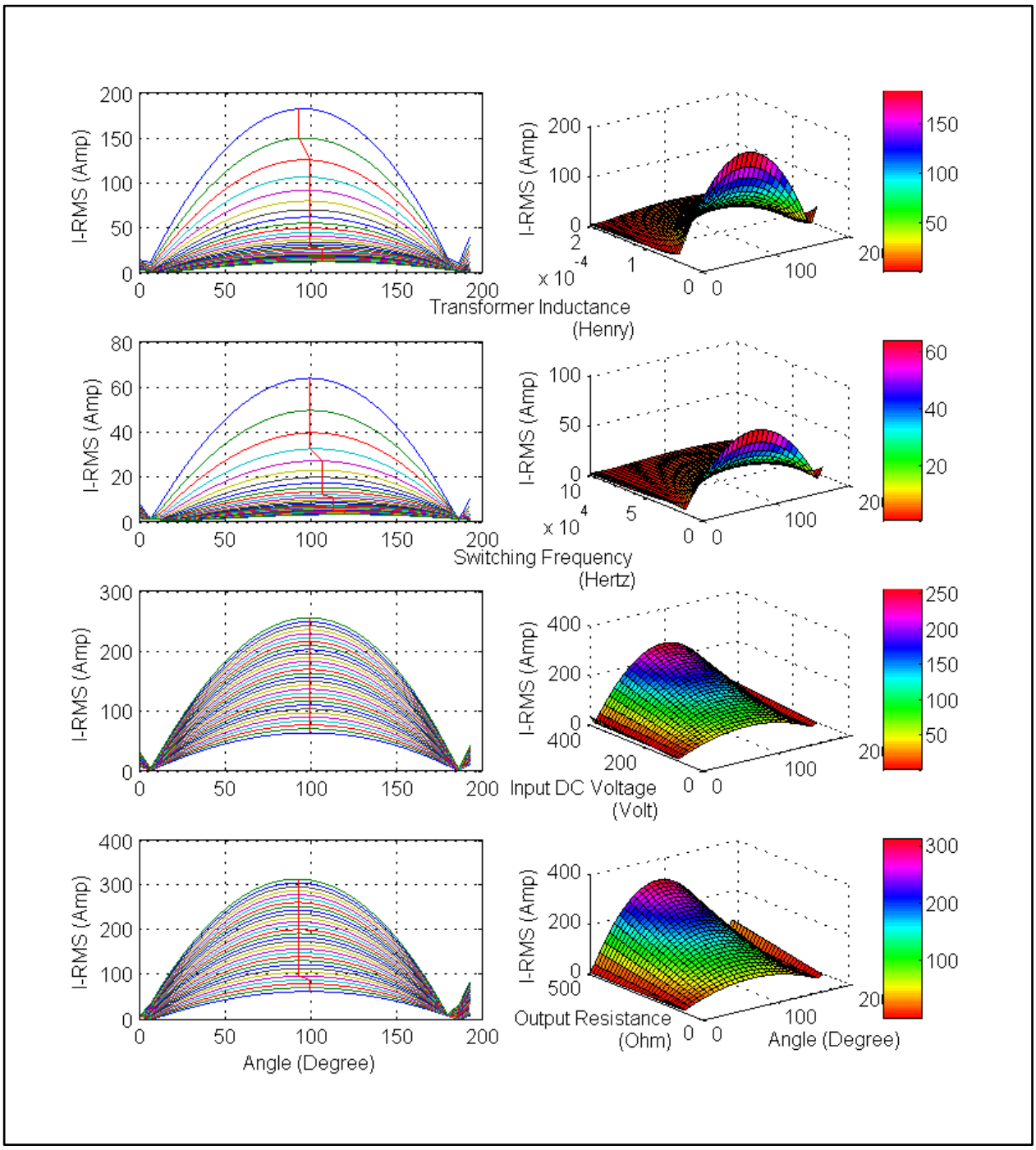

Fig. 5.25 Transformer RMS current vs. L, f_{sw}, V_{DC} and R for 180 degrees phase shift range for resistive load

Another load to be considered is constant voltage load. This may happen if the capacitor has a very big value compared to the resistor. Battery as a load is an example. In this case the value of M in the equations is determined by the voltage of the load, for example, the voltage of the battery pack which depends on SoC. Study of specific points of inductor current such as I_0, I_1, I_2 and also average load current provides important information which is useful in the analysis of effect of inductor value on circuit operation for different phase shift angles. We mention related equations here again:

$$I_0 = \frac{-V_{dc}}{\omega L}\left[M\left(\varphi - \frac{\pi}{2}\right) + \frac{\pi}{2}\right] \tag{5.144}$$

$$I_1 = \frac{V_{dc}}{\omega L}\left[\frac{\pi}{2}(M-1) + \varphi\right] \tag{5.145}$$

$$I_2 = \frac{V_{dc}}{\omega L}\left[M\left(\varphi - \frac{\pi}{2}\right) + \frac{\pi}{2}\right] \tag{5.146}$$

$$I_{Load} = \frac{V_{dc}}{\omega L}\varphi\left(1 - \frac{\varphi}{\pi}\right) \tag{5.147}$$

The graph of these parameters versus φ is shown in Fig. 5.26 to get a more clear idea about their variations versus phase shift angle. The values for the parameters have been chosen

$$V_{dc} = 200V, f_{sw} = 20kHz, L = 85\mu H \tag{5.148}$$

as follows as will be described later in this section:

Since the load is constant voltage type load the value of M is dependent on the load voltage. As described in CHAPTER.2 and Fig. 2.12 the battery voltage changes from 382 V to

389 V in the SoC range of 30% to 90%. So the value of M will range from 382/200=1.91 to 389/200=1.945.

The lines shown in Fig. 5.26 can be shifted and moved by changing the parameters of the circuit. For example, slope of the lines or the point at which they begin can be changed. This is useful in analyzing and coming up with an optimum solution for a specific goal. For example the value of current ripple going to the filter capacitor can be changed be variation of these lines.

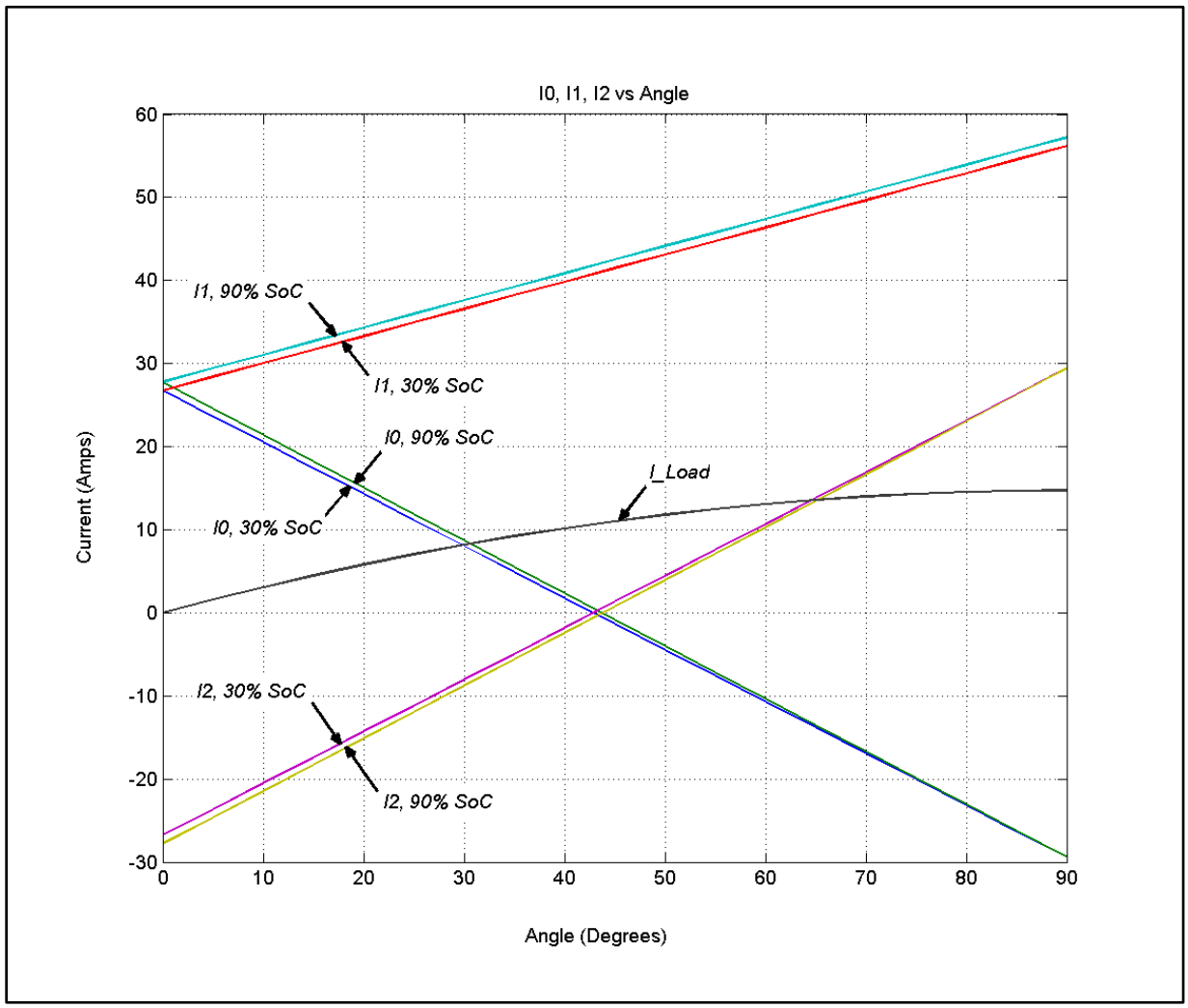

Fig. 5.26 I0, I1 & I2 vs. angle for constant voltage load

However, any change in one parameter will affect other parameters of the circuit. For example, minimizing the required value of capacitor may increase the required value of the inductor and this will lead to a higher DC link input voltage for delivering the same amount of power. To see the effect of different parameters of the circuit on the shape of the lines in Fig. 5.26 their characteristics have been calculated here:

$$Crossing\ angle\colon\ I_0 = 0 \Longrightarrow M\left(\varphi_{0,x} - \frac{\pi}{2}\right) = -\frac{\pi}{2} \Longrightarrow \varphi_{0,x} = \frac{-\pi/2}{M} + \frac{\pi}{2}$$
$$\Longrightarrow \varphi_{0,x} = \frac{\pi}{2}\left(\frac{M-1}{M}\right) = \frac{\pi}{2}\left(\frac{V_o - V_{dc}}{V_o}\right) \tag{5.149}$$

$$Initial\ value\ of\ I_0\colon \varphi = 0 \Longrightarrow I_{0,i} = \frac{-V_{dc}}{\omega L}\left[-\frac{\pi}{2}M + \frac{\pi}{2}\right] = \frac{-V_{dc}}{\omega L} * \frac{\pi}{2}(1-M) \tag{5.150}$$

$$Final\ value\ of\ I_0\colon \varphi = \pi \Longrightarrow I_{0,f} = \frac{-V_{dc}}{\omega L}\left[\frac{\pi}{2}M + \frac{\pi}{2}\right] = \frac{-V_{dc}}{\omega L} * \frac{\pi}{2}(1+M)$$
$$= \frac{-V_{dc}}{\omega L} * \frac{\pi}{2} * \frac{V_{dc} + V_o}{V_{dc}} \Longrightarrow I_{0,f} = -\frac{\pi}{2} * \frac{V_o + V_{dc}}{\omega L} \tag{5.151}$$

$$slope\ of\ I_0\colon\ \alpha = \frac{-V_{dc}}{\omega L} * M = \frac{-V_{dc}}{\omega L} * \frac{V_o}{V_{dc}} = -\frac{V_o}{\omega L} \tag{5.152}$$

The same procedure can be followed for I_1 and I_2 to calculate different points and slope. The results have been summarized in Table 5.1.

	I_0	I_1	I_2
$Crossing\ angle: \varphi_{n,x}$	$\frac{\pi}{2}\left(\frac{M-1}{M}\right)$	$\frac{\pi}{2}(1-M)$	$\frac{\pi}{2}\left(\frac{M-1}{M}\right)$
$Initial\ value: I_{n,i}$	$\frac{V_{dc}}{\omega L} * \frac{\pi}{2}(M-1)$	$\frac{V_{dc}}{\omega L} * \frac{\pi}{2}(M-1)$	$-\frac{V_{dc}}{\omega L} * \frac{\pi}{2}(M-1)$
$Final\ value: I_{n,f}$	$-\frac{V_{dc}}{\omega L} * \frac{\pi}{2} * (M+1)$	$\frac{V_{dc}}{\omega L} * \frac{\pi}{2} * M$	$\frac{V_{dc}}{\omega L} * \frac{\pi}{2} * (M+1)$
$slope: \alpha_n$	$-\frac{V_o}{\omega L}$	$\frac{V_{dc}}{\omega L} * \frac{\pi}{2}$	$\frac{V_o}{\omega L}$

Table 5.1 Characteristics of I0, I1 & I2

The value of the parallel filter capacitor and its effect on the operation of DAB should also be analyzed. Since capacitor mainly deals with output current of secondary of the circuit which is a full-bridge converter the current waveform of the secondary being injected to the load relative to the inductor current is depicted in Fig. 5.27. Average load current denoted as I_{Load} which is a positive value is also shown. Assuming that all the ripple component of i_{Load} flows through the capacitor and its average component flows through the load resistor, the shaded area in Fig. 5.27 represents an additional charge ΔQ which produces ΔV in the capacitor. ΔQ can be written as:

$$\Delta Q = \frac{1}{2}[(I_1 - I_{Load}) + (I_2 - I_{Load})] * \frac{(\pi - \varphi)}{2\pi} T_s + \frac{1}{2}(I_2 - I_{Load}) * \frac{(\omega t_c - \pi)}{2\pi} T_s \tag{5.153}$$

The parameter ωt_c is unknown and should be calculated:

$\pi < \omega t < \pi + \varphi$:

$$i_{Load}(\omega t) = I_2 - \frac{V_{dc}(1+M)}{\omega L}(\omega t - \pi) = \frac{V_{dc}}{\omega L}\left[M\left(\varphi - \frac{\pi}{2}\right) + \frac{\pi}{2}\right] - \frac{V_{dc}(1+M)}{\omega L}(\omega t - \pi) \quad (5.154)$$

$$i_{Load}(\omega t_c) = I_{Load} \quad (5.155)$$

$$\Longrightarrow \frac{V_{dc}}{\omega L}\left[M\left(\varphi - \frac{\pi}{2}\right) + \frac{\pi}{2}\right] - \frac{V_{dc}(1+M)}{\omega L}(\omega t_c - \pi) = \frac{V_{dc}}{\omega L}\varphi\left(1 - \frac{\varphi}{\pi}\right) \quad (5.156)$$

$$\Longrightarrow \omega t_c = \pi + \frac{1}{1+M}\left[M\left(\varphi - \frac{\pi}{2}\right) + \frac{\pi}{2} - \varphi\left(1 - \frac{\varphi}{\pi}\right)\right] \quad (5.157)$$

Substituting for all the required parameters in (5.153) we can write:

$$\Delta V_o = \frac{\Delta Q}{C} \quad (5.158)$$

$$\Longrightarrow \Delta V_o = \frac{V_{dc}}{8\pi^2 {f_s}^2 LC}\left[\left[\varphi(1+M) - 2\varphi\left(1 - \frac{\varphi}{\pi}\right)\right] * (\pi - \varphi) + \left[M\left(\varphi - \frac{\pi}{2}\right) + \frac{\pi}{2} - \varphi\left(1 - \frac{\varphi}{\pi}\right)\right] * \left(\pi + \frac{1}{1+M}\left[M\left(\varphi - \frac{\pi}{2}\right) + \frac{\pi}{2} - \varphi\left(1 - \frac{\varphi}{\pi}\right)\right]\right)\right] \quad (5.159)$$

Equation (5.159) provides the relation between capacitor value and output voltage ripple based on other parameters of the circuit. One can be calculated based on the other one depending on which one is known or to be designed. One way to determine the value of capacitor can be accomplished using frequency domain analysis. Since the current ripple is the summation of

waveforms with integer multiplies of switching frequency, the frequency response of the filter capacitor can help in determining the capacitor value. As the impedance value of capacitor suggests:

$$Z_C = \frac{1}{j\omega C} \Longrightarrow |Z_C| = \frac{1}{\omega C} \tag{5.160}$$

The angular frequency equals 2πf where f is usually the switching frequency, however, in this case as can be seen from Fig. 5.27 the frequency applied to the capacitor is twice the switching frequency, so for the impedance value at switching frequency we have:

$$\left|Z_{C,f_{sw}}\right| = \frac{1}{2\pi * 2f_{sw} * C} \tag{5.161}$$

The same way, the impedance values for the integral multiplies of switching frequency are:

$$\left|Z_{C,n*f_{sw}}\right| = \frac{1}{2\pi * 2nf_{sw} * C} \tag{5.162}$$

Depending on the desired impedance values at switching frequency or other frequencies the capacitor value can be calculated. Using above-mentioned equations and running simulation the capacitor value of 75 mF provides a good trade-off between current ripple of around 10% for phase shift of 45º which is the midpoint of the 90º operational range. For smaller phase shifts the ripple will increase and for bigger phase shifts the ripple will decrease. The current ripple may increase up to 20% for very small phase shift angles like 5º however these small values may be rarely used during operation since they provide small power ratings to the battery pack. Nevertheless, the capacitor value can be increased to reach smaller current ripples for small phase shift angles; however, the weight and price of the capacitor and the whole converter will increase.

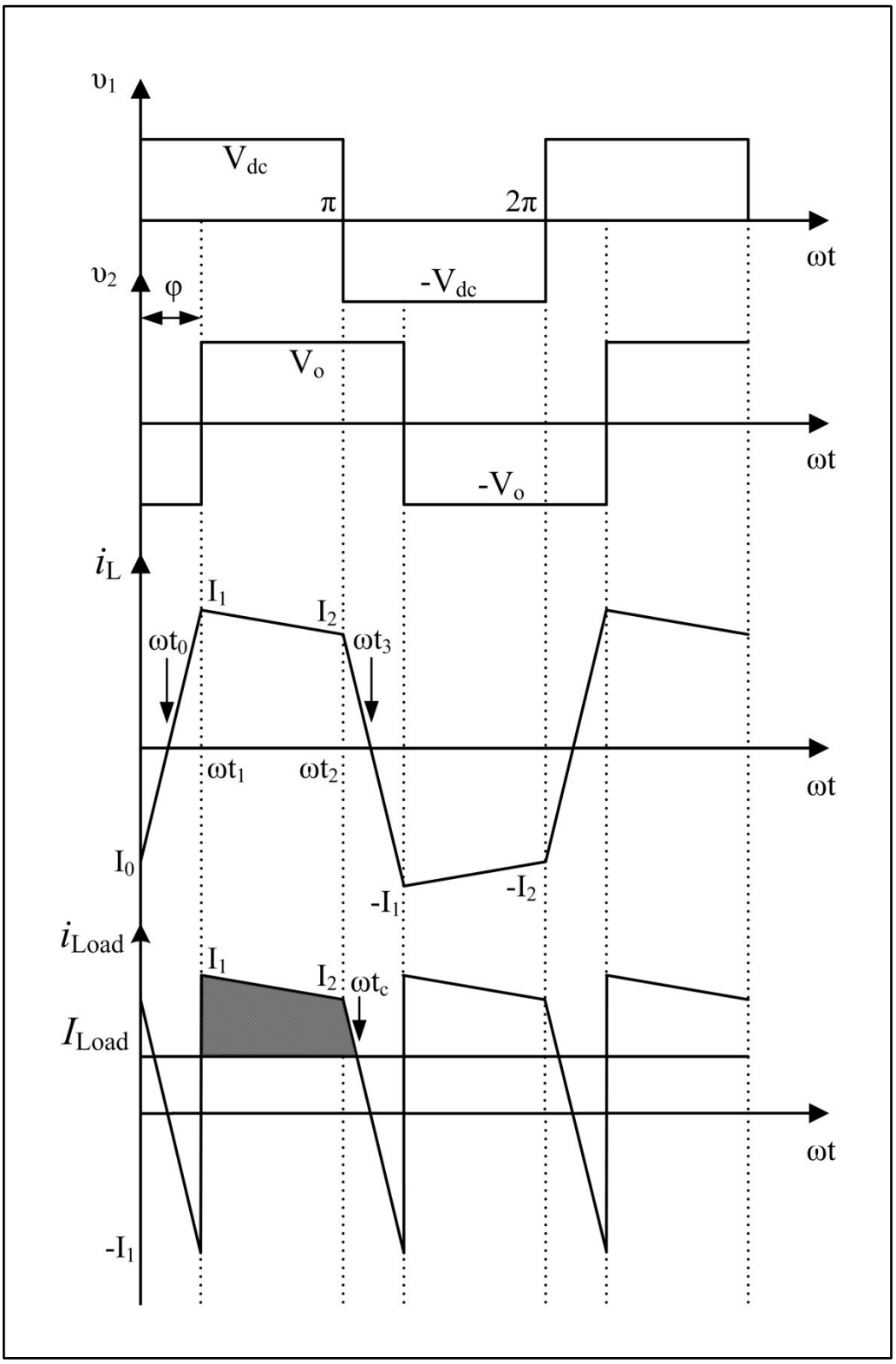

Fig. 5.27 Voltage and current waveforms of inductor and load of DAB

In the previous case which is formulated in (5.153) and as shown in Fig. 5.27 it is assumed that I_{Load} is less than both I_1 and I_2; however, in some cases I_{Load} may be less than I_1 but bigger than I_2. As depicted in Fig. 5.26 this may happen for phase shift angles less than around 65º. In such cases ΔQ will be equal to:

$$\Delta Q = \frac{1}{2}(I_1 - I_{Load}) * \frac{(\omega t_c - \varphi)}{2\pi} T_s \tag{5.163}$$

In this case ωt_c can be calculated as follows:

$\pi < \omega t < \pi + \varphi$:

$$\begin{aligned} i_{Load}(\omega t) &= I_1 + \frac{V_{dc}(1-M)}{\omega L}(\omega t - \varphi) \\ &= \frac{V_{dc}}{\omega L}\left[\frac{\pi}{2}(M-1) + \varphi\right] + \frac{V_{dc}(1-M)}{\omega L}(\omega t - \pi) \end{aligned} \tag{5.164}$$

$$i_{Load}(\omega t_c) = I_{Load} \tag{5.165}$$

$$\Longrightarrow \frac{V_{dc}}{\omega L}\left[\frac{\pi}{2}(M-1) + \varphi\right] + \frac{V_{dc}(1-M)}{\omega L}(\omega t - \pi) = \frac{V_{dc}}{\omega L}\varphi\left(1 - \frac{\varphi}{\pi}\right) \tag{5.166}$$

$$\Longrightarrow \omega t_c = \varphi + \frac{1}{M-1}\left[\frac{\varphi^2}{\pi} + \frac{\pi}{2}(M-1)\right] \tag{5.167}$$

$$\Delta V_o = \frac{\Delta Q}{C} \tag{5.168}$$

$$\Longrightarrow \Delta V_o = \frac{V_{dc}}{8\pi^2 {f_s}^2 LC} * \frac{1}{M-1}\left(\frac{\varphi^2}{\pi} + \frac{\pi}{2}(M-1)\right)^2 \tag{5.169}$$

Average current of the load was previously calculated in (5.110); however, while running simulations we observe some difference between the measured values in simulations and calculated values using (5.110). Finding the source of this difference and formulating it provides useful insight to the analysis of the circuit. For deriving (5.110) we had considered Fig. 5.19. As shown in this figure output voltage is ideally constant in each interval and has no ripples, however, in practice and while running simulations the alternating output current will cause some output voltage ripples even very small. This ripple is a periodic waveform with a frequency equal to switching frequency around an average output voltage value. For non-sinusoidal repetitive waveforms we can use Fourier Transform to analyze the circuit in a general form. Not mentioning the background theories of Fourier series, any periodic waveform can be represented as sum of an average value and infinite number of sinusoidal waveforms with frequencies equal to integral multiples of fundamental frequency. In other words:

$$f_{(t)} = A_0/2 + A_1 \cos \omega_s t + A_2 \cos 2\,\omega_s t + A_3 \cos 3\omega_s t + A_4 \cos 4\omega_s t + \cdots + B_1 \sin \omega_s t + B_2 \sin 2\,\omega_s t + B_3 \sin 3\,\omega_s t + B_4 \sin 4\,\omega_s t + \cdots \tag{5.170}$$

$$\Longrightarrow f_{(t)} = \frac{A_0}{2} + \sum_{n=1}^{\infty} (A_n \cos n\omega_s t + B_n \sin n\omega_s t) \tag{5.171}$$

So we can write load current and load voltage which is output voltage as:

$$v_{o(t)} = V_o + \sum_{n=1}^{\infty} V_n \sin(n\omega_s t + \alpha_n) \tag{5.172}$$

$$i_{Load(t)} = I_{Load} + \sum_{n=1}^{\infty} I_n \sin(n\omega_s t + \beta_n) \tag{5.173}$$

Calculating instantaneous and average power we will get:

$$p_{(t)} = v_{(t)}.\, i_{(t)} \tag{5.174}$$

$$P = \frac{1}{T}\int_{t_0}^{t_0+T} p_{(t)}\, dt = \frac{1}{T}\int_{t_0}^{t_0+T} v_{(t)}.\, i_{(t)}\, dt \tag{5.175}$$

$$\Longrightarrow P = \frac{1}{T}\int_{t_0}^{t_0+T} \left[V_o + \sum_{n=1}^{\infty} V_n \sin(n\omega_s t + \alpha_n)\right].\left[I_{Load} + \sum_{n=1}^{\infty} I_n \sin(n\omega_s t + \beta_n)\right] \tag{5.176}$$

Using trigonometric properties, the integral of products of non-similar frequency terms are zero so the result will include only product of similar frequency terms and we will have:

$$P = V_o I_{Load} + \sum_{n=1}^{\infty} (1/2) V_n I_n \cos(\alpha_n - \beta_n) \tag{5.177}$$

$$\Longrightarrow P = V_o I_{Load} + \sum_{n=1}^{\infty} V_{rms,n} I_{rms,n} \cos(\alpha_n - \beta_n) \tag{5.178}$$

If DAB is voltage controlled good enough then (5.178) gets closer to (5.37).

Now we have enough equations to begin the design process. To begin the calculation of inductor and capacitor values, some parameters of the circuit should be defined arbitrarily first. For example, switching frequency can be chosen any value in a reasonable range usually used for power electronics. The bigger the switching frequency, the smaller and lighter the required inductor and capacitor will be and also the system will respond faster to the changes in conditions or references. However, on the other side the switching losses will increase and overall efficiency of the system will reduce. Besides, as mentioned before, the battery pack has a very slow dynamic and we don't need a very fast dynamic system to deal with the changes in the battery specifications such as SoC and voltage. Initially, we choose 20 kHz according to the desired power rating of DAB which should be around 6 kW as will be shown. This guarantees the losses to be kept as low as possible. As shown in Fig. 2.12 in the operating SoC window of

30% to 90% the voltage of the battery pack ranges from 382 to 389 so we consider the voltage of the battery almost equal to 380 volts. The maximum current used for charging the battery was 15 amps so the maximum power of the DAB should be 380*15=5700 W. For considering practical conditions such as transients and inrush currents at start-up we consider 20% of possible overload which will lead to 5700*1.2 ≈ 6850 W.

Another parameter to be chosen is the nominal voltage of the input DC link. The higher voltage of DC link will lead to reduced required current ratings for the same power and consequently lower ohmic losses in wires and devices. However, higher voltage switches and capacitors will be required which are more expensive and also electrical isolation will be harder and more expensive to implement. Initially, we choose 400 V as a reasonable DC link nominal voltage for our system. According to Fig. 5.15 DC link voltage is equal to $2*V_{DC}$, so V_{DC} will be equal to 200 V. Again, it should be mentioned that these parameters such as switching frequency and DC link voltage can be initially chosen arbitrarily and are not a unique value and any designer can choose their own values based on experience, allowable price and available devices and technology; however, there are always trade-offs contradicting each other in choosing parameters which should be considered.

Based on 6850 W maximum transferrable power, 20 kHz switching frequency, V_{DC} = 200 V and using Fig. 5.37 we can calculate the value of L. It should be noted that 6850 W is the maximum power that DAB can deliver. As previously was shown in Fig. 5.20 this maximum power happens at $\varphi = \pi/2$. Hence:

$$P = \frac{V_{dc}\, V_o/n}{\omega L}\varphi\left(1 - \frac{|\varphi|}{\pi}\right) \tag{5.179}$$

$$\Longrightarrow 6850 = \frac{200 * 380/n}{2\pi * 20000 * L} * \frac{\pi}{2} * \left(1 - \frac{\pi/2}{\pi}\right) \tag{5.180}$$

$$\Longrightarrow L = \frac{69.34}{n}\mu H \tag{5.181}$$

Where "n" is transformer turn ratio as shown in Fig. 5.15. For considering practical issues such as current spikes during switching we increase the inductance value by 20% which will lead to:

$$L \simeq \frac{85}{n}\ \mu H \tag{5.182}$$

Increasing the turn ratio of the transformer will reduce the required inductance; however, practically manufacturing price will increase because of required isolation. For simplicity we choose the turn ratio equal to one so the required inductance will be 85 μH.

5.4.6 DAB Controllers Design

Now all the parameters are ready to design the controller. Using (5.99) through (5.107) different small signal transfer functions can be calculated as follows:

- *Small-signal control-to-output transfer function:*

$$G_{\varphi x_2(s)} = \frac{2.427 * 10^6}{s^2 + 1.433 * 10^4\, s + 3.655 * 10^4} \tag{5.183}$$

- *Small-signal control-to-state transfer function:*

$$G_{\varphi x_1(s)} = \frac{4.806 * 10^5\, s + 3.152 * 10^4}{s^2 + 1.433 * 10^4\, s + 3.655 * 10^4} \tag{5.184}$$

- *Small-signal source-to-output transfer function:*

$$G_{ux_{2}(s)} = \frac{4.107 * 10^4}{s^2 + 1.433 * 10^4\, s + 3.655 * 10^4} \tag{5.185}$$

- *Small-signal source-to-state transfer function:*

$$G_{ux_{1}(s)} = \frac{8132\, s + 533.4}{s^2 + 1.433 * 10^4\, s + 3.655 * 10^4} \tag{5.186}$$

According to Fig. 5.24 to design the controllers C_i and C_v first the inner current loop is considered. Assuming that inner current loop operates much faster than the outer voltage loop, C_i can be designed assuming the outer loop has no effect on the operation of inner loop or in other words C_i can be designed independent of the outer loop. For controller design SISO tool in Matlab/Simulink has been used. Bode plot, step response and pole-zero map of the control-to-state transfer function are shown in Fig. 5.28, Fig. 5.30 and Fig. 5.29 respectively.

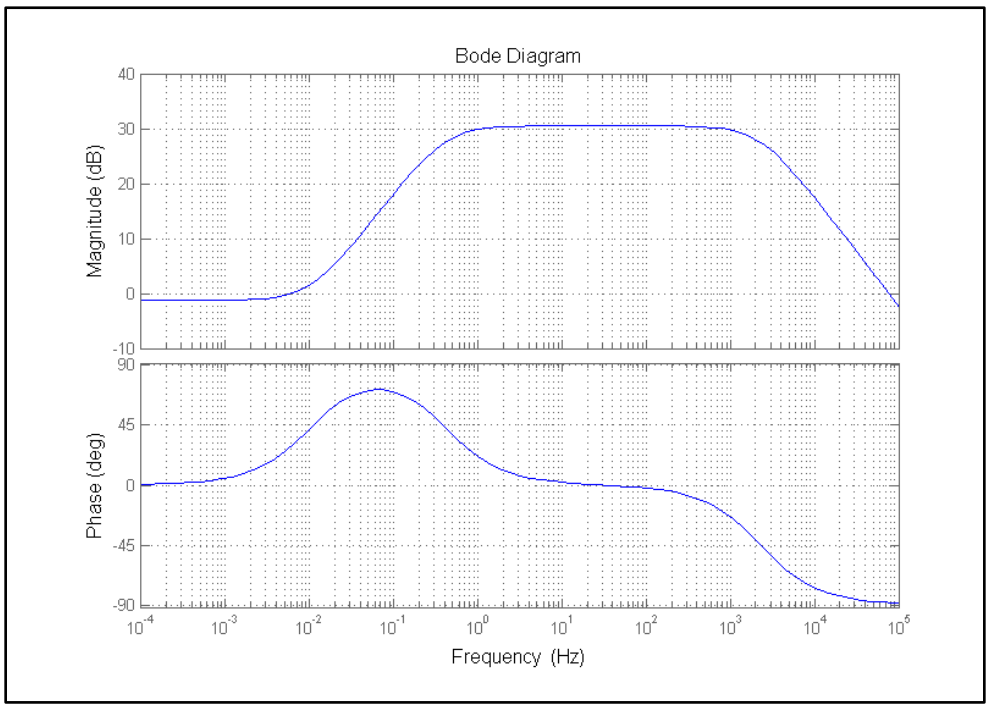

Fig. 5.28 Bode plot for control-to-state transfer function

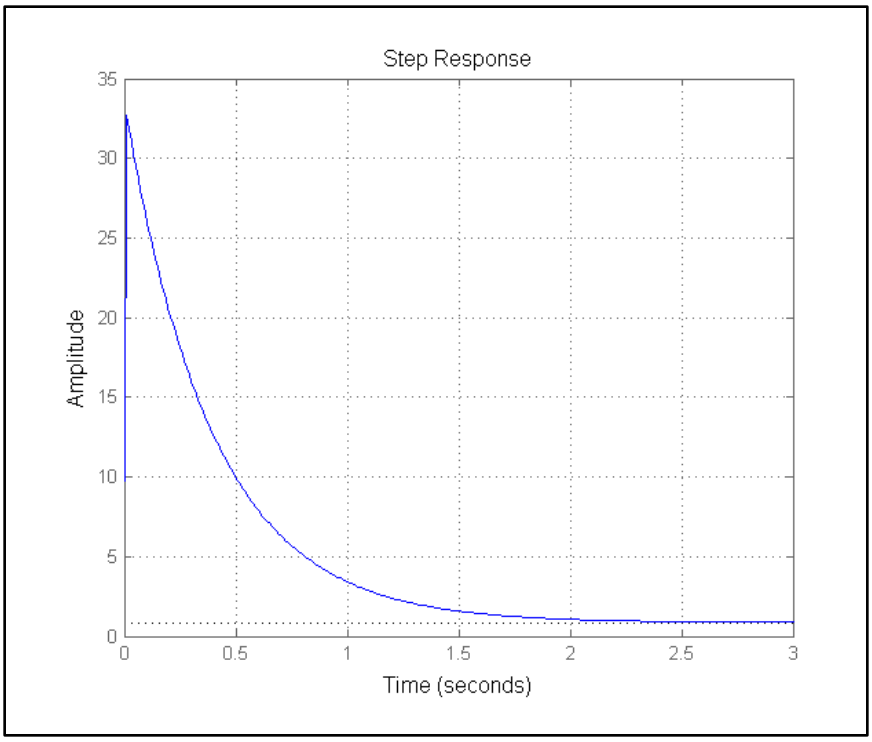

Fig. 5.30 Step response of control-to-output transfer function

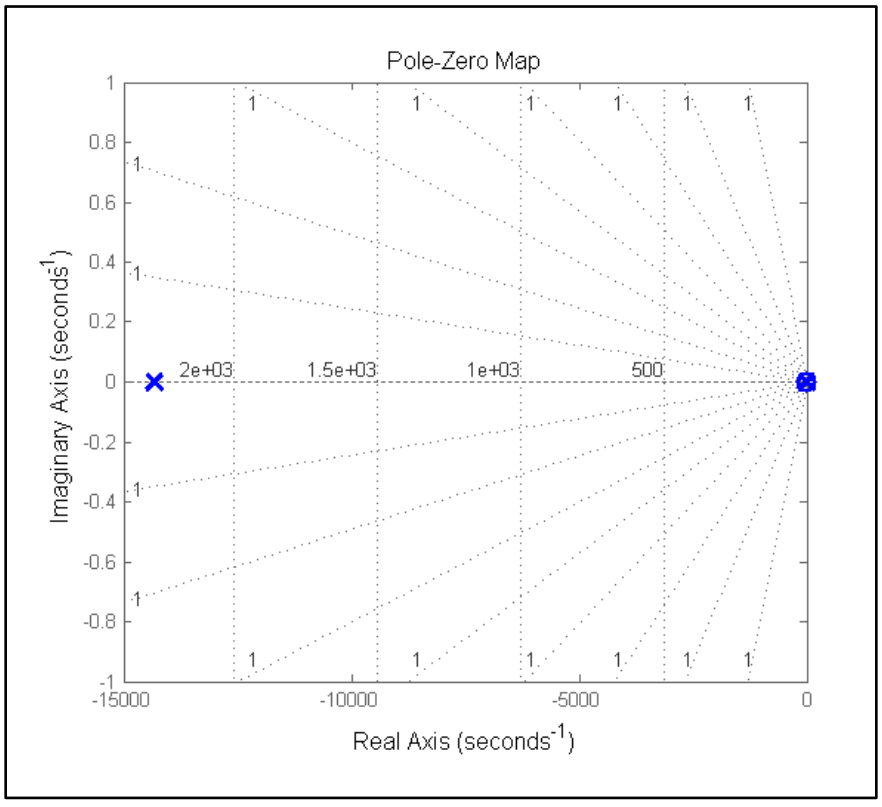

Fig. 5.29 Poles and zeros of control-to-output transfer function

Cross over frequency has been chosen 5% of the switching frequency which is equal to 1 kHz. As depicted in Fig. 5.28 the slope of the magnitude plot equals 0 dB/dec, -20 dB/dec and -20 dB/dec at low frequencies, cross over frequency and high frequencies which suggests the use of a PI controller type 2 constituting of one integrator, one pole and one zero. Different phase margins have been analysed, however; only 45º and 70º have been mentioned here:

$$PM = 45° \Longrightarrow C_{i,45} = \frac{139.7022\ (s + 9202)}{s\ (s + 4290)} \tag{5.187}$$

$$PM = 70° \Longrightarrow C_{i,70} = \frac{218.0717\ (s + 5895)}{s\ (s + 6697)} \tag{5.188}$$

Bode plot of new open loop transfer function including C_i and $G_{\varphi x1}$ is shown in Fig. 5.31.

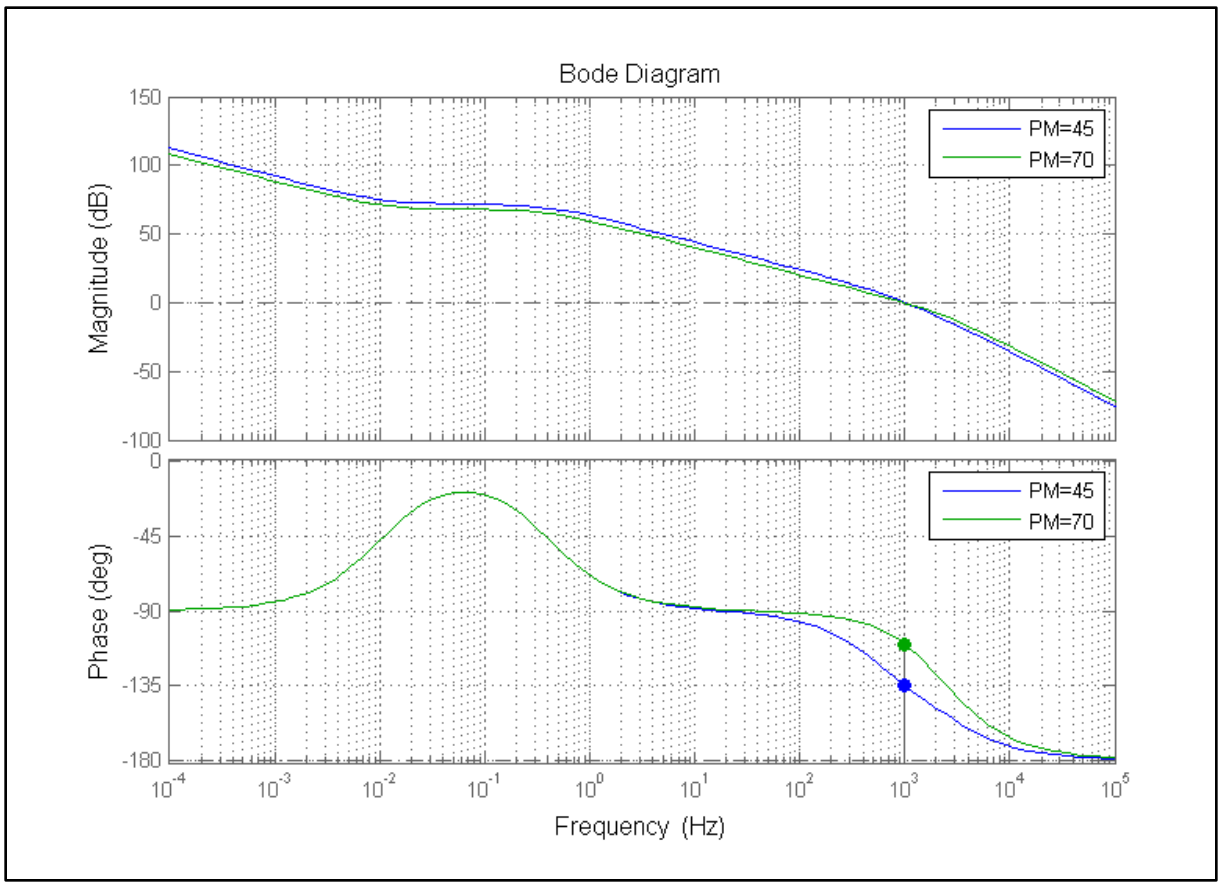

Fig. 5.31 Bode diagram of open loop control-to-state transfer function and Ci

Step response of the inner closed loop along with peak response and settling time points for phase margins of 45º and 70º are shown in Fig. 5.32.

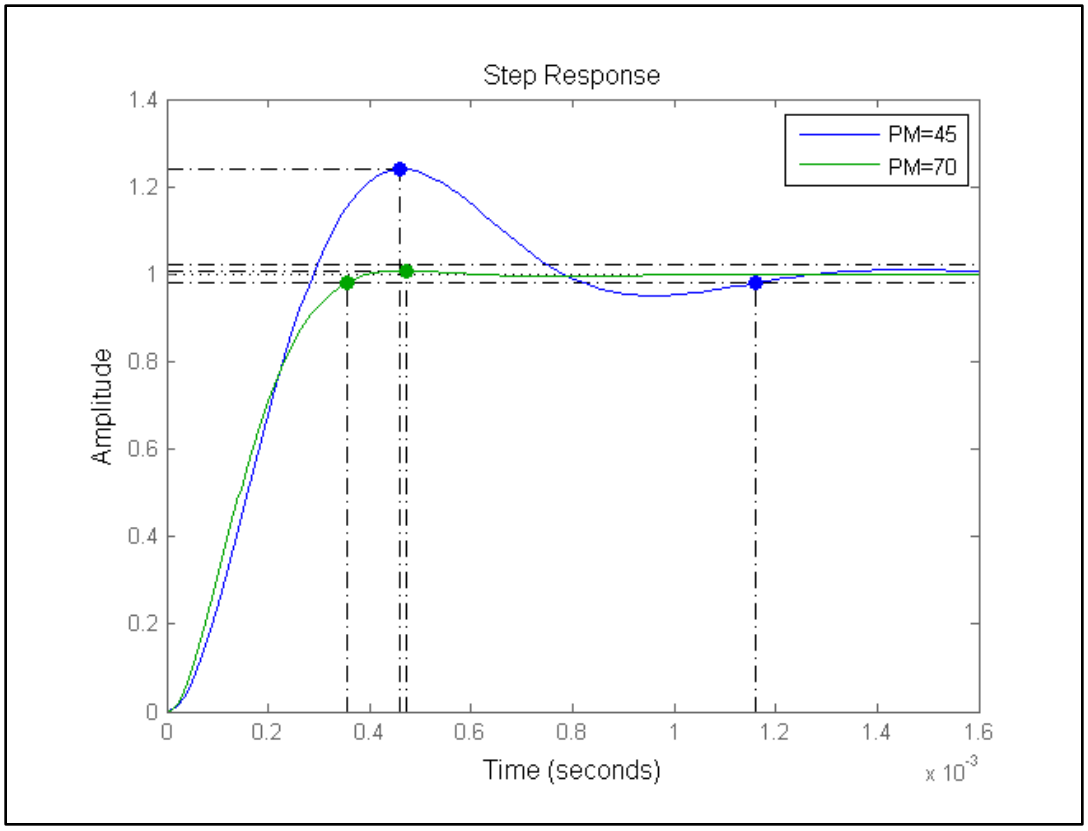

Fig. 5.32 Step response of inner closed loop for 45º and 70º phase margin

Phase margin of 45º leads to 24% of overshoot which is high and may be dangerous as it may cause overvoltage and overheating of the battery pack. This overshoot may also be amplified by the outer loop. However, phase margin of 70º leads to only 0.796% of overshoot which is negligible. Besides, with 45º of phase margin the settling time is 1.16 ms while 70º provides 0.354 ms which is 3.3 times faster. So 70º of phase margin is chosen for the controller. The root locus diagram for the 70º phase margin controller along with design requirements of settling time of less than 1 ms and overshoot of less than 5% is depicted in Fig. 5.33.

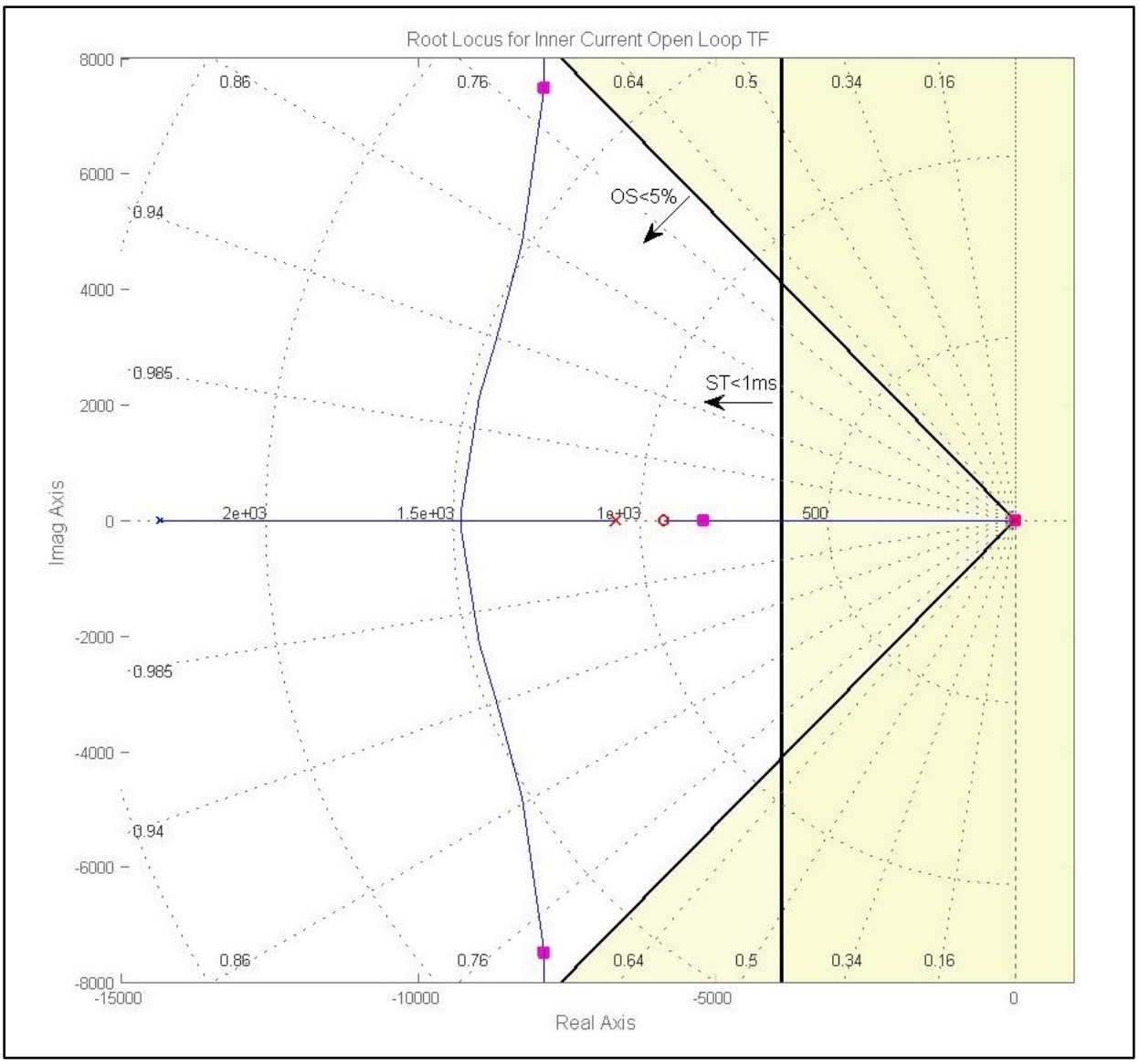

Fig. 5.33 Root Locus diagram for current loop with the controller

Some tests have been done to evaluate the performance of the designed current controller. The results are shown in Fig. 5.34. The simulation has started with the battery SoC of 30%. Reference current is changing each one second as shown in the first row. Although the steps in reference are high, as shown in the second row, the actual current tracks the reference quite fast and accurate. Voltage, SoC and power of the battery are shown in row three to five respectively.

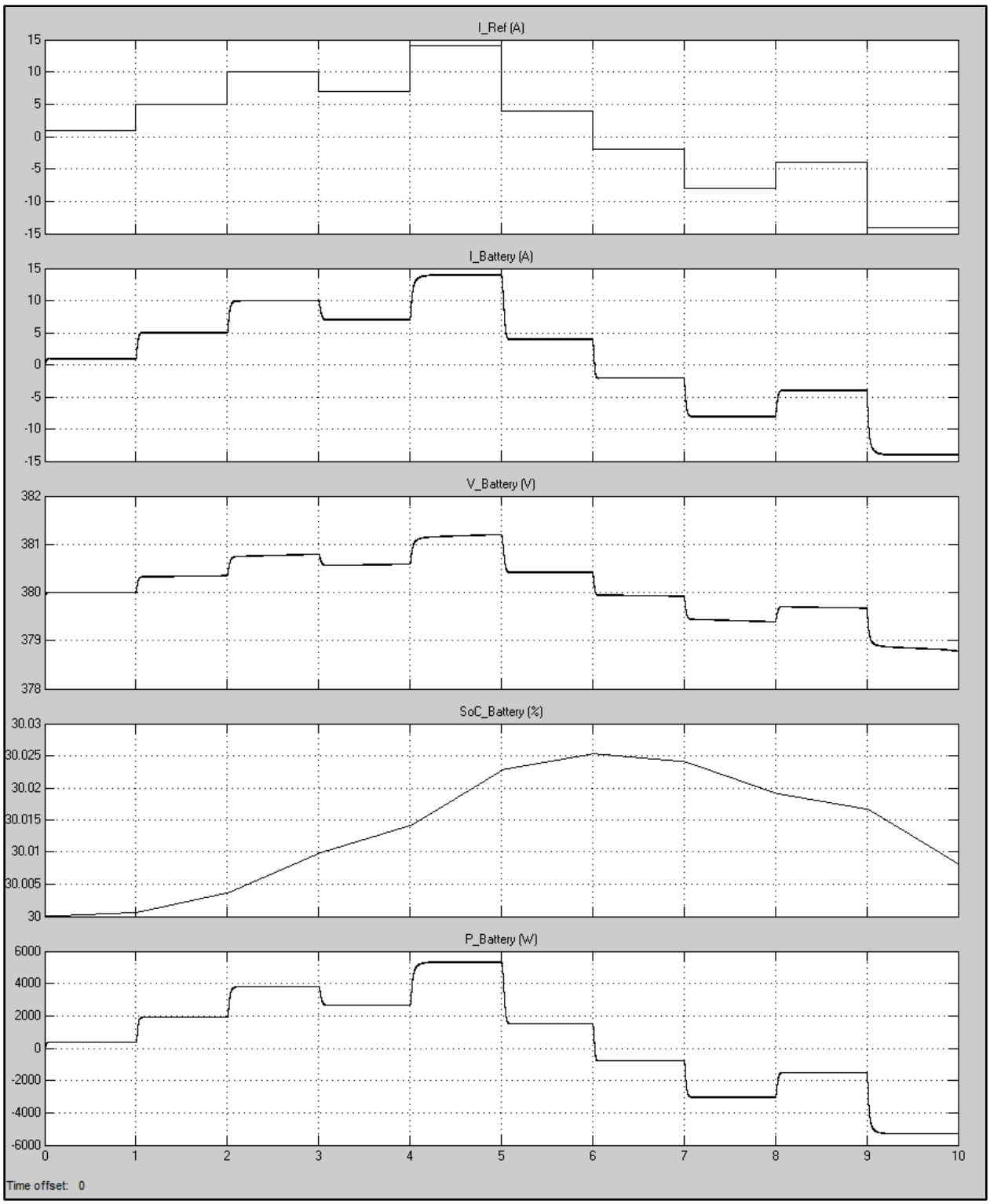

Fig. 5.34 Simulation results for current controller of DAB

Now the outer voltage loop controller can be designed. According to Fig. 5.24 the open loop transfer function in this case constitutes of inner current closed loop including the current controller and control-to-output transfer function which is calculated as follows:

$$G_{OL,v} = \frac{2.5435 * 10^{14}\ (s + 5895) * (s + +0.06559)}{(s + 14330)(s + 5229)(s + 2.55)(s + 0.065)(s^2 + 1.58 * 10^4\ s + 1.182 * 10^8)} \quad (5.189)$$

The bode plot of $G_{OL,v}$ is depicted in Fig. 5.35.

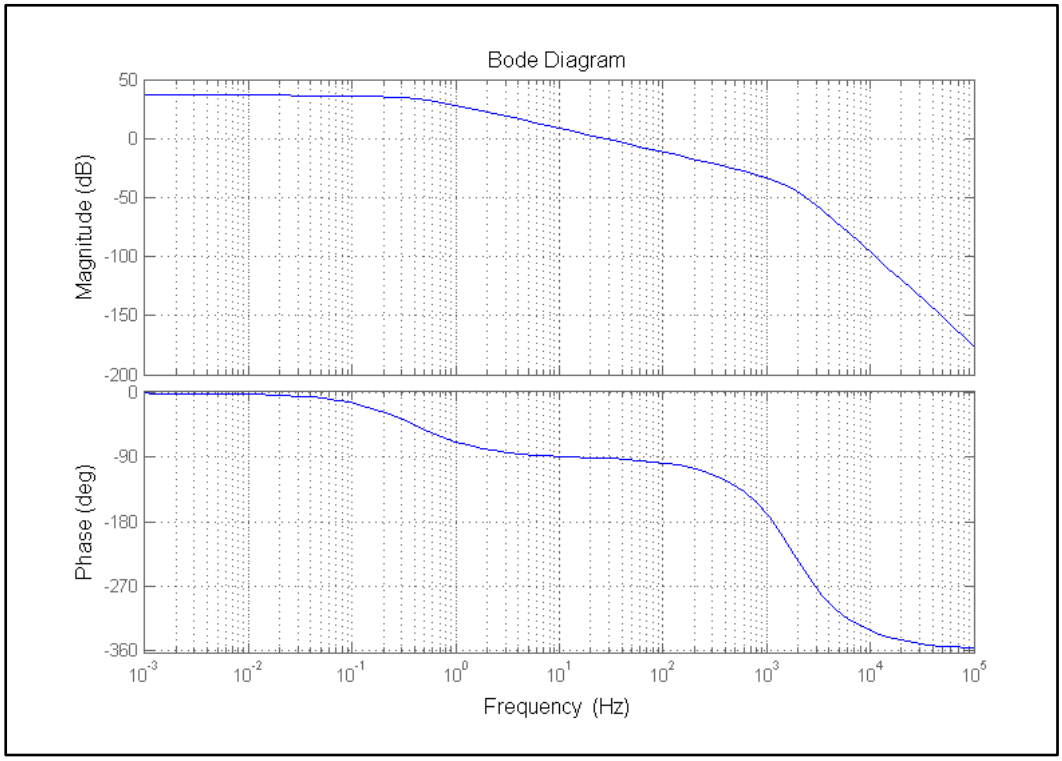

Fig. 5.35 Bode diagram of voltage open loop transfer function

Ideally, the speed of response of inner loop should be at least ten times faster than the outer loop. Rise time has an almost inverse relation with bandwidth. Hence, for a damped system the maximum bandwidth of outer loop should be chosen one tenth of the inner loop. Therefore,

we choose the cross-over frequency of the voltage loop to be one tenth of the inner loop which will be equal to 100 Hz. As Fig. 5.35 shows the slope of the magnitude diagram is 0 dB/dec, -20 dB/dec and -40 dB/dec at low frequencies, cross-over frequency and high frequencies which suggests the use of a PI regulator type 1 constituting of one integrator and one real zero. Different phase margins have been analyzed but only phase margins of 60º and 80º have been mentioned here for comparison.

$$PM = 60° \Longrightarrow C_{v,60} = 3.4474\ \frac{s + 255.6}{s} \tag{5.190}$$

$$PM = 80° \Longrightarrow C_{v,80} = 3.7191\ \frac{s + 23.44}{s} \tag{5.191}$$

Bode plots of new voltage open loop transfer functions are shown in Fig. 5.36.

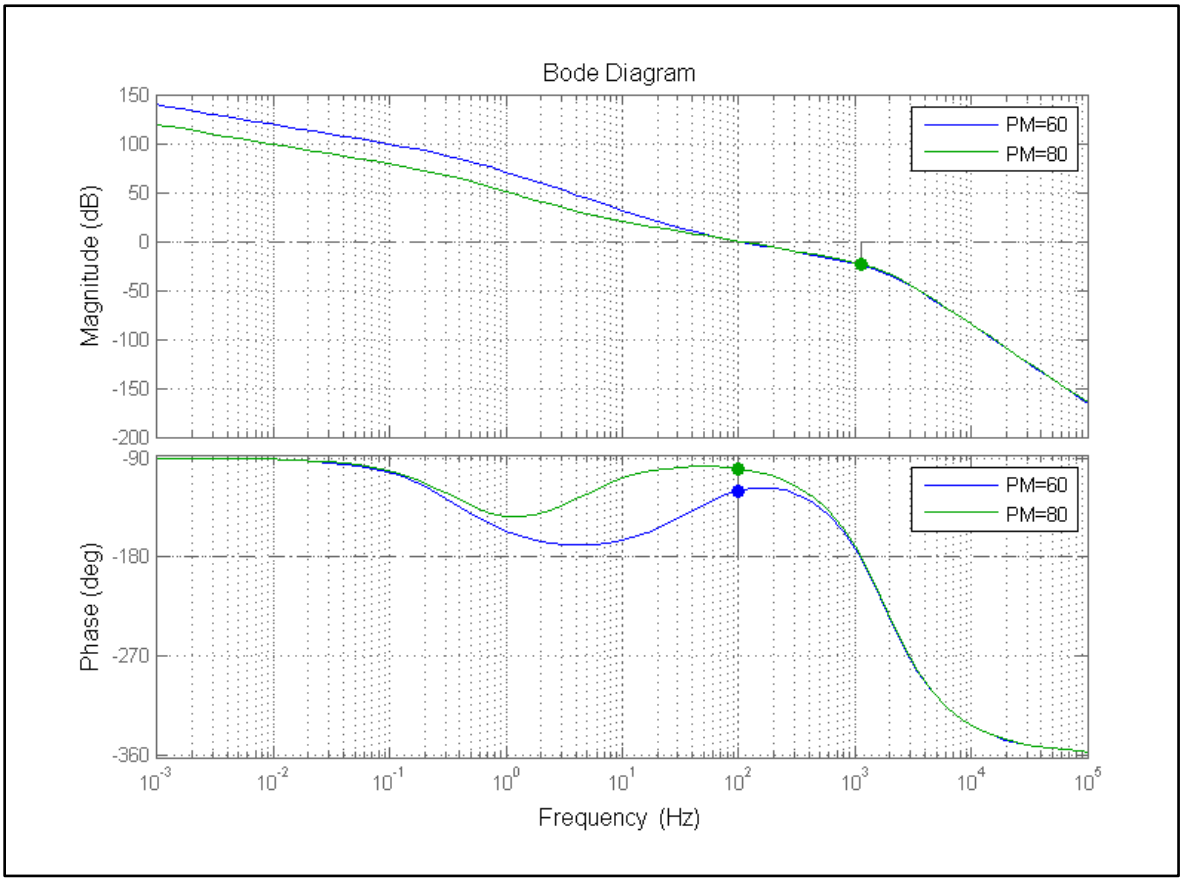

Fig. 5.36 Bode plot of voltage open loop including $G_{OL,v}$ and $G_{\varphi x2}$

Step response of the outer closed loop along with peak response and settling time points for phase margins of 60º and 80º are shown in Fig. 5.37. As can be seen in Fig. 5.37 the phase

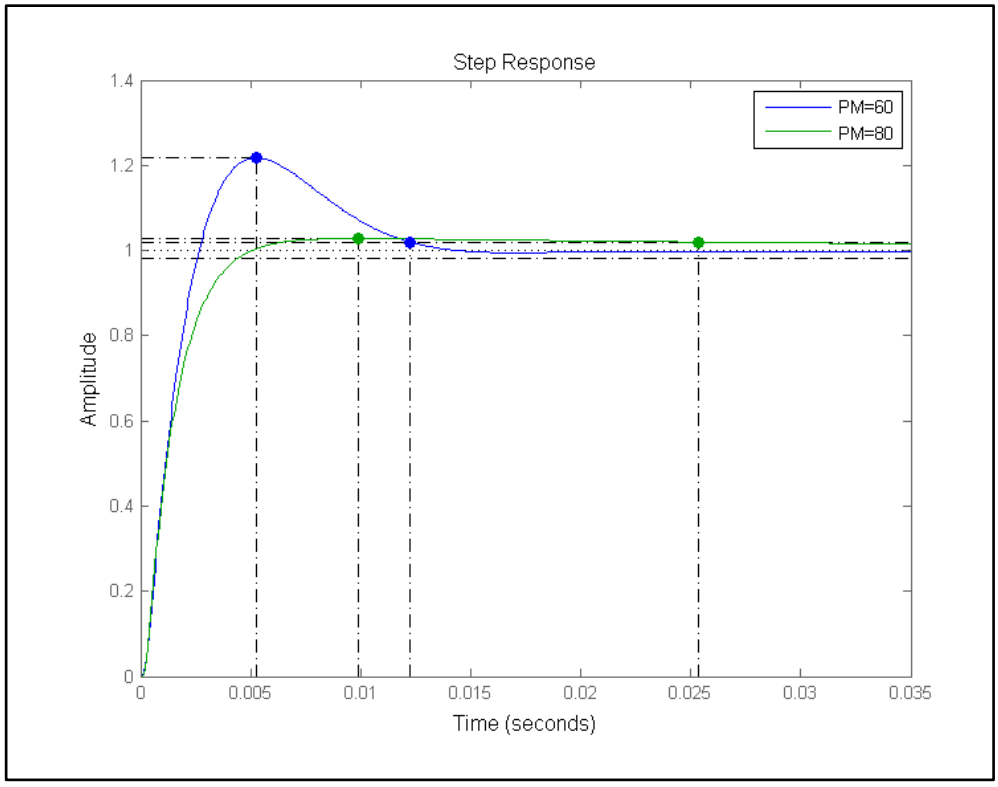

Fig. 5.37 Step response of outer closed loop for 60º and 70º phase margin

margin of 60º leads to an overshoot of 21.8% which is very high for our application, since overshoots in the battery pack voltage can be dangerous and should be avoided. However, phase margin of 80º leads to only 2.8% overshoot which is acceptable. Settling times are 12.2 ms and 25 ms for 60º and 80º respectively. Since 80º of phase margin leads to better results it is used. Simulation results for voltage controller are shown in Fig. 5.38. Simulation starts with SoC of 75% leading to battery voltage of 383.94 V. At t = 1 sec the reference voltage is set to 385 V. After the battery voltage reaches the desired value, as can be seen in the second row, the controller reduces the battery current to keep the voltage equal to 385 V. Third row shows the phase shift angle that controller applies to the DAB.

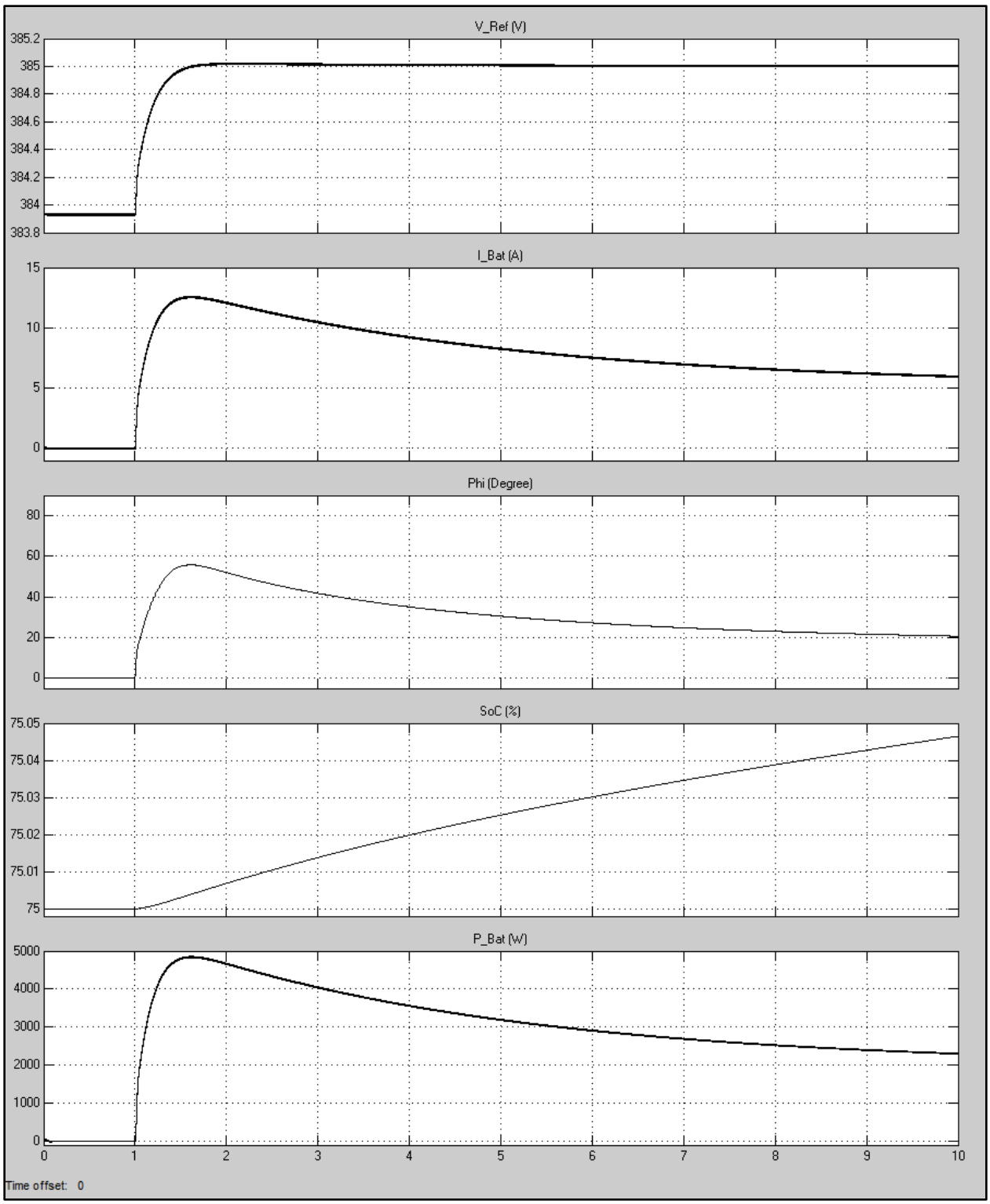

Fig. 5.38 Simulation results for voltage controller of DAB

5.5 Summary

In this chapter models of all stages of the system were introduced. PV stage was modeled as a constant power source in Matlab/Simulink which can be varied using a set point. Some tests were done to verify the operation of the proposed model. Rectifier / Inverter stage or Voltage Source Converter (VSC) was modeled mathematically and the required transfer functions for controller design purposes were obtained. Hysteresis Current Control (HCC) approach was utilized for designing the controller. Bode plots, root locus and step functions of open-loop and closed-loop systems were graphed. Some tests were applied to verify the validity of the approach and designed controller.

Simplified circuit model of DAB was firstly obtained through some assumptions. Steady state operation of DAB was described thoroughly. Afterwards, state space average model of ADB was obtained. This model was shown to be non-linear. Hence, small-signal linear model of DAB was obtained according to small-signal perturbation. Small-signal transfer functions were obtained using small-signal linear model. They mainly include control to output, control to state, source to output and source to state transfer functions. DAB is a more complicated case compared to simple buck or boost converters, since; the duty ratio of the switches cannot be controlled independently and is dependent on states and inputs. Required theoretical background for such cases was mentioned and utilized to achieve accurate results. All the four small-signal transfer functions together completely describe the behavior of DAB. Small-signal representation of the regulated DAB suggests the design procedure of cascaded inner current loop and outer voltage loop.

For designing the parameters of DAB a systematic set of equations were introduced to calculate different parameters of the circuit such as inductor average current, inductor RMS current, load average current, load RMS current and etc. Graphs were used to show the impact of different parameters such as phase shift angle, frequency and output resistance on inductor RMS current which is important in designing the transformer. Effects of battery SoC were investigated on transformer current waveform which will finally affect RMS and average transformer current. Required equations for designing the capacitor were derived. Finally, inner current loop and outer voltage loop controllers were designed using SISO design tool of Matlab/Simulink based on different frequency domain requirements. The results were compared in time domain and more satisfactory ones were selected as controllers. Bode plots, root locus diagram and step functions were analyzed to achieve the expected results.

Finally, some appropriate tests were conducted using Matlab/Simulink to verify the validity of the results and approve the functionality and performance of the design. Simulations showed satisfactory results.

CHAPTER.6

SIMULATION RESULTS

When the control loops are closed the system can be operated under different situations and the overall performance can be analyzed. Different modes of operation as were defined in Fig. 4.11 are tested and simulated in this chapter. One mode which has not been defined in Fig. 4.11 can happen when the power is being generated only by the PV stage and absorbed only by the battery pack. If the PV stage is working under maximum power point tracking mode, then the power absorbed by the battery pack should be exactly equal to P_{max} generated by PV stage. Otherwise, the voltage of DC link will begin to increase/decrease if the absorbed battery pack power is less/more than PV stage maximum power because of energy increase/decrease in the DC link capacitor. This situation can lead to instability or malfunction of the system and should be avoided. For example, if the DC link capacitor voltage begins to increase, this can explode the capacitor. Conversely, decrease of DC link capacitor voltage will cause the charger stage not to be able to reach the desired reference current or voltage value at the output. So this situation is not useful to be considered and not defined as a mode of operation. The only way to avoid this situation is to operate the PV stage under voltage controlled mode which will not let the system to use the full capacity of the solar power available at PV panels; hence, the overall efficiency of the system decreases a lot and this is not acceptable.

6.1 Mode 1

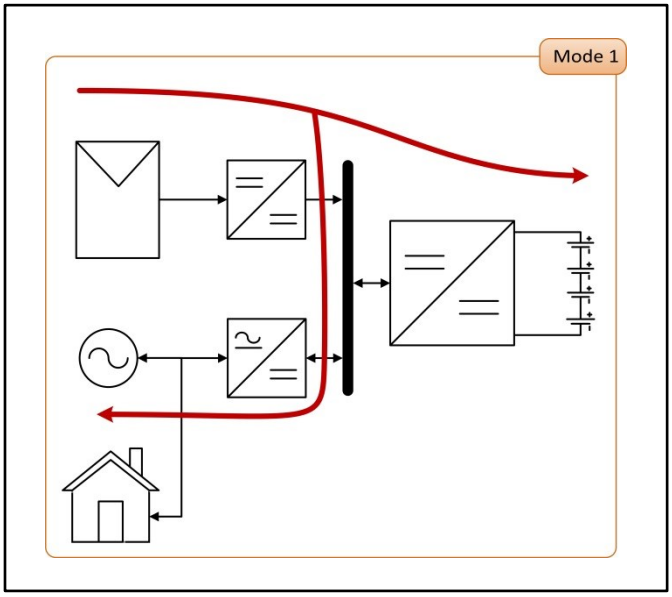

Fig. 6.1 Mode 1 of operation

As shown in Fig. 6.1 in this mode of operation PV generated power is more than power absorbed by the battery so the difference is injected to the grid. Simulation results is shown in Fig. 6.2. Since the rectifier/inverter stage acts as a Voltage Source Converter (VSC) it is named as VSC in Fig. 6.2. Absorbed power by battery ($P_{Battery}$), produced power by VSC (P_{VSC}) and produced power by PV (P_{PV}) are shown in black, magenta and green, respectively. As shown in the third row, P_{PV} is changed at different times. Besides, battery reference charging current is also changed each two seconds, hence changing the $P_{Battery}$. As can be seen in the power section, VSC changes the produced power (since it is negative it means absorbed power) to keep the DC link voltage constant and equal to 400 V. Variations of the control parameter for VSC (I_P) and the control parameter for DAB (Phi) are graphed. As the last row shows the variations of DC link voltage during transients, the VSC controller is performing pretty good keeping the voltage in the range of ±5% of 400 V.

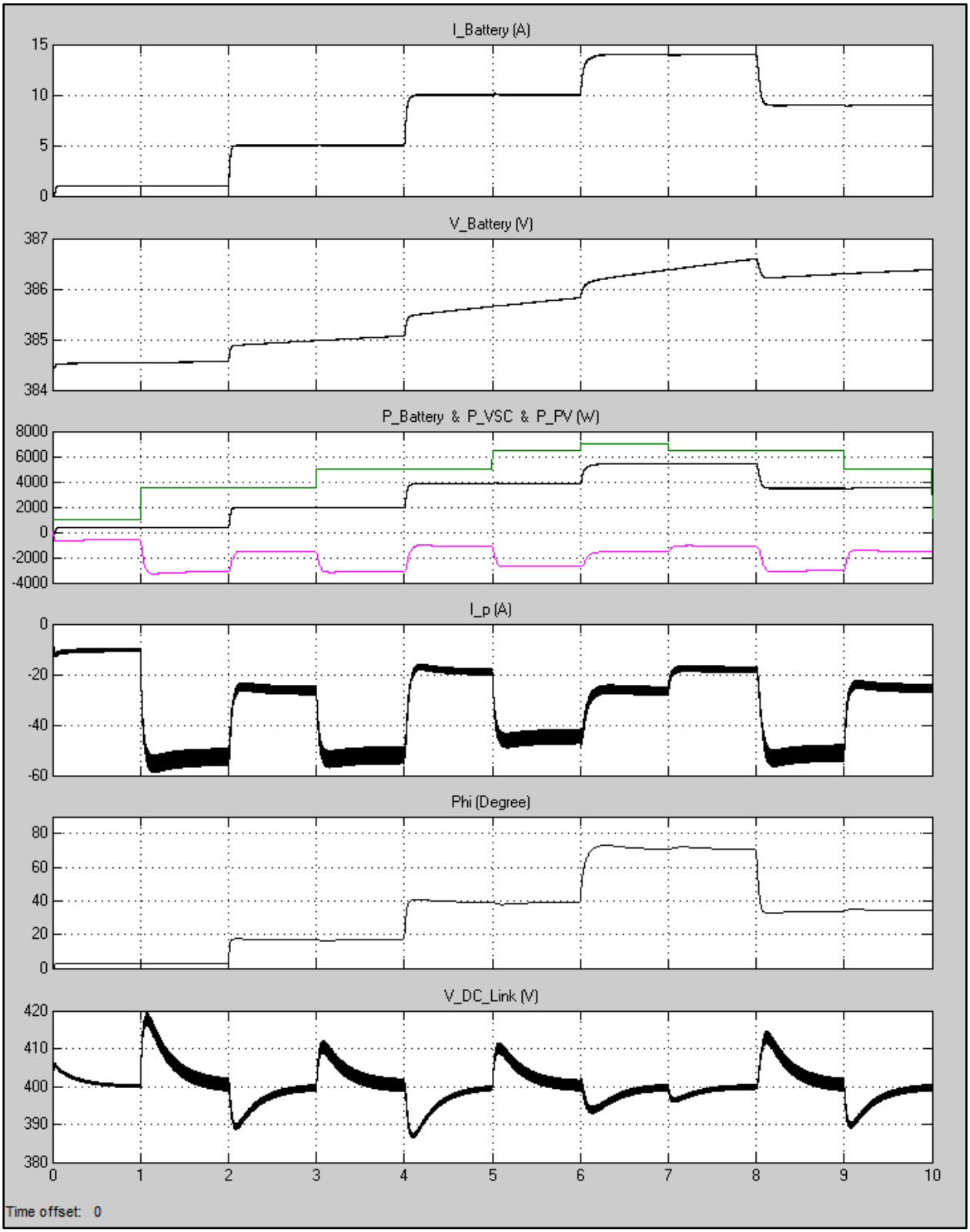

Fig. 6.2 Simulation results for Mode 1

6.2 Mode 2

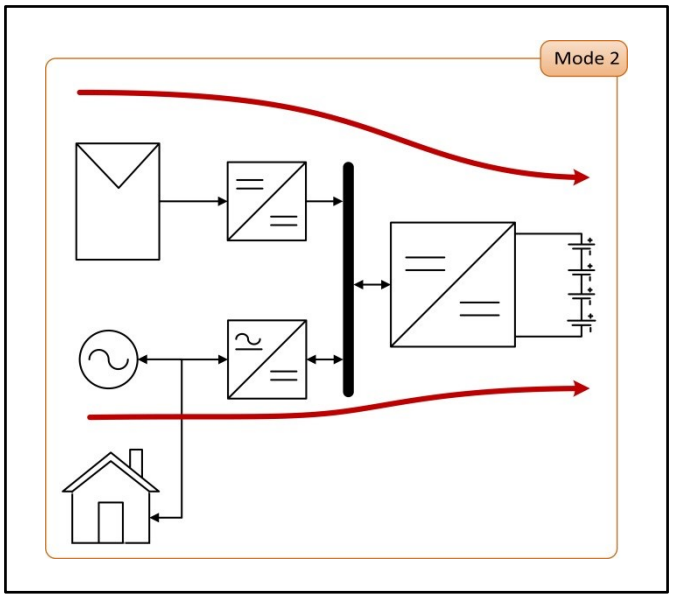

Fig. 6.3 Mode 2 of operation

When the PV power is not enough for charging the battery pack, grid will inject power to the DC link as shown in Fig. 6.3. This mode is simulated and the results are graphed in Fig. 6.4. As previous case absorbed power by battery ($P_{Battery}$), produced power by VSC (P_{VSC}) and produced power by PV (P_{PV}) are shown in black, magenta and green, respectively. As the PV power steps at different times, VSC changes its injected power to supply the remaining required power by the battery. So the summation of P_{PV} and P_{VSC} will be equal to $P_{Battery}$. Battery reference current changes each two seconds to change the absorbed battery power and test the performance of controllers. Variations of DC link voltage are shown in last row which shows the VSC controller is performing quite well keeping the voltage in the range of ±5%. DC link voltage increases every time that P_{PV} increases and decreases every time that P_{PV} decreases or battery current increases.

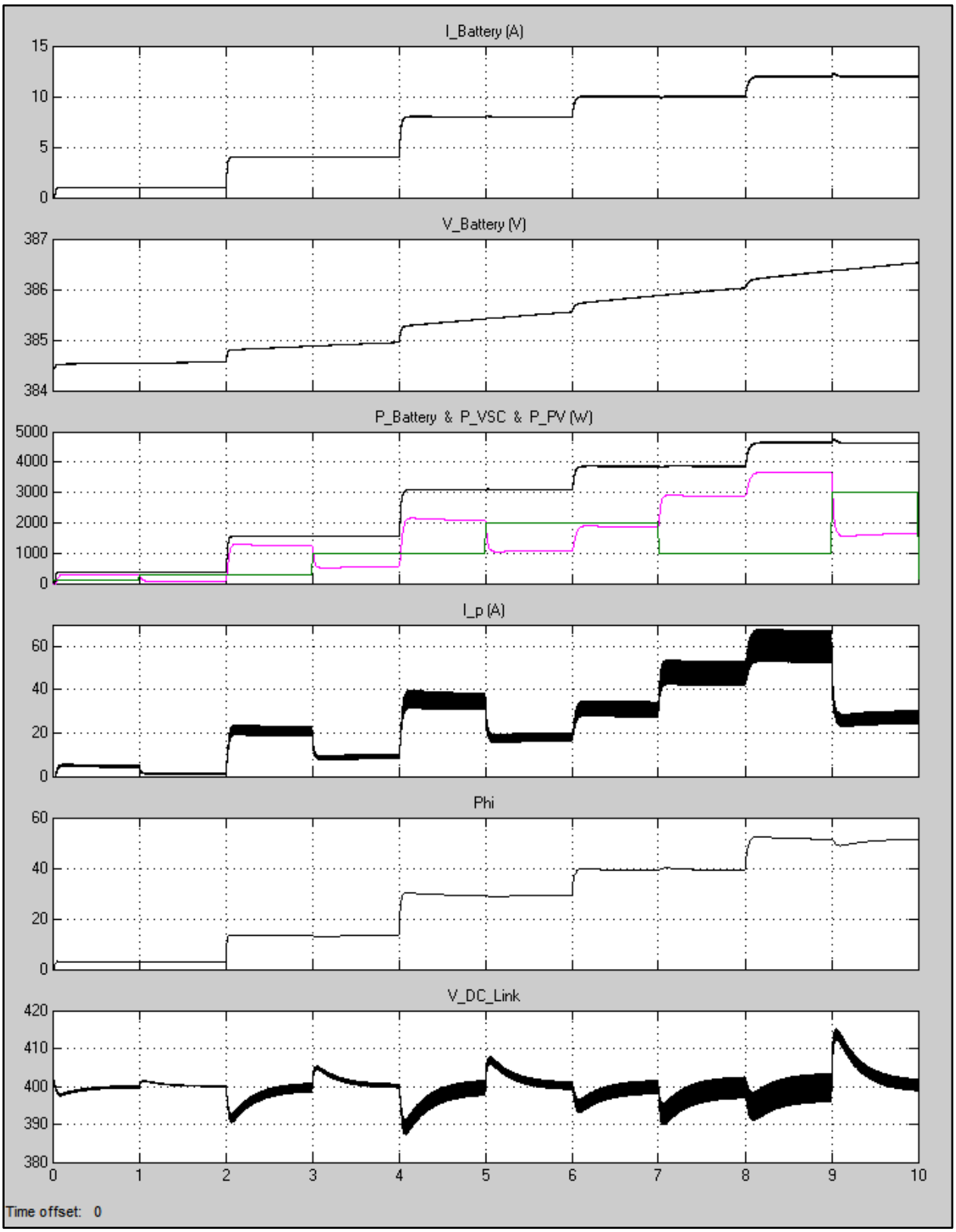

Fig. 6.4 Simulation results for Mode 2

6.3 Mode 3

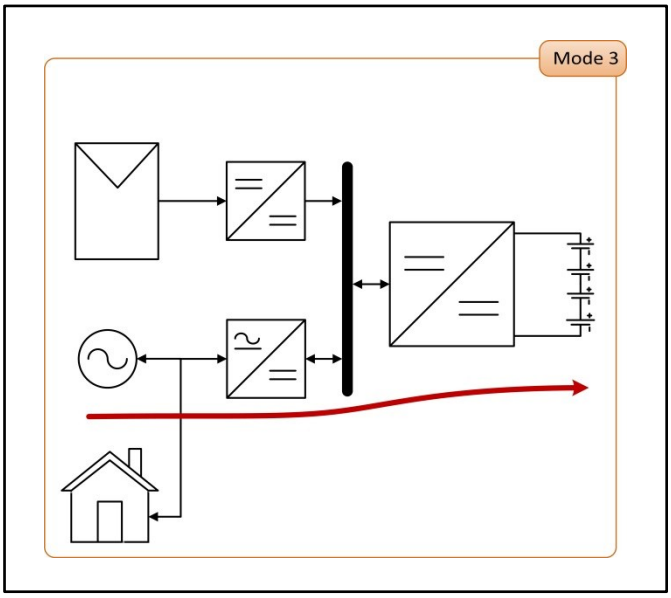

Fig. 6.5 Mode 3 of operation

When no power is available from PV panels, e.g. during the night, all the required power should be supplied from the grid. This happens in mode 3 as depicted in Fig. 6.5. Simulation results for different reference currents are shown in Fig. 6.6. As can be seen in the third row, VSC power completely follows battery power and almost coincides it. Battery current is changed each second to change the absorbed battery power. This is achieved through the current controller by means of controlling the phase shift angle. The current steps are fairly high and actually are large signal disturbances, not small signal. Nevertheless, both the controllers perform very well. DC link voltage is always kept in 5% tolerance range which is pretty good.

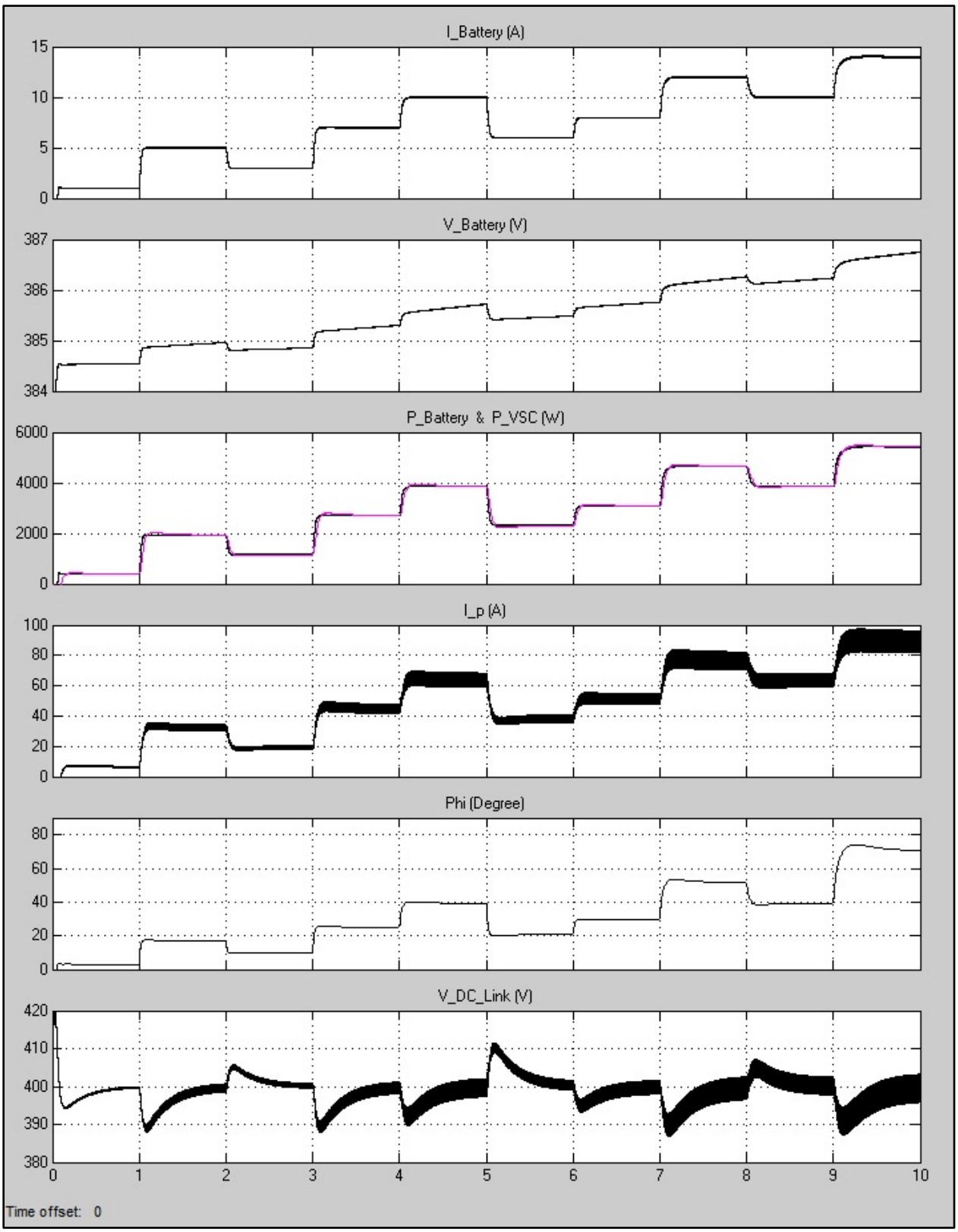

Fig. 6.6 Simulation results for Mode 3

6.4 Mode 4

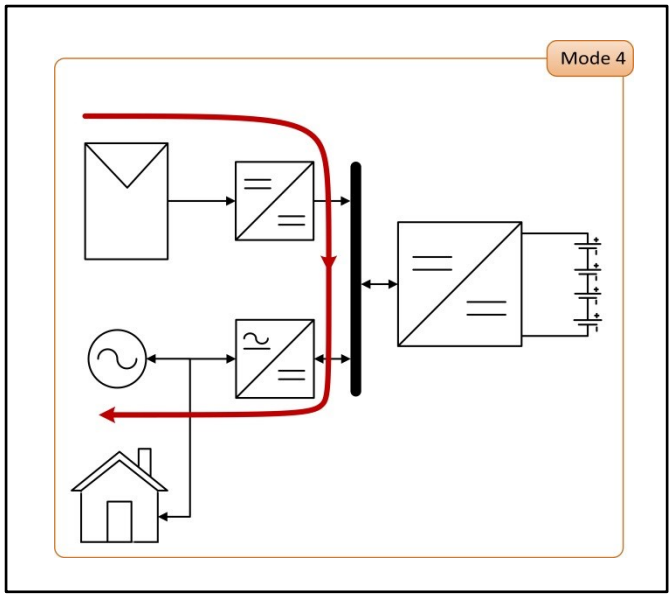

Fig. 6.7 Mode 4 of operation

If the battery pack is not connected to the system or when the battery is fully charged and also power is available from PV stage, this power can be injected to the grid through DC link to reduce electricity cost. This is defined as mode 4 as shown in Fig. 6.7 and the results of simulations are plotted in Fig. 6.8. Produce PV power is shown in first row and produced power by VSC (since it is negative it means absorbed power) is graphed in second row. VSC power follows PV power to keep the DC link voltage constant and equal to 400 V. During transients DC link voltage increases when PV power steps up and decreases when PV power steps down. This is due to temporary increase or decrease in DC link capacitor energy.

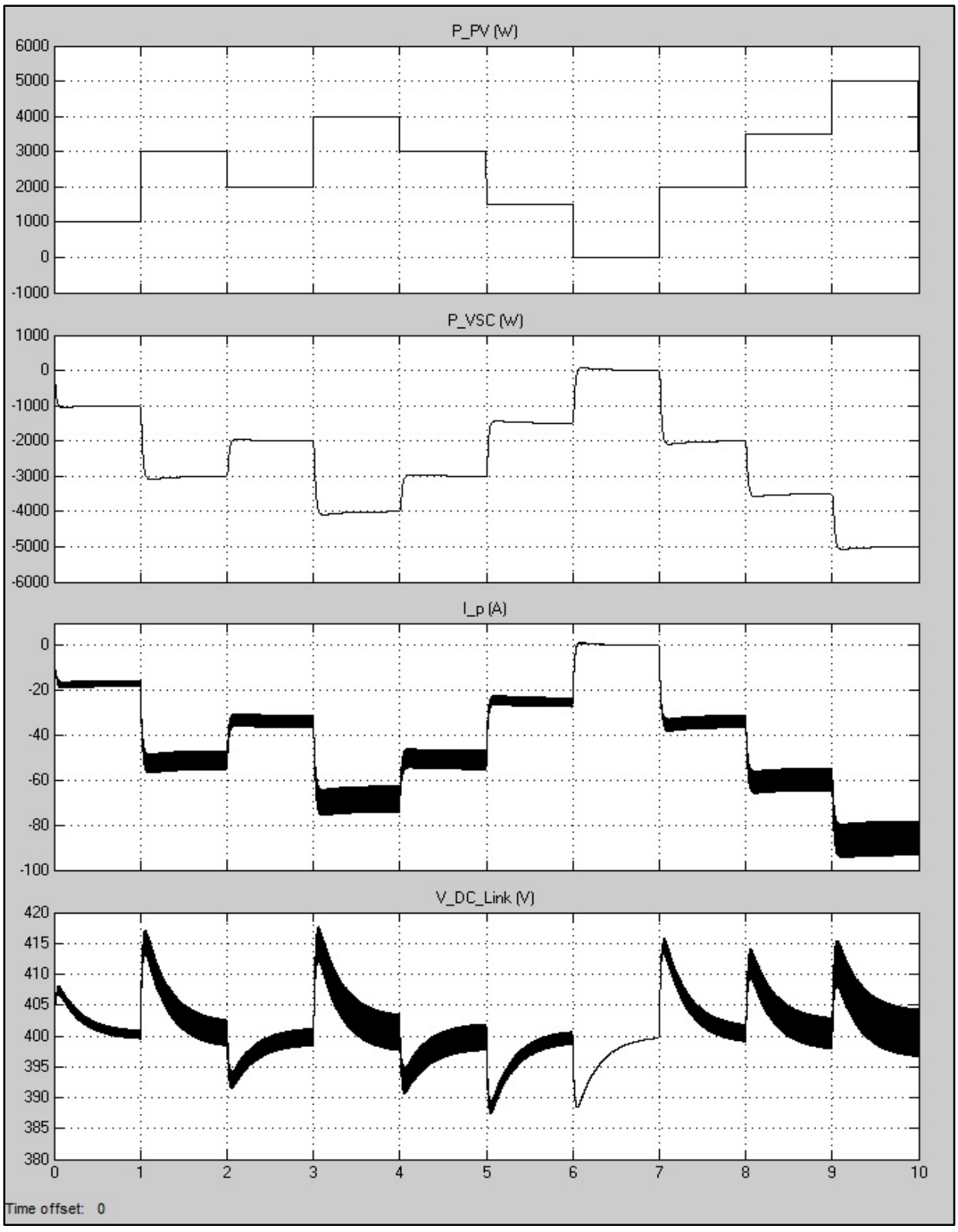

Fig. 6.8 Simulation results for Mode 4

6.5 Mode 5

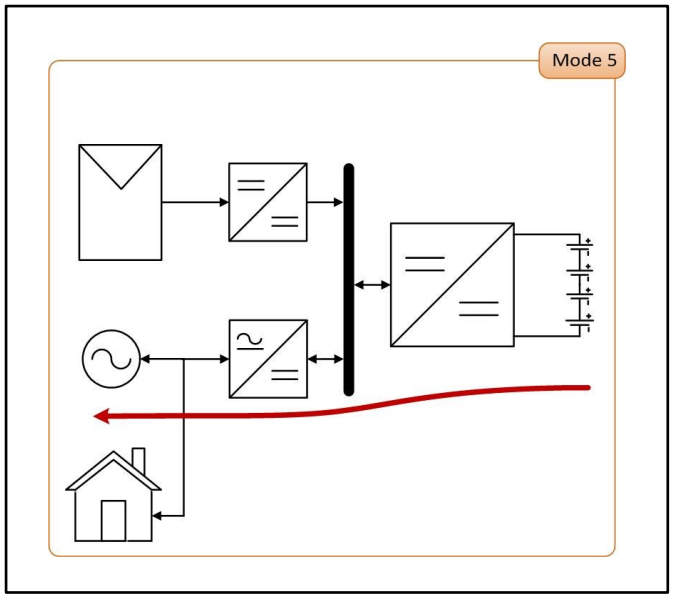

Fig. 6.9 Mode 5 of operation

Smart grid concepts such as Vehicle to Grid (V2G) involve injection of power from the battery pack to the grid to shift the load profile as shown in Fig. 6.9. Simulation results for different reference currents are illustrated in Fig. 6.10. The battery pack current is negative which shows injection of power to the DC link. This is achieved through negative phase shift which is controlled with the controller to follow the reference current. As the third row depicts the SoC of the battery pack is reducing which shows discharge process of the battery pack. Variations of DC link voltage are graphed in the last row illustrating the good performance of the hysteresis current controller of VSC.

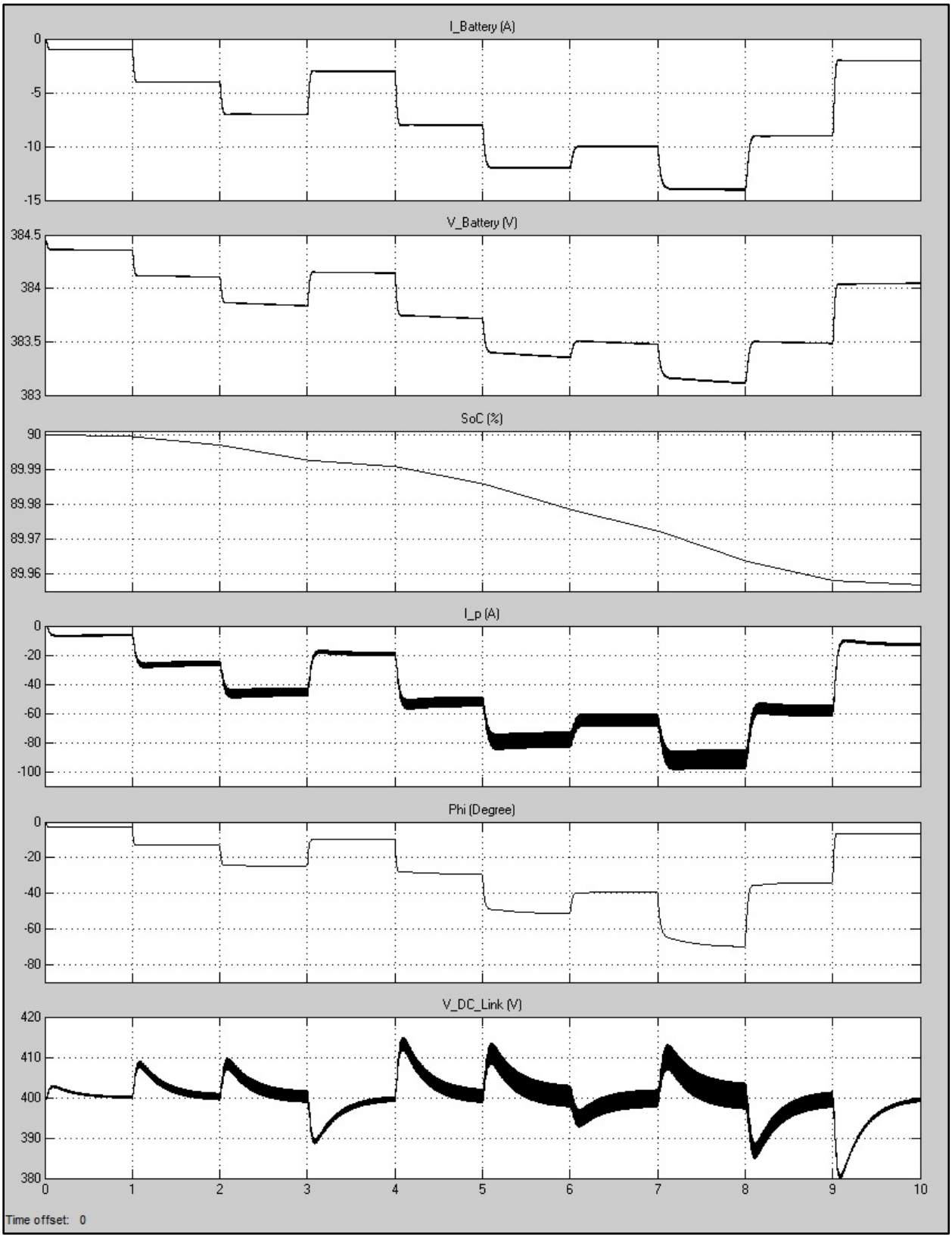

Fig. 6.10 Simulation results for Mode 5

6.6 Mode 6

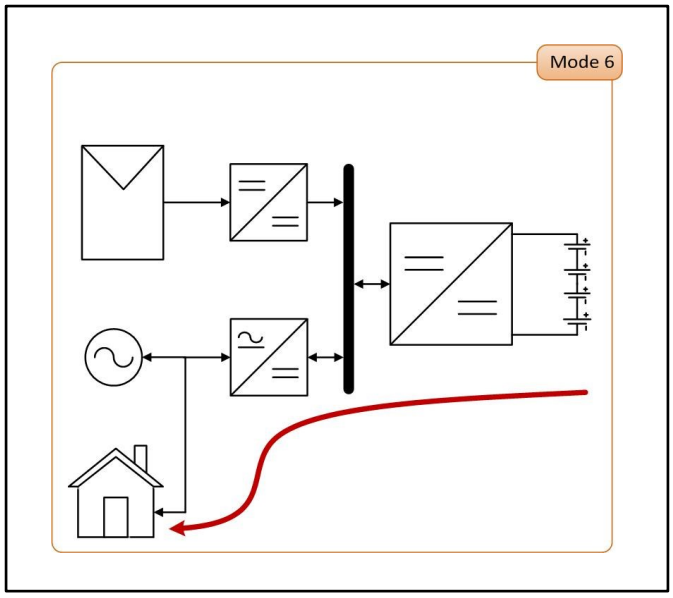

Fig. 6.11 Mode 1 of operation

The last mode of operation which is mode 6 is useful during power grid blackouts. In this mode, battery pack of the electric vehicle can supply power to the house for some time depending on the capacity and SoC of the battery pack. In fact in this mode, the system acts as an Uninterruptable Power Supply (UPS). Considering controller structure, this mode of operation is different from other modes. In previous modes, the AC side of the rectifier / inverter stage was an ideal AC source, hence the voltage was constant value constant frequency and there was no need to control the voltage. So the rectifier / inverter stage was performing under current control mode. However, since the grid is not connected to the system in mode 6, the rectifier / inverter stage should act as a regulated sinusoidal wave voltage source. This can be achieved with controllers and Sinusoidal Pulse Width Modulation (SPWM) switching scheme if the DC side of rectifier / inverter stage is a regulated constant DC source. So the role of DAB stage also changes. In previous modes, the battery pack side (right side) of DAB was considered as the

output and the battery pack voltage and current were to be controlled. However, in mode 6, the DC link is considered as the output side (load) and the battery pack as the input side (source) of DAB. The goal of the controllers of DAB will be to keep the DC link voltage constant. So in mode 6, DAB acts as a voltage source converter (VSC) instead of rectifier / inverter stage. Designing for this mode requires completely different models and transfer functions and new controllers should be designed which have not been considered here for the sake of briefness. Nevertheless, the procedure of controller designing will be the same as was described in long as the required transfer functions are provided.

CHAPTER.7

CONCLUSIONS AND POTENTIAL FUTURE WORK

7.1 Conclusions

Since large-scale industrialization began around 150 years ago, levels of several important greenhouse gasses have increased by about 40%. This has caused the Earth temperature rise over the past century leading to noticeable climate change evidences such as ice mass loss and decreasing snow cover in both the northern and southern hemispheres, rising sea levels, more frequent extreme weather events, floods, more sever tropical storms and hurricanes, volcanoes, acidification of oceans and much more. All of these have caused the attraction towards renewable energies in sectors such as transportation and introduction of EVs/HEVs/PHEVs. Charging these vehicles should be done using renewable energies, otherwise, the green has gasses will be only transferred from streets to fossil fuel power plants. In this work a solar powered grid tied battery pack charger was designed and many issues related to battery features, power electronics interface; modeling and control of the system were studied and analysed.

In chapter 2 characteristics of commonly used batteries in vehicular applications were studied. Various charging schemes were mentioned. Several termination methods were reviewed. Cell balancing which is a very important issue in extending the life time of battery packs was described and its effects were investigated. Different cell balancing techniques were studied. Importance of SoC estimation in the performance of battery charger was mentioned and different SoC estimation techniques were investigated. Various types of battery models such as

electrochemical models, stochastic models, analytical models, electrical circuit models, thermal models and etc. were comprehensively studied in this chapter and finally according to battery charging application and the required accuracy a simplified battery model was utilized which showed acceptable accuracy.

In chapter 3 various MPPT techniques and their applications were studied. Pros and cons of each method were mentioned. A new PV model suitable for Simulink was proposed to avoid algebraic loop problem. A novel MPPT technique was proposed for battery charging applications. This method mainly finds the maximum power point of the PV panel by increasing the current reference of the power converter until the operating point which is unable to be tracked by the converter. This point leads to saturation in the controller which will be used as a set point indicating the maximum power point. The main advantage of this method is its independency from the power converter topology. Finally, appropriate tests were conducted and simulation results verified the validity of the proposed technique.

In chapter 4 conventional structures of PV systems, their applications and pros and cons were reviewed. The phenomenon of local maximum power points and their reasons were introduced. A configuration was proposed which makes it possible to inject all the available power from PV panels to the battery pack and drain just the remaining required power from the grid. Advantages of this configuration were outlined, one of which is providing the power flow in all possible directions and supporting modes such Vehicle to Grid (V2G) which can be used in smart grid applications. The most useful six modes of operations were shown graphically. Finally, suitable power converter topologies were chosen for each part of the system.

In chapter 5 models of all stages of the system were introduced. PV stage was modeled as a constant power source in Matlab/Simulink which can be varied using a set point. Some tests were done to verify the operation of the proposed model. Rectifier / Inverter stage or Voltage Source Converter (VSC) was modeled mathematically and the required transfer functions for controller design purposes were obtained. Hysteresis Current Control (HCC) approach was utilized for designing the controller. Bode plots, root locus and step functions of open-loop and closed-loop systems were graphed. Some tests were applied to verify the validity of the approach and designed controller. Simplified circuit model of DAB was firstly obtained through some assumptions. Steady state operation of DAB was described thoroughly. Afterwards, state space average model of ADB was obtained. This model was shown to be non-linear. Hence, small-signal linear model of DAB was obtained according to small-signal perturbation. Small-signal transfer functions were obtained using small-signal linear model. They mainly include control to output, control to state, source to output and source to state transfer functions. DAB is a more complicated case compared to simple buck or boost converters, since; the duty ratio of the switches cannot be controlled independently and is dependent on states and inputs. Required theoretical background for such cases was mentioned and utilized to achieve accurate results. All the four small-signal transfer functions together completely describe the behavior of DAB. Small-signal representation of the regulated DAB suggests the design procedure of cascaded inner current loop and outer voltage loop. For designing the parameters of DAB a systematic set of equations were introduced to calculate different parameters of the circuit such as inductor average current, inductor RMS current, load average current, load RMS current and etc. Graphs were used to show the impact of different parameters such as phase shift angle, frequency and output resistance on inductor RMS current which is important in designing the transformer.

Effects of battery SoC were investigated on transformer current waveform which will finally affect RMS and average transformer current. Required equations for designing the capacitor were derived. Finally, inner current loop and outer voltage loop controllers were designed using SISO design tool of Matlab/Simulink based on different frequency domain requirements. The results were compared in time domain and more satisfactory ones were selected as controllers. Bode plots, root locus diagram and step functions were analyzed to achieve the expected results. Finally, some appropriate tests were conducted using Matlab/Simulink to verify the validity of the results and approve the functionality and performance of the design. Simulations showed satisfactory results.

In chapter 6 all modes of operation were tested using appropriate scenarios in Matlab/Simulink and the results were graphed accordingly. Different parameters were varied with a high percentage leading to large disturbance to the system, nevertheless, the overall system remained stable and within acceptable ranges during the tests. The performance of designed system along with controllers was verified in this chapter.

7.2 Potential Future Work

In this work, for simplicity some assumptions were made, which are usually used in analysis of power converters. Because of the complexity and high number of parts of the system, the components of the converters were assumed to be ideal. For example, all the switches and filter capacitors were considered ideal with no losses and zero turn-on or turn-off time. Considering the parasitic elements such as resistors, inductors, capacitors and ESR may increase the order of the system and will change the system model and finally will change transfer

functions. Derivation of transfer functions will be more difficult since the order of the system will increase. Another important component is transformer, which was modeled as a single inductor. More accurate models of transformer will also lead to more accurate results, however; will highly increase the complexity of the system.

Another assumption was operation of the system under Continuous Conduction Mode (CCM). This can be not valid under some circumstances such as light loads. In these situations power converters may work under Discontinuous Conduction Mode (DCM), which will add to the possible number of configurations. For example, for a simple single switch boost converter, working under CCM will lead to only two possible different configurations; however, DCM will add one more possible configuration to the system introducing a new time interval which will change the state space averaged model. For DAB converter this will be more complicated. Analyzing DAB working under DCM can be considered as future work.

Another potential work can be considered as analysing other switching and control schemes. Only turn-on time constant frequency scheme was considered here for DAB. Other schemes, such as variable frequency control, turn-off time control operating at DCM, and turn-off time control at intermittent mode can be considered and analysed.

REFERENCES

[1] IEEE spectrum, Software Fix Extends Failing Batteries in 2006-2008 Honda Civic Hybrids: Is Cost Acceptable? http://spectrum.ieee.org/riskfactor/green-tech/advanced-cars/software-fix-extends-failing-batteries-in-20062008-honda-civic-hybrids-is-cost-acceptable. Accessed 23 August 2011

[2] Crompton TR (2000) Battery reference book, 3rd Edition, Newnes

[3] Buchmann I (2001) Batteries in a portable world: a handbook on rechargeable batteries for non-engineers, 2nd edn, Cadex Electronics Inc

[4] Chen LR (2008) Design of duty-varied voltage pulse charger for improving li-ion battery-charging response, IEEE Trans. on Industrial Electronics, vol. 56, no. 2, pp. 480-487

[5] Park SY, Miwa H, Clark BT, Ditzler D, Malone G, D'souza N S, Lai J S (2008) A universal battery charging algorithm for Ni-Cd, Ni-MH, SLA, and Li-Ion for wide range voltage in portable applications, in Proc. IEEE Power Electronics Specialists Conf., Rhodes, Greece, pp. 4689-4694.

[6] Hua CC, Lin M. Y (2000) A study of charging control of lead acid battery for electric vehicles, in *Proc. IEEE International Symp. on Industrial Electronics*, vol. 1, pp. 135-140.

[7] West S, Krein PT (2000) Equalization of valve-regulated lead acid batteries: issues and life tests, in *Proc. IEEE International Telecommunications Energy Conf*., pp. 439-446.

[8] Brost RD (1998) Performance of valve-regulated lead acid batteries in EV1 extended series strings, in *Proc. IEEE Battery Conf. on Applications and Advances*, Long Beach, CA, pp. 25-29.

[9] Bentley WF (1997) Cell balancing considerations for lithium-ion battery systems, in *Proc. IEEE Battery Conf. on Applications and Advances*, Long Beach, CA, pp. 223-226.

[10] Krein PT, Balog RS (2002) Life extension through charge equalization of lead-acid batteries, in *Proc. IEEE International Telecommunications Energy Conf*., pp. 516-523.

[11] Lohner A, Karden E, DeDoncker RW (1997) Charge equalizing and lifetime increasing with a new charging method for VRLA batteries, in *Proc. IEEE International Telecommunications Energy Conf*., pp. 407-411.

[12] Moore SW, Schneider PJ (2001) A review of cell equalization methods for lithium ion and lithium polymer battery systems, in *Proc. SAE 2001 World Congress*, Detroit, MI.

[13] Nishijima K, Sakamoto H, Harada K (2000) A PWM controlled simple and high performance battery balancing system, in *Proc. IEEE 31st Annual Power Electronics Specialists Conference*, vol. 1, Galway, Ireland, pp. 517-520.

[14] Isaacson MJ, Hoolandsworth RP, Giampaoli PJ (2000) Advanced lithium ion battery charger, in *Proc. IEEE Battery Conf. on Applications and Advances*, pp. 193-198.

[15] Pascual C, Krein PT (1997) Switched capacitor system for automatic series battery equalization," in *Proc. 12th Annual Applied Power Electronics Conf. and Expo.*, Atlanta, GA, vol. 2, pp. 848-854.

[16] Hung ST, Hopkins DC, Mosling CR (1993) Extension of battery life via charge equalization control, *IEEE Trans. On Industrial Electronics*, vol. 40, no. 1, pp. 96-104.

[17] Cao J, Schofield N, Emadi A (2008) Battery balancing methods: a comprehensive review, in *Proc. IEEE Vehicle Power and Propulsion Conf.*, Harbin, China, pp. 1-6.

[18] Lee YS, Wang WY, Kuo TY (2008) Soft computing for battery state-of-charge (BSOC) estimation in battery string systems, *IEEE Trans. on Industrial Electronics*, vol. 55, no. 1, pp. 229-239.

[19] Shen WX, Chan CC, Lo EWC, Chau KT (2002) Adaptive neuro-fuzzy modeling of battery residual capacity for electric vehicles, *IEEE Trans. on Industrial Electronics*, vol. 49, no. 3, pp. 677-684.

[20] Piller S, Perrin M, Jossen A (2001) Methods for state-of-charge determination and their applications, *Journal of Power Sources*, vol. 96, no. 1, pp. 113-120.

[21] Ullah Z, Burford B, Dillip S (1996) Fast intelligent battery charging: neural-fuzzy approach, *IEEE Aerospace and Electronics Systems Magazine*, vol. 11, no. 6, pp. 26-34.

[22] Atlung S, Zachau-Christiansen B (1994) Failure mode of the negative plate in recombinant lead/acid batteries, *Journal of Power Sources*, vol. 52, no. 2, pp. 201-209.

[23] Feder DO, Jones WEM (1996) Gas evolution, dryout, and lifetime of VRLA cells an attempt to clarify fifteen years of confusion and misunderstanding, in *Proc. IEEE International Telecommunications Energy Conf.*, pp. 184-192.

[24] Jones WEM, Feder DO (1996) Behavior of VRLA cells on long term float. II. The effects of temperature, voltage and catalysis on gas evolution and consequent water loss, in *Proc. IEEE International Telecommunications Energy Conf.*, pp. 358–366.

[25] Nelson RF, Sexton ED, Olson JB, Keyser M, Pesaran A (2000) Search for an optimized cyclic charging algorithm for valve-regulated lead–acid batteries," *Journal of Power Sources*, vol. 88, no. 1, pp. 44-52.

[26] Sung Park; Andreas Savvides; Mani B. Srivastava; , "Battery capacity measurement and analysis using lithium coin cell battery," International symposium on Low power electronics and design, 2001. ISLPED 01. Proceedings. August 2001

[27] James F. Manwell; Jon G. McGowan; , "Lead acid battery storage model for hybrid energy systems," Elsevier Journal of Solar Energy, vol.50, Issue 5, pp.399-405, May 1993

[28] Rakhmatov, D.; Vrudhula, S.; Wallach, D.A., "A model for battery lifetime analysis for organizing applications on a pocket computer," Very Large Scale Integration (VLSI) Systems, IEEE Transactions on , vol.11, no.6, pp. 1019- 1030, Dec. 2003..

[29] Jongerden, M.R.; Haverkort, B.R.; , "Which battery model to use?," Software, IET , vol.3, no.6, pp.445-457, December 2009

[30] Min Chen; Rincon-Mora, G.A.; , "Accurate electrical battery model capable of predicting runtime and I-V performance," Energy Conversion, IEEE Transactions on , vol.21, no.2, pp. 504- 511, June 2006

[31] “Basics of Electrochemical Impedance Spectroscopy”, Application note, 2007, Gamry Instruments (www.gamry.com).

[32] Ramamurthy, A.; Notani, S.; Bhattacharya, S., "Advanced lithium ion battery modeling and power stage integration technique," *Energy Conversion Congress and Exposition (ECCE), 2010 IEEE* , vol., no., pp.1485-1492, 12-16 Sept. 2010

[33] E. Barsoukov, J. H. Kim, C. O. Yoon, and H. Lee, “Universal battery parameterization to yield a nonlinear equivalent circuit valid for battery simulation at arbitrary load,” J. Power Sources, vol. 83, no. 1–2, pp. 61–70, 1999.

[34] Jaemoon Lee; Jaeho Lee; Onyong Nam; Jonghun Kim; Bo Hyung Cho; Han-Seok Yun; Soo-Seok Choi; Kiho Kim; Kim, J.H.; Sonu Jun; , "Modeling and Real Time Estimation of Lumped Equivalent Circuit Model of a Lithium Ion Battery," *Power Electronics and Motion Control Conference, 2006. EPE-PEMC 2006. 12th International* , vol., no., pp.1536-1540, Aug. 30 2006-Sept. 1 2006

[35] Xuezhe Wei, Bing Zhu, Wei Xu, "Internal Resistance Identification in Vehicle Power Lithium-Ion Battery and Application in Lifetime Evaluation," icmtma, vol. 3, pp.388-392, 2009 International Conference on Measuring Technology and Mechatronics Automation, 2009

[36] Low Wen Yao; Aziz, J.A.; , "Modeling of Lithium Ion battery with nonlinear transfer resistance," *Applied Power Electronics Colloquium (IAPEC), 2011 IEEE* , vol., no., pp.104-109, 18-19 April 2011

[37] Shafiei, A.; Williamson, S.S.; , "Plug-in hybrid electric vehicle charging: Current issues and future challenges," *Vehicle Power and Propulsion Conference (VPPC), 2010 IEEE* , vol., no., pp.1-8, 1-3 Sept. 2010

[38] A. Pesaran and V. Johnson, "Battery Thermal Models for Hybrid Vehicle Simulations," J. Power Sources, vol. 110, pp. 377-382, 2002.

[39] Bharathan, D.; Pesaran, A.; Vlahinos, A.; Kim, G.-H.; , "Improving battery design with electro-thermal modeling," *Vehicle Power and Propulsion, 2005 IEEE Conference* , vol., no., pp. 8 pp., 7-9 Sept. 2005

[40] Hu, X.; Lin, S.; Stanton, S.; Lian, W.; , "A Foster Network Thermal model for HEV/EV Battery Modeling," *Industry Applications, IEEE Transactions on* , vol.PP, no.99, pp.1, 0

[41] V.H. Johnson; , "Battery performance models in ADVISOR", Elsevier Journal of Power Sources, vol.110, Issue 2, pp.321-329, 22 August 2002

[42] Lahiri, K.; Raghunathan, A.; Dey, S.; Panigrahi, D.; , "Battery-driven system design: a new frontier in low power design ," Design Automation Conference, 2002. Proceedings of ASP-DAC 2002. 7th Asia and South Pacific and the 15th International Conference on VLSI Design. Proceedings. , vol., no., pp.261-267, 2002

[43] Knauff, M.; Dafis, C.; Niebur, D.; , "A new battery model for use with an extended Kalman filter state of charge estimator," American Control Conference (ACC), 2010 , vol., no., pp.1991-1996, June 30 2010-July 2 2010

[44] B. O. Anderson and J. B. Moore, *Optimal Filtering*. Englewood Cliffs, NJ: Prentice-Hall, 1979.

[45] Hanlei Zhang; Mo-Yuen Chow; , "Comprehensive dynamic battery modeling for PHEV applications," Power and Energy Society General Meeting, 2010 IEEE , vol., no., pp.1-6, 25-29 July 2010

[46] Kumar, P.; Bauer, P.; , "Parameter extraction of battery models using multiobjective optimization genetic algorithms," Power Electronics and Motion Control Conference (EPE/PEMC), 2010 14th International , vol., no., pp.T9-106-T9-110, 6-8 Sept. 2010

[47] W. Banzhaf, P. Nordin, R. Keller, and F. Francone, Genetic Programming, an Introduction. San Francisco, CA: Morgan Kaufmann Publishers, 1998.

[48] D. E. Goldberg, Genetic Algorithms in Search, Optimization, and Machine Learning. Reading, MA: Addison-Wesley, l989.

[49] Tremblay, O., Dessaint, L.-A. "Experimental Validation of a Battery Dynamic Model for EV Applications." World Electric Vehicle Journal. Vol. 3 - ISSN 2032-6653 - © 2009 AVERE, EVS24 Stavanger, Norway, May 13 - 16, 2009.

[50] H. Abea, T. Muraia and K. Zaghibb (1999). Vapor-grown carbon fiber anode for cylindrical lithium ion rechargeable batteries. Journal of Power Sources 77:2, February 1999, pp. 110–115.

[51] Dong-Yun Lee; Hyeong-Ju Noh; Dong-Seok Hyun; Choy, I., "An improved MPPT converter using current compensation method for small scaled PV-applications," Applied

Power Electronics Conference and Exposition, 2003. APEC '03. Eighteenth Annual IEEE , vol.1, no., pp.540,545 vol.1, 9-13 Feb. 2003

[52] Esram, T.; Chapman, P.L., "Comparison of Photovoltaic Array Maximum Power Point Tracking Techniques," Energy Conversion, IEEE Transactions on , vol.22, no.2, pp.439,449, June 2007

[53] Chiang, S. J.; Chang, K.T.; Yen, C. Y., "Residential photovoltaic energy storage system," *Industrial Electronics, IEEE Transactions on* , vol.45, no.3, pp.385,394, Jun 1998

[54] Enrique, J. M.; Durán, E.; Sidrach-de-Cardona, M.; Andújar, J. M., "Theoretical assessment of the maximum power point tracking efficiency of photovoltaic facilities with different converter topologies," Sol. Energy, vol. 81, no. 1, pp. 31--38, Jan. 2007.

[55] Shmilovitz, D., "On the control of photovoltaic maximum power point tracker via output parameters," *Electric Power Applications, IEE Proceedings* - , vol. 152, no. 2, pp. 239- 248, March 2005.

[56] Gow, J.A.; Manning, C.D., "Development of a photovoltaic array model for use in power-electronics simulation studies," *Electric Power Applications, IEE Proceedings* - , vol. 146, no. 2, pp. 193-200, Mar.1999.

[57] González-Longatt, F. M., "Model of photovoltaic module in Matlab, "in *2do congreso iberoamericano de estudiantes de ingenierıacute;a eléctrica, electrónicay computación, ii cibelec*, 2005, pp. 1--5.

[58] Iov, F.; Ciobotaru, M.; Sera, D.; Teodorescu, R.; Blaabjerg, F., "Power Electronics and Control of Renewable Energy Systems," *Power Electronics and Drive Systems, 2007. PEDS '07. 7th International Conference on* , vol., no., pp.P-6,P-28, 27-30 Nov. 2007

[59] T. Shimizu, M. Hirakata, T. Kamezawa, H. Watanabe, "Generation Control Circuit for Photovoltaic Modules", IEEE Trans. On Power Electronics, Vol. 16, No. 3, May, 2001, pp. 293-300.

[60] H. Haeberlin, "Evolution of Inverters for Grid connected PV systems from 1989 to 2000", Proc. of Photovoltaic Solar Energy Conference, 2001.

[61] D. Picault , B. Raison , S. Bacha , J. de la Casa and J. Aguilera "Forecasting photovoltaic array power production subject to mismatch losses", Solar Energy, vol. 84, no. 7, pp.1301 -1309 2010

[62] Chouder, A. et al., 2009. Analysis model of mismatch losses in PV systems. Journal of Solar Energy Engineering 131 (May), 024504

[63] Gautam, N.K. et al., 2002. An efficient algorithm to simulate the electrical performance of solar photovoltaic arrays. Energy 27, 347–361.

[64] Kaushika, N.D. et al., 2003. Energy yield simulations of interconnected solar PV arrays. IEEE Transactions on Energy Conversion 18 (1), 127–134

[65] Kaushika, N.D. et al., 2007. An investigation of mismatch losses in solar photovoltaic cell networks. Energy 32, 755–759

[66] Meyer, E.L. et al., 2004. Assessing the reliability and degradation of photovoltaic module performance parameters. IEEE Transactions on Reliability 53 (1), 83–92.

[67] Van der Borg N.J.C.M. et al., 2003. Energy loss due to shading in BIPV application. In: 3rd World Conference on Photovoltaic Energy Conversion, Osaka, Japan, May 11–18, 2003, pp. 2220–2222.

[68] R. Bruendlinger, B. Bletterie, M. Milde, and H. Oldenkamp, "Maximum power point tracking performance under partially shaded PV array conditions," in Proc. 21st EUPVSEC, Dresden, Germany, Sept. 2006, pp. 2157–2160

[69] Weidong Xiao; Ozog, N.; Dunford, W.G., "Topology Study of Photovoltaic Interface for Maximum Power Point Tracking," Industrial Electronics, IEEE Transactions on , vol.54, no.3, pp.1696,1704, June 2007

[70] Karatepe, E. et al., 2007. Development of a suitable model for characterizing photovoltaic arrays with shaded solar cells. Solar Energy 81, 977–992

[71] Nguyen, D. et al., 2008. An adaptive solar photovoltaic array using model-based reconfiguration algorithm. IEEE Transactions on Industrial Electronics 55 (7), 980–986

[72] M.H. Kheraluwala, R. W. DeDoncker, D. M. Divan, " Power conversion apparatus for dc-dc conversion using dual active bridges", U.S patent, patent number 5,027,264, June 1991.

[73] M.H. Kheraluwala, R. W. DeDoncker, D. M. Divan, "Performance characterisation of a high-power Dual-Active Bridge dc-to-dc converter", IEEE Transc. on power electronics, Vol. 28, No. 6 November/December 1992

[74] M.H. Kheraluwala, R. W. DeDoncker, D. M. Divan, “A three-phase soft switched high-power-density dc-dc converter for high-power applications”, IEEE Transc. on industry applications, Vol. 27, No. 1, January/February 1991

[75] Gatlan, C.; Gatlan, L., "AC to DC PWM voltage source converter under hysteresis current control," *Industrial Electronics, 1997. ISIE '97., Proceedings of the IEEE International Symposium on* , vol.2, no., pp.469,473 vol.2, 7-11 Jul 1997

[76] H. Tao, “ Integration of sustainable energy sources through power electronic converters in small distributed electricity generation systems”, PhD Thesis, Eindhoven University of Technology, 2008.

[77] R. Erickson, “Fundamentals of power electronics”, Kluwer Academic, Publishers Group, ISBN 0-412-08541-0

[78] D. M. Mitchell, “DC-DC switching regulator analysis”, Published by DMMitchel Consultants, ISBN 0-07-042597-3

[79] R. D. Middlebrook, S. Cúk, “A general unified approach to modelling switching-converter power stages”, IEEE Power electronics specialists conference record, June 1976, pp. 18-34

[80] F. Barzegar, S. Cúk, R. D. Middlebrook, “ Using small computers to model and measure magnitude and phase of regulator transfer functions and loop gain”, Eighth international solid-state power electronics conference, April 1981

[81] S. Cúk, R. D. Middlebrook, “A general unified approach to modelling switching DC-to-DC converters in discontinuous conduction mode”, IEEE Power electronics specialists conference record, June 1977

[82] G. D. Demetriades, “On small-signal analysis and control of the single and the dual active bridge topologies,” KTH, Doctoral thesis, 2005.